UC Santa Barbara

UC Santa Barbara Electronic Theses and Dissertations

Title

Remote detection and localization of explosive volcanic eruptions, mass wasting, and ambient noise sources using infrasound: Applications in Alaska and Washington, USA

Permalink

Author

Sanderson, Richard

Publication Date

2021

Supplemental Material

Peer reviewed|Thesis/dissertation

UNIVERSITY OF CALIFORNIA

Santa Barbara

Remote Detection and Localization of Explosive Volcanic Eruptions, Mass Wasting, and

Ambient Noise Sources Using Infrasound: Applications in Alaska and Washington, USA

A dissertation submitted in partial satisfaction of the

requirements for the degree Doctor of Philosophy

in Earth Science

by

Richard W. Sanderson

Committee in charge:

Professor Robin Matoza, Chair

Professor Toshiro Tanimoto

Professor Chen Ji

December 2021

The dissertation of Richard W. Sanderson is approved.

_____

Toshiro Tanimoto

_____

Chen Ji

_____

Robin Matoza, Committee Chair

December 2021

Remote Detection and Localization of Explosive Volcanic Eruptions, Mass Wasting, and

Ambient Noise Sources Using Infrasound: Applications in Alaska and Washington, USA

iii

ACKNOWLEDGEMENTS

VITA OF RICHARD W. SANDERSON

December 2021

EDUCATION

Bachelor of Science in Geophysical Sciences, University of East Anglia, UK, July 2005

Master of Science in Geophysics, New Mexico Institute of Mining and Technology, May 2010
(after transferring from the University of New Hampshire)

Doctor of Philosophy in Earth Science, University of California, Santa Barbara, December 2021
(expected)

PROFESSIONAL EMPLOYMENT

2016–2021: Research, lab, field, and teaching assistant, University of California, Santa Barbara

2014–2015: Senior project scientist, International Earth Science IESE Ltd., Auckland

2012–2014: Seismology technician, Institute of Earth Science and Engineering, Auckland

2007–2011: Research, field, and teaching assistant, New Mexico Institute of Mining and Tech.

2006–2007: Research, field, and teaching assistant, University of New Hampshire

2005–2006: Research and field assistant, Universidad de Colima

PUBLICATIONS

ORCID: https://orcid.org/0000-0003-3772-4144

IN REVIEW

Sanderson, R. W., Matoza, R. S., Fee, D., Haney, M. M., and Lyons, J. J. (2021). Improving detection and localization of explosive volcanism in Alaska via infrasound noise reduction: backprojection and array processing applications. Submitted to *Geophysical Journal International*.

JOURNAL ARTICLES

Mendo-Pérez, G., Arciniega-Ceballos, A., Matoza, R. S., Rosado-Fuentes, A., **Sanderson, R. W.**, and Chouet, B. A. (2021). Ground-coupled airwaves template match detection using broadband seismic records of explosive eruptions at Popocatépetl volcano, Mexico. *Journal of Volcanology and Geothermal Research*, 419, 107378. https://doi.org/10.1016/j.jvolgeores.2021.107378

Sanderson, R. W., Matoza, R. S., Haymon, R. M., and Steidl, J. H. (2021). A pilot experiment on infrasonic lahar detection at Mount Adams, Cascades: Ambient infrasound and wind-noise characterization at a quiescent stratovolcano. *Seismological Research Letters*, 92(5), 3065–3086. https://doi.org/10.1785/0220200361

Fee, D., Toney, L., Kim, K., **Sanderson, R. W.**, Iezzi, A. M., Matoza, R. S., De Angelis, S., Jolly, A. D., Lyons, J. J., and Haney, M. M. (2021). Local explosion detection and infrasound localization by reverse time migration using 3-D finite-difference wave propagation. *Frontiers in Earth Science*, 9. https://doi.org/10.3389/feart.2021.620813

Sanderson, R. W., Matoza, R. S., Fee, D., Haney, M. M., and Lyons, J. J. (2020). Remote detection and location of explosive volcanism in Alaska with the EarthScope Transportable Array. *Journal of Geophysical Research: Solid Earth*, 125(4), e2019JB018347. https://doi.org/10.1029/2019JB018347

Matoza, R. S., Arciniega-Ceballos, A., **Sanderson, R. W.**, Mendo-Pérez, G., Rosado-Fuentes, A., and Chouet, B. A. (2019). High-broadband seismo-acoustic signature of Vulcanian explosions at Popocatépetl volcano, Mexico. *Geophysical Research Letters*, 46, 148–157. https://doi.org/10.1029/2018GL080802

Sanderson, R. W., Johnson, J. B., and Lees, J. M. (2010). Ultra-long period seismic signals indicate cyclic deflation coincident with eruptions at Santiaguito volcano, Guatemala. *Journal of Volcanology and Geothermal Research*, 198, 1–2. http://dx.doi.org/10.1016/j.jvolgeores.2010.08.007

Varley, N., Arambula-Mendoza, R., Reyes-Davila, G., **Sanderson, R.**, and Stevenson, J. (2010). Generation of Vulcanian activity and long-period seismicity at Volcán de Colima, Mexico. *Journal of Volcanology and Geothermal Research*, 198, 1–2. http://dx.doi.org/10.1016/j.jvolgeores.2010.08.009

Johnson, J. B., **Sanderson, R.**, Lyons, J., Escobar-Wolf, R., Waite, G., and Lees, J. M. (2009). Dissection of a composite volcanic earthquake at Santiaguito, Guatemala. *Geophysical Research Letters*, 36, L16308. http://dx.doi.org/10.1029/2009GL039370

CONFERENCES

ORAL PRESENTATIONS

Sanderson, R. W., Matoza, R. S., Fee, D., Haney, M. M., and Lyons, J. J. (2019). Remote detection and location of explosive volcanism in Alaska with the EarthScope Transportable Array. *American Geophysical Union (AGU) Fall Meeting, San Francisco, CA*.

Sanderson, R. W., and Lyons, J. J. (2019). Deployment and data collection: Permanent deployments (INVITED). *Community Network for Volcanic Eruption Response (CONVERSE) Infrasound Workshop, Fairbanks, AK*.

Neilsen, T. B., Matoza, R. S., Maher, S., McKay, M. G., **Sanderson, R. W.**, Valentine, G. A., Sonder, I., and Harp, A. G. (2019). Preliminary analyses of seismo-acoustic wave propagation in outdoor field-scale analog volcanic explosions (INVITED). *177th Meeting of the Acoustical Society of America (ASA), Louisville, KY*.

Sanderson, R. W., Matoza, R. S., Fee, D., Haney, M. M., and Lyons, J. J. (2018). Remote monitoring of explosive volcanism in Alaska with the EarthScope Transportable Array (INVITED). *American Geophysical Union (AGU) Fall Meeting, Washington, DC*.

Sanderson, R. W., Matoza, R. S., Fee, D., Haney, M. M., and Lyons, J. J. (2018). Remote explosive volcanic eruption detection, location, and characterization using the EarthScope Transportable Array in Alaska (INVITED). *Seismology of the Americas: Joint conference of the Seismological Society of America (SSA) and Latin American and Caribbean Seismological Commission (LACSC), Miami, FL*.

Johnson, J. B., Anderson, J., **Sanderson, R. W.**, Goto, A., Waite, G. P., and Palma, J. (2011). Intense monotonic infrasound at Volcan Villarrica: Insights from an Integrated seismo-acousto-optico-thermo-UV imager field approach (INVITED). *American Geophysical Union (AGU) Fall Meeting, San Francisco, CA*.

Johnson, J., Anderson, J., **Sanderson, R.**, Waite, G., and Palma, J. L. (2011). Into the vent – probing the basaltic lava lake at Volcan Villarrica (Chile). *25th International Union of Geodesy and Geophysics (IUGG) General Assembly, Melbourne, Australia.*

Johnson, J. B., **Sanderson, R.**, Lyons, J. J., Escobar-Wolf, R. P., Waite, G. P., and Lees, J. M. (2009). Dissection of a composite volcanic earthquake at Santiaguito, Guatemala (INVITED). *American Geophysical Union (AGU) Fall Meeting, San Francisco, CA.*

Sanderson, R. W., West. M., Shuler, A., and Lopez, T. (2009). Explosive seismic signals at Karymsky volcano 2008 (INVITED). *6th Biennial Workshop on Japan-Kamchatka-Alaska Subduction Processes (JKASP), Fairbanks, AK.*

Johnson, J. B, **Sanderson, R.**, Lees, J. M., Ruiz, M., Gerst, A., Hort, M., Scharff, L., Varley, N., and Sahagian, D. (2008). Lava dome soufflé: Long period earthquakes and co-eruptive volcano respirations captured with seismometers, video camera, and a Doppler radar. *International Association of Volcanology and Chemistry of the Earth's Interior (IAVCEI) Scientific Assembly*, Reykjavík, Iceland.

Johnson, J. B., Lees, J. M., and **Sanderson, R.** (2008). Co-eruptive earthquakes and lava dome respiration captured with seismometers and a video camera. *Seismological Society of America (SSA) Annual Meeting, Santa Fe, NM.*

Johnson, J. B., Varley, N., **Sanderson, R.**, Gerst, A., Lees, J., Dalton, M., Marcillo, O., Every, S., Normand, J., and Ruiz, M. (2007). Eruption dynamics at the active Santiaguito dome inferred from a multidisciplinary geophysical experiment. *American Geophysical Union (AGU) Fall Meeting, San Francisco, CA.*

Johnson, J. B., Lees, J. M., **Sanderson, R.**, Sahagian, D., and Normand, J. A. (2007). Dome surges, long period earthquake generation, and pyroclastic eruptions at Santiaguito dome, Guatemala. *American Geophysical Union (AGU) Fall Meeting, San Francisco, CA.*

Johnson, J. B., **Sanderson, R.**, Every, S., Normand, J., and Marcillo, O. (2007). Eruption dynamics at the active Santiaguito dome inferred from a multidisciplinary geophysical experiment. *Geological Society of America Northeastern Section Meeting, Durham, NH.*

Varley, N., Stevenson, J., Johnson, J. B., Colvin, A., Weber, K., **Sanderson, R.**, Hébert, M.-C., and Reyes, G. (2006). Modeling conduit processes at Volcán de Colima, Mexico: interpretation of monitoring data. *Reunión Anual Unión Geofísica Mexicana (UGM), Puerto Vallarta, Mexico.*

Varley, N., Stevenson, J., Johnson, J. B., Reyes, G., Sword-Daniels, V., Colvin, A., Weber, K., **Sanderson, R.**, and Harwood, R. (2006). Modeling conduit processes at Volcán de Colima, Mexico. *Physics of Fluid Oscillations in Volcanic Systems Workshop, Lancaster, UK.*

POSTER PRESENTATIONS

Mendo-Pérez, G. M., Arciniega-Ceballos, A., Matoza, R. S., Rosado-Fuentes, A., **Sanderson, R. W.**, and Chouet, B. A. (2021). Automatic detection of seismic signals associated with infrasound airwaves in broadband seismic records from Popocatépetl Volcano, Mexico. *American Geophysical Union (AGU) Fall Meeting, New Orleans, LA.*

Sanderson, R. W., Matoza, R. S., Fee, D., Haney, M. M., and Lyons, J. J. (2020). Infrasonic backprojection with the EarthScope Transportable Array in Alaska: Improving detection and localization of explosive volcanism via noise reduction. *American Geophysical Union (AGU) Fall Meeting, Online.*

Maher, S. P., Matoza, R. S., Gee, K. L., de Groot-Hedlin, C., Fee, D., Jolly, A. D., Yokoo, A., Arciniega, A., **Sanderson, R. W.,** and Ortiz, H. D. (2020). Nonlinear acoustic propagation single-point spectral indicator: Comparative performance analyses for Sakurajima, Yasur, Popocatépetl, Augustine, Nabro, Reventador, Tungurahua, Villarrica, Cotopaxi, and Calbuco explosion waveforms. *American Geophysical Union (AGU) Fall Meeting, Online*.

Fee, D., Toney, L. D., Matoza, R. S., **Sanderson, R. W.**, Haney, M. M., Lyons, J. J., Iezzi, A. M., Kim, K., De Angelis, S., Diaz Moreno, A., and Jolly, A. D. (2019). A framework for improved infrasound back-projection on local and regional scales. *American Geophysical Union (AGU) Fall Meeting, San Francisco, CA*.

Mendo-Pérez, G. M., Matoza, R. S., Arciniega-Ceballos, A., Rosado-Fuentes, A., **Sanderson, R. W.,** Castaneda, E., and Chouet, B. A. (2019). Automated detection of air-ground coupled waves at Popocatépetl Volcano, Mexico. *American Geophysical Union (AGU) Fall Meeting, San Francisco, CA*.

Mendo-Pérez, G. M., Matoza, R. S., Arciniega-Ceballos, A., Rosado-Fuentes, A., Castaneda, E., **Sanderson, R. W.**, and Chouet, B. A. (2019). Automated explosion detection using ground-coupled air-waves at Popocatépetl volcano, Mexico. *27th International Union of Geodesy and Geophysics (IUGG) General Assembly, Montreal, Canada.*

Sanderson, R. W., Matoza, R. S., Haymon, R. M., Steidl, J. H., and Hegarty, P. (2018). Lahar detection using infrasound: Pilot experiment at Mount Adams, WA. *American Geophysical Union (AGU) Fall Meeting, Washington, DC.*

Neilsen, T. B., Matoza, R. S., Waite, G. P., Medici, E. F., Valentine, G., Sonder, I., Harp, A., Maher, S., **Sanderson, R. W.**, Butts, C., Escobedo, J. A., Hawkes, M. R., Lopez, C. A., Lysenko, E., and McKay, M. G. (2018). Seismo-acoustic measurements of an outdoor, field-scale, explosive "volcano". *American Geophysical Union Fall Meeting, Washington, DC.*

Sanderson R. W., Matoza, R. S., Haymon, R. M., Steidl, J. H., and Hegarty, P. (2018). Investigating the utility of infrasound arrays for lahar detection: Pilot experiment at Mount Adams, WA. *Incorporated Research Institutions for Seismology (IRIS) Workshop: Foundations, Frontiers, and Future Facilities for Seismology, Albuquerque, NM.*

Sanderson, R. W., Matoza, R. S., Fee, D., Haney, M. M., and Lyons, J. J. (2018). Remote explosive volcanic eruption detection, location, and characterization using the EarthScope Transportable Array in Alaska. *Incorporated Research Institutions for Seismology (IRIS) Workshop: Foundations, Frontiers, and Future Facilities for Seismology, Albuquerque, NM.*

Arciniega-Ceballos, A., Matoza, R., **Sanderson, R.**, Mendo-Pérez, G., Rosado-Fuentes, A., and Chouet, B. (2018). Infrasound array study at Popocatépetl. *European Geosciences Union (EGU) General Assembly, Vienna, Austria.*

Sanderson, R. W., Matoza, R. S., Fee, D., Haney, M. M., and Lyons, J. J. (2017). Remote explosive volcanic eruption detection, location, and characterization using the EarthScope Transportable Array in Alaska. *International Association of Volcanology and Chemistry of the Earth's Interior (IAVCEI) Scientific Assembly, Portland, OR.*

Sanderson, R. W., Matoza, R. S., Fee, D., Haney, M. M., and Lyons, J. J. (2017). Remote explosive volcanic eruption detection, location, and characterization using the EarthScope Transportable Array in Alaska. *EarthScope National Meeting, Anchorage, AK.*

Sanderson, R. W., Johnson, J. B., Waite, G. P., Lees, J. M. (2009). Ultra-long period seismic signals indicate cyclic deflation coincident with eruptions at Santiaguito volcano, Guatemala. *American Geophysical Union (AGU) Fall Meeting, San Francisco, CA*.

Goto, A., Johnson, J. B., **Sanderson, R. W.**, Anderson, J., and Varley, N. R. (2010). Vent geometry detected from infrasound observation on Villarrica volcano, Chile. *American Geophysical Union (AGU) Fall Meeting, San Francisco, CA.*

Sanderson, R. W., Johnson, J. B., and Lees, J. M. (2008). Seismic precursors to episodic eruptive events at Santiaguito volcano. *Seismological Society of America (SSA) Annual Meeting, Santa Fe, NM.*

Sanderson, R. W., and Johnson, J. B. (2007). Pre-eruptive seismicity associated with explosive events at Santiaguito volcano, Guatemala. *American Geophysical Union (AGU) Fall Meeting, San Francisco, CA.*

Varley, N., Stevenson, J., Johnson, J. B., Reyes, G., Weber, K., and **Sanderson, R.** (2006). Vulcanian explosions at Volcán de Colima, Mexico: Modelling the conduit processes. *American Geophysical Union (AGU) Fall Meeting, San Francisco, CA.*

Sanderson, R., Varley, N., Reyes-Davila, G., Johnson, J. B., and Murphy, C. (2005). The relationships between explosive plumes generated and the corresponding seismic and acoustic waveforms received at Volcán de Colima, Mexico. *Reunión Anual Unión Geofísica Mexicana (UGM), Puerto Vallarta, Mexico.*

FIELD EXPERIENCE

Broadband seismic and/or infrasound station deployments and/or maintenance (volcanoes):

Mount Adams, Washington, USA (2017, 2018, 2021)
Popocatépetl, Mexico (2017)
Villarrica, Chile (2010, 2011)
Chaitén, Chile (2010)
Karymsky, Kamchatka, Russia (2008)
Bezymianny, Kamchatka, Russia (2008)
Santa Maria/Santiaguito, Guatemala (2007, 2009)
Tungurahua, Ecuador (2007)
Volcán de Colima, Mexico (2005, 2006)

Borehole seismic station deployments and/or maintenance (geothermal fields, tectonic settings):

Okuaizu, Japan (2015)
Hyderabad, India (2014)
Latrobe, Australia (2014)
Rangitoto, New Zealand (2014)
Whataroa, New Zealand (2013)
Wairakei, New Zealand (2012–2015)

AWARDS

Through the Department of Earth Science, University of California, Santa Barbara:

Harry Glicken Memorial Graduate Fellowship (2021)
Coast Geological Society Scholarship (2020)
Richard V. Fisher Scholarship in Volcanology (2019)
Preston Cloud Memorial Award (2019)
Geophysics Award (2018)
Graduate Opportunity Award (2017, 2018)
Global Field Travel Award (2017)

ABSTRACT

Remote Detection and Localization of Explosive Volcanic Eruptions, Mass Wasting, and

Ambient Noise Sources Using Infrasound: Applications in Alaska and Washington, USA

by

Richard W. Sanderson

The majority of potentially active volcanoes worldwide are not well monitored. Eruptions and surficial mass wasting activity can go entirely undetected. Low-frequency acoustic waves known as infrasound can provide valuable information for remotely detecting, locating, and modeling these hazardous volcanic processes. Infrasound is produced by sources coupled to the atmosphere, with signals often able to propagate further than seismicity in the solid earth, and without need for line of sight (e.g., cloud cover).

The overall aim and contribution of this dissertation is toward improving volcanic event detection and localization workflows at local (< 15 km), regional (15–250 km), and remote (> 250 km) distances from the source, using a variety of sensor network configurations. These topics include effective use of dense regional infrasound networks, the impact of pre- and post-recording data noise-reduction, and the role of local infrasound monitoring in surficial mass wasting observations. Together, three principal projects demonstrate some of the benefits and limitations of various signal processing and detection techniques, site selections, and station hardware designs.

Dense infrasound sensor deployments on a regional scale, such as the EarthScope Transportable Array (TA) in Alaska, can fill the observational gap between local and global scale volcano monitoring. The rolling TA uses ~80 km spaced single-sensor stations. In comparison, several small infrasound arrays (< 1 km), each with multiple sensors, already populate the area. Volcanic explosion detection and location using a backprojection (delay and stack) scheme achieves relatively limited success solely using TA-type sensors. Backprojection with the small arrays offers greater performance in terms of the number of events detected, and location accuracy. This is due to their shorter source-station distances, lower interstation spacing, higher azimuthal coverage, and more efficient wind-noise reduction hardware. Traditional array processing with the small arrays typically offers higher event detection rates than backprojection.

Improvements can be made to the aforementioned detection and location schemes by using signal processing techniques to first isolate volcanic events from background noise sources. Such sources include incoherent wind noise, and pervasive ambient infrasound, primarily microbaroms (ocean wave-wave interaction source). Microbarom reduction typically improves array processing and enhances detection of weak events. Wind-noise reduction does not affect such detection rates, indicating sufficient turbulence can make coherent signal information unrecoverable. This approach does, however, improve the signal-to-noise ratios of isolated or stacked waveforms.

At local infrasound monitoring scales relevant to relatively low-amplitude mass wasting signal detection, an additional ambient infrasound noise source with critical influence on detection capability arises from waterfalls, and other fluvial turbulence (river noise). At structurally unstable locations such as Mount Adams, Washington, large mass wasting events (e.g., lahars) are expected to propagate down the same fluvial channels

responsible for this clutter. In addition to wind and microbaroms, this temporally and spatially varying fluvial infrasound can significantly affect detection thresholds. Wind noise precluded detection of several witnessed small debris flows below the summit. Conversely, such flows were not visually observed for a range of signals that are characteristic of mass wasting. A well-constrained glacial avalanche provides an exception, permitting assessment of detection and location schemes, and other techniques.

TABLE OF CONTENTS

Chapter 1. Introduction

1. Overview

Volcanoes exist in a range of states, from extinct, to dormant, to actively erupting (e.g., Carn et al., 2009). Tracking and understanding the transition between such states is a key objective in volcanology (e.g., Gottsmann et al., 2019). Monitoring for activity inside and outside the edifice ideally involves adding different kinds of sensors directly on and nearby the volcano, and then analyzing the data in close to real time (e.g., McNutt, 2015). Many volcanoes worldwide have limited to no on-ground monitoring stations, however, despite potential hazards to local populations and air traffic (National Academies of Sciences, Engineering, and Medicine, 2017). Detection of volcanic activity at such locations from remote stations provides a means to identify hazards sooner, and so potentially provide useful warnings (e.g., Coombs et al., 2018). This research aims to identify and evaluate data processing algorithms which can improve the current state of remote detection and location systems. Infrasound, i.e., far-reaching, low frequency sound waves, provides the main data source in this work (e.g., Evers and Haak, 2010; Matoza et al., 2019). This chapter will provide an introduction to the study by first providing the broader context and identifying knowledge gaps, then developing research aims and objectives, and finally, laying out the key contributions to the field.

2. Background

2.1. What is Infrasound?

Physical perturbations of the atmosphere generate acoustic waves, which consist of compressions (high pressure), and rarefactions (low pressure). Oscillations of the medium are in the same direction as that of propagation. Such waves traveling through the ground are

termed seismic P-waves, and those in water as hydro-acoustic. Liquids and gases are unable to support the shear motions comprising other elastic wave types. The frequency of a wave, measured in Hz, not only reflects how quickly the source was vibrating, but also the dimensions of that source. Low frequency waves are more easily produced by phenomena with larger length scales. Humans are typically able to hear frequencies between 20 Hz, and 20,000 Hz, with many animals able to hear outside of this range. Infrasound is the name given to sub-20 Hz frequencies, with those above 20 kHz referred to as ultrasound.
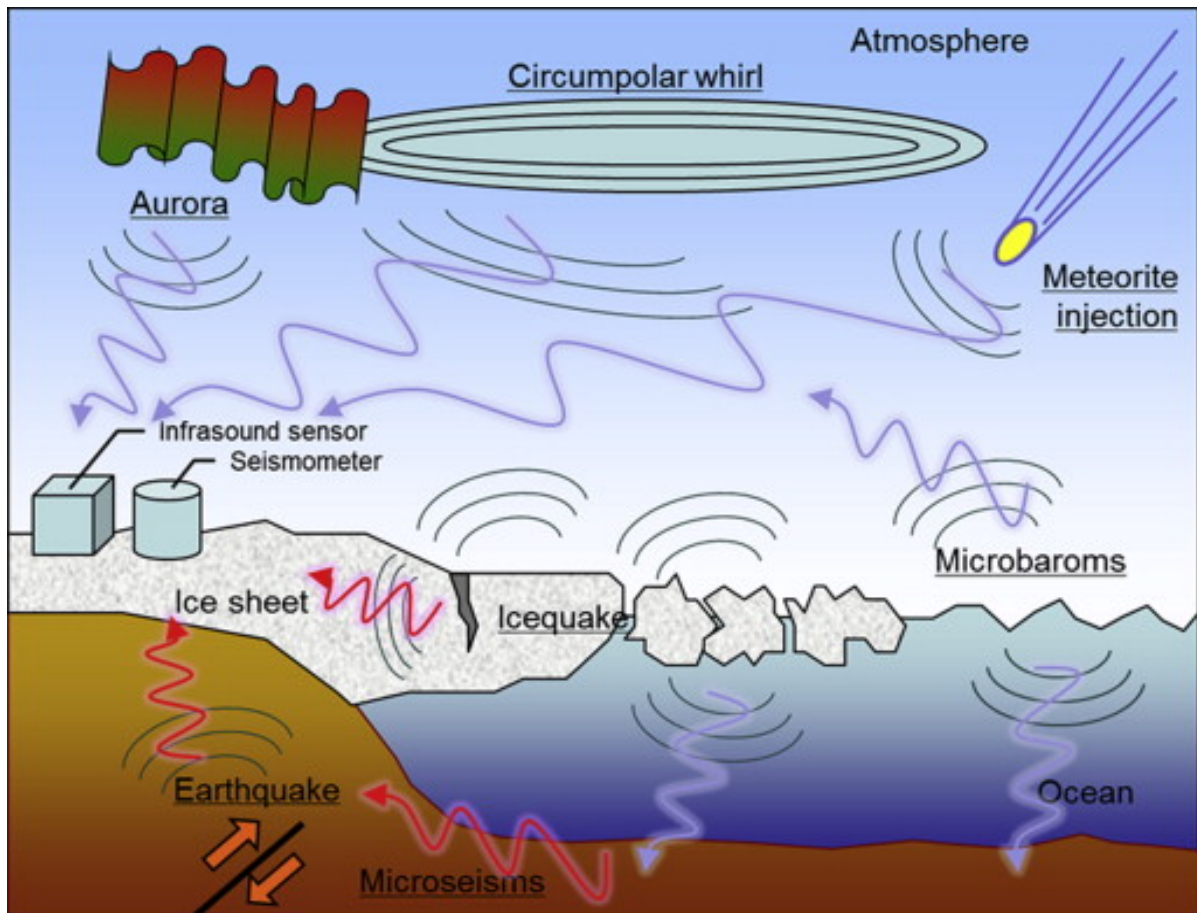
Figure 1. Generation and recording of elastic waves by natural processes. Depending on the medium of travel, these vibrations are termed acoustic (atmosphere), seismic (ground, ice), or hydro-acoustic waves (water). Compressional waves can travel through all materials, whereas shear waves are only supported by solids. At interfaces, waves may be transmitted (coupled), refracted, or reflected, sometimes involving a change of wave type, e.g., from shear to compressional. Figure reprinted from Murayama et al. (2015), with permission from Elsevier.

There are many natural and artificial sources of infrasound worldwide (e.g., Campus and Christie, 2010, and references therein). Natural causes include nonlinear wave-wave interactions in the ocean (microbaroms), volcanoes, earthquakes, aurorae, lightning, bolides, tornadoes, and mass movements. Common anthropogenic sources include mine and military blasts, aircraft, rocket launches, and wind turbines. Figure 1 illustrates some examples of these processes, and how the resulting vibrations can travel through different media.

Coupling between the ground and air means that not all infrasound is necessarily directly radiated into the atmosphere at an original source (i.e., primary, or epicentral infrasound). For instance, in the case of earthquakes, much of the energy travels through the ground as seismic waves before arriving back at the surface, a fraction of which is then coupled into the atmosphere as secondary/indirect infrasound. Such coupling is typically observed in regions of topography (e.g., Arrowsmith et al., 2010; Shani-Kadmiel et al., 2018b). Similarly, air-to-ground coupling may also occur, where infrasound is recorded on seismic sensors (e.g., Braun and Ripepe, 1983; Chunchuzov et al., 2013).

Infrasound propagation is largely controlled by changes in temperature with elevation, as well as wind speed, and wind direction. In an ideal gas, the speed of sound is proportional to the square-root of temperature (Pierce, 1981). At sea level, 338 m/s is typical speed for temperatures of 10 °C, for example. As elevation increases through the troposphere, the temperature decreases, before increasing again through the stratosphere (e.g., Evers and Haak, 2010). This temperature structure causes infrasound to refract upwards from sources close to the ground. Once the infrasound waves reach an elevation where the sound speed is greater than that at their origin, the waves will refract downward. Tropospheric and stratospheric winds in particular can affect this refraction by either positively contributing to the wind speed, or detracting from it (e.g., Georges and Beasley,

1977). Sources are generally more detectable downwind due more refraction toward the ground, but shadow zones may still exist between predicted atmospheric returns (e.g., Hedlin and Walker, 2013). Reflections at the surface, and again in the upper atmosphere, set up waveguides that lead to long-range infrasound ducting. Relatively little energy is lost from the resulting cylindrical, rather than spherical, wave-front spreading (Pierce, 1981). Energy absorption is still an attenuating factor, however, particularly at higher frequencies (Sutherland and Bass, 2004). Spatially and temporally varying atmospheric properties mean that records of infrasound vary with azimuth, as well as distance from the source (e.g., Schwaiger et al., 2020). Repeating sources of infrasound can be used to help model atmospheric structures, just as earthquakes provide information on the interior of the earth (e.g., Haney, 2009).

Infrasound is predominantly detected by microphones that measure pressure fluctuations relative to ambient atmospheric levels (e.g., Johnson and Ripepe, 2011; Nief et al., 2019). These sensors are typically arranged in configurations known as an array such that there are multiple sensors detecting each passing wavelength (e.g., Marty et al., 2019). These waves are considered to be coherent across the different sensors, and wavefield parameters can be calculated, including the back azimuth, and apparent velocity. If sensors are further apart, and coherence is not present, then the configuration is known as a network. Different sets of processing techniques are used to locate events with arrays or networks to take advantage of each geometry (e.g., Fee et al., 2016; Park et al., 2017).

Recorded infrasound signals will be a mixture of those of interest, and those that are not. This latter group is sometimes described as "clutter" in the sense that such features clutter up the data landscape (e.g., Matoza et al., 2007). The most common clutter source tends to be microbaroms, as these low frequency signals (~0.1–0.5 Hz) have sources

globally, and also can propagate great distances (e.g., Willis et al., 2004). Amplitudes tend to be low, however, typically < 0.5 Pa. Turbulent waters in the form of rapids and waterfalls can also be ongoing clutter sources (e.g., Johnson et al., 2006; Schmandt et al., 2013). Wind is the primary noise source in infrasound data, and is not an acoustic wave, but rather reflects air masses moving due to spatial differences in atmospheric pressure (e.g., Raspet et al., 2006). Wind noise may mask signals of interest, unless care is taken in station design, site location, and other approaches detailed in later sections (e.g., Raspet et al., 2019).

2.2. Volcano Infrasound

Shallow and subaerial volcanic processes such as eruptions are able to efficiently perturbate the atmosphere, making volcanoes excellent sources of sound at a range of frequencies. Whereas those living around volcanoes would typically have been able to hear any eruptive activity, it is only since the invention of pressure recording technologies that the full frequency spectrum has been documented. The following is a brief summary of a historical review of volcano infrasound by Fee and Matoza (2013): Barometers were able to capture < 1 Hz information from several major eruptions between the late 19th and mid-20th centuries, including Krakatau Volcano, Indonesia (1883), Mount Pelée, Martinique (1902), and Bezymianny, Russia, (1956) (e.g., Strachey, 1888; Tempest and Flett, 1903; Gorshkov, 1960). These types of large events are able to generate signal frequencies of only a few mHz, enabling waves to circle the earth multiple times. Developments in sensor and recording technology, particularly since the 1980s (e.g., Dibble et al., 1984), have facilitated recordings of eruptions across wider parts of the acoustic spectrum, with most volcanic activity observed in the infrasound range from 0.1 to 20 Hz (e.g., Johnson, 2003).

Just as infrasound technology has advanced, so has the range of investigations being conducted. From distinguishing between eruptions and seismic-only sources (e.g., Omori,

1912, at Mount Asama, Japan), to early atmospheric propagation studies (e.g., Wilson et al., 1966), the aim of many recent works has been a combination of event detection, location, characterization, and modeling. Common measurements extracted from infrasound records are arrival times, waveform shape, cumulative energy, frequency content, peak pressures, and coda durations (e.g., Johnson and Ripepe, 2011). Such metrics are comparable over time at the same location, as well as between volcanoes (Figure 2). These basic measures can help infer useful information about eruption style, the flux of gas, solids, and energy (e.g., Vergniolle et al., 2004; Delle Donne et al., 2016), which of several craters are active (e.g., Ripepe and Marchetti, 2002; Fee et al., 2021), geometries of craters and conduits (e.g., Buckingham and Garcés, 1996; Watson et al., 2019), source directivity (e.g., Kim et al., 2012; Jolly et al., 2017), plume height (e.g., Caplan-Auerbach et al., 2010; Fee et al., 2017a), and explosion source depths (e.g., Ruiz et al., 2006; Iezzi et al., 2020). Infrasound is thereby also able to help validate observations in multi-disciplinary studies (and vice-versa), by providing an independent estimate of source parameters (e.g., Fee et al., 2017b). The ratio between acoustic and seismic amplitudes (e.g., Johnson and Aster, 2005), energy (Hibert et al., 2015), or frequencies (e.g., Fee et al., 2020), can also offer some insight into volcanic conditions, as partitioning of eruption energy between the ground and atmosphere can depend on magma composition, conduit geometry, and plume density, among other factors.

Infrasound studies will be tailored to the behavior at a specific volcano, with different source processes leading to variable observable activity and acoustic characteristics. Following is a brief summary of this spectrum, with the reader referred to e.g., reviews by Johnson and Ripepe (2011), and Fee and Matoza (2013), for more comprehensive information. Hawaiian-style activity typically features lava fountaining, degassing, and gentle, if rapid, effusions, rather than explosions. Resonance and oscillations in materials and

cavities during these processes generate sustained tremor signals that may be broadband (containing a wide range of frequencies), or harmonic (exhibiting one or more spectral peaks) (e.g., Garcés et al., 2003). Strombolian and Vulcanian styles are more explosive, often producing short-duration N-waves (a compression then rarefaction), followed by variable length and style of tremor. The underlying mechanisms differ, however. Strombolian activity is characterized by bursting gas slugs at a relatively low-viscosity magma surface (e.g., Hagerty et al., 2000). In contrast, Vulcanian explosions occur following the pressure-induced failure of a solidified magma cap or plug (e.g., Peterson et al., 2006). Subplinian, and Plinian, are names given to the largest and most explosive eruption styles. Such events may last from minutes to hours, with high-amplitude broadband infrasound principally generated by turbulence-inducing jets of rapidly rising material (e.g., Fee et al., 2010b). A secondary source of infrasound, particularly for larger eruptions, are pyroclastic density currents (PDCs). These are hot mixtures of gas and fragmented magma that flow down volcanoes following the collapse of lava fountains or eruption columns. Moving, broadband acoustic sources, are the result (e.g., Ripepe et al., 2010).

Volcanoes can produce other hazardous activity than eruptions, and such events are also critical to monitor closely for mitigation and scientific purposes. Examples include mass movements in the form of lava dome rock falls, edifice collapse, and remobilization of existing loose material by rain or glacial melt (e.g., Allstadt et al., 2018). These latter cases may generate fluidized debris flows known as lahars, which can travel 10s of kilometers and bury towns in mud (e.g., Pierson et al., 1990). As with PDCs, such flows can produce infrasound, as well as seismic signals, as air is displaced and made turbulent though flow surface interactions (e.g., Johnson and Palma, 2015; Bosa et al., 2020). Large avalanches may be detected more than 100 km away (e.g., Toney et al., 2021).

Local distances ($<$ 15 km) are usually optimal for quantifying and interpreting volcanic processes, where atmospheric heterogeneities are reduced, and attenuation due to geometric spreading is limited. In this region, acoustic waves are often assumed or found to behave linearly (e.g., Fee et al., 2017b). Under these conditions, amplitudes decay as $1/r$, where r is the radius from the vent. Such a decay rate allows computation of "reduced amplitudes", i.e., what the pressure would be at a specific recording distance (Figure 2). This enables measurement comparisons between volcanoes which often have different network geometries. However, some scenarios preclude source processes being clearly preserved in infrasound waveforms. For large, and/or supersonic eruptions recorded at close range, nonlinear behavior and wave distortion may be observed, resulting from highly compressed air (Hamilton and Blackstock, 2008). In addition, the effects of volcanic topography can manifest in proximal measurements, given that craters, and sometimes multiple cones, can reflect and refract waves, as well as create shadow zones (e.g., Matoza et al., 2009). These effects offer exciting research opportunities in their own right, with advances facilitated by modern computer power, digital elevation models, and suites of propagation modeling codes (e.g., Kim and Lees, 2014; Waxler et al., 2017). Being aware of, and potentially compensating for any such distortions, is important for valid infrasound data interpretation.

2.3. Remote Detection of Volcanic Processes – an Overview

Many volcanoes worldwide are directly or indirectly monitored at remote distances ($>$ 15 km), potentially in complement to having a sparse or dense network of telemetered instruments on the volcano itself (e.g., Fee et al., 2010b; Le Pichon et al., 2021). For volcanoes where there is little concern about potential eruptions or activity, remote observations may be the only eventual insight. Such remote data types may include
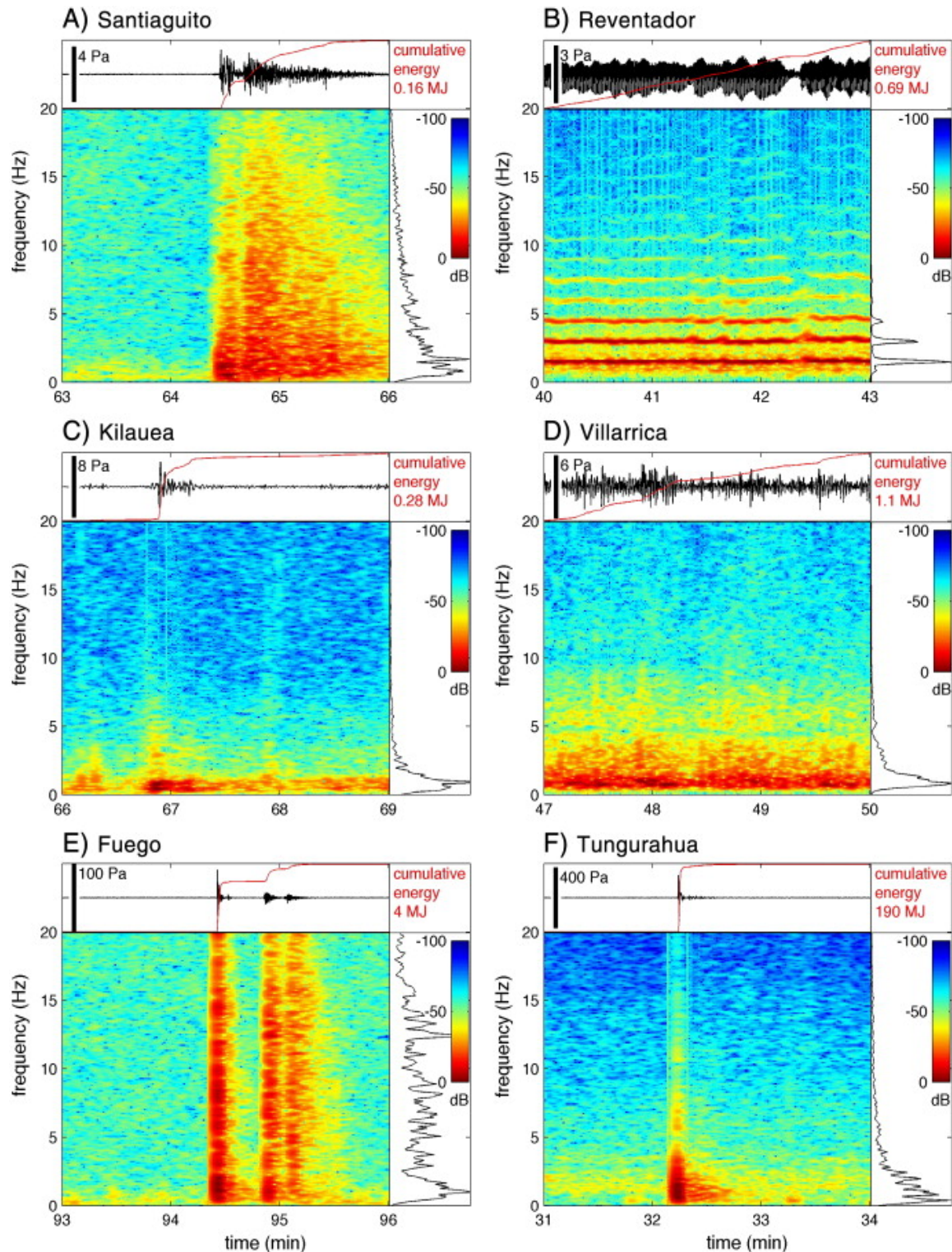
Figure 2. Volcanoes can produce a wide range of infrasound signals during eruptions in terms of duration, frequency, amplitude, and other characteristics. Here are six examples of waveforms (top panels), cumulative energy (red line and text), spectrograms, (bottom left panels), and mean power spectra (bottom right panels) from a variety of volcanoes in Hawai'i, Central America, and South America. Data are filtered 0.5–50 Hz. Waveform amplitudes in units of Pa are the equivalent values at 1 km from the respective volcanic vents. Figure reprinted from Johnson and Ripepe (2011), with permission from Elsevier.

seismicity, indicative of both pre-eruptive (e.g., Chouet and Matoza, 2013) and eruptive process, as well as infrasound, and radio signals from in-plume lightning (e.g., Van Eaton et al., 2016). Satellite observations may come in the form of visual records, temperature, gas type, ash, and deformation (e.g., Pyle et al., 2013, and references therein).

The effectiveness of monitoring instruments is often limited by the area of which they can provide useful information about, as well as signal to noise ratios (SNR). Infrasound signals from eruptions are frequently observed at greater distance from the source than seismic waves (overviews by Arrowsmith et al., 2010; Fee and Matoza, 2013). Such large distances can be attributed to: 1) relatively low attenuation and scattering of the atmosphere vs. the solid earth; 2) atmospheric waveguides that minimize energy loss; and 3) efficient eruptive source coupling with the atmosphere via direct injection. Consequently, many remote eruptions are detectable through infrasound at distant stations, and in some cases, these detections may reflect the only record that an event is occurring (e.g. Matoza et al., 2011; De Angelis et al., 2012). Such factors also mean that infrasound can often offer greater insights into eruption dynamics than seismicity. Satellite observations, and marine or aircraft reports can also contribute to the knowledge on a new or developing situation, but these cannot be relied upon as a primary tool due to sporadic, weather affected observation (e.g., Webley and Mastin, 2009; Coombs et al., 2019).

3. Research Problem

3.1. Problem to be Addressed

Despite recent developments and expansion in volcano monitoring, the vast majority of potentially active volcanoes worldwide are not well monitored by ground-based sensors, despite the potential hazards (National Academies of Sciences, Engineering, and Medicine,

2017). This scenario may be for monetary, logistical, technical, or other reasons. Consequently, it is important to be able to devise means to still effectively monitor such volcanoes during various stages of volcanic unrest despite these limitations. It is further critical to be able to perform the process in close to real time, particularly when hazard to aviation can be the most immediate danger, rather than to local populations (e.g., Neal et al., 1997; Dean et al., 2002). As outlined earlier, infrasound can be an important part of the solution, and forms the principal data type in this dissertation.

3.2. Key Facets of the Problem

Some of the principal aspects of the above posited issue are as follows: (1) designing and siting stations to be able to record physical processes of interest; (2) identifying effective processing techniques to locate distant and possibly small eruptive or other subaerial events; (3) understanding source, path, and site effects on recorded waveforms and, therefore, on interpretation/modeling; (4) determining strategies to efficiently use systems in a real time and ongoing manner.

3.3. Previous Work

3.3.1. Network and Array Concepts

The remote detection capability of infrasound has led to its use in observations of large eruptions worldwide (e.g., Modrak et al., 2010; Dabrowa et al., 2011; Matoza et al., 2011; Matoza et al., 2017) through the use of the International Monitoring System (IMS) – a global sensor network (53 of the planned 60 stations have been completed at the time of writing; https://www.ctbto.org/map/). The network includes infrasound sensors and is designed for nuclear blast detection (e.g., Marty et al., 2019). These infrasound stations have an average station spacing of 2,000 km, however, and provide limited resolution in terms of

location accuracy and detection sensitivity. For volcanoes, the detection threshold corresponds to a volcanic explosivity index (VEI) of ~VEI 4 (Matoza et al., 2017).

At regional scales, examples of infrasound networks are few, particularly with a dense station spacing. From ~2007–2021, the EarthScope Transportable Array (TA) provided such a resource. The TA was a set of hundreds of multi-disciplinary stations that moved across the US, spaced on the order of tens of kilometers (Busby et al., 2018; Busby and Aderhold, 2020). Initially designed primarily around seismic sensors, infrasound sensors were included from ~2011. Air-to-ground coupling was recorded on seismometers prior to this date, however (e.g., Walker et al., 2010; Nippress et al., 2014). The ubiety of the TA in Alaska (~2014–2021) was unprecedented from a volcanological and geophysical standpoint. At this outset, the Alaska Volcano Observatory (AVO) had four infrasound arrays covering mainland Alaska and the Aleutian Islands (e.g., Dixon et al., 2019), amongst other instrumentation. The value of these arrays has been well demonstrated in the years since (e.g., Lyons et al., 2019), justifying the number of arrays growing to 9 at the time of writing. The contemporary presence of the TA significantly increased azimuthal and spatial coverage of infrasound sources, as well as decreasing the average station spacing.

Studies of volcanic infrasound use analytical techniques applicable to the scale of their networks and the spatial configuration of sensors. Such scales have been of a local, regional or global dimension, with use of single sensors or dense arrays (e.g., Fee et al., 2010a, Fee et al., 2016 locally/regionally; Dabrowa et al., 2011, Matoza et al., 2017, globally). Array processing is traditionally limited to instances where the wavelengths of signals are coherent across multiple stations. Three or more arrays are commonly required for source locations from back-azimuth triangulation, with crosswinds affecting source estimates (e.g. Le Pichon et al., 2005; Green et al., 2012). IMS operation/design uses a

minimum of two station detection, however. Array processing is useful for detecting moving infrasound sources such as storm-induced microbaroms (Blom et al., 2014), tornadoes (e.g., Frazier et al., 2014), and mass movements (e.g., Allstadt et al., 2018, and references therein).

Typical sound speeds (300–350 m/s) and infrasound frequencies of interest (~0.1–20 Hz), provide a limit to how far stations can be from each other before coherence-dependent techniques breakdown. For instance, to avoid spatial aliasing, two sensors are required per wavelength. One way to deal with this limitation is to create envelopes of the original data (a smoothed positive version of the original signal) by taking the magnitude of a Hilbert transform of the data (e.g., Walker et al., 2010). This serves to make the wavelength more appropriate for the spacing of the available stations as well as emphasizing the main variability of the data. Conversely, accurately resolving fine-scale locations is more challenging with these low-frequency time-series (Walker et al., 2010; de Groot-Hedlin and Hedlin, 2015).

3.3.2. TA-Implemented Detection and Location Algorithms

The following is a brief review of some example signal detection and location methodologies previously applied to TA acoustic data, which serves to provide background for TA-related material in the remainder of this chapter, and as general insight into some of the range of detection and location schemes available.

Both Walker et al. (2010), and Walker et al. (2011), describe application of a Reverse Time Migration (RTM) method to locate infrasound-generating events recorded on seismometers. Briefly, RTM identifies potential locations as those that would lead to the largest amplitude stack of waveforms or envelopes, if aggregated using an acoustic velocity model. For any particular area, a spatial or volumetric grid is set up so that each grid intersection is tested as a likely source position. Further, the origin time of the signal is also

assessed using a similar grid of equally spaced trial times. RTM had previously been applied, for example, by Shearer (1994) on seismic, rather than infrasound, data. Stacking is an approach most effective when large numbers of stations are available, so that constructive and deconstructive interference effects are emphasized. Using waveform envelopes helps ensure coherence when using acoustic data recorded on TA stations.

Nippress et al. (2014) also locate events with air-to-ground coupled waves, here using an iterative least-squares inversion (Geiger, 1910, 1912). This approach identifies a source location and origin time by minimizing the residual between observed arrival times at stations, and those predicted by trialed combinations of spatial and velocity parameters. Two studies that use both arrival time information for TA stations, and back azimuth information from nearby arrays are those by Pinsky et al. (2017) and Vergoz et al. (2019). Probability density functions give source location estimates. All three methods mentioned here incorporate information about atmospheric propagation to improve location estimates.

In a another approach, de Groot-Hedlin and Hedlin (2015) subdivided the TA into numerous nonoverlapping triangles of three stations and then applied array processing methods to determine signal origin directions. Combining similar results from multiple subnetwork groups helps define likely events. This approach is similar to array processing algorithms which evaluate wavefield parameters from combinations of three-element subarrays within larger array configurations (e.g., progressive multi-channel correlation, PMCC; Cansi, 1995). Such approaches tend to avoid sensitivity to atmospheric propagation complexity, which can affect methods that combine records from wide areas.

3.3.3. Signal Quality

Results from data analysis are limited by the quality of the data available. Consequently, designing robust stations, and choosing sites which can sample wavefields

from sources of interest, while minimizing noise from natural and artificial sources, requires considerable research. For high-grade stations like those at the IMS, elaborate spatial averaging hardware using pipes significantly reduces the effects of wind (e.g., Marty, 2019). For smaller, but still permanent arrays e.g., those operated by AVO, dome structures can provide a similar outcome (e.g., Raspet et al., 2019). At the sensor level, different types of shrouds around sensors allow for the atmosphere to be sampled from different directions in order to achieve the spatial averaging effect. Sites in forested areas, and those with snow cover, can also reduce wind noise, but potentially with attenuation of higher frequency signals (e.g., Adam et al., 1998).

Such technical designs may not always have been present when data was recorded, however, and data conditioning steps can be used in an attempt to clean the data from undesirable elements. This contamination may include wind noise, electrical noise, microbarom and fluvial clutter, etc. SNR-enhancing strategies may range from simple bandpass filtering (e.g., Arnoult et al., 2010), to combining separate traces into travel-time corrected stacks/beams (e.g., Olson and Szuberla, 2008), or comparing traces to identify similar elements (e.g., Olson, 1982). The effectiveness of such approaches often depends on there being a distinction in the inter- or intrasensor/station characteristics of signals and noise, as well as the original SNR. Methods that operate just using a single trace are uncommon in seismoacoustics, however, despite having potential widespread use. These data processing techniques are more established in engineering fields such as the music and telecommunications industries, with algorithms tailored to specific signal and noise characteristics (e.g., Boll, 1979). For volcanic infrasound and seismicity, with applications only beginning relatively recently (e.g., Cabras et al., 2012; Carniel et al., 2014), formal evaluation and developments are still required.

3.4. Unanswered Questions

3.4.1. Remote Explosions

The TA-based event location methods described thus far each have their strengths and weaknesses in terms of what can be resolved, how accurately, the performance in real time and, thereby, utility in an active monitoring setup. Such methods have not previously been applied to volcanic events, however. The nature of volcanic data is highly variable, but at remote distances will tend to present as multi-pathed infrasound arrivals coalescing in emergent, complex records at only a subset of available stations. In order to utilize the capability of dense regional networks for detecting and locating volcanic eruptions, appropriate data techniques will need to be implemented, some well-established, some novel. Many other analyses can be undertaken to take advantage of this new densely sampled data. For example, volcanic energy partitioning and radiation patterns at the source, radial and azimuthal atmospheric propagation effects on waveforms and ray paths, the presence and exploitability of air-ground coupling, and detection of nonvolcanic events.

3.4.2. Data Cleaning

Noise reduction data processing as applied to individual volcanic infrasound traces is still in its infancy. To date there has been very limited uptake by authors not involved in tool development (e.g., Williams et al., 2020). As such there is a currently an opportunity to rapidly enhance the utility of existing and new infrasound data by reducing ocean and wind noise components, thereby enhancing remaining signals. Some of the challenges stem from how ambient noise variably presents on different station hardware, at different times of day, and in different locations, just as signals of interest are recorded differently depending on source, site, and path factors. Processing speed can be another issue when many stations are

involved (especially in real time), with complex denoising operations adding extra steps to existing workflows. Algorithms must be efficient if they are to become widely implemented.

3.4.3. Mass Movements

For moving sources, remote assessment via infrasound is a rapidly developing area, with a limited range of case studies spanning a variety of event types. For mass movements, the majority of prior research has gone toward regions that produce relatively predictable events such as snow avalanches (e.g., Naugolnykh et al., 2002), and debris flows specific to particular mountain valleys (e.g., Schimmel and Hübl, 2016), rather than sporadic events in volcanic environments (e.g., Allstadt et al., 2018, and references therein). Consequently, there is limited knowledge on topics that include the following: which processing algorithms are most effective for tracking potentially multiple moving sources, how flow-atmosphere coupling operates under different flow conditions, and how clutter affects detection of transient events. Another important research area is low-cost station designs that can offer real-time feeds of useful data in harsh environments, such as those with heavy rains, easily erodible stream banks, and so forth.

4. Outline

The structure of the dissertation is as follows, with chapters 2, 3, and 4, consisting of three largely self-contained original research works. In chapter 2, an RTM algorithm is developed and applied to the nine-month eruption from Bogoslof volcano, Alaska, primarily exploiting the temporary presence of a dense network nearby. Chapter 3 follows from the findings of chapter 2, where now the same volcanic data is treated using several denoising algorithms to identify improvements to detection and location algorithms among other analyses. Chapter 4 focuses on infrasound generated by mass wasting as well as other, less

hazardous sources at Mount Adams volcano, Washington. In chapter 5, the key findings from these works will be summarized, and the overall conclusions drawn. The importance and implications of the research will be reviewed, and recommendations given for future work. Chapters 2–4 are each followed by supplemental material. Three additional appendices following chapter 5 cover further experiments relating to chapters 1 and 2, as well as infrasound deployments in Mexico. The remainder of this chapter expands upon the research aims and objectives for each of these principal chapters.

4.1. Chapter 2

Given the opportunity presented by the recent deployment of the TA in Alaska, a major aim of this dissertation is to establish how this kind of dense configuration can be used to quickly and accurately locate volcanic eruptions using acoustic data, as well as to resolve wavefields on a scale between local networks (e.g., AVO) and those on a global scale (e.g., IMS). A core RTM algorithm will be evaluated, with this technique able to provide coarse initial locations, even without identifying specific arrivals or knowledge of atmospheric structure. Future work would refine these locations using wavefield propagation methods (chapter 5). The character of known signal properties can be exploited (for example, long duration eruptions) to make a more robust detection system (e.g., Matoza et al., 2017). Questions focus on the impact on detection and location results by source-station geometries, station hardware, signal to noise ratios, propagation conditions, and processing choices.

4.2. Chapter 3

The value of seismoacoustic data is potentially not being fully maximized by researchers due to ambient noise contamination. Effective wind noise reduction hardware in Alaska is restricted to a handful of arrays, leaving the majority of stations (largely the TA)

heavily affected by wind noise. The core aim here is to identify if fundamentals like event detection and location accuracy established via RTM and array processing can be improved via wind noise and microbarom reduction in pre-recorded data. This work surveys a range of open source processing methods that can isolate signals of interest from wind and microbaroms using data that is already to hand. There is a focus on strategies that can operate on single channels, without the need for large training sets in order to promote flexibility and ease of use. Important aspects include labeling of data as signal or noise prior to separation, and how source-station distances, station hardware, event-noise similarity, and original SNR impact results.

4.3. Chapter 4

Mount Adams, in Washington, USA, is prone to regular failures owing to a hydrothermally-weakened summit (e.g., Finn et al., 2007). Local communities are at risk of lahar inundation, with some historic flows reaching 27 km downstream from the volcano. The aim here is to investigate the potential for detecting and tracking local mass wasting events, primarily with infrasound, as well as to establish ambient noise sources, and noise levels, over several years. A complex watershed contributes to annually-varying waterfalls and other clutter sources, which can impact event detectability. Following the design and installation of a long-term infrasound array at a suitable site, the main objective is estimating the locations of signal and clutter sources. This effort will be aided by additional temporary infrasound arrays, records from an existing seismic station, as well as visual observations. Other tasks are to characterize mass wasting events where possible in terms of volume and runout, and to examine the influence of wind noise, station hardware, local weather, and array geometry on detection capability.

References

Adam, V., Chritin, V., Rossi, M., and Lancker, E. (1998). Infrasonic monitoring of snow-avalanche activity: What do we know and where do we go from here? *Annals of Glaciology*, 26, 324–328. https://doi.org/10.3189/1998AoG26-1-324-328

Alaska Volcano Observatory (2016). *How often do Alaskan Volcanoes erupt?* https://www.avo.alaska.edu/volcanoes/about.php. Last accessed August 2021.

Allstadt, K. E., Matoza, R. S., Lockhart, A. B., Moran, S. C., Caplan-Auerbach, J., Haney, M. M., Thelen, W. A., and Malone, S. D. (2018). Seismic and acoustic signatures of surficial mass movements at volcanoes. *Journal of Volcanology and Geothermal Research*, 364, 76–106. https://doi.org/10.1016/j.jvol-geores.2018.09.007

Arnoult, K. M., Olson, J. V., Szuberla, C. A. L., McNutt, S. R., Garcés, M. A., Fee, D., and Hedlin, M. A. H. (2010). Infrasound observations of the 2008 explosive eruptions of Okmok and Kasatochi volcanoes, Alaska. *Journal of Geophysical Research: Atmospheres*, 115, D00L15. https://doi.org/10.1029/2010jd013987

Arrowsmith, S. J., Johnson J. B., Drob D. P., and Hedlin, M. A. H. (2010). The seismoacoustic wavefield: A new paradigm in studying geophysical phenomena. *Reviews of Geophysics*, 48, RG4003. https://doi.org/10.1029/2010RG000335

Blom, P., Waxler, R., Frazier, W. G., and Talmadge, C. (2014). Observations of the refraction of microbaroms generated by large maritime storms by the wind field of the generating storm. *Journal of Geophysical Research: Atmospheres*, 119, 7179–7192. https://doi.org/10.1002/2014JD021795

Boll, S. (1979). A spectral subtraction algorithm for suppression of acoustic noise in speech. *ICASSP'79 / IEEE international conference on acoustics, speech, and signal processing*, 4, 200–203. https://doi.org/10.1109/ICASSP.1979.1170696

Bosa, A., Johnson, J. B., De Angelis, S., Lyons, J. J., Escobar-Wolf, R. P., Roca, A., and Pineda, A. (2020). Tracking secondary lahar flow paths and characterizing pulses and surges using infrasound array networks at Volcán Fuego, Guatemala. Abstract [V009-03] presented at *2020 Fall Meeting, AGU*.

Braun, T., and Ripepe, M. (1983). Interaction of seismic and air waves recorded at Stromboli Volcano. *Geophysical Research Letters*, 20, 65–68. https://doi.org/10.1029/92GL02543

Buckingham, M., and Garcés, M. A. (1996). Canonical model of volcano acoustics. *Journal of Geophysical Research*, 101, B4, 8129–8151. https://doi.org/10.1029/95JB01680

Busby, R. W., Woodward, R. L., Hafner, K. A., Vernon, F. L., and Frassetto, A. M. (2018). *The design and implementation of EarthScope's USArray Transportable Array in the Conterminous United States and Southern Canada*. Retrieved from: http://www.usarray.org/researchers/obs/transportable/l48_ta_report

Busby, R. W., and Aderhold, K. (2020). The Alaska Transportable Array: As Built. *Seismological Research Letters,* 91(6), 3017–3027. https://doi.org/10.1785/0220200154

Campus, P., and Christie, D. R. (2010). Worldwide observations of infrasonic waves. In A. Le Pichon, E. Blanc, and A. Hauchecorne (Eds.), *Infrasound Monitoring for Atmospheric*

Studies, (pp. 185–234). Dordrecht: Springer. https://doi.org/10.1007/978-1-4020-9508-5_6

Cansi, Y. (1995). An automated seismic event processing for detection and location: The P.M.C.C. method. *Geophysical Research Letters*, 22, 1021–1024. https://doi.org/10.1029/95GL00468

Caplan-Auerbach, J., Bellesiles, A., and Fernandes, J. K. (2010). Estimates of eruption velocity and plume height from infrasonic recordings of the 2006 eruption of Augustine Volcano, Alaska. *Journal of Volcanology and Geothermal Research*, 189(1–2), 12–18. https://doi.org/10.1016/j.jvolgeores.2009.10.002

Carn, S. A., Pallister, J. S., Lara, L., Ewert, J. W., Watt, S., Prata, A. J., Thomas, R. J., and Villarosa, G. (2009). The unexpected awakening of Chaitén volcano, Chile. *Eos Transactions American Geophysical Union*, 90(24), 205–206. https://doi.org/10.1029/2009EO240001

Chouet, B. A., and Matoza, R. S. (2013). A multi-decadal view of seismic methods for detecting precursors of magma movement and eruption. *Journal of Volcanology and Geothermal Research*, 252, 108–175. https://doi.org/10.1016/j.jvolgeores.2012.11.013

Chunchuzov, I., Kulichkov, S., Popov, O., and Hedlin, M. (2014). Modeling propagation of infrasound signals observed by a dense seismic network. *The Journal of the Acoustical Society of America,* 135, 38–48. https://doi.org/10.1121/1.4845355

Coombs, M. L., Wallace, K., Cameron, C., Lyons, J. J., Wech, A., Angeli, K., and Cervelli, P. (2019). Overview, chronology, and impacts of the 2016–2017 eruption of Bogoslof volcano, Alaska. *Bulletin of Volcanology,* 81(11), 1–23. https://doi.org/10.1007/s00445-019-1322-9

Coombs, M. L., Wech, A. G., Haney, M. M., Lyons, J. J., Schneider, D. J., Schwaiger, H. F., et al. (2018). Short-term forecasting and detection of explosions during the 2016–2017 eruption of Bogoslof volcano, Alaska. *Frontiers of Earth Science*, 6(122). https://doi.org/10.3389/feart.2018.00122

Dabrowa, A. L., Green, D. N., Rust, A. C., and Phillips, J. C. (2011). A global study of volcanic infrasound characteristics and the potential for long-range monitoring. *Earth and Planetary Science Letters*, 310(3–4), 369–379. https://doi.org/10.1016/j.epsl.2011.08.027

Dean, K. G., Dehn, J., McNutt, S., Neal, C. A., Moore, R. W., and Schneider, D. (2002). Satellite imagery proves essential for monitoring erupting Aleutian Volcano. *Eos, Transactions American Geophysical Union*, 83, 241–247. https://doi.org/10.1029/2002EO000168

De Angelis, S., Fee, D., Haney, M., and Schneider, D. (2012). Detecting hidden volcanic explosions from Mt. Cleveland Volcano, Alaska with infrasound and ground-coupled airwaves. *Geophysical Research Letters*, 39, L21312. https://doi.org/10.1029/2012GL053635

de Groot-Hedlin, C. D., and Hedlin, M. A. H. (2015). A method for detecting and locating geophysical events using groups of arrays. *Geophysical Journal International*, 203(2), 960–971. https://doi.org/10.1093/gji/ggv345

Delle Donne, D., Ripepe, M., Lacanna, G., Tamburello, G., Bitetto, M., and Aiuppa, A. (2016). Gas mass derived by infrasound and UV cameras: Implications for mass flow rate. *Journal of Volcanology and Geothermal Research*, 325, 169–178. https://doi.org/10.1016/j.jvolgeores.2016.06.015

Dibble, R. R., Kienle, J., Kyle, P. R., and Shibuya, K. (1984). Geophysical studies of Erebus Volcano, Antarctica, from 1974 December to 1982 January. *New Zealand Journal of Geology and Geophysics*, 27(4), 425–455. https://doi.org/10.1080/00288306.1984.10422264

Dixon, J. P., Stihler, S. D., Haney, M. M., Lyons, J. J., Ketner, D. M., Mulliken, K. M., Parker, T., and Power, J. A. (2019). Catalog of earthquake parameters and description of seismograph and infrasound stations at Alaskan volcanoes—January 1, 2013, through December 31, 2017. *U.S. Geological Survey Data Series*, 1115. https://doi.org/10.3133/ds1115

Evers, L. G., and Haak, H. W. (2010). The characteristics of infrasound, its propagation and some early history. In A. Le Pichon, E. Blanc, and A. Hauchecorne (Eds.), *Infrasound monitoring for atmospheric studies*, (pp. 3–27). Dordrecht: Springer. https://doi.org/10.1007/978-1-4020-9508-5_1

Fee, D., Garcés, M., Patrick, M., Chouet, B., Dawson, P., and Swanson, D. (2010a). Infrasonic harmonic tremor and degassing bursts from Halemaʻumaʻu Crater, Kīlauea Volcano, Hawaiʻi. *Journal of Geophysical Research: Solid Earth*, 115, B11316. https://doi.org/10.1029/2010JB007642

Fee, D., Haney, M., Matoza, R., Szuberla, C., Lyons, J., and Waythomas, C. (2016). Seismic envelope-based detection and location of ground-coupled airwaves from volcanoes in Alaska. *Bulletin of the Seismological Society of America*, 106(3), 1–12. https://doi.org/10.1785/ 0120150244

Fee, D., Haney, M. M., Matoza, R. S., Van Eaton, A. R., Cervelli, P., Schneider, D. J., and Iezzi, A. M. (2017a). Volcanic tremor and plume height hysteresis from Pavlof Volcano, Alaska. *Science*, 355(6320), 45–48. https://doi.org/10.1126/science.aah6108

Fee, D., Izbekov, P., Kim, K., Yokoo, A., Lopez, T., Prata, F., Kazahaya, R., Nakamichi, H., and Iguchi, M. (2017b). Eruption mass estimation using infrasound waveform inversion and ash and gas measurements: evaluation at Sakurajima Volcano, Japan. *Earth and Planetary Science Letters*, 480, 42–52. https://doi.org/10.1016/j.epsl.2017.09.043

Fee, D., and Matoza, R. S. (2013). An overview of volcano infrasound: From Hawaiian to Plinian, local to global. *Journal of Volcanology and Geothermal Research*, 249, 123–139. https://doi.org/10.1016/j.jvolgeores.2012.09.002

Fee, D., Steffke, A., and Garcés, M. (2010b). Characterization of the 2008 Kasatochi and Okmok eruptions using remote infrasound arrays. *Journal of Geophysical Research*, 115, D00L10. https://doi.org/10.1029/2009JD013621

Fee, D., Toney, L., Kim, K., Sanderson, R. W., Iezzi, A. M., Matoza, R. S., De Angelis, S., Jolly, A. D., Lyons, J. J., and Haney, M. M. (2021). Local explosion detection and infrasound localization by reverse time migration using 3-D finite-difference wave propagation. *Frontiers in Earth Science*, 9. https://doi.org/10.3389/feart.2021.620813

Finn, C. A., Desczcz-Pan, M., Anderson, E. D., and John, D. A. (2007). Three-dimensional geophysical mapping of rock alteration and water content at Mount Adams, Washington: Implications for lahar hazards. *Journal of Geophysical Research*, 112, B10204. https://doi.org/10.1029/2006JB004783

Frazier, W. G., Talmadge, C., Park, J., Waxler, R., and Assink, J. (2014). Acoustic detection, tracking, and characterization of three tornadoes. *The Journal of the Acoustical Society of America*, 135, 1742–1751. https://doi.org/10.1121/1.4867365

Garcés, M., Harris, A., Hetzer, C., Johnson, J., Rowland, S., Marchetti, E., and Okubo, P. (2003). Infrasonic tremor observed at Kīlauea Volcano, Hawai'i. *Geophysical Research Letters*, 30(20), 2023. http://dx.doi.org/10.1029/2003GL018038

Geiger, L. (1910). Herdbestimmung bei Erdbeben aus den Ankunftszeiten. *Nachrichten der Königlichen Gesellschaft der Wissenschaften zu Göttingen, mathematisch-physikalische Klasse*, 4, 331–349 (in German).

Geiger, L. (1912). Probability method for the determination of earthquake epicenters from the arrival time only. *Bulletin of Saint Louis University*, 8, 60–71. Available at http://digitalcollections.slu.edu/digital/collection/catalogs/id/6310/rec/118 (last accessed August 2020).

Georges, T. M. and Beasley, W. H. (1977). Refraction of infrasound by upper-atmospheric winds. *The Journal of the Acoustical Society of America*, 61, 28–34. https://doi.org/10.1121/1.381263

Gorshkov, G. S. (1960). Determination of the explosion energy in some volcanoes according to barograms. *Bulletin of Volcanology*, 23, 141–144. https://doi.org/10.1007/BF02596639

Gottsmann J., Komorowski J. C., and Barclay J. (2017). Volcanic unrest and pre-eruptive processes: a hazard and risk perspective. In: J. Gottsmann, J. Neuberg, and B. Scheu (Eds.), *Volcanic unrest. Advances in volcanology*, (pp. 1–21). Cham: Springer. https://doi.org/10.1007/11157_2017_19

Green, D. N., Matoza, R. S., Vergoz, J., and Le Pichon, A. (2012). Infrasonic propagation from the 2010 Eyjafjallajökull eruption: Investigating the influence of stratospheric solar tides. *Journal of Geophysical Research*, 117, D21202. https://doi.org/10.1029/2012JD017988

Hamilton, M. F., and Blackstock, D. T. (Eds.) (2008). *Nonlinear acoustics*. Melville, NY: Academic Press.

Haney, M. M. (2009). Infrasonic ambient noise interferometry from correlations of microbaroms. *Geophysical Research Letters*, 36, L19808. https://doi.org/10.1029/2009GL040179

Hedlin, M. A. H., and Walker, K. T. (2013). A study of infrasonic anisotropy and multipathing in the atmosphere using seismic networks. *Philosophical Transactions of the Royal Society A*, 371, 20110542. https://doi.org/10.1098/rsta.2011.0542

Hibert, C., Mangeney, A., Polacci, M., Muro, A., Vergniolle, S., Ferrazzini, V., et al. (2015). Toward continuous quantification of lava extrusion rate: Results from the multidisciplinary analysis of the 2 January 2010 eruption of Piton de la Fournaise

volcano, La Réunion. *Journal of Geophysical Research: Solid Earth*, 120, 3026–3047. https://doi.org/10.1002/2014JB011769

Iezzi, A. M., Fee, D., Haney, M. M., and Lyons, J. J. (2020). Seismo-acoustic characterization of Mount Cleveland volcano explosions. *Frontiers in Earth Science*, 8(573368). https://doi.org/10.3389/feart.2020.573368

Johnson, J. B. (2003). Generation and propagation of infrasonic airwaves from volcanic explosions. *Journal of Volcanology and Geothermal Research*, 121, 1–14. https://doi.org/10.1016/S0377-0273(02)00408-0

Johnson, J. B., and Aster, R. C. (2005). Relative partitioning of acoustic and seismic energy during Strombolian eruptions. *Journal of Volcanology and Geothermal Research*, 148(3–4), 334–354. https://doi.org/10.1016/j.jvolgeores.2005.05.002

Johnson, J. B., Lees, J. M., and Yepes, H. (2006). Volcanic eruptions, lightning, and a waterfall: Differentiating the menagerie of infrasound in the Ecuadorian jungle. *Geophysical Research Letters*, 33, L06308. https://doi.org/10.1029/2005GL025515

Johnson, J. B., and Ripepe, M. (2011). Volcano infrasound: A review. *Journal of Volcanology and Geothermal Research*, 206(3–4), 61–69. http://dx.doi.org/10.1016/j.jvolgeores.2011.06.006

Johnson, J. B., and Palma, J. (2015). Lahar infrasound associated with Volcan Villarrica's 3 March 2015 eruption. *Geophysical Research Letters*, 42(15), 6324–6331. https://doi.org/10.1002/2015GL065024

Jolly, A. D., Matoza, R. S., Fee, D., Kennedy, B. M., Iezzi, A. M., Fitzgerald, R. H., et al. (2017). Capturing the acoustic radiation pattern of Strombolian eruptions using infrasound sensors aboard a tethered aerostat, Yasur volcano, Vanuatu. *Geophysical Research Letters*, 44, 9672–9680. https://doi.org/10.1002/2017GL074971

Kim, K. and Lees, J. M. (2014). Local volcano infrasound and source localization investigated by 3D simulation. *Seismological Research Letters*, 85(6), 1177–1186. https://doi.org/10.1785/0220140029

Kim, K., Lees, J. M., and Ruiz, M. (2012). Acoustic multipole source model for volcanic explosions and inversion for source parameters. *Geophysical Journal International*, 191, 1192–1204. https://doi.org/10.1111/j.1365-246X.2012.05696.x

Le Pichon, A., Blanc, E., Drob, D., Lambotte, S., Dessa, J. X., Lardy, M., Bani, P., and Vergniolle, S. (2005). Infrasound monitoring of volcanoes to probe high-altitude winds. *Journal of Geophysical Research: Atmospheres*, 110, D13. https://doi.org/10.1029/2004JD005587

Le Pichon, A., Pilger, C., Ceranna, L., Marchetti, E., Lacanna, G., Souty, V., et al. (2021). Using dense seismo-acoustic network to provide timely warning of the 2019 paroxysmal Stromboli eruptions. *Scientific Reports*, 11(14464). https://doi.org/10.1038/s41598-021-93942-x

Lyons, J. J., Haney, M. M., Fee, D., Wech, A. G., and Waythomas, C. F. (2019). Infrasound from giant bubbles during explosive submarine eruptions of Bogoslof volcano, Alaska. Nature Geoscience, 12(11), 952–958. https://doi.org/10.1038/s41561-019-0461-0

Marty, J. (2019). The IMS infrasound network: Current status and technological developments. In A. Le Pichon, E. Blanc, and A. Hauchecorne (Eds.), *Infrasound monitoring for atmospheric studies: Challenges in middle‑atmosphere dynamics and societal benefits*, (pp. 91–124). Cham: Springer. https://doi.org/10.1007/978-3-319-75140-5_1

Matoza, R., Fee, D., Green, D., and Mialle, P. (2019). Volcano infrasound and the International Monitoring System. In: A. Le Pichon, E. Blanc, and A. Hauchecorne (Eds.), *Infrasound monitoring for atmospheric studies: Challenges in middle‑atmosphere dynamics and societal benefits*, (pp. 1023–1077). Cham: Springer. https://doi.org/10.1007/978-3-319-75140-5_33

Matoza, R. S., Garcés, M. A., Chouet, B. A., D'Auria, L., Hedlin, M. A. H., de Groot-Hedlin, C., and Waite, G. P. (2009). The source of infrasound associated with long-period events at Mount St. Helens. *Journal of Geophysical Research*, 114, B04305. https://doi.org/10.1029/2008JB006128

Matoza, R. S., Green, D. N., Le Pichon, A., Shearer, P. M., Fee, D., Mialle, P., and Ceranna, L. (2017). Automated detection and cataloging of global explosive volcanism using the International Monitoring System infrasound network. *Journal of Geophysical Research: Solid Earth*, 122, 2946–2971. https://doi.org/10.1002/2016JB013356

Matoza, R. S., Hedlin, M. A. H., and Garcés, M. A. (2007). An infrasound array study of Mount St. Helens. *Journal of Volcanology and Geothermal Research,* 160(3–4), 249–262. https://doi.org/10.1016/j.jvolgeores.2006.10.006

Matoza, R. S., Le Pichon, A., Vergoz, J., Herry, P., Lalande, J., Lee, H., Che, I., and Rybin, A. (2011). Infrasonic observations of the June 2009 Sarychev Peak eruption, Kuril Islands: Implications for infrasonic monitoring of remote explosive volcanism. *Journal of Volcanology and Geothermal Research*, 200, 35–48. https://doi.org/10.1016/j.jvolgeores.2010.11.022

McNutt, S. R. (2015). Part VIII Eruption Response and Mitigation. In: H. Sigurdsson (Ed.), *The encyclopedia of volcanoes (second edition)*, (pp. 1069–1070). Cambridge: Academic Press. https://doi.org/10.1016/B978-0-12-385938-9.02010-1

Modrak, R. T., Arrowsmith, S. J., and Anderson, D. N. (2010). A Bayesian framework for infrasound location. *Geophysical Journal International*, 181, 399–405. https://doi.org/10.1111/j.1365-246X.2010.04499.x

Murayama, T., Kanao, M., Yamamoto, M.-Y., Ishihara, Y., Matshushima, T., Kakinami, Y. (2015). Infrasound array observations in the Lützow-holm bay region, east Antarctica. *Polar Science*, 9, 35–50. https://doi.org/10.1016/j.polar.2014.07.005

National Academies of Sciences, Engineering, and Medicine (2017). Volcanic eruptions and their repose, unrest, precursors, and timing. *Washington, DC: The National Academies Press*. https://doi.org/10.17226/24650

Naugolnykh, K., and Bedard, B. (2002). A model of the avalanche infrasound radiation. *Proceedings of the 2002 IEEE International Geoscience and Remote Sensing Symposium/24th Canadian Symposium Remote Sensing*, 871–872. https://10.1109/IGARSS.2002.1025713

Neal, C. A., Casadevall, T. J., Miller, T. P., Hendley, J. W. II, and Stauffer, P. H. (1997). Volcanic ash - Danger to aircraft in the North Pacific. *U.S. Geological Survey Fact Sheet*, FS 030-97, 2 p. https://doi.org/10.3133/fs03097

Nief, G., Talmadge, C., Rothman, J., and Gabrielson, T. (2019). New generations of infrasound sensors: technological developments and calibration. In: A. Le Pichon, E. Blanc, and A. Hauchecorne (Eds.), *Infrasound monitoring for atmospheric studies: Challenges in middle-atmosphere dynamics and societal benefits*, (pp. 63–89). Cham: Springer. https://doi.org/10.1007/978-3-319-75140-5_2

Nippress, A., Green, D. N., Marcillo, O. E., and Arrowsmith, S. J. (2014). Generating regional infrasound celerity-range models using ground-truth information and the implications for event location. *Geophysical Journal International*, 197(2), 1154–1165. https://doi.org/10.1093/gji/ggu049

Olson, J. V. (1982). Noise suppression using data-adaptive polarization filters: Applications to infrasonic array data. *The Journal of the Acoustical Society of America*, 72(5), 1456–1460. https://doi.org/10.1121/1.388679

Olson, J. V, and Szuberla, C. A. L. (2008). Processing infrasonic array data, In D. Havelock., S. Kuwano, and M. Vorländer (Eds.), *Handbook of Signal Processing in Acoustics*, (pp. 1487–1496). New York: Springer. https://doi.org/10.1007/978-0-387-30441-0_81

Omori, F. (1912). The eruptions and earthquakes of the Asama-Yama. *Bulletin of the Imperial Earthquake Investigation Committee*, 6(1).

Park, J., Hayward, C. T., Zeiler, C. P., Arrowsmith, S. J., and Stump, B. W. (2017). Assessment of infrasound detectors based on analyst review, environmental effects, and detection characteristics. *Bulletin of the Seismological Society of America*, 107(2), 674–690. https://doi.org/10.1785/0120160125

Petersen, T., De Angelis, S., Tytgat, G., and McNutt, S. R. (2006). Local infrasound observations of large ash explosions at Augustine Volcano, Alaska, during January 11 – 28, 2006. *Geophysical Research Letters*, 33, L12303. https://doi.org/10.1029/2006GL026491

Pierce, A.D. (1981). *Acoustics—An introduction to its physical principles and applications*. New York: McGraw-Hill. https://doi.orig/10.1007/978-3-030-11214-1

Pierson, T. C., R. J. Janda, J.-C. Thouret, and Borrero, C. A. (1990). Perturbation and melting of snow and ice by the 13 November eruption of Nevado del Ruiz, Colombia, and consequent mobilization, flow and deposition of lahar. *Journal of Volcanology and Geothermal Research*, 41(1–4), 17–66. https://doi.org/10.1016/0377-0273(90)90082-Q

Pinsky, V., Blom, P., Polozov, A., Marcillo, O., Arrowsmith, S., and Hofstetter, A. (2017). Towards an accurate real-time locator of infrasonic sources. *Journal of Seismology*, 21(6), 1361–1383. https://doi.org/10.1007/s10950-017-9670-4

Pyle, D. M., Mather, T. A., and Biggs, J. (Eds.). (2013). Remote sensing of volcanoes and volcanic processes: Integrating observation and modelling. *Geological Society, London, Special Publications*, 380. https://doi.org/10.1144/SP380.0

Raspet, R., Abbott, J.-P., Webster, J., Yu, J., Talmadge, C., Alberts, K. II, et al. (2019). New systems for wind noise reduction for infrasonic measurements. In: A. Le Pichon, E. Blanc, and A. Hauchecorne (Eds.), *Infrasound monitoring for atmospheric studies: Challenges in middle‑atmosphere dynamics and societal benefits*, (pp. 91–124). Cham: Springer. https://doi.org/10.1007/978-3-319-75140-5_3

Raspet, R., Webster, J., and Dillon, K. (2006). Framework for wind noise studies. *Journal of the Acoustical Society of America*, 199, 834–843. https://doi.org/10.1121/1.2146113

Ripepe, M., and Marchetti, E. (2002). Array tracking of infrasonic sources at Stromboli volcano. *Geophysical Research Letters*, 29(22), 2076. https://doi.org/10.1029/2002GL015452

Ripepe, M., De Angelis, S., Lacanna, G., and Voight, B. (2010). Observation of infrasonic and gravity waves at Soufrière Hills Volcano, Montserrat, *Geophysical Research Letters*, 37, L00E14. https://doi.org/10.1029/2010GL042557

Ruiz, M. C., Lees, J. M., and Johnson, J. B. (2006). Source constraints of Tungurahua volcano explosion events. *Bulletin of Volcanology,* 68**,** 480–490. https://doi.org/10.1007/s00445-005-0023-8

Schimmel, A., and Hübl, J. (2016). Automatic detection of debris flows and debris floods based on a combination of infrasound and seismic signals. *Landslides*, 13, 1181–1196. https://doi.org/10.1007/s10346-015-0640-z

Schmandt, B., Aster, R. C., Scherler, D., Tsai, V. C., and Karlstrom, K. (2013). Multiple fluvial processes detected by riverside seismic and infrasound monitoring of a controlled flood in the Grand Canyon. *Geophysical Research Letters*, 40(18), 4858–4863. https://doi.org/10.1002/grl.50953

Schwaiger, H. F., Lyons, J. J., Iezzi, A. M., Fee, D., and Haney, M. M. (2020). Evolving infrasound detections from Bogoslof volcano, Alaska: Insights from atmospheric propagation modeling. *Bulletin of Volcanology*, 82(27). https://doi.org/10.1007/s00445-020-1360-3

Shearer, P. (1994). Global seismic event detection using a matched filter on long-period seismograms. *Journal of Geophysical Research: Solid Earth*, 99, B7. https://doi.org/10.1029/94JB00498

Strachey, R. (1888). On the air waves and sounds caused by the eruption of Krakatoa in August 1883. Part 2. In: G. J. Symons (Ed.), *The eruption of Krakatoa, and subsequent phenomena, report of the Krakatoa Committee of the Royal Society*, (pp. 57–88). London: Trübner and Co.

Sutherland, L. C., and Bass, H. E. (2004). Atmospheric absorption in the atmosphere up to 160 km. *Journal of the Acoustical Society of America*, 115(3), 1012–1032. https://doi.org/10.1121/1.1631937

Tempest, A., and Flett, J. S. (1903). Report on the eruptions of the Soufrière, in St. Vincent, in 1902, and on a visit to Montagne Pelée, in Martinique.—Part I. *Philosophical Transactions of the Royal Society of London, Series A*, 200, 353–553. https://doi.org/10.1098/rspl.1902.0042

Toney, L., Fee, D., Allstadt, K. E., Haney, M. M., and Matoza, R. S. (2021). Reconstructing the dynamics of the highly similar May 2016 and June 2019 Iliamna Volcano (Alaska) ice–rock avalanches from seismoacoustic data. *Earth Surface Dynamics*, 9, 271–293. https://doi.org/10.5194/esurf-9-271-2021

Van Eaton, A. R., Amigo, À., Bertin, D., Mastin, L. G., Giacosa, R. E., González, J., et al. (2016). Volcanic lightning and plume dynamics reveal evolving hazards during the April 2015 eruption of Calbuco volcano, Chile. *Geophysical Research Letters*, 43, 3563–3571. https://doi.org/10.1002/2016GL068076

Vergniolle, S., Boichu, M., and Caplan-Auerbach, J. (2004). Acoustic measurements of the 1999 eruption of Shishaldin volcano, Alaska: 1) origin of Strombolian activity. *Journal of Volcanology and Geothermal Research*, 137(1–3), 109–134. https://doi.org/10.1016/j.jvolgeores.2004.05.003

Vergoz, J., Le Pichon, A., and Millet, C. (2019). The Antares explosion observed by the USArray: An unprecedented collection of infrasound phases recorded from the same event. In: A. Le Pichon, E. Blanc, and A. Hauchecorne (Eds.), *Infrasound monitoring for atmospheric studies: Challenges in middle-atmosphere dynamics and societal benefits*, (pp. 349–386). Cham: Springer. https://doi.org/10.1007/978-3-319-75140-5_9

Walker, K. T., Hedlin, M. A. H., de Groot-Hedlin, C., Vergoz, J., Le Pichon, A., and Drob, D. P. (2010). Source location of the 19 February 2008 Oregon bolide using seismic networks and infrasound arrays. *Journal of Geophysical Research: Solid Earth*, 115, B12. https://doi.org/ 10.1029/2010JB007863

Walker, K. T., Shelby, R., Hedlin, M. A., Groot-Hedlin, C., and Vernon, F. (2011). Western US infrasonic catalog: Illuminating infrasonic hot spots with the USArray. *Journal of Geophysical Research: Solid Earth*, 116, B12. https://doi.org/10.1029/2011JB008579

Watson, L. M., Dunham, E. M., and Johnson, J. B. (2019). Simulation and inversion of harmonic infrasound from open-vent volcanoes using an efficient quasi-1D crater model. *Journal of Volcanology and Geothermal Research*, 380, 64–79. https://doi.org/10.1016/j.jvolgeores.2019.05.007

Waxler, R., Assink, J., Hetzer, C. and Velea, D. (2017). NCPAprop—A software package for infrasound propagation modeling. *The Journal of the Acoustical Society of America*, 141, 3627. https://doi.org/10.1121/1.4987797

Webley, P., and Mastin, L. (2009). Improved prediction and tracking of volcanic ash clouds. *Journal of Volcanology and Geothermal Research*, 186(1–2), 1–9. https://doi.org/10.1016/j.jvolgeores.2008.10.022

Williams, R. A., Perttu, A., and Taisne, B. (2020). Processing of volcano infrasound using film sound audio post-production techniques to improve signal detection via array processing. *Geoscience Letters*, 7(9). https://doi.org/10.1186/s40562-020-00158-4

Willis, M., Garcés, M., Hetzer, C., and Businger, S. (2004). Infrasonic observations of open ocean swells in the Pacific: Deciphering the song of the sea. *Geophysical Research Letters*, 31, L19303. https://doi.org/10.1029/2004GL020684

Wilson, C. R., Nichparenko, S., and Forbes, R. B. (1966). Evidence of two sound channels in the polar atmosphere from infrasonic observations of the eruption of an Alaskan volcano. *Nature*, 211, 163–165. https://doi.org/10.1038/211163a0

Chapter 2. Remote Detection and Location of Explosive Volcanism in Alaska with the EarthScope Transportable Array

This chapter appeared in this form in:

[1]Department of Earth Science and Earth Research Institute, University of California, Santa Barbara, California, USA, [2]Wilson Alaska Technical Center, Alaska Volcano Observatory, Geophysical Institute, University of Alaska Fairbanks, Alaska, USA, [3]U.S. Geological Survey Volcano Science Center, Alaska Volcano Observatory, Anchorage, Alaska, USA

Abstract

The current deployment of the EarthScope Transportable Array (TA) in Alaska affords an unprecedented opportunity to study explosive volcanic eruptions using a relatively dense regional seismoacoustic network. Infrasound monitoring has demonstrated utility for the remote (> 250 km range) detection and characterization of volcanic explosions, but previous studies have used relatively sparse regional or global networks. Seventy explosive events from the locally unmonitored Bogoslof volcano (2016–2017) provide a unique validation data set to examine the ability of the TA and other regional networks to detect and locate remote explosive volcanic eruptions in Alaska. With a simple envelope-based reverse time migration (RTM) technique, we are able to detect and locate more than 72% of the 61 Bogoslof infrasound events detected by the Alaska Volcano Observatory. Notably, RTM using only sparse regional infrasound arrays produces results similar to when incorporating the extensive single-sensor TA network, likely due to favorable signal-to-noise ratios, seasonal propagation conditions, and source-receiver geometries. Our implementation also detects and locates explosive eruptions from Cleveland volcano, Alaska, and Bezymianny volcano, Kamchatka, as well as infrasound from nonvolcanic events such as earthquakes. We characterize the success of the RTM algorithm and associated parameter choices using receiver operating characteristic curves, event detection rates, and location accuracy. Our methods are useful for explosive volcanic and nonvolcanic event detection and localization using real-time data and for scanning continuous waveform data archives.

1. Introduction

1.1. Motivation and Background

The deployment of the EarthScope Transportable Array (TA) in Alaska has brought one of the densest ever seismoacoustic networks to one of the world's most active volcanic regions (Figure 1a). Alaska is home to 130 potentially active volcanoes, of which more than 50 have been active in historical times (Cameron et al., 2018). On average, two volcanoes are in a state of eruption every year (Figure 1b) and are capable of sudden, explosive, ash cloud-forming eruptions, which are potentially hazardous to passenger and freight aircraft along this heavily traveled air corridor (Webley and Mastin, 2009). Monitoring of these volcanoes is performed at the Alaska Volcano Observatory (AVO) by integrating multiple ground-based and satellite monitoring technologies (e.g., Coombs et al., 2018). However, Aleutian volcanoes in particular represent a formidable monitoring challenge. Because of their remote locations, many volcanoes are not instrumented, which is also the case for the majority of potentially active volcanoes worldwide (National Academies of Sciences, Engineering, and Medicine, 2017). Eruptions of Okmok and Kasatochi in 2008 exemplify these challenges, as each volcano produced large atmospheric ash releases with little warning. Despite local instrumentation, precursory indicators at Okmok were few (Haney, 2010). In contrast, precursors at Kasatochi were more numerous but limited to seismic observation from more than 40 km away (Waythomas et al., 2010).

Volcanic eruptions produce seismic, acoustic, and air-ground coupled wavefields, each of which help provide constraints on internal and external volcanic processes (Johnson and Ripepe, 2011; Chouet and Matoza, 2013; Fee and Matoza, 2013; Matoza et al., 2019). Infrasound (acoustic waves < 20 Hz) is well suited to remote detection (Matoza et al., 2007; Garcés et al., 2008; De Angelis et al., 2012; Matoza et al., 2011a, 2011b; Fee et al., 2013; …
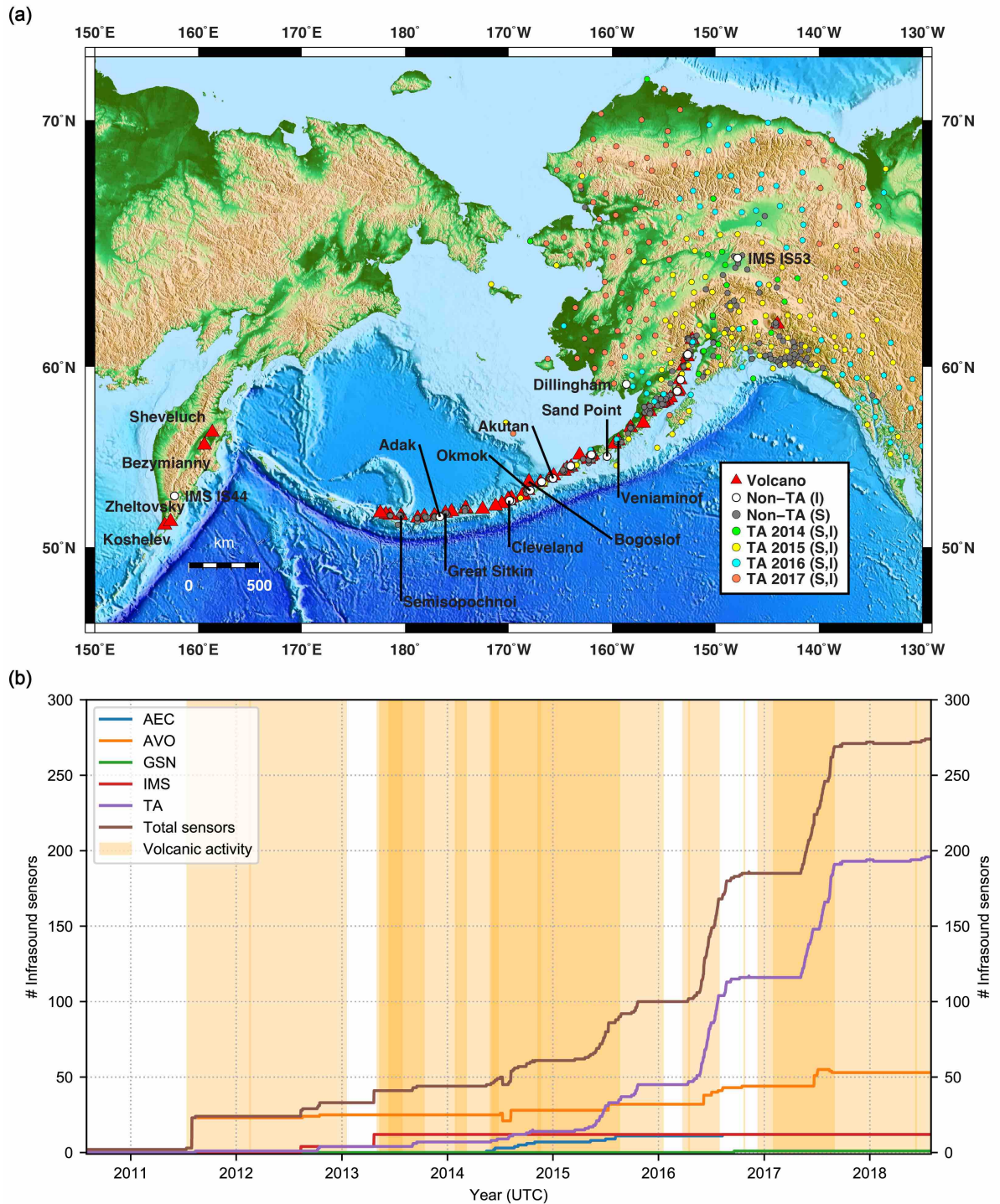
Figure 1. (a) Locations of historically active volcanoes and available seismic (S) and infrasound (I) data in Alaska. Volcanoes and infrasound arrays that are referenced in this study are labeled. (b) Evolution of the number of infrasound sensors deployed within 3,000 km of Bogoslof, 2011–2018. The TA has greatly increased the infrasound recording capacity in Alaska, with TA capacity outnumbering all other networks combined. Orange bars indicate eruptive episodes from volcanoes, some of which are occurring concurrently (Alaska Volcano Observatory, 2019).

Matoza et al., 2013; Ripepe et al., 2018). Infrasound attenuation is low, and infrasound can often be recorded thousands of kilometers from the source (Drob et al., 2003; Le Pichon et al., 2009; Waxler, 2017). Further, infrasound data reduces ambiguity in explosive eruption detection compared to seismic data alone and thus also provides value in the quantification and modeling of subaerial eruptive processes (Marchetti et al., 2004; Johnson and Aster, 2005; Vergniolle and Caplan-Auerbach, 2006; Marchetti et al., 2013; Harris and Ripepe, 2007; Matoza et al., 2007; Ripepe et al., 2007). In cloudy weather conditions, satellite observations of hot material and plumes are limited, where infrasound is unaffected (Garcés et al., 2008; Fee et al., 2010b; Matoza et al., 2011a; Pyle et al., 2013). Lighting detection can also serve as a useful proxy for atmospheric injection, but not all ash-producing eruptions produce lightning (McNutt and Williams, 2010; Behnke and McNutt, 2014; Van Eaton et al., 2016; Haney et al., 2020b).

Global infrasound networks have been shown to be effective at detecting relatively violent eruptions, even in remote locations (Liszka and Garcés, 2002; Evers and Haak, 2005; Le Pichon et al., 2005; Fee et al., 2010b; Dabrowa et al., 2011; Matoza et al., 2011a, 2011b; Fee et al., 2013; Matoza et al., 2017; Matoza et al., 2018). Local infrasound networks (sources < 15 km distant), however, are better placed for identifying smaller explosions, degassing, or effusive behavior within a limited radius (e.g., Johnson et al., 2003; Petersen and McNutt, 2007; Fee et al., 2010b; Matoza et al., 2010; De Angelis et al., 2012; Fee et al., 2016; Jolly et al., 2017). A dense regional seismoacoustic network such as the TA falls between these two endmember network geometries, affording an unprecedented opportunity to evaluate explosive volcanic eruptions, wave propagation, coupling, and signal evolution for source-sensor ranges out to a few thousand kilometers (e.g., study of the Pavlof March 2016 eruption by Fee et al., 2017). Regional infrasound coverage on a similar scale to the

TA is currently limited to combinations of national networks such as those in the Euro-Mediterranean region (Tailpied et al., 2017). Other national infrasound networks include those in Iceland (Jónsdóttir et al., 2015), Japan (Batubara et al., 2018), Chile (Matoza et al., 2018), and Singapore (Perttu et al., 2018).

Regional-scale studies using seismoacoustic TA data have previously considered nonvolcanic events in the contiguous United States, with signals ranging from short and impulsive (e.g., Walker et al., 2011; Edwards et al., 2014; de Groot-Hedlin and Hedlin, 2015), to long and emergent (e.g., de Groot-Hedlin et al., 2014; Fan et al., 2018). Infrasound produced by explosive volcanism can be equally complex, from minutes to days in duration, with impulsive or emergent signals of time-varying frequency (e.g., Lees et al., 2004; Petersen et al., 2006; Ruiz et al., 2006; Johnson and Ripepe, 2011; Fee and Matoza, 2013; Matoza et al., 2017; Matoza et al., 2019). Here we describe how seismoacoustic signals from a range of Alaskan and Kamchatkan volcanoes are recorded on regional and seasonal scales and present a method derived from those observations for the detection, location, and characterization of these eruptions. We use existing volcano catalog information to validate our results and determine the capabilities and limitations of the method for this data set.

1.2. Monitoring Networks

This study incorporates data from regional seismoacoustic networks including the TA, those of the AVO and Alaska Earthquake Center (AEC), and local elements of the International Monitoring System (IMS) and Global Seismograph Network (Figure 1). Telemetered data sampled at 20 Hz and higher are available in real time for public download from servers operated by Incorporated Research Institutions for Seismology and the U.S. Geological Survey. Stations in these networks include both stand-alone seismic and

infrasound sensors (Busby et al., 2018; USArray, 2019), as well as seven infrasound arrays (Lyons et al., 2020). AVO arrays are located at Adak, Akutan, Cleveland, Okmok, Sand Point, and Dillingham, with the Fairbanks array (IMS IS53) operated by the University of Alaska Fairbanks Geophysical Institute (Figure 1a). During the study period, there are up to 274 infrasound sensors from these networks within 3,000 km of Bogoslof volcano (Figure 1b). The term "array" is typically used for sensor geometries where signal wavelengths of interest (here, 1 km or less) are of the order of the sensor spacing (Havskov and Alguacil, 2016). To avoid ambiguity, hereafter "arrays" should be interpreted to mean only the AVO and IMS arrays, which have sensor spacing of 1 km or less. Stations in the TA will be referred to as single-sensor stations, which have typical sensor spacings of 85 km in Alaska.

1.3. Bogoslof Volcano Eruption

The 2016–2017 eruption sequence of the remote Bogoslof volcano, Alaska, provided a unique data set for developing and testing our algorithm. Seventy distinct eruptive events were characterized by AVO between 12 December 2016 and 30 August 2017, using a combination of geophysical data at local AVO stations (within 900 km), satellite images, lightning records, and eyewitness accounts (Coombs et al., 2019). The vast majority of these eruptions produced detectable infrasound, which, depending on event size, vent exposure/submersion, and atmospheric conditions, is observed at distances of up to 2,000 km or more (Figure 2). Infrasound signal durations lasted from minutes to hours, with infrasound frequencies extending from below 0.1 Hz to more than 10 Hz (Lyons et al., 2019, 2020; Fee et al., 2020; Schwaiger et al., 2020). The AVO eruption chronology catalog (Coombs et al., 2019) represents the best possible record of Bogoslof activity, and thus provides a metric by which to test our trial detection algorithms. Additional seismoacoustic
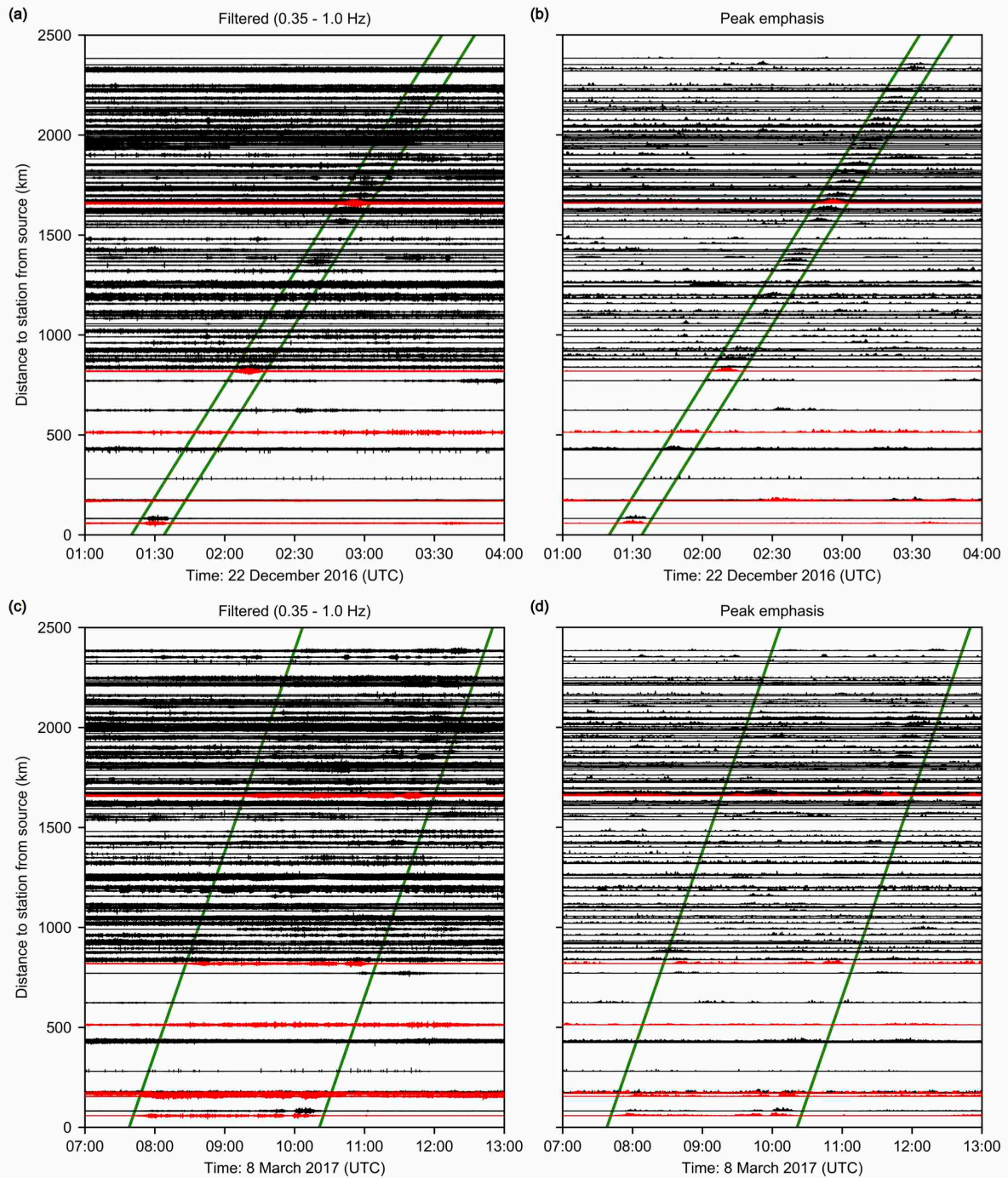
Figure 2. (a) Infrasound record section for Bogoslof eruption on 22 December 2016 using data filtered 0.35–1.0 Hz. The 14-min event signal is enclosed by diagonal green lines (celerity: 315 m/s). Traces for array sensors are colored red, and nonarray sensors colored black. (b) Traces from (a) following all data preprocessing stages which increase interstation event coherence (section 2.2). (c and d) Record sections for 8 March 2017 eruption. Event signal ~2.5 hours; best fit celerity: 280 m/s. Other details per (a) and (b). Although both these events are relatively large for the Bogoslof eruption sequence, sensors may not always record clear event arrivals due to atmospheric propagation paths and/or wind noise.

studies of Bogoslof using proximal stations include those by Tepp et al. (2020), who characterize seismic and hydroacoustic data from swarms and eruptive activity; Haney et al. (2020b), who describe thunder and electromagnetic signals produced by volcanic lightning from Bogoslof; Wech et al. (2018), who incorporate hydroacoustic T phases to model magma intrusion and eruption dynamics; Fee et al. (2020), who examine the relation between vent submersion and seismoacoustic ratios; and Lyons et al. (2019), who model low-frequency infrasound signals as giant, explosion-driven gas bubbles. Details of historical eruptions and hazards at Bogoslof are given by Waythomas and Cameron (2018) and Waythomas et al. (2020).

2. Methodology

2.1. Reverse Time Migration Overview

Reverse time migration (RTM) is a method for acoustic signal source localization; it is a time domain backprojection technique that identifies potential locations as those with the largest corresponding stack amplitude of waveform envelopes time-aligned with an appropriate velocity model. RTM has been used with seismic data (e.g., Shearer, 1994; Xu et al., 2009; Arrowsmith et al., 2018), as well as infrasonic ground-coupled airwaves (e.g., Walker et al., 2010, 2011, with TA data). Alternatives to RTM have been proposed for seismoacoustic event location with TA data; for example, de Groot-Hedlin and Hedlin (2015, 2018) and Park et al. (2018) employed a mesh of subnetworks in an array processing scheme. Other recent methods for locating volcanic infrasound using combinations of single sensors are available (e.g., Szuberla et al., 2006; Jones and Johnson, 2011; Kim and Lees, 2015; Pinsky et al., 2017). Here we choose to evaluate the ability of RTM to provide coarse initial locations as starting points for more accurate techniques and for near-real-time

operation at remote distances (< 2,000 km) from the source. Our approach builds upon the formulation of Walker et al. (2010, 2011), who applied RTM over a large grid (western United States) for a range of celerities (defined as the total distance along the Earth's surface, or range traveled, divided by the travel time). To develop our algorithm, we use data from 15 December 2016 to 14 January 2017. This period contains frequent Bogoslof explosions with a range of amplitudes and durations. Furthermore, stratospheric wind directions were typically toward the bulk of the network, thereby improving signal-to-noise ratios (SNR). The same algorithm is subsequently applied to all data from 1 December 2016 to 30 September 2017. All dates and times in this paper are in Coordinated Universal Time (UTC). Additional details about the various stages of our methodology are included in the supplemental material.

2.2. Preprocessing of Data

Significant preprocessing of data is necessary to improve SNR and waveform coherency between stations. Our pre-stack processing performs the following steps for each sensor trace: (1) demean; (2) taper with a Tukey window (to reduce filtering artifacts); (3) filter with a zero-phase order-2 band-pass Butterworth filter 0.35–1.0 Hz (a balance between eruption signal and background noise); (4) form envelopes (to increase interstation coherence); (5) decimate to one sample per 5 s after applying an anti-alias filter (computational efficiency); (6) smooth with a Gaussian window of width 75 s and standard deviation 10 s (to further increase interstation coherence and reduce spatial aliasing); (7) detrend via subtraction of a running minimum function with a 7-hr low-pass setting, hereafter called subtrending and inspired by Blackburn (2015) (to reduce wind noise while avoiding filter artifacts); (8) apply automatic gain correction (AGC) using a 3,600 s window

(to further suppress wind and emphasize weak signals); (9) demean and set any negative values to 0 (to emphasize peaks); (10) normalize on a 0 to 1 scale (to avoid dominance by noisy stations and account for attenuation). Figure 3 illustrates the main preprocessing steps for a single trace from the 8 March 2017 Bogoslof event (Figures 2c and 2d).
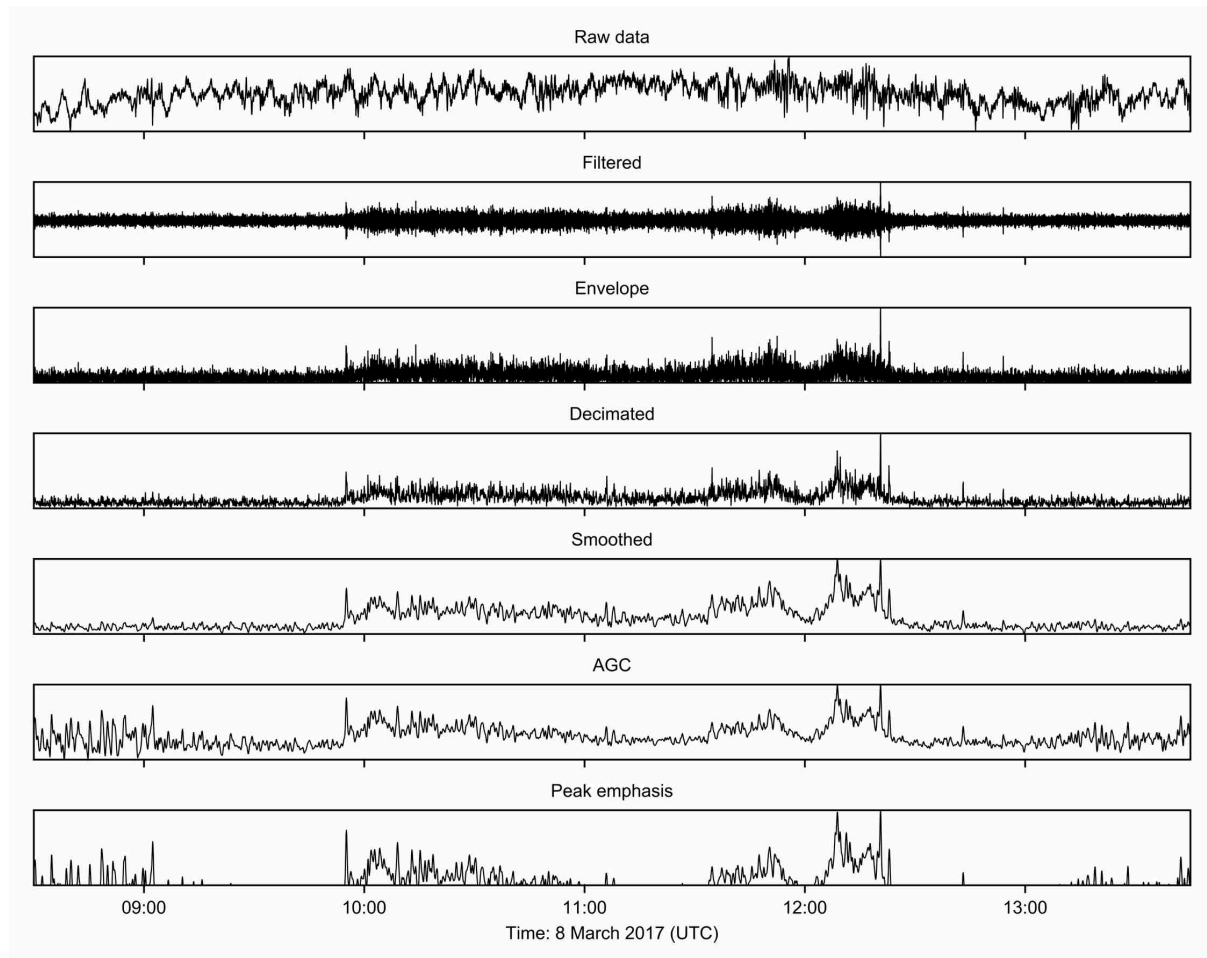
Figure 3. Sequence of the main preprocessing steps (going from top to bottom) for infrasound data recorded by station TA. N32M, located 2,210 km from Bogoslof at Quiet Lake, Yukon, Canada, on 8 March 2017.

As the preprocessing steps do not preserve signal shape, the resultant stack cannot be directly and quantitatively linked to source process and event size. However, in general, larger and more sustained volcanic explosive eruptions will produce higher SNR and longer-duration signals across more stations, resulting in higher stack values. Similarly, our location approach relies on increasing SNR through stacking rather than relying on the

amplitudes of nonnormalized traces. Preprocessing generally improves the SNR of stacked data, but the degree of improvement varies with parameter choices and varies from event to event. For the example in Figure 3, the smoothing stage provides the clearest signal, but for other stations and events, this is typically not the case. Noise emphasized by AGC is less coherent across the network than signals from events and does not often stack constructively during RTM. The waveform data in this study are processed in nonoverlapping 24-hr sections, with additional data padding to accommodate all travel times.

2.3. Stacking of Data

We search for potential source locations across a 2-D spatial grid covering Alaska at 1.0° intervals in latitude and longitude. We test each grid node by delaying and linearly stacking waveform data from all sensors within 2,000 km of Bogoslof using 11 trial celerities, linearly spaced between 250 and 350 m/s (Figures 4a–4d). Rather than repeat the spatial grid search at a series of trial origin times, we treat the data samples themselves as a time grid, and the intersample spacing (5 s) as time windows. The grid search produces 11 sets of stacks, one set for each celerity. These 11 sets are then reduced to an adopted final set by retaining the highest stack amplitude at each time step (Walker et al., 2010, 2011); this is analogous to the beamforming approach of, for example, Green and Nippress (2019). Before and after the celerity-set reduction, the stacks for each grid node are subtrended with a 6-hr low-pass setting. Applying these detrending steps here produces higher SNR than if applied in subsequent steps, and also ensures similar background amplitudes when concatenating multiple data sections.

Although infrasound for some Bogoslof events is detected to more than 2,000 km (Figure 2), we limit the station radius for this study to 2,000 km to preserve detectability for

small events from Bogoslof, while retaining the bulk of stations. For RTM, including data from more sensors in the stack does not necessarily improve SNR and can worsen it as more noisy traces are added; this can be exacerbated by coherent noise and certain network geometries (Koper et al., 2012).

We treat the data from each sensor in an array as an individual contribution to the stack, rather than beamforming the array elements together to produce a single waveform for the array. Furthermore, in contrast to other backprojection studies (e.g., Xu et al., 2009; Walker et al., 2010), we do not apply any trace weighting based on sensor spacing. The rationale is that the sensors closest to each other (i.e., those at arrays, rather than single-sensor stations) are also those with the best wind-noise-reduction systems. Effects of different station subsets are explored in section 3.3.
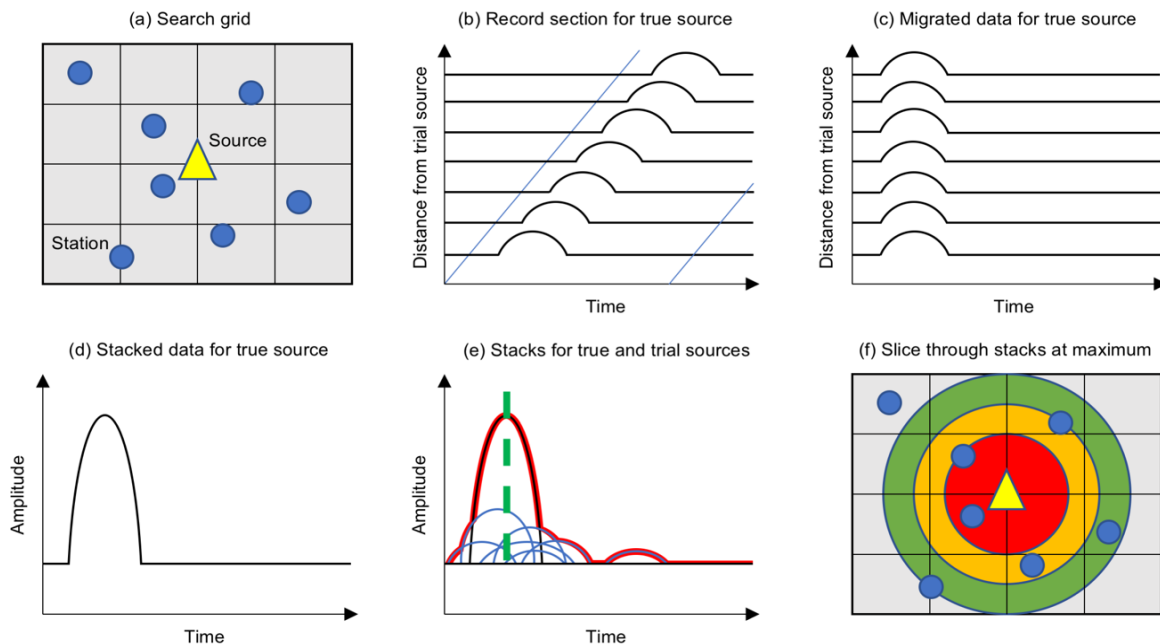
Figure 4. (a) Signal source and stations within a grid of trial source nodes. (b) Envelopes recorded by stations when using true source as the trial source. Data sections are extracted according to modeled celerity (diagonal blue lines). (c) Data sections from (b) are reverse migrated in time to the projected origin time. (d) The migrated data are stacked. (e) Stacks for all grid nodes. The stack for the true source (colored black) has the highest amplitude; stacks far from the true origin have small stacks (colored blue). A simple DF is the running maxima of all these stacks (colored red). The time of the DF maximum is marked with a green dashed line. (f) Contoured map of stack amplitudes at the time of the DF maximum in (e). Hotter colors toward the center are associated with stacks with higher amplitudes. Correct source locations are only provided by choosing times from (e) when the stack from the true source node is the highest.

2.4. Event Detection Method

Identifying and locating events in the stack requires stack metrics that provide an optimal balance between detecting volcanic events while minimizing false positive signals. This process begins by using a detector function (DF) in order to identify events (Walker et al., 2010, 2011; Arrowsmith et al., 2018). The DF shown in Figure 4e is simply a time series made up of the maximum amplitude of stacks. High DF values result from higher SNR signals across more sensors. Source locations are defined by regions with spatially coherent and high DF values (Figure 4f).

We refine this DF approach for volcanic eruptions, which can differ significantly in signal character from event to event and station to station. Importantly, variability in eruption durations (from minutes to hours) means that signals cannot be decimated to single impulses (a method employed by Walker et al., 2010, 2011). However, such expected properties of volcanic signals can be exploited to enhance detection using a regional-global network (Matoza et al., 2017). Here we specifically take advantage of the extended-duration signal property by using a summation window to increase SNR and simultaneously reduce the prevalence of artifacts and short, nonvolcanic signals. Due to this temporal summation process in forming the DF, the DF amplitude can be higher than the number of normalized waveform envelopes being stacked. The maximum possible DF value is the product of the number of traces and the number of time windows summed. We will continue to use DF when referring to this approach, or explicitly as a *time-summed DF* (TS-DF), to distinguish the method from the standard *single-time-window DF* (STW-DF) approach when needed. Similarly, we will use *stack* to indicate the time-summed stacks from which the DF derives.

Event detection is performed on DF time series using a minimum threshold of 12.5 dB, which is the typical maximum background level for our data. DF samples above this

detection threshold are grouped automatically into *peaks* (requiring a minimum gap of 1,800 s), which are then located automatically. DFs are converted to an SNR in decibel (dB) units using the following equation (adapted from Walker et al., 2010):

$$DF_{SNR} = 20log_{10}\left(\frac{|DF_{filt}|}{median(|DF_{filt}|)}\right)$$

where DF_{filt} is a DF that has been high-pass filtered above a particular period to remove the DF background offset. Here, to calculate DF_{filt} we subtrend with a 48-hr low-pass setting. All results in this paper derive from event detection and location on month-long time series, except when focusing on individual events. In such cases, we use 24-hr time periods instead.

2.5. Event Localization

We locate events based on spatial and temporal maxima in the RTM stacks, exploring two primary methods. Given that each sample in a DF is tied to a particular grid location, simply taking the maximum value of a peak in the DF provides a nominal event location (Figures 4e and 4f). We define the resulting distance between the calculated and true location as the *mislocation*. However, in some cases there is no clear maximum to the peak, while the derived source location may be offset due to atmospheric propagation artifacts (section 3.6). Furthermore, as the shape of the peak is dependent upon network geometry, choosing the median DF sample of the peak is not a robust approach. Consequently, we focus on two alternate strategies to locate events, each using a windowed section of the peak, rather than just one sample. For each peak, k number of DF_{SNR} samples above a location threshold (LT) are assessed, where LT is defined as the 75th percentile of the DF_{SNR} samples in the peak. The location methods applied to the corresponding time period are as follows: (i) *MAX* (maximum): for $DF_{SNR}(k) > LT$, the final location is the average of the locations corresponding to samples within ±75 s of the maximum amplitude; (ii) *COM3* (center of

mass in three dimensions): the final location derives from the weighted-mean of all stack samples while $DF_{SNR}(k) > LT$.

3. Results

3.1. RTM of Bogoslof Eruption Sequence

For each Bogoslof explosion, detection of infrasound by AVO did not necessarily correspond with the start of eruptive activity, nor was infrasound observed for all eruptive activity (Coombs et al., 2019; Lyons et al., 2020; Schwaiger et al., 2020). AVO detected 61 of the 70 Bogoslof events with their infrasound array data (Figure 5, red lines) using analyses deriving from least squares beamforming (e.g., Szuberla and Olson, 2004; Lyons et al., 2020). When including all available sensors, our RTM method detects 44 of 61 of these cataloged infrasound events (72%, Figure 5, green stars), and 46 of 70 of the events as a whole (66%, Figure 5, white stars). Notably, our RTM implementation identifies two cataloged eruptions that were reported by AVO as having below-detection threshold levels of infrasound (22:10 14 December 2016 and 11:17 27 June 2017).

Monthly DFs for December 2016 to September 2017 are presented in section S3 of the supplemental material. These figures include further details on AVO and RTM detections for each event. In addition to the confirmed explosions from Bogoslof, the DFs suggest additional events that were not cataloged. For example, on 11–12 January 2017, a relatively large peak in the Alaska-wide DF is observed, with the corresponding location less than 200 km from Bogoslof. However, as no AVO monitoring data types showed any volcanic activity (Wech et al., 2018; Coombs et al., 2019; Searcy and Power, 2020), we interpret this as a nonvolcanic infrasound source. Similar examples occur on, for example, 1, 9, 16, and 24 February 2017, several in April 2017, and also 24 July 2017.
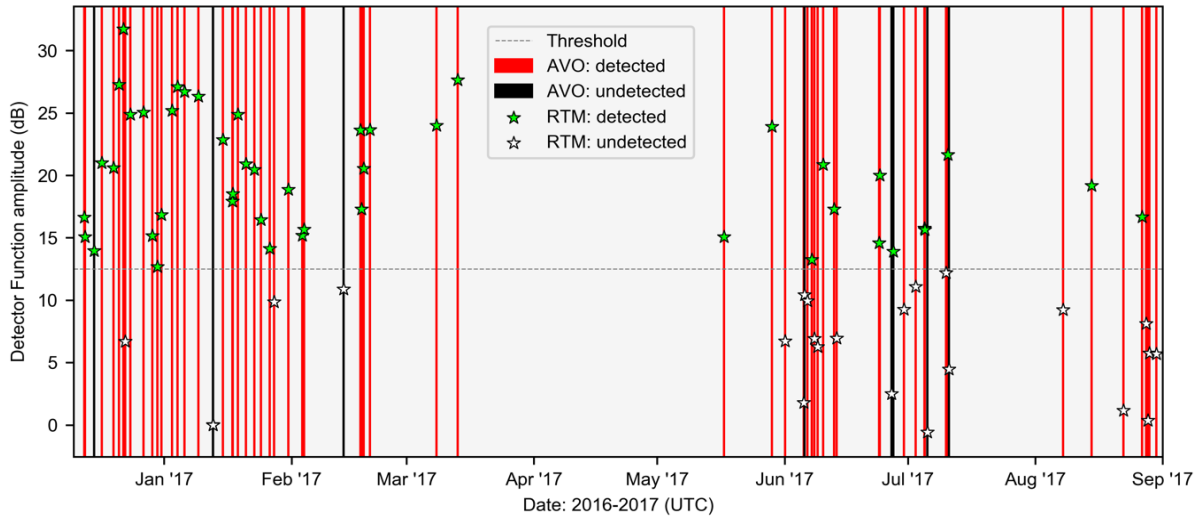
Figure 5. Time series of infrasound detection for the Bogoslof eruption sequence. Eruptions are marked by red lines if AVO registered infrasound for the events, and black if AVO did not (eruptions were confirmed through other data types). Similarly, events detected by RTM above the 12.5 dB detection threshold are marked with green stars, and events below this threshold are marked with white stars. The vertical scale represents the maximum amplitude of the DF within 15 min of the cataloged event.

3.2. RTM of 8 March 2017 Bogoslof Event

To illustrate the event detection and location procedure, we continue to focus on the 8 March 2017 eruption of Bogoslof. This event is of interest for being one of the largest across all of the monitoring categories used by AVO, including plume height, SO_2 mass, number of lightning strikes, event duration, and geographical range of seismoacoustic observations (Coombs et al., 2019). DFs for this event (Figure 6a, top panel) retain the two subpeaks broadly seen in Figures 2d and 3. With the chosen detection threshold, only the larger subpeak is automatically located. A lower threshold or manual analysis would allow for locating both subpeaks separately. Divergence of the Alaska-wide DF (colored) from the Bogoslof-specific DF (black) during the eruption is due to the contributions from stacks at nonsource grid nodes (as per Figure 4e). Changes in the mislocation value with time (Figure 6a, bottom panel) reflect the evolving location of these nonsource grid nodes in response to Alaska-wide infrasound sources.
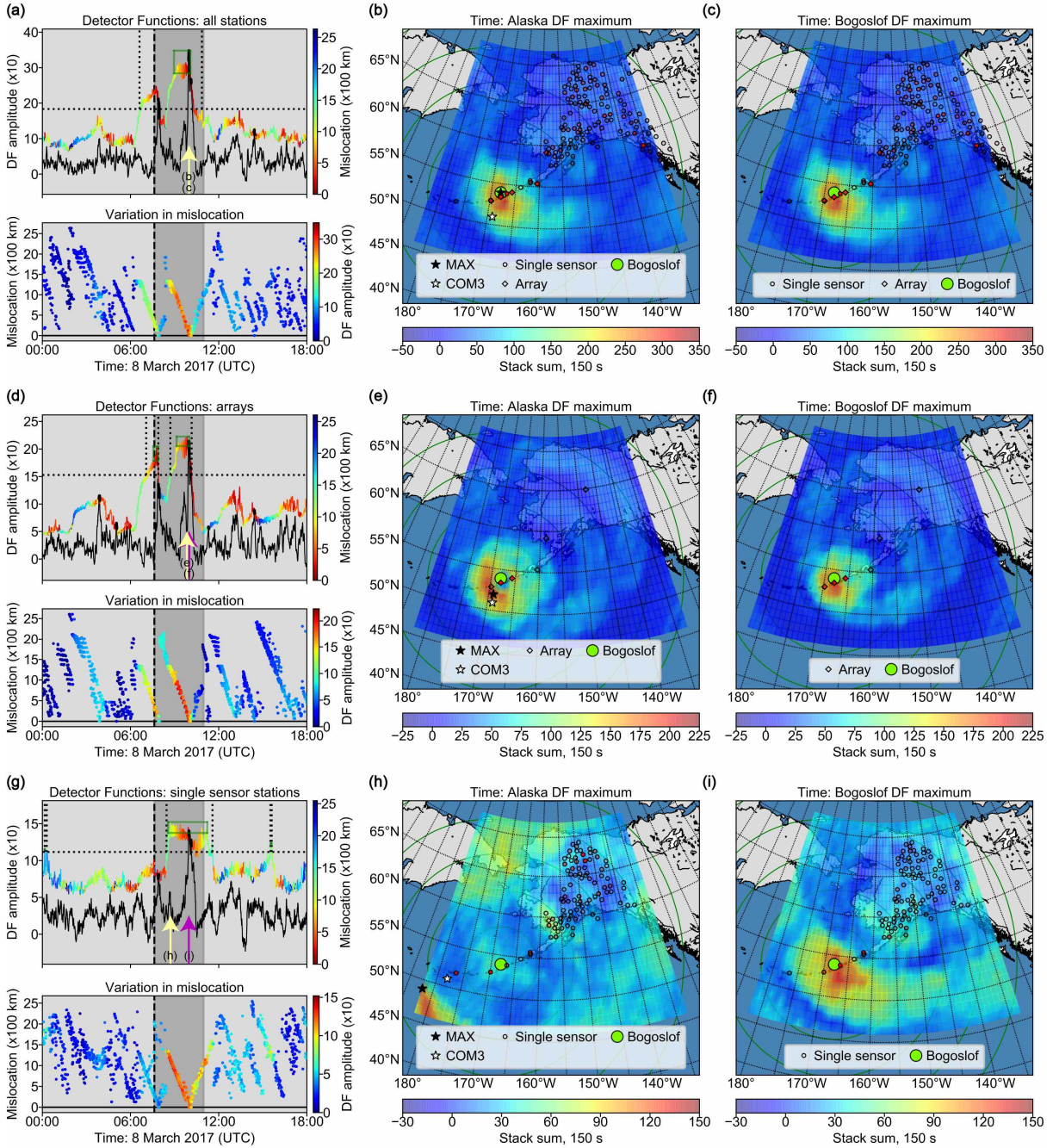
Figure 6. (a) Top panel: Alaska-wide DF (colored by mislocation) and Bogoslof-specific DF (colored black) for the 8 March 2017 Bogoslof explosion. The Bogoslof-specific DF is the stack corresponding to the trial source location (grid point) at Bogoslof. Matching amplitudes between the two DFs (marked with bold black line segments) indicate zero mislocation. Final location estimates for peaks are performed only on the high amplitude values boxed with solid green lines. Data are from all available infrasound sensors within 2,000 km of Bogoslof. The vertical dashed line is the AVO cataloged event onset, and the dark gray section the period of AVO cataloged infrasound. Dotted lines earmark samples above the 12.5 dB detection threshold. Bottom panel: Variation in mislocation from Bogoslof for each DF sample. (b) Time slice of results corresponding to larger subpeak in the Alaska-wide DF. The timestamp of the map is that of the DF maximum amplitude, marked by a yellow arrow in (a). The color scale represents the amplitude of time-aligned data stacks at each grid location. Locations provided by the MAX and COM3 methods are marked. Sensors are shaded red

proportional to stack contribution for the corresponding source time. Circles are at 500 km spacing. (c) As per (b) but at the time of the maximum in the Bogoslof-specific DF. A purple arrow in (a) is typically used to mark the corresponding time; however, in this case the two map times are identical so the purple arrow is not distinguishable. (d–f) As for (a–c) but using data from only the infrasound arrays. (g–i) As for (a–c) but using data from only the single-sensor stations.

A time slice through the stack information (Figure 6b) also shows the two location estimates for the event. The time of the map corresponds to that of the highest Alaska-wide DF amplitude (as per Figures 4e and 4f). The color scale represents the amplitude of time-aligned data stacks at each grid location. The MAX event location coincides with Bogoslof (zero mislocation), and the COM3 method locates the event 341 km SSW of Bogoslof. Sensor shading (red) is proportional to relative stack contributions assuming the MAX location is the true source. Such sensors comprise those in nearby arrays as well as several single-sensor stations to 2,000 km range with no clear distribution pattern. A time slice during the Bogoslof-specific DF maximum (Figure 6c) is identical to that of Figure 6b.

3.3. Subnetwork Influence

Here we assess the relative contributions to stacks from single-sensor stations and arrays in order to understand their respective impact. The first influential factor is proximity to volcanic sources. With infrasound arrays making up the majority of sensors within 900 km of Bogoslof (Lyons et al., 2020), these sites are nominally better placed to have higher SNR than stations at greater distance. Mitigating factors, however, include potential shadow zones within the first few hundred kilometers (Fee and Matoza, 2013, and references therein) and higher local wind noise away from the Alaskan interior. The second factor is mechanical noise suppression. Half of the sensors comprising the infrasound arrays in this study use physical noise canceling technology, such as wind domes (Walker and Hedlin, 2010; Raspet et al., 2019; Lyons et al., 2020). The TA stations in contrast, which make up the bulk of the

single-sensor stations, do not use spatial wind filtering devices. The third factor is sensor separation. The seven arrays in our study contain between four (AVO OKIF) and eight (IMS IS53) sensors. Data recorded by each sensor in an array are typically highly similar because of their close proximity (tens of meters to a few kilometers depending on the frequency range of interest). Hence, stacked envelope data for a single array will provide a higher SNR compared to an equal number of nonarray stations.

Array and single-sensor station results for the 8 March 2017 event are compared in Figure 6. For the array data, the two subpeaks (Figure 6d) are similar to those of the combined station data (Figure 6a). The MAX location for the second subpeak here has a mislocation of 233 km (Figure 6e), compared to no mislocation when using all sensors. In contrast, the single-sensor DF has a low SNR, and does not resolve the first subpeak (Figure 6g). Further, the location estimates for the second subpeak (Figure 6h) are highly inaccurate. This occurs because the relatively high samples in the Alaska-wide DF represent grid nodes far from Bogoslof. Accurate automated locations are only obtained if the highest Alaska-wide DF amplitudes are from stacks for grid nodes close to Bogoslof (e.g., Figures 6a–c). The absolute prominence of the Bogoslof- specific DF in Figure 6g, or its similar appearance to those in Figures 6a and 6d is therefore not a factor in event localization. Rather, the relative amplitudes of the Bogoslof and Alaska-wide DFs are important. More accurate locations for the single-sensor station example would be provided by automated or manual selection of DF samples when the Alaska and Bogoslof DFs intersect at ~09.45 (Figure 6i). Animations showing the time-evolution of Figure 6 are provided in the supplemental material as Movies S1–S3.

The relative location accuracy of the three station groupings is in part a consequence of the source-station geometry, with the single-sensor stations having the lowest azimuthal

coverage of Bogoslof. Hence with the addition of noise, and increased wavefield dispersion with source-receiver distance (e.g., Green and Nippress, 2019), stacked data at grid nodes other than the true source may have the highest amplitudes (Figures 6h). This scenario is reflected by the contrast in mean mislocation for the background/nonevent DF samples in Figures 6a, 6d, and 6g (bottom panels). The array-only data (Figure 6d) have a majority of location values close to Bogoslof, whereas the single-sensor station data (Figure 6g) have typical mislocations of 1,000–2,000 km, reflecting grid nodes in mainland Alaska. Therefore, for stations with good azimuthal coverage of the source, or for stations that are close to the source, selecting nonoptimal DF samples can still give a reasonable position (Figures 6b and 6e). The 15 January 2017 Bogoslof eruption is another event widely recorded across Alaska (Figure 7). In contrast to the 8 March 2017 event (Figure 6), here, each of the three groups of stations under consideration locate the event more similarly.

Given the anticipated effects of seasonal stratospheric wind direction on signal detection (Le Pichon et al., 2009), Figure 8 explores how the Alaska-wide DF maxima for AVO-cataloged infrasound events varied during 2016–2017. We compare results from single-sensor stations and arrays, as well as account for the number of sensors in operation. DF amplitudes for both data sets are lower for June through August 2017 (Figures 8a and 8b) compared to earlier in the year, despite the increase in installed sensors. Figure 8c shows that in relative terms, there is a positive relation between sensor contributions to DFs for either station category. In absolute terms, the array sensors contribute more to DFs than single sensors. For both data sets, the DF contributions per sensor are higher from December to March, than June to August. A switch in stratospheric wind direction from eastward to westward over the time period does not, however, preferentially affect one set of stations

over the other, despite the arrays having better azimuthal coverage of Bogoslof (Figure 1a).

Schwaiger et al. (2020) provide analysis of atmospheric behavior during events at Bogoslof.
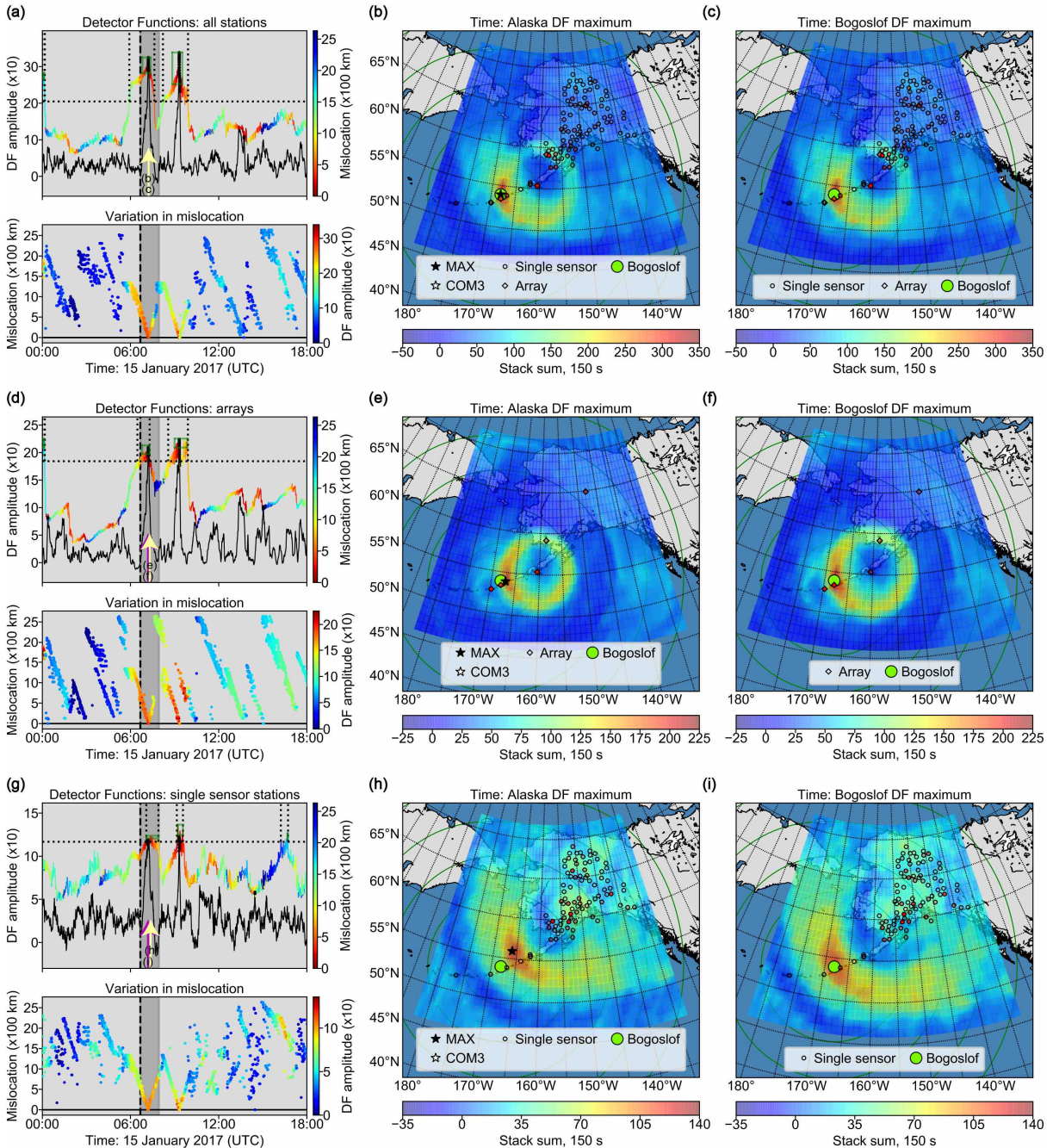
Figure 7. As for Figure 6 but using data from the 15 January 2017 Bogoslof eruption. Each map plots the location for the first peak, which has AVO cataloged infrasound, whereas the second peak does not have such information. In each case, the MAX and COM3 location estimates are collocated. The event locations from each sensor grouping are relatively similar compared to those in Figure 6.

Accounting for event size in the observations from Figure 8 is challenging as independent metrics of volcanic intensity such as plume height, SO_2 mass, and number of lightning strikes (Coombs et al., 2019), do not robustly correlate with infrasound signal characteristics (e.g., Lopez et al., 2020). A particular complication in this regard is accounting for the fluctuating vent conditions (submarine to subaerial), dome building activity, and any cloud coverage which hampers satellite observations. Given these constraints, however, no particular decrease in event magnitude is identified over the course of the eruption. Similar event size comparisons exist for precursory seismicity (Tepp and Haney, 2019), and eruptive seismicity (Haney et al., 2020a; Tepp et al., 2020).
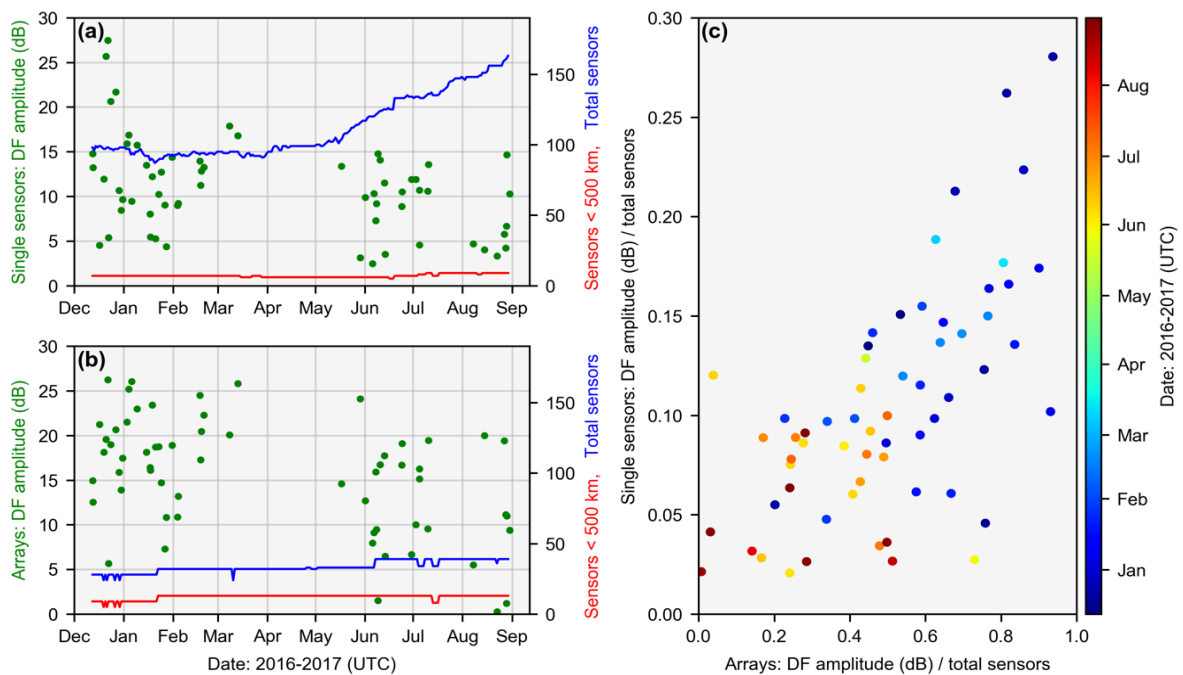
Figure 8. (a) Single-sensor station DF amplitude (in dB) and sensor number versus time, for infrasound-generating events cataloged by AVO (±15 min). Sensor quantity is shown for both total sensors (blue line) and sensors within 500 km of Bogoslof (red line). (b) As per (a) but for arrays. (c) Sensor contribution to DFs in absolute and relative terms for the arrays and single-sensor stations, shaded by time.

3.4. Algorithm Performance for Bogoslof Eruption Sequence

We use receiving operator characteristic (ROC) curves (Fawcett, 2006) to compare the ability of different RTM algorithms to correctly classify events. These ROC curves plot the true-positive rate (TP rate) versus false-positive rate (FP rate) of a DF for a range of detection thresholds (Figure 9). An algorithm that classifies events perfectly will have a threshold that gives a TP rate of 1, and an FP rate of 0. For such an algorithm, the area under the curve (AUC) accounts for 100% of the total possible area. AUC values close to 50% are equivalent to classifications being a random guess. A ROC curve is equivalent to plotting the probability of an eruption versus the probability of a false alarm. We automatically classify detections by comparing AVO infrasound catalogs for Bogoslof to DF samples at equivalent times, on a sample by sample basis. Other volcanic events such as those from Cleveland are not treated as cataloged events, nor are known nonvolcanic events. ROC calculations are performed on month-long DF_{filt} time series.

ROC curves are also useful for comparing RTM parameter choices, station choices, and time of year, all factors which can affect the SNR of DFs (Figures 5 and 8). For instance, to further illustrate seasonal weather influences for the three station groups, Figure 10 compares ROC results for each month using AUC as a classification metric. Figure 10 also compares implementation of the TS-DF and STW-DF approaches to assess if there are differences in classification performance between the two methods. We find that for both DF formats, AUC values are typically at or above 75% for the majority of the year. Only July and August 2017 have AUC values close to 50%. The classification performance for the single-sensor stations is poorer than the other two station configurations. Overall, TS-DFs classify volcanic events marginally better than STW-DFs.
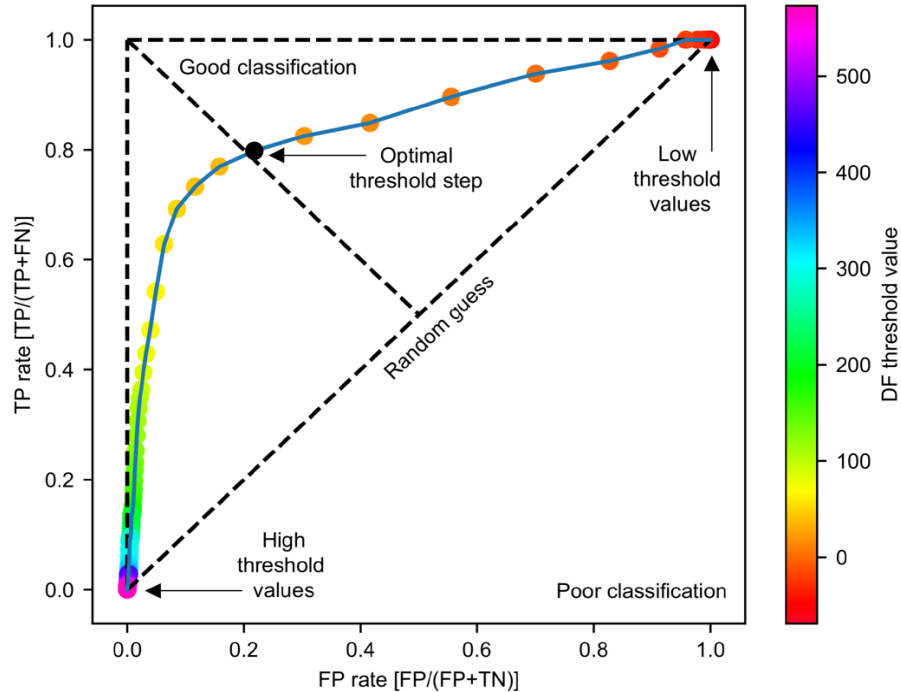
Figure 9. ROC curve for December 2016 data. A DF detection threshold of 29.4 gives a moderately high TP rate (~0.8) and moderately low FP rate (~0.2). The area under the curve (AUC) is 85%. TP, true positive = eruption with DF > threshold T; FP, false positive = no eruption with DF > T; TN, true negative = no eruption with DF < T; FN, false negative = eruption with DF < T.

We also evaluate seasonal effects on algorithm performance over the Bogoslof eruption sequence by plotting (1) the percentage of AVO cataloged infrasound events detected by RTM (allowing a ±15-min margin), and (2) the location accuracy of those detected events using monthly averages (Figure 10). As with the ROC classification performance, the event detection rates and location accuracy are typically better from December 2016 to May 2017, and poorer subsequently. Notable differences between the DF methods include STW-DFs being relatively strong for event detection rates (up to 85% overall), with the greatest difference being for the single-sensor stations. Similarly, for the location methods, STW-DFs perform relatively well for the single-sensor station data, though direct comparison is challenging given the contrasting event detection rates.
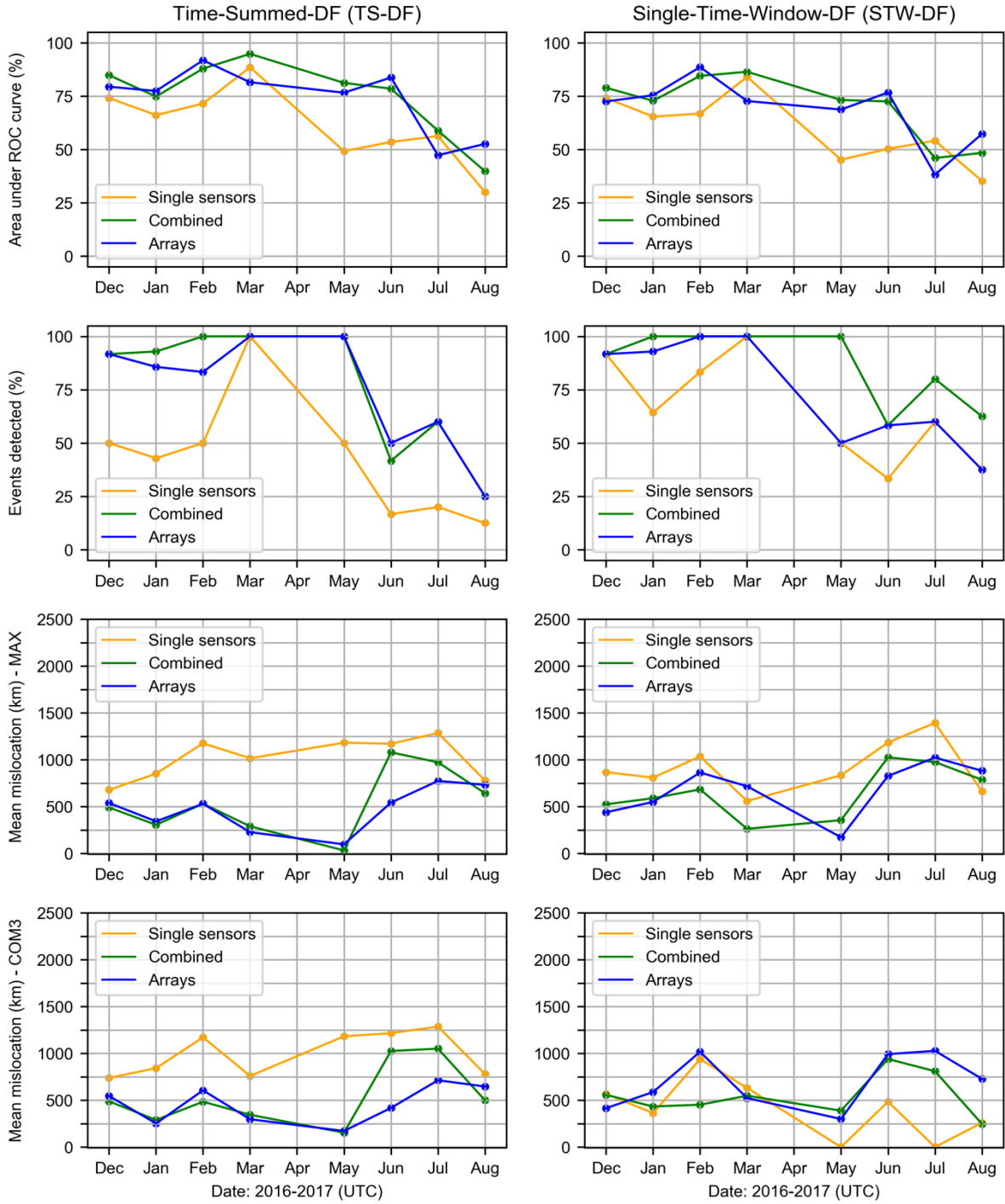
Figure 10. Comparison of detection and location results using TS-DF (left column) and STW-DF (right column) approaches. Though broadly similar, the TS-DF method, as used throughout the paper, is relatively strong for array-only stations versus single-sensor stations, whereas the STW-DF is particularly advantageous for single-sensor station and combined sensor results in terms of event detection. Bogoslof events were cataloged by AVO for every month except April 2017. Absence of markers for a particular month here indicates no detections by the method.

3.5. Algorithm Performance for Non-Bogoslof Events

Since the beginning of the Bogoslof eruption sequence in December 2016, many other volcanoes in the North Pacific have erupted. The volcanoes from Alaska are: Cleveland, Great Sitkin, Semisopochnoi, and Veniaminof (Figure 1) (Alaska Volcano Observatory, 2019), and from Kamchatka: Bezymianny, Ebeko, Kambalny, Karymsky, Khangar, Klyuchevskoy, Koshelev, Sarychev Peak, Sheveluch, Zheltovsky, and Zhupanovsky (KVERT, Institute of Volcanology and Seismology FEB RAS, 2019). We assessed a subset of these (Table S2 of the supplemental material) based on network proximity, event size, and plume direction. Of the Alaska events, only the Cleveland explosions are clearly detected by RTM (using the same parameter set for Bogoslof). These results are somewhat expected as most of the nondetected eruptions were relatively small. Of the five Kamchatka events focused on, only the Bezymianny explosion on 20 December 2017 is clearly identified. Candidate events from near Koshelev and Zheltovsky are suggested by RTM but these do not match events in KVERT catalogs. Unfavorable propagation and attenuation conditions may explain the lack of clear observations from nondetected Kamchatka events, which were on a similar scale to that of Bogoslof on 8 March 2017. Detection performance for eruptions in Kamchatka and the western Aleutians could increase with inclusion of data from the IMS stations in Kamchatka (IS44) and others in the northern Pacific region (Fee et al., 2010b; Matoza et al., 2017), as well as any local infrasound networks in those areas (Gordeev et al., 2013; Matoza et al., 2019).

Additional nonvolcanic events are regularly seen in our DFs (section S3, supplemental material). The IMS IS53 array in central Alaska is particularly well positioned to record urban noise, industrial and military blasts (Gibbons et al., 2019; Schneider et al., 2018), and rocket launches (de Groot-Hedlin et al., 2008) from the Poker Flat Research

Range. Many of these types of events, and others such as debris flows (IRIS DMC, 2014; Toney et al., 2019) and bolides (Walker et al., 2010; Edwards et al., 2014; [appendix 1]), were recorded by the TA while it was traversing the continental United States. Such observations are detailed in the TA Infrasound Reference Event Database (IRIS DMC, 2012; de Groot-Hedlin and Hedlin, 2015). Several M6+ earthquakes in Alaska were also located by applying our RTM algorithm to air-coupled ground waves [detailed in appendix 1] (also see Shani-Kadmiel et al., 2018a, and a review by Mikumo and Watada, 2010).

3.6. Source Resolvability and Stack Artifacts

The stacked data here contain significant artifacts, manifesting as event data being smeared across space-time in a phenomenon known as swimming (e.g., Meng et al., 2012). A correctly tuned RTM algorithm should generate event-based stack maxima only at the physical source, rather than earlier or later along a swimming track. Swimming is clearly apparent in Figures 6 and 7 by comparing the widths of peaks in the Alaska-wide and Bogoslof-specific DFs, as well as by observing the evolving mislocation during the event. Movies S1–S3 show this migration particularly well prior to, during, and after the 8 March 2017 event. Swimming is principally a consequence/function of the network geometry's response to a series of impulses (Koper et al., 2012). The artifacts are emphasized where sources are complex and outside the majority of the network (due to poor azimuthal coverage). Consequently, there are implications for being able to clearly resolve and accurately locate a source using stack information even under ideal atmospheric propagation and noise conditions.

To illustrate the impact of network geometry and source type further, Figure 11 compares synthetic sources (1- and 10-min durations) at 3 locations across the north Pacific.
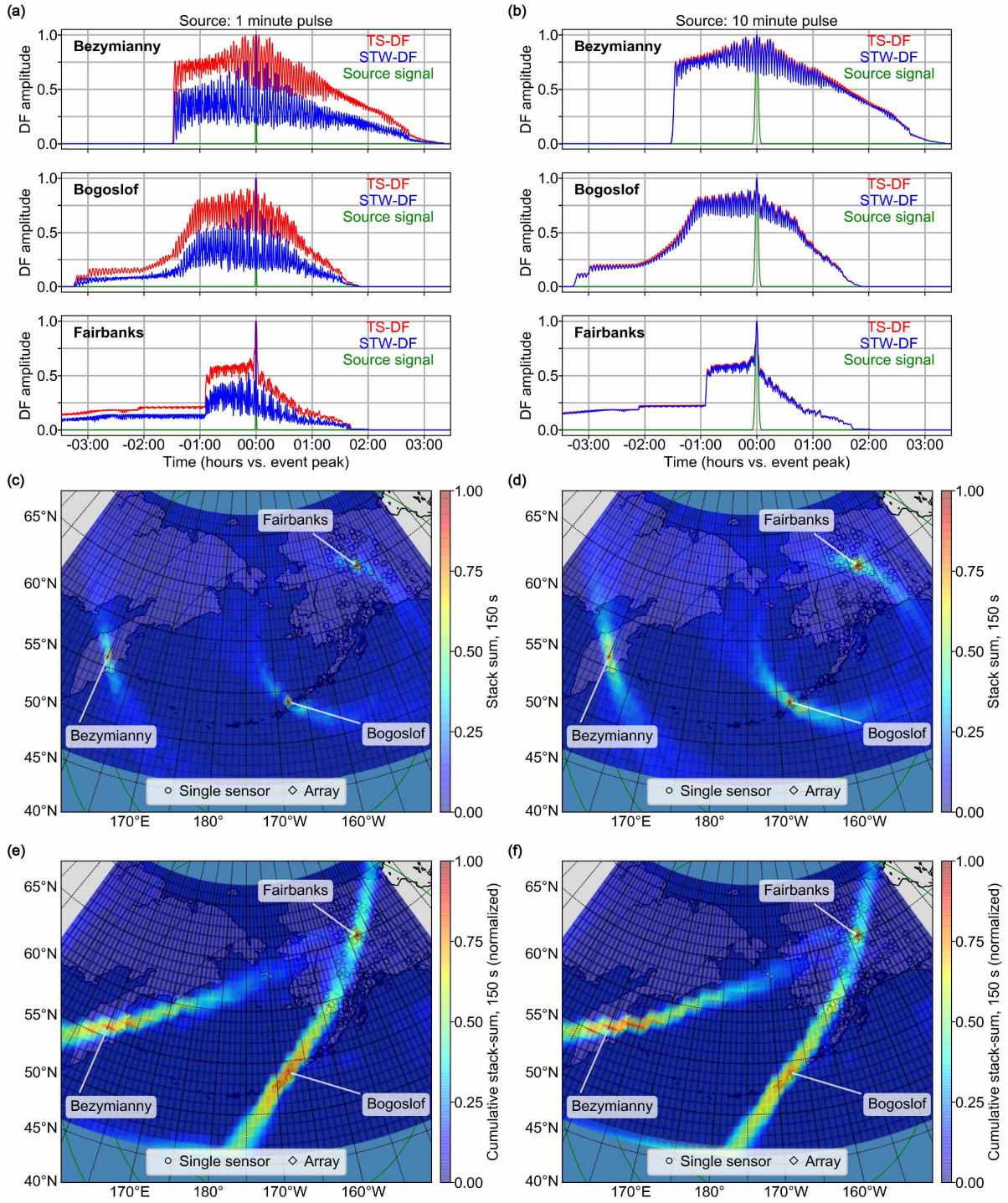
Figure 11. (a) Normalized DFs for a 1-min synthetic Gaussian source pulse, placed at three locations and propagated to all marked stations with a 300 m/s celerity. Sharp steps in the Bezymianny and Fairbanks DFs are a result of proximity to the grid boundary. (b) As per (a) but with 10-min Gaussian source pulse. (c, d) Maps showing time slices through time- summed stack data at times 00:00. Rings are at 500-km intervals. (e, f) Maps showing cumulative time-summed stack values at each grid node for the 1- and 10-min pulses.

These locations represent sources within the network center (Fairbanks, Alaska), network margin (Bogoslof, Alaska) and far outside the network (Bezymianny, Kamchatka). During each DF shown, the stack for each true source is only represented briefly at time 00:00. For shorter impulse sources (Figure 11a), DFs at all three source locations have larger oscillations and generally clearer peaks than for longer, emergent sources (Figure 11b). These oscillations are simply the original source information stacking at non–true grid nodes with lower amplitudes. As the source duration grows (and/or grid spacing decreased), these peaks merge together. Relatively clear DF peaks occur for sources closer to the network center due to improved azimuthal coverage. Further, peak sharpness is also celerity dependent—the narrower the celerity search range, the narrower the DF (Figure 11 uses a single celerity of 300 m/s for simplicity).

Figures 11c and 11d show the stack information at time 00:00 in map form. Here, RTM location estimates are reflected by the intersection of ring features around individual sensors. When particular sensors contribute heavily to the location, the rings centered on those sensors are more pronounced. Such features are commonly seen around arrays which contain multiple equally weighted sensors, for example, Figure 7 and Movies S1–S3. Figures 11e and 11f plot cumulative stack amplitudes, illustrating the swimming tracks along the respective source-station axes. Stacked energy is more concentrated for short events and for source proximity to the network center, providing higher location resolution. The azimuthal coverage of these sources has parallels to how the groupings of combined, array, and single sensors are positioned in relation to Bogoslof.

The swimming artifact for the 8 March 2017 Bogoslof event is explicitly illustrated by Figure 12. The DFs in Figure 12a are the same as those from Figure 6a, but here the time slice map (Figure 12b) corresponds to the maximum amplitude of the first, smaller subpeak

of the Alaska-wide DF, rather than the second. The location of the highest stack energy is to the SW of Bogoslof, rather than at the true source. For subsequent time slices, the region of maximum stack energy migrates NE, passing Bogoslof at 07:53 (Figure 12c). A similar migration is observed for the second subpeak from 08:30–11:00. Figure 12d shows the cumulative stack amplitude at each grid node for the time period covering both DF subpeaks (06:00–12:00). Though the highest cumulative amplitude is at Bogoslof, there is significant energy distributed elsewhere. In particular, the SW corner of the grid accumulates amplitude values that would otherwise locate SW of the grid edge if it were not for this boundary. Consequently, the corner node is masked here to avoid dominating the color scale.

Limiting the grid search (or DF components) to nodes that are on land is a potential approach for mitigating swimming artifacts applicable to arc volcanism. Given the direction of swimming here is from SW to NE, the initial swimming artifact is entirely over the ocean until the Aleutian Islands are reached. By excluding grid nodes over the ocean, this pre-artifact can be removed from the DF, though post-artifacts remain due to the remaining land (Figure 12e). Locations for the first subpeak are now accurate compared to without the mask (Figure 12f vs. 12b). The evolution of mislocation with time also becomes unclear (Figure 12g) and the cumulative stack energy now shows a constrained distribution (Figure 12h). More severe masks could be used in order to restrict DFs to particular regions of interest (indeed the Bogoslof-specific DFs are an extreme case of this). Notably Landès et al. (2012) conversely mask grid values over the continents to avoid locating microbaroms on the continents. Arrowsmith et al. (2018) describe a range of related methods.

Other strategies to minimize or account for swimming include time-frame averaging (Koper et al., 2012), reference windows (Meng et al., 2012), as well as combining results from azimuthally distinct subnetworks, and exotic stacking techniques (e.g., Xu et al., 2009...
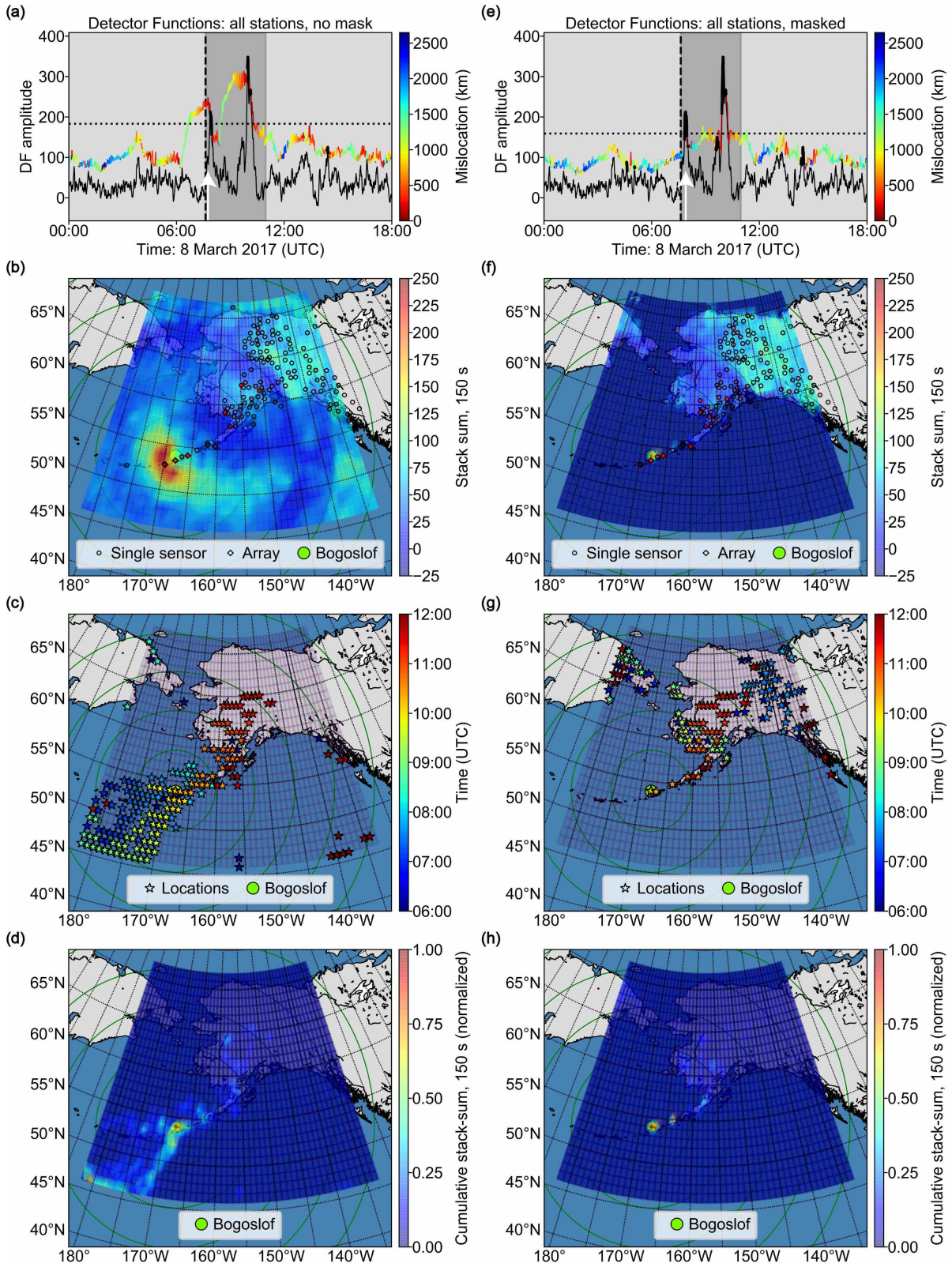
Figure 12. (a) DFs for the 8 March 2017 explosion from Bogoslof without a mask. Other details per Figure 6a. There is no mislocation of the maximum of the larger subpeak. The mislocation of the maximum of the smaller subpeak is ~200 km, however. (b) Time slice map corresponding to maximum of smaller subpeak

(marked with arrow in Figure 12a). Other details per Figure 6b. (c) RTM locations for each sample in the Alaska-wide DF (Figure 12a), color-coded by time. (d) Location data from the Alaska-wide DF is binned by grid node and tallied. (e–h) As for (a)–(d) with a mask applied such that the DF is formed only from stacks for grid nodes close to land.

and references therein). In evaluating three such stacking methods (Nth root, semblance, and F-ratio) we find that though swimming artifacts improve in some cases, in other cases the artifacts remain. Use of azimuthally distinct subnetworks for this study is problematic given the progressive deployment of the TA during the Bogoslof eruption. The westernmost stations (well placed to help constrain events) were only deployed at the end of the eruption sequence (Figure 1).

4. Discussion

Bogoslof was a complex seismoacoustic source, with the vent submerged for most of the nine-month eruption, impacting acoustic coupling with the atmosphere (Godin, 2008; Ichihara et al., 2009; Lyons et al., 2019, 2020; Fee et al., 2020). Infrasound from some explosions is detectable at ranges of 2,000 km or more by regional networks (Figure 2). Distant arrivals are sometimes clearer than those more proximal due to refractive shadow zones and atmospheric waveguides (Drob et al., 2003). The dense regional network in Alaska is, despite poor azimuthal coverage of the Aleutian Arc, capable in principle of identifying and locating explosions to subdegree accuracy using RTM. However, detection and location capability depends upon the number of arrivals, their azimuthal distribution, SNR, and processing methods.

One demonstrated shortcoming of RTM, though not unique to it, is that for sources outside the network, the location estimate has a spatiotemporal error ellipse along the source-network axis (Cochran and Shearer, 2006), manifesting as swimming artifacts (Figures 6, 7, 11, and 12). These artifacts result in locations for both background and

high-amplitude DF samples migrating over the grid space. Thus, having an event trigger based only on whether a volcano-specific DF matches the Alaska-wide DF will have many false alarms, even during background noise. Without adequate azimuthal coverage of the source, a DF amplitude threshold is an insufficient control to resolve this issue (Figure 11). The majority of volcanoes of interest in Alaska are outside the margins of the bulk of monitoring stations, and consequently incorporation of an independent location estimate provided by local infrasound arrays would provide this azimuthal control. These arrays can provide individual back azimuths (Gibbons et al., 2005; Le Pichon et al., 2005; Ripepe et al., 2007; Fee et al., 2010b; Fee et al., 2016; Iezzi et al., 2019), and distances (Szuberla et al., 2006; Shani-Kadmiel et al., 2018b; Green and Nippress, 2019; Shang et al., 2019), in addition to source triangulation through a cross-bearings approach (e.g., Le Pichon et al., 2008; Matoza et al., 2011a; Matoza et al., 2011b; Mialle et al., 2015; Matoza et al., 2017). The relative consistency with which stacked array data characterizes eruption records, when compared to a network of single sensors demonstrates the importance of these arrays. Similarly, deriving locations by treating the existing network as a mesh of three-station triads is another approach (de Groot-Hedlin and Hedlin, 2015).

The success of the RTM method also depends on the alignment and shape of envelopes being stacked. For instance, events tend to locate well if the original waveforms have features that are sharp/impulsive enough, or can be processed in such a way that a DF reflects that sharp feature (Figure 7). The contrary is also true—broadly topped DFs may not locate well, particularly if the DF maximum is taken arbitrarily (Figures 6g and 6h). An important related factor is that RTM stacks energy rather than phases, and thus stack amplitudes and the ability to locate an event are impacted by the change in wavefield between source and receiver. Such changes are typically proportional to source-receiver

distance on the order of the scales in this study (Green and Nippress, 2019). In the presence of realistic atmospheric multipathing, observing interstation similarity on the order of the 8 March 2017 Bogoslof eruption (Figure 2) across 2,000+ km is unlikely, particularly for weak signals. Short signals can be incorporated into a single envelope, and thus easily stacked (e.g., Hedlin and Walker, 2013). However, for signals longer than a few minutes and for sources outside the network, stacking is more challenging and thus the true locations become difficult to resolve (Figure 11). In such cases, phase association and variable window lengths may be advantageous (Park et al., 2018), as well as allowing for multiple celerities at each time step between grid nodes and stations.

Seasonal variability in dominant stratospheric wind direction affects detection capability (Le Pichon et al., 2008; Le Pichon et al., 2009; Mutschlecner and Whitaker, 2010; Hedlin and Walker, 2013; Tailpied et al., 2017). In the Alaskan winter months, stratospheric winds typically blow eastward (from west to east) from the Aleutians toward the network, whereas in the summer the case is the opposite (De Angelis et al., 2012). In both cases, however, tropospheric and thermospheric ducting may still take place under different influences (De Angelis et al., 2012; de Groot-Hedlin, 2017; Iezzi et al., 2019; Schwaiger et al., 2019, 2020). Surface winds can also mask signals of interest, though such winds are typically weaker inland. Increased snow cover during winter can be beneficial by isolating sensors from turbulence and gusts (Woodward et al., 2005). It is reasonable that different parameter choices would work better at some times of year than others, for different event characteristics, and for different station combinations (Figure 10). For example, the lower frequency filter limit of 0.35 Hz is set in order to retain data above the microbarom peak and reduce wind noise. However, given the seasonal change in strength of the microbarom in the

northern Pacific (Garcés et al., 2010; Walker, 2012), such a lower limit could be made flexible to take advantage of this situation.

The factors discussed above are interpreted here to affect the ROC classification, event-detection rates, and location accuracy results presented in section 3.4. The temporal features observed in Figure 10 are also reflected in results from other AGC and stacking methods (section S4, supplemental material). However, the number of events in any particular month and their relative or absolute amplitudes are also important considerations when interpreting temporal statistics (including Figures 5 and 8). Given that ROC classification is performed with only Bogoslof events, rather than all known volcanic or nonvolcanic infrasound-generating signals, a more detailed assessment may produce improved results. In a similar vein, it is worth noting that the final AVO catalog was a retroactive assessment of data products, with some infrasound detections based on just a single array.

The choice of the DF type also affects the capacity for isolating, detecting, and locating explosive events, depending on the station configuration and event duration. Synthetic results show clear differences between DF types for the 1-min events (Figure 11a), and would be expected for sources up to several minutes. For Bogoslof, AVO cataloged infrasound durations vary from 2–409 min (median 14 min), with 17 of the 61 events ≤ 5 min. For out-of-network sources, STW-DFs have relatively clear peaks compared to TS-DFs (Figure 11a). This factor may contribute to the relatively high event detection rates for the single-sensor stations using STW-DFs (Figure 10). These implications extend to Cleveland, which is more remote than Bogoslof, and typically exhibits brief explosive eruptions (De Angelis et al., 2012; Werner et al., 2017; Iezzi et al., 2019; Table S2).

However, Figure 10 shows that for combined and array station configurations, TS-DFs have a slight advantage for both reducing false positives, and location accuracy of detected events.

Overall, 72% and 85% of known infrasound-generating events from Bogoslof were identified with TS-DF and STW-DF methodologies respectively, when using all sensors. Successful detections include the onset of the Bogoslof eruption sequence on 12 December 2016, and the following three events (section S2, supplemental material), something not observed at the time by routine AVO monitoring (Coombs et al., 2018). Had Bogoslof been suspected of unrest, however, alarms at AVO arrays would likely have been set and triggered by the eruptions (Lyons et al., 2020). Detection of these events with RTM is in addition to several other cataloged events not documented as having detectable infrasound by AVO (section 3.1). Larger explosive events, such as the 2008 eruptions of Kasatochi and Okmok volcanoes, Alaska (Fee et al., 2010b), would likely be detected and located well with the RTM algorithm, even in the presence of unfavorable acoustic propagation or other conditions. Supplementing the network with strategically placed sensors in quiet locations would also likely improve RTM performance (e.g., Tailpied et al., 2017; Biasi and Alvarez, 2018), as would refined wind noise suppression for TA sensors. Improved algorithm performance is expected in areas with less challenging network geometries and weather.

5. Conclusions

We have shown that simple RTM methods using the TA and other regional network infrasound data are capable of detecting and locating relatively small and emergent events from remote Alaskan volcanoes such as Bogoslof and Cleveland. Our RTM implementation is able to detect and locate more than 72% of the Bogoslof infrasound events cataloged by AVO. Such statistics, as well as those for location accuracy and classification success, vary

significantly with RTM parameters choices. Identification and location of events with RTM is improved by the presence of the TA; however, individually, the TA typically performs worse than existing infrasound arrays in the region. This deficit is likely due to a combined function of greater source-station distances, lower azimuthal coverage, and lower intersensor signal coherence. Our efforts to locate infrasound signals from known eruptions in Kamchatka had a low success rate (one of five) due to more extreme cases of the above factors. The presence of spatial wind noise filters at most arrays is also a key difference versus TA sites. The effectiveness of RTM in the region also varies seasonally, with no apparent dependence on event size. Lower event detection rates during the summer, when stratospheric winds typically blow away from the network, show that increased azimuthal coverage of remote volcanoes is crucial and not compensated for by high sensor quantity alone. Opportunities for refining and improving these RTM strategies include data-adaptive processing, provision for atmospheric specifications, and incorporating azimuthal information from arrays. The frequent eruptions and dense regional network in Alaska provide an excellent opportunity to continue assessing the capability of regional-scale seismoacoustic networks for remote volcanic monitoring.

Acknowledgments

References

Alaska Volcano Observatory (2019). *Volcano information: Eruption search*. Retrieved from https://www.avo.alaska.edu/volcanoes/eruptsearch.php

Arnoult, K. M., Olson, J. V., Szuberla, C. A. L., McNutt, S. R., Garcés, M. A., Fee, D., and Hedlin, M. A. H. (2010). Infrasound observations of the 2008 explosive eruptions of Okmok and Kasatochi volcanoes, Alaska. *Journal of Geophysical Research: Atmospheres*, 115, D00L15. https://doi.org/10.1029/2010jd013987

Arrowsmith, S., Young, C., and Pankow, K. (2018). Implementation of the Waveform Correlation Event Detection System (WCEDS) method for regional seismic event detection in Utah. *Bulletin of the Seismological Society of America*, 108(6), 3548–3356. https://doi.org/10.1785/0120180097

Batubara, M., Saito, H., and Yamamoto, M. Y. (2018). Results from infrasound monitoring using integrated sensors data by means of a network along multisite point over Japan. Abstract [S53D-0438] presented at *2018 Fall Meeting, AGU*, Washington, DC.

Behnke, S. A., and McNutt, S. R. (2014). Using lightning observations as a volcanic eruption monitoring tool. *Bulletin of Volcanology*, 76(8), 1–12. https://doi.org/10.1007/s00445-014-0847-1

Biasi, G. P., and Alvarez, M. G. (2018). Station and telemetry impact metrics for earthquake early warning seismic network performance evaluation (abstract). *Seismological Research Letters*, 89(2B), 717–996.

Blackburn, L. (2015). *Point and focus algorithms*. Retrieved from https://eht-wiki.haystack.mit.edu/Public_Area/LMT/Point_and_focus_ algorithms

Bowman, J. R. (2005). Meteorological conditions at infrasound stations. *Inframatics*, 9.

Bueno, A., Diaz-Moreno, A., Álvarez, I., De la Torre, A., Lamb, O. D., Zuccarello, L., and De Angelis, S. (2019). VINEDA – Volcanic INfrasound Explosions Detector Algorithm. *Frontiers in Earth Science*, 7(335). https://doi.org/10.3389/feart.2019.00335

Busby, R. W., Woodward, R. L., Hafner, K. A., Vernon, F. L., and Frassetto, A. M. (2018). *The design and implementation of EarthScope's USArray Transportable Array in the Conterminous United States and Southern Canada*. Retrieved from: http://www.usarray.org/ researchers/obs/transportable/l48_ta_report

Cameron, C. E., Schaefer, J. R., and Mulliken, K. M. (2018). Historically active volcanoes of Alaska. *Alaska Division of Geological and Geophysical Surveys Miscellaneous Publication*, 133 v. 3, 2 sheets. http://doi.org/10.14509/30142

Carniel, R., Cabras, G., Ichihara, M., and Takeo, M. (2014). Filtering wind in infrasound data by non-negative matrix factorization. *Seismological Research Letters*, 85(5), 1056–1062. https://doi.org/10.1785/0220130142

Chouet, B. A., and Matoza, R. S. (2013). A multi-decadal view of seismic methods for detecting precursors of magma movement and eruption. *Journal of Volcanology and Geothermal Research*, 252, 108–175. https://doi.org/10.1016/j.jvolgeores.2012.11.013

Cochran, E., and Shearer, P. (2006). Infrasound events detected with the Southern California Seismic Network. *Geophysical Research Letters*, 33, L19803. https://doi.org/10.1029/2006GL026951

Coombs, M. L., Wallace, K., Cameron, C., Lyons, J. J., Wech, A., Angeli, K., and Cervelli, P. (2019). Overview, chronology, and impacts of the 2016–2017 eruption of Bogoslof volcano, Alaska. *Bulletin of Volcanology*, 81(11), 1–23. https://doi.org/10.1007/s00445-019-1322-9

Coombs, M. L., Wech, A. G., Haney, M. M., Lyons, J. J., Schneider, D. J., Schwaiger, H. F., et al. (2018). Short-term forecasting and detection of explosions during the 2016–2017 eruption of Bogoslof volcano, Alaska. *Frontiers of Earth Science*, 6(122). https://doi.org/10.3389/feart.2018.00122

Dabrowa, A. L., Green, D. N., Rust, A. C., and Phillips, J. C. (2011). A global study of volcanic infrasound characteristics and the potential for long-range monitoring. *Earth and Planetary Science Letters*, 310(3–4), 369–379. https://doi.org/10.1016/j.epsl.2011.08.027

De Angelis, S., Fee, D., Haney, M., and Schneider, D. (2012). Detecting hidden volcanic explosions from Mt. Cleveland Volcano, Alaska with infrasound and ground-coupled airwaves. *Geophysical Research Letters*, 39, L21312. https://doi.org/10.1029/2012GL053635

de Groot-Hedlin, C. D. (2017). Infrasound propagation in tropospheric ducts and acoustic shadow zones. *The Journal of the Acoustical Society of America*, 142(4), 1816–1827. https://doi.org/10.1121/1.5005889

de Groot-Hedlin, C. D., and Hedlin, M. A. H. (2015). A method for detecting and locating geophysical events using groups of arrays. *Geophysical Journal International*, 203(2), 960–971. https://doi.org/10.1093/gji/ggv345

de Groot-Hedlin, C. D., and Hedlin, M. A. H. (2018). A new automated approach to detecting and locating seismic events using data from a large network. *Bulletin of the Seismological Society of America*, 108(4), 2032–2045. https://doi.org/10.1785/0120180072

de Groot-Hedlin, C. D., Hedlin, M. A. H., and Walker, K. T. (2014). Detection of gravity waves across the USArray: A case study. *Earth and Planetary Science Letters*, 402, 346–352. https://doi.org/10.1016/j.epsl.2013.06.042

de Groot-Hedlin, C. D., Hedlin, M. A. H., Walker, K. T., Drob, D. P., and Zumberge, M. A. (2008). Evaluation of infrasound signals from the shuttle Atlantis using a large seismic network. *The Journal of the Acoustical Society of America*, 124(3), 1442–1451. https://doi.org/10.1121/1.2956475

Drob, D. P., Picone, J. M., and Garcés, M. (2003). Global morphology of infrasound propagation. *Journal of Geophysical Research: Atmospheres*, 108, D21. https://doi.org/10.1029/2002JD003307

Edwards, W. N., de Groot-Hedlin, C. D., and Hedlin, M. A. H. (2014). Forensic investigation of a probable meteor sighting using USArray acoustic data. *Seismological Research Letters*, 85(5), 1012–1018. https://doi.org/10.1785/0220140056

Evers, L. G., and Haak, H. W. (2005). The detectability of infrasound in the Netherlands from the Italian volcano Mt. Etna. *Journal of Atmospheric and Solar: Terrestrial Physics*, 67(3), 259–268. https://doi.org/10.1016/j.jastp.2004.09.002

Fan, W., de Groot-Hedlin, C. D., Hedlin, M. A. H., and Ma, Z. (2018). Using surface waves recorded by a large mesh of three-element arrays to detect and locate disparate seismic sources. *Geophysical Journal International*, 215(2), 942–958. https://doi.org/10.1093/gji/ggy316

Fawcett, T. (2006). An introduction to ROC analysis. Pattern Recognition Letters, 27, 861–874. https://doi.org/10.1016/j.patrec.2005.10.010

Fee, D., and Garcés, M. (2007). Infrasonic tremor in the diffraction zone. *Geophysical Research Letters*, 34, L16826. https://doi.org/10.1029/2007GL030616

Fee, D., Garcés, M., Patrick, M., Chouet, B., Dawson, P., and Swanson, D. (2010a). Infrasonic harmonic tremor and degassing bursts from Halemaʻumaʻu Crater, Kīlauea Volcano, Hawaiʻi. *Journal of Geophysical Research: Solid Earth*, 115, B11316. https://doi.org/10.1029/2010JB007642

Fee, D., Haney, M., Matoza, R., Szuberla, C., Lyons, J., and Waythomas, C. (2016). Seismic envelope-based detection and location of ground-coupled airwaves from volcanoes in Alaska. *Bulletin of the Seismological Society of America*, 106(3), 1–12. https://doi.org/10.1785/0120150244

Fee, D., Haney, M. M., Matoza, R. S., Van Eaton, A. R., Cervelli, P., Schneider, D. J., and Iezzi, A. M. (2017). Volcanic tremor and plume height hysteresis from Pavlof Volcano, Alaska. *Science*, 355(6320), 45–48. https://doi.org/10.1126/science.aah6108

Fee, D., Lyons, J., Haney, M., Wech, A., Waythomas, C. F., Diefenbach, A. K., et al. (2020). Seismo-acoustic evidence for vent drying during shallow submarine eruptions at Bogoslof volcano, Alaska. *Bulletin of Volcanology*, 82(1), 1–14. https://doi.org/10.1007/s00445-019-1326-5

Fee, D., and Matoza, R. S. (2013). An overview of volcano infrasound: From Hawaiian to Plinian, local to global. *Journal of Volcanology and Geothermal Research*, 249, 123–139. https://doi.org/10.1016/j.jvolgeores.2012.09.002

Fee, D., McNutt, S. R., Lopez, T. M., Arnoult, K. M., Szuberla, C. A. L., and Olson, J. V. (2013). Combining local and remote infrasound recordings from the 2009 Redoubt Volcano eruption. *Journal of Volcanology and Geothermal Research*, 259, 100–114. https://doi.org/10.1016/j.jvolgeores.2011.09.012

Fee, D., Steffke, A., and Garcés, M. (2010b). Characterization of the 2008 Kasatochi and Okmok eruptions using remote infrasound arrays. *Journal of Geophysical Research: Atmospheres*, 115, D00L10. https://doi.org/10.1029/2009JD013621

Garcés, M., Fee, D., Steffke, A., McCormack, D., Servranckx, R., Bass, H., et al. (2008). Capturing the acoustic fingerprint of stratospheric ash injection. *EOS Transactions AGU*, 89(40), 377–380. https://doi.org/10.1029/2008EO400001

Garcés, M., Willis, M., and Le Pichon, A. (2010). Infrasonic observations of open ocean swells in the Pacific: Deciphering the song of the sea. In: A. Le Pichon, E. Blanc, and A.

Hauchecorne (Eds.), *Infrasound monitoring for atmospheric studies*, (pp. 235–248). Dordrecht: Springer. https://doi.org/10.1007/978-1-4020-9508-5_7

Gibbons, S., Kværna, T., and Näsholm, P. (2019). Characterization of the infrasonic wavefield from repeating seismo-acoustic events. In: A. Le Pichon, E. Blanc, and A. Hauchecorne (Eds.), *Infrasound monitoring for atmospheric studies: Challenges in middle-atmosphere dynamics and societal benefits*, (pp. 387–407). Cham: Springer. https://doi.org/10.1007/978-3-319-75140-5_10

Gibbons, S. J., Kværna, T., and Ringdal, F. (2005). Monitoring of seismic events from a specific source region using a single regional array: A case study. *Journal of Seismology*, 9(3), 277–294. https://doi.org/10.1007/s10950-005-5746-7

Godin, O. A. (2008). Sound transmission through water–air interfaces: New insights into an old problem. *Contemporary Physics*, 49(2), 105–123. https://doi.org/10.1080/00107510802090415

Gordeev, E. I., Firstov, P. P., Kulichkov, S. N., and Makhmudov, E. R. (2013). *Izvestiya, Atmospheric and Oceanic Physics*, 49(4), 420–431. https://doi.org/10.1134/S0001433813030080

Green, D. N., Matoza, R. S., Vergoz, J., and Le Pichon, A. (2012). Infrasonic propagation from the 2010 Eyjafjallajökull eruption: Investigating the influence of stratospheric solar tides. *Journal of Geophysical Research: Atmospheres*, 117, D21202. https://doi.org/10.1029/2012JD017988

Green, D. N., and Nippress, A. (2019). Infrasound signal duration: The effects of propagation distance and waveguide structure. *Geophysical Journal International*, 216(3), 1974–1988. https://doi.org/10.1093/gji/ggy530

Ham, F. M., Iyengar, I., Hambebo, B. M., Garcés, M., Deaton, J., Perttu, A., and Williams, B. (2012). A neurocomputing approach for monitoring Plinian volcanic eruptions using infrasound. *Procedia Computer Science*, 13, 7–17. https://doi.org/10.1016/j.procs.2012.09.109

Haney, M. M. (2010). Location and mechanism of very long period tremor during the 2008 eruption of Okmok Volcano from interstation arrival times. *Journal of Geophysical Research: Solid Earth*, 115, B00B05. https://doi.org/10.1029/2010JB007440

Haney, M. M., Fee, D., McKee, K. F., Lyons, J. J., Matoza, R. S., Wech, A. G., et al. (2020a). Co-eruptive tremor from Bogoslof volcano: Seismic wavefield composition at regional distances. *Bulletin of Volcanology*, 82(2), 1–14. https://doi.org/10.1007/s00445-019-1347-0

Haney, M. M., Van Eaton, A. R., Lyons, J. J., Kramer, R. L., Fee, D., Iezzi, A. M., et al. (2020b). Characteristics of thunder and electromagnetic pulses from volcanic lightning at Bogoslof volcano, Alaska. *Bulletin of Volcanology*, 82(2), 1–16. https://doi.org/10.1007/s00445-019-1349-y

Harris, A., and Ripepe, M. (2007). Synergy of multiple geophysical approaches to unravel explosive eruption conduit and source dynamics—A case study from Stromboli. *Geochemistry*, 67(1), 1–35. https://doi.org/10.1016/j.chemer.2007.01.003

Havskov, J., and Alguacil, G. (2016). Seismic Arrays. In: *Instrumentation in earthquake seismology*, (pp. 309–329). Cham: Springer. https://doi.org/10.1007/978-3-319-21314-9_9

Hedlin, M. A. H., and Walker, K. T. (2013). A study of infrasonic anisotropy and multipathing in the atmosphere using seismic networks. *Philosophical Transactions of the Royal Society A*, 371, 20110542. https://doi.org/10.1098/rsta.2011.0542

Ichihara, M., Ripepe, M., Goto, A., Oshima, H., Aoyama, H., Iguchi, M., et al. (2009). Airwaves generated by an underwater explosion: Implications for volcanic infrasound. *Journal of Geophysical Research: Solid Earth*, 114, B03210. https://doi.org/10.1029/2008JB005792

Iezzi, A. M., Schwaiger, H. F., Fee, D., and Haney, M. M. (2019). Application of an updated atmospheric model to explore volcano infrasound propagation and detection in Alaska. *Journal of Volcanology and Geothermal Research*, 371, 192–205. https://doi.org/10.1016/j. jvolgeores.2018.03.009

IRIS DMC (2012). *Data services products: Infrasound TA infrasound data products*. https://doi.org/10.17611/DP/IS.1

IRIS DMC (2014). *TA infrasound reference event database: Mudslide, OSO WA*. Retrieved from http://ds.iris.edu/spud/infrasoundevent/12677316

Johnson, J. B., and Aster, R. C. (2005). Relative partitioning of acoustic and seismic energy during Strombolian eruptions. *Journal of Volcanology and Geothermal Research*, 148(3–4), 334–354. https://doi.org/10.1016/j.jvolgeores.2005.05.002

Johnson, J. B., Aster, R. C., Ruiz, M. C., Malone, S. D., McChesney, P. J., Lees, J. M., and Kyle, P. R. (2003). Interpretation and utility of infrasonic records from erupting volcanoes. *Journal of Volcanology and Geothermal Research*, 121(1–2), 15–63. https://doi.org/10.1016/S0377-0273(02)00409-2

Johnson, J. B., and Ripepe, M. (2011). Volcano infrasound: A review. *Journal of Volcanology and Geothermal Research*, 206(3–4), 61–69. https://doi.org/10.1016/j.jvolgeores.2011.06.006

Jolly, A. D., Matoza, R. S., Fee, D., Kennedy, B. M., Iezzi, A. M., Fitzgerald, R. H., et al. (2017). Capturing the acoustic radiation pattern of Strombolian eruptions using infrasound sensors aboard a tethered aerostat, Yasur volcano, Vanuatu. *Geophysical Research Letters*, 44, 9672–9680. https://doi.org/10.1002/2017GL074971

Jones, K. R., and Johnson, J. B. (2011). Mapping complex vent eruptive activity at Santiaguito, Guatemala using network infrasound semblance. *Journal of Volcanology and Geothermal Research*, 199(1–2), 15–24. https://doi.org/10.1016/j.jvolgeores.2010.08.006

Jónsdóttir, K., Ripepe, M., Barsotti, S., Björnsson, H., Del Donne, D., and Vogfjörð, K. (2015). Infrasound network implementation in Iceland - examples of volcano monitoring in an extreme environment. *Geophysical Research Abstracts*, 17, EGU2015-11869.

Kim, K., and Lees, J. M. (2015). Imaging volcanic infrasound sources using time reversal mirror algorithm. *Geophysical Journal International*, 202(3), 1663–1676. https://doi.org/10.1093/gji/ggv237

Koper, K. D., Hutko, A. R., Lay, T., and Sufri, O. (2012). Imaging short-period seismic radiation from the 27 February 2010 Chile (MW 8.8) earthquake by back-projection of P, PP, and PKIKP waves. *Journal of Geophysical Research: Solid Earth*, 117, B02308. https://doi.org/10.1029/2011JB008576

KVERT, Institute of Volcanology and Seismology FEB RAS (2019). *VONA/KVERT information releases*. Retrieved from: http://www.kscnet.ru/ivs/kvert/van/index.php

Landès, M., Ceranna, L., Le Pichon, A., and Matoza, R. S. (2012). Localization of microbarom sources using the IMS infrasound network. *Journal of Geophysical Research: Atmospheres*, 117, D06102. https://doi.org/10.1029/2011JD016684

Le Pichon, A., Blanc, E., Drob, D., Lambotte, S., Dessa, J. X., Lardy, M., et al. (2005). Infrasound monitoring of volcanoes to probe high-altitude winds. *Journal of Geophysical Research: Atmospheres*, 110, D13106. https://doi.org/10.1029/2004JD005587

Le Pichon, A., Vergoz, J., Blanc, E., Guilbert, J., Ceranna, L., Evers, L., and Brachet, N. (2009). Assessing the performance of the International Monitoring System's infrasound network: Geographical coverage and temporal variabilities. *Journal of Geophysical Research: Atmospheres*, 114, D08112. https://doi.org/10.1029/2008JD010907

Le Pichon, A., Vergoz, J., Herry, P., and Ceranna, L. (2008). Analyzing the detection capability of infrasound arrays in central Europe. *Journal of Geophysical Research: Atmospheres*, 113, D12115. https://doi.org/10.1029/2007JD009509

Lees, J. M., Gordeev, E. I., and Ripepe, M. (2004). Explosions and periodic tremor at Karymsky Volcano, Kamchatka, Russia. *Geophysical Journal International*, 158(3), 1151–1167. http://doi.org/10.1111/j.1365-246X.2004.02239.x

Liszka, L., and Garcés, M. A. (2002). Infrasonic observations of the Hekla eruption of February 26, 2000. *Journal of Low Frequency Noise, Vibration and Active Control*, 21(1), 1–8. https://doi.org/10.1260/02630920260374934

Lopez, T., Clarisse, L., Schwaiger, H., Van Eaton, A., Loewen, M., Fee, D., et al. (2020). Constraints on eruption processes and event masses for the 2016–2017 eruption of Bogoslof volcano, Alaska, through evaluation of IASI satellite SO2 masses and complementary datasets. *Bulletin of Volcanology*, 82(2), 1–17. https://doi.org/10.1007/s00445-019-1348-z

Lyons, J. J., Haney, M. M., Fee, D., Wech, A. G., and Waythomas, C. F. (2019). Infrasound from giant bubbles during explosive submarine eruptions of Bogoslof volcano, Alaska. *Nature Geoscience*, 12(11), 952–958. https://doi.org/10.1038/s41561-019-0461-0

Lyons, J. J., Iezzi, A. M., Fee, D., Schwaiger, H. F., Wech, A. G., and Haney, M. M. (2020). Infrasound generated by the 2016–17 shallow submarine eruption of Bogoslof volcano, Alaska. *Bulletin of Volcanology*, 82(19). https://doi.org/10.1007/s00445-019-1355-0

Marchetti, E., Ichihara, M., and Ripepe, M. (2004). Propagation of acoustic waves in a viscoelastic two-phase system: Influence of gas bubble concentration. *Journal of Volcanology and Geothermal Research*, 137(1–3), 93–108. https://doi.org/10.1016/j.jvolgeores.2004.05.002

Marchetti, E., Ripepe, M., Delle Donne, D., Genco, R., Finizola, A., and Garaebiti, E. (2013). Blast waves from violent explosive activity at Yasur Volcano, Vanuatu. *Geophysical Research Letters*, 40, 5838–5843. https://doi.org/10.1002/2013GL057900

Matoza, R. S., Fee, D., and Garcés, M. A. (2010). Infrasonic tremor wavefield of the Pu'u'Ō'ō crater complex and lava tube system, Hawai'i, in April 2007. *Journal of Geophysical Research: Solid Earth*, 115, B12312. https://doi.org/10.1029/2009JB007192

Matoza, R., Fee, D., Green, D., and Mialle, P. (2019). Volcano infrasound and the International Monitoring System. In: A. Le Pichon, E. Blanc, and A. Hauchecorne (Eds.), *Infrasound monitoring for atmospheric studies: Challenges in middle-atmosphere dynamics and societal benefits*, (pp. 1023–1077). Cham: Springer. https://doi.org/10.1007/978-3-319-75140-5_33

Matoza, R. S., Fee, D., Green, D. N., Le Pichon, A., Vergoz, J., Haney, M. M., et al. (2018). Local, regional, and remote seismo-acoustic observations of the April 2015 VEI 4 eruption of Calbuco volcano, Chile. *Journal of Geophysical Research: Solid Earth*, 123, 3814–3827. https://doi.org/10.1002/2017JB015182

Matoza, R. S., Green, D. N., Le Pichon, A., Shearer, P. M., Fee, D., Mialle, P., and Ceranna, L. (2017). Automated detection and cataloging of global explosive volcanism using the International Monitoring System infrasound network. *Journal of Geophysical Research: Solid Earth*, 122, 2946–2971. https://doi.org/10.1002/2016JB013356

Matoza, R. S., Hedlin, M. A. H., and Garcés, M. A. (2007). An infrasound array study of Mount St. Helens. *Journal of Volcanology and Geothermal Research*, 160(3–4), 249–262. https://doi.org/10.1016/j.jvolgeores.2006.10.006

Matoza, R. S., Landès, M., Le Pichon, A., Ceranna, L., and Brown, D. (2013). Coherent ambient infrasound recorded by the International Monitoring System. *Geophysical Research Letters*, 40, 429–433. https://doi.org/10.1029/2012GL054329

Matoza, R. S., Le Pichon, A., Vergoz, J., Herry, P., Lalande, J.-M., Lee, H.-I., et al. (2011a). Infrasonic observations of the June 2009 Sarychev Peak eruption, Kuril Islands: Implications for infrasonic monitoring of remote explosive volcanism. *Journal of Volcanology and Geothermal Research*, 200, 35–48. https://doi.org/10.1016/j.jvolgeores.2010.11.022

Matoza, R. S., Vergoz, J., Le Pichon, A., Ceranna, L., Green, D. N., Evers, L. G., et al. (2011b). Long-range acoustic observations of the Eyjafjallajökull eruption, Iceland, April–May 2010. *Geophysical Research Letters*, 38, L06308. https://doi.org/10.1029/2011GL047019

McNutt, S. R., and Williams, E. R. (2010). Volcanic lightning: Global observations and constraints on source mechanisms. *Bulletin of Volcanology*, 72(10), 1153–1167. https://doi.org/10.1007/s00445-010-0393-4

Meng, L., Ampuero, J. P., Luo, Y., Wu, W., and Ni, S. (2012). Mitigating artifacts in back-projection source imaging with implications for frequency-dependent properties of the Tohoku-Oki earthquake. *Earth, Planets and Space*, 64(12), 1101–1109. https://doi.org/10.5047/eps.2012.05.010

Mialle, P., Brachet, N., Gaillard, P., Le Pichon, A., Blanc, E., Tailpied, D., et al. (2015). Towards a volcanic notification system with infrasound data: Use of infrasound data in support of the VAACs in the framework of ARISE project. Abstract [T1.1-O4] presented at *2015 Science and Technology Conference*, Vienna, Austria.

Mikumo, T., and Watada, S. (2010). Acoustic-gravity waves from earthquake sources. In: A. Le Pichon, E. Blanc, and A. Hauchecorne (Eds.), *Infrasound monitoring for atmospheric studies*, (pp. 263–279). Dordrecht: Springer. https://doi.org/10.1007/978-1-4020-9508-5_9

Mutschlecner, J. P., and Whitaker, R. W. (2010). Some atmospheric effects on infrasound signal amplitudes. In: A. Le Pichon, E. Blanc, and A. Hauchecorne (Eds.), *Infrasound monitoring for atmospheric studies*, (pp. 455–474). Dordrecht: Springer. https://doi.org/10.1007/978-1-4020-9508-5_14

National Academies of Sciences, Engineering, and Medicine (2017). Volcanic eruptions and their repose, unrest, precursors, and timing. *Washington, DC: The National Academies Press*. https://doi.org/10.17226/24650

Olson, J. V. (1982). Noise suppression using data-adaptive polarization filters: Applications to infrasonic array data. *The Journal of the Acoustical Society of America*, 72(5), 1456–1460. https://doi.org/10.1121/1.388679

Park, J., Hayward, C., and Stump, B. W. (2018). Assessment of infrasound signals recorded on seismic stations and infrasound arrays in the western United States using ground truth sources. *Geophysical Journal International*, 213(3), 1608–1628. https://doi.org/10.1093/gji/ggy042

Perttu, A., Taisne, B., Williams, R., and Tailpied, D. (2018). Quantifying detection capability of a regional infrasound network using a combination of film sound techniques and array processing. *Geophysical Research Abstracts*, 20, EGU2018–EGU13229.

Petersen, T., De Angelis, S., Tytgat, G., and McNutt, S. R. (2006). Local infrasound observations of large ash explosions at Augustine Volcano, Alaska, during January 11–28, 2006. *Geophysical Research Letters*, 33, L12303. https://doi.org/10.1029/2006GL026491

Petersen, T., and McNutt, S. R. (2007). Seismo-acoustic signals associated with degassing explosions recorded at Shishaldin Volcano, Alaska, 2003–2004. *Bulletin of Volcanology*, 69(5), 527–536. https://doi.org/10.1007/s00445-006-0088-z

Pinsky, V., Blom, P., Polozov, A., Marcillo, O., Arrowsmith, S., and Hofstetter, A. (2017). Towards an accurate real-time locator of infrasonic sources. *Journal of Seismology*, 21(6), 1361–1383. https://doi.org/10.1007/s10950-017-9670-4

Pyle, D. M., Mather, T. A., and Biggs, J. (Eds.). (2013). Remote sensing of volcanoes and volcanic processes: Integrating observation and modelling. *Geological Society, London, Special Publications*, 380. https://doi.org/10.1144/SP380.0

Raspet, R., Abbott, J.-P., Webster, J., Yu, J., Talmadge, C., Alberts, K. II, et al. (2019). New systems for wind noise reduction for infrasonic measurements. In: A. Le Pichon, E. Blanc, and A. Hauchecorne (Eds.), *Infrasound monitoring for atmospheric studies:*

Challenges in middle-atmosphere dynamics and societal benefits, (pp. 91–124). Cham: Springer. https://doi.org/10.1007/978-3-319-75140-5_3

Ripepe, M., Marchetti, E., Delle Donne, D., Genco, R., Innocenti, L., Lacanna, G., and Valade, S. (2018). Infrasonic early warning system for explosive eruptions. *Journal of Geophysical Research: Solid Earth*, 123, 9570–9585. https://doi.org/10.1029/2018JB015561

Ripepe, M., Marchetti, E., and Ulivieri, G. (2007). Infrasonic monitoring at Stromboli volcano during the 2003 effusive eruption: Insights on the explosive and degassing process of an open conduit system. *Journal of Geophysical Research*, 112, B09207. https://doi.org/10.1029/2006JB004613

Ruiz, M., Lees, J., and Johnson, J. B. (2006). Source constraints of Tungurahua volcano explosion events. *Bulletin of Volcanology*, 68(5), 480–490. https://doi.org/10.1007/s00445-005-0023-8

Runco, A. M. Jr., Louthain, J. A., and Clauter, D. A. (2014). Optimizing the PMCC algorithm for infrasound and seismic nuclear treaty monitoring. *Open Journal of Acoustics*, 4, 204–213. https://doi.org/10.4236/oja.2014.44020

Schneider, F. M., Fuchs, F., Kolínský, P., Caffagni, E., Serafin, S., Dorninger, M., Bokelmann, G., and AlpArray Working Group (2018). Seismo-acoustic signals of the Baumgarten (Austria) gas explosion detected by the AlpArray seismic network. *Earth and Planetary Science Letters*, 502, 104–114. https://doi.org/10.1016/j.epsl.2018.08.034

Schwaiger, H. F., Iezzi, A. M., and Fee, D. (2019). AVO-G2S: A modified, open-source Ground-to-Space atmospheric specification for infrasound modeling. *Computers & Geosciences*, 125, 90–97. https://doi.org/10.1016/j.cageo.2018.12.013

Schwaiger, H. F., Lyons, J. J., Iezzi, A. M., Fee, D., and Haney, M. M. (2020). Evolving infrasound detections from Bogoslof volcano, Alaska: Insights from atmospheric propagation modeling. *Bulletin of Volcanology*, 82(27). https://doi.org/10.1007/s00445-020-1360-3

Searcy, C. K., and Power, J. A. (2020). Seismic character and progression of explosive activity during the 2016–2017 eruption of Bogoslof volcano, Alaska. *Bulletin of Volcanology*, 82(1), 1–15. https://doi.org/10.1007/s00445-019-1343-4

Shang, C., Teng, P., Lyu, J., Yang, J., and Sun, H. (2019). Infrasonic source altitude localization based on an infrasound ray tracing propagation model. *The Journal of the Acoustical Society of America*, 145(6), 3805–3816. https://doi.org/10.1121/1.5110712

Shani-Kadmiel, S., Assink, J., Fee, D., and Evers, L. (2018a). Special event: North of Anchorage, Alaska: International Monitoring System (IMS) array IM.I53US. Retrieved from http://ds.iris.edu/ds/nodes/dmc/specialevents/2018/11/30/north-of-anchorage-alaska

Shani-Kadmiel, S., Assink, J. D., Smets, P. S. M., and Evers, L. G. (2018b). Seismoacoustic coupled signals from earthquakes in central Italy: Epicentral and secondary sources of infrasound. *Geophysical Research Letters*, 45. https://doi.org/10.1002/2017GL076125

Shearer, P. (1994). Global seismic event detection using a matched filter on long-period seismograms. *Journal of Geophysical Research: Solid Earth*, 99, B7. https://doi.org/10.1029/94JB00498

Sit, S., Brudzinski, M., and Kao, H. (2012). Detecting tectonic tremor through frequency scanning at a single station: Application to the Cascadia margin. *Earth and Planetary Science Letters*, 353–354, 134–144. https://doi.org/10.1016/j.epsl.2012.08.002

Szuberla, C. A. L., Arnoult, K. M., and Olson, J. V. (2006). Discrimination of near-field infrasound sources based on time-difference of arrival information. *The Journal of the Acoustical Society of America*, 120(3), EL23–EL28. https://doi.org/10.1121/1.2234517

Szuberla, C. A. L., and Olson, J. V. (2004). Uncertainties associated with parameter estimation in atmospheric infrasound arrays. *The Journal of the Acoustical Society of America*, 115(1), 253–258. https://doi.org/10.1121/1.1635407

Tailpied, D., Le Pichon, A., Marchetti, E., Assink, J., and Vergniolle, S. (2017). Assessing and optimizing the performance of infrasound networks to monitor volcanic eruptions. *Geophysical Journal International*, 208(1), 437–448. https://doi.org/10.1093/gji/ggw400

Tepp, G. (2018). A repeating event sequence alarm for monitoring volcanoes. *Seismological Research Letters*, 89(5), 1863–1876. https://doi.org/10.1785/0220170263

Tepp, G., Dziak, R. P., Haney, M. M., Lyons, J. J., Searcy, C., Matsumoto, H., and Haxel, J. (2020). Seismic and hydroacoustic observations of the 2016–17 Bogoslof eruption. *Bulletin of Volcanology*, 82(1), 1–21. https://doi.org/10.1007/s00445-019-1344-3

Tepp, G., and Haney, M. M. (2019). Comparison of short-term seismic precursors and explosion parameters during the 2016–2017 Bogoslof eruption. *Bulletin of Volcanology*, 81(11), 1–15. https://doi.org/10.1007/s00445-019-1323-8

Toney, L. D., Fee., D., Allstadt, K., Haney, M. M., and Matoza, R. S. (2019). A tale of two very large avalanches: Probing the limits of seismoacoustic avalanche characterization on Iliamna Volcano, Alaska. Abstract [S23D-0658] presented at *2019 Fall Meeting, AGU*, San Francisco, CA.

USArray (2019). Transportable Array deployment to Alaska and Western Canada. Retrieved from http://www.usarray.org/alaska#station-design

Van Eaton, A. R., Amigo, À., Bertin, D., Mastin, L. G., Giacosa, R. E., González, J., et al. (2016). Volcanic lightning and plume dynamics reveal evolving hazards during the April 2015 eruption of Calbuco volcano, Chile. *Geophysical Research Letters*, 43, 3563–3571. https://doi.org/10.1002/2016GL068076

Vergniolle, S., and Caplan-Auerbach, J. (2006). Basaltic thermals and Subplinian plumes: Constraints from acoustic measurements at Shishaldin volcano, Alaska. *Bulletin of Volcanology*, 68(7–8), 611–630. https://doi.org/10.1007/s00445-005-0035-4

Walker, K. T. (2012). Evaluating the opposing wave interaction hypothesis for the generation of microbaroms in the eastern North Pacific. *Journal of Geophysical Research: Oceans*, 117, C12016. https://doi.org/10.1029/2012JC008409

Walker, K. T., and Hedlin, M. A. (2010). A review of wind-noise reduction methodologies. In: A. Le Pichon, E. Blanc, and A. Hauchecorne (Eds.), *Infrasound monitoring for atmospheric studies*, (pp. 141–182). Dordrecht: Springer. https://doi.org/10.1007/978-1-4020-9508-5_5

Walker, K. T., Hedlin, M. A. H., de Groot-Hedlin, C., Vergoz, J., Le Pichon, A., and Drob, D. P. (2010). Source location of the 19 February 2008 Oregon bolide using seismic networks and infrasound arrays. *Journal of Geophysical Research: Solid Earth*, 115, B12. https://doi.org/ 10.1029/2010JB007863

Walker, K. T., Shelby, R., Hedlin, M. A., Groot-Hedlin, C., and Vernon, F. (2011). Western US infrasonic catalog: Illuminating infrasonic hot spots with the USArray. *Journal of Geophysical Research: Solid Earth*, 116, B12. https://doi.org/10.1029/2011JB008579

Waxler, R. M. (2017). Infrasound phenomenology, propagation, and detection. *The Journal of the Acoustical Society of America*, 142(4), 2529–2529. https://doi.org/10.1121/1.5014242

Waythomas, C. F., and Cameron, C. E. (2018). Historical eruptions and hazards at Bogoslof volcano, Alaska. *U.S. Geological Survey Scientific Investigations Report*, 2018–5085. https://doi.org/10.3133/sir20185085

Waythomas, C. F., Loewen, M., Wallace, K. L., Cameron, C. E., and Larsen, J. F. (2020). Geology and eruptive history of Bogoslof volcano. *Bulletin of Volcanology*, 82(2), 1–23. https://doi.org/10.1007/s00445-019-1352-3

Waythomas, C. F., Scott, W. E., Prejean, S. G., Schneider, D. J., Izbekov, P., and Nye, C. J. (2010). The 7–8 August 2008 eruption of Kasatochi Volcano, central Aleutian Islands, Alaska. *Journal of Geophysical Research: Solid Earth*, 115, B00B06. https://doi.org/10.1029/2010JB007437

Webley, P., and Mastin, L. (2009). Improved prediction and tracking of volcanic ash clouds. *Journal of Volcanology and Geothermal Research*, 186(1–2), 1–9. https://doi.org/10.1016/j.jvolgeores.2008.10.022

Wech, A., Tepp, G., Lyons, J., and Haney, M. (2018). Using earthquakes, T waves, and infrasound to investigate the eruption of Bogoslof volcano, Alaska. *Geophysical Research Letters*, 45(14), 6918–6925. https://doi.org/10.1029/2018GL078457

Werner, C., Kern, C., Coppola, D., Lyons, J. J., Kelly, P. J., Wallace, K. L., et al. (2017). Magmatic degassing, lava dome extrusion, and explosions from Mount Cleveland volcano, Alaska, 2011–2015: Insight into the continuous nature of volcanic activity over multi-year timescales. *Journal of Volcanology and Geothermal Research*, 337, 98–110. https://doi.org/10.1016/j.jvolgeores.2017.03.001

Woodward, R., Israelsson, H., Bondár, I., McLaughlin, K., Bowman, J. R., and Bass, H. (2005). Understanding wind-generated infrasound noise. *Proceedings of the 27th Seismic Research Review: Ground-based nuclear explosion monitoring technologies*, 866–875. Retrieved from https://www.osti.gov/servlets/purl/1027447

Xu, Y., Koper, K. D., Sufri, O., Zhu, L., and Hutko, A. R. (2009). Rupture imaging of the Mw 7.9 12 May 2008 Wenchuan earthquake from back projection of teleseismic P waves. *Geochemistry, Geophysics, Geosystems*, 10, Q04006. https://doi.org/10.1029/2008GC002335

Zhu, W., Mousavi, S. M., and Beroza, G. C. (2019). Seismic signal denoising and decomposition using deep neural networks. *IEEE Transactions on Geoscience and Remote Sensing*, 57(11), 9476–9488. https://doi.org/10.1109/TGRS.2019.2926772

Supplemental Material

The supplemental material initially provides the methodological details on our algorithm, ranging from data pre-processing to event location. We also show monthly time-series of reverse time migration (RTM) results for the 2016–2017 Bogoslof volcanic eruption sequence, as well as the corresponding classification, detection and location statistics. Further, we include RTM observations of other volcanic events in Alaska and Kamchatka. Finally, we list the software packages utilized for our data processing, data analysis and plotting of results. All dates and times provided are in Coordinated Universal Time (UTC).

S1. Algorithm Details

S1.1. Subtrending

Multiple stages within the reverse time migration (RTM) algorithm use a special detrending process in order to remove prevalent wind noise. This noise, in envelope form, manifests as much longer period signals than those of eruptions (section 2, main article). The detrending process, which we refer to as *subtrending* (inspired by Blackburn, 2015) causes less distortion in the positive-only signals compared to normal filtering, and is also more easily tuned. Subtrending is so called because it operates via subtraction of a filtered running minimum function. Specifics of the process follow in three primary stages:

(1) Finding initial points for detrending the waveform by using a running minimum window: (a) at 1-hour intervals, take 30 minutes of data before/after this reference point; (b) sort the windowed hour of data by amplitude; (c) store the amplitude value at the 5th percentile; (d) of the stored values, only keep those greater than the 2.5^{th} percentile of the amplitude range of the full waveform (in order to avoid detrending by using points with very small amplitudes); (e) interpolate and extrapolate the kept values to the full length of the data to create a minimum time-series;

(2) Filtering the minimum time-series below frequencies of interest: (a) demean the minimum time-series, pad ends by 10% of the time-series' length with values equal to the mean of the edge values (mean determined for a section of edge values equal in length to the padded section); (b) filter the padded minimum time-series by desired frequency; (c) remove the padding from the result; (d) add the original mean back in;

(3) Subtract the final trend (determined in stage 2) from the original trace to get the final subtrended trace.

S1.2. Automatic Gain Control (AGC)

As part of the study, two AGC algorithms are tested for efficacy; (1) AGC1 – the algorithm included with GISMO (Thompson and Reyes, 2017, reference provided in section S5); (2) AGC2 – the algorithm from Walker et al. (2010). Differences in results over the Bogoslof eruption sequence are further detailed in sections S1.3 and S4, but broadly, AGC1 gives overall higher detection rates vs. AGC2, and similarly accurate locations, with AGC2 being typically better at volcanic signal classification (section 3.4, main article and Figure S13). Running simultaneous AGC1 and AGC2 algorithms would take advantage of the strengths of both, or if preferential, one can skip using AGC at all. For documenting the method in the main article, we choose to use AGC1, with all references there to AGC inferring this choice.

S1.3. Processing Parameters

Here we address in more detail the rationale for parameter choices in the RTM processing, and their relative importance to signal-to-noise ratios and location accuracy. In general, we are aiming for coarse initial locations that can be obtained either in real-time, or from an archive, on a reasonably common computer platform. The notes in Table S1 come from more than 150 parameter permutations applied to Alaska data from 15 December 2016 to 14 January 2017, as well as a selection of other days and events from several volcanoes (Table S2). An exhaustive statistical treatment of the complex relation between each of the parameters and the impact on the full Bogoslof eruption sequence is beyond the scope of this study however. Additional: Steps 5 and 6 of pre-processing could be reversed, but lead to a decrease in SNR and greater computational expense (also see section S4). Instrument responses are flat in the passband of the filter; hence these responses are not removed during pre-processing.

S1.4. Detector Function Formation

Here we elaborate on the two types of detector function (DF) introduced in section 2.4 (main article). In this study, we specifically exploit the extended duration property of volcanic eruptions by forming the DF from not simply the sample-wise maxima of stacks, but by applying a running 150 s anticausal window to each stack and taking the maximum sum from each window as the DF (Figure S1). The effect on the DF is twofold: (1) there is a reduction in the number of very short, i.e., nonvolcanic events in the DF; (2) the DF is smoother and thus analyses are less sensitive to fine scale features which may be spurious. As noted in the main article, for brevity throughout, we use DF to indicate the *time-summed DF* (TS-DF) method, and *stack* to indicate time-summed-stacks, unless otherwise implied by context. The summation process produces different results to simply smoothing/filtering a *single-time-window DF* (STW-DF). Comparisons using synthetic data are presented in section 3.6, main article.

S1.5. Detection and Location Methods

Sections 2.4 and 2.5 of the main article briefly address automated event detection and location. This process is illustrated by Figures 6 and 7 (main article) and detailed below:

(1) A DF is converted to a signal-to-noise ratio in decibel (dB) format using the following equation (adapted from Walker et al., 2010):

$$DF_{SNR} = 20log_{10}\left(\frac{|DF_{filt}|}{median(|DF_{filt}|)}\right)$$

where DF_{filt} is a DF high-pass filtered above a particular period to remove the DF background offset. To calculate DF_{filt} we subtrend (section S1.1) with a 48-hour low-pass setting.

(2) DF_{SNR} samples above a detection threshold (12.5 dB) are grouped automatically into *peaks* (requiring a minimum gap of 1,800 seconds) which are then located automatically.

(3) For each peak, k number of DF_{SNR} samples above a location threshold (LT) are assessed, where LT is defined as the 75th percentile of the DF_{SNR} samples in the peak. The location methods applied to the corresponding time period are as follows:

(i) *MAX* (maximum): for $DF_{SNR}(k) > LT$, the final location is the average of the locations corresponding to samples within ±75 seconds of the maximum amplitude;

(ii) *COM* (center of mass): as above, but using the weighted-mean instead of the maximum value as a reference point;

(iii) *COM3* (center of mass in three dimensions): the final location derives from the weighted-mean of all stack samples while $DF_{SNR}(k) > LT$. As COM consistently provides less accurate locations than COM3, we proceed with MAX and COM3 only.

Using synthetic data (section 3.6, main article), it is clear that events < 60 s are more resolvable using a STW-DF, and such an approach could be taken when looking for short signals (the volcanic events in the Bogoslof catalog are all > 150 s however). An alternate but not fully explored location strategy is to use the location corresponding to the most concentrated stack amplitudes, rather than the center of mass. In the presence of multiple regions of varying dimension, determining which option is ideal is challenging, however.

S1.6. Classification Curves and Performance

Alternative and complementary classification curves to basic receiver operating characteristic (ROC) analyses (section 3.4, main article) can be computed once the detector function (DF) samples have been classified as true-positives (TP), false-positives (FP), true-negatives (TN) and false-negatives (FN). For example, ROC analysis can be conducted in more than two-dimensions, by making a third axis the true-detection rate, or false-detection rate (Ham et al., 2012), thereby offering more insight into algorithm behavior. Detection Error Trade-off (DET) curves (FN-rate vs. FP-rate) emphasize differences between algorithms that perform almost equally well in ROC space. Another common analysis tool is the Precision-Recall (PR) curve (TP/TP+FP vs TP-rate). By ignoring the TN class, PR curves focus on the ability of the algorithm to class positive outcomes rather than positive and negative outcomes. Using PR curves on a sample by sample basis however suffers from biases in the false-positives provided by swimming artifacts. Another approach for addressing the class imbalance and potential of missed events in a catalog is using pseudo-ROC curves, which scale the x-axis by time (Runco Jr. et al., 2014; Bueno et al., 2019). The percentage area under our ROC and such pseudo-ROC curves are identical however. In this initial study, we limit our scope to the 2D ROC curves described though acknowledge that the classes are imbalanced.

S1.7. Wind Masking

Wind noise is an inescapable feature in the data used in this study, varying by station and time of year. Though we partly approach mitigating wind noise through the aforementioned subtrending (section S1.1), we also investigate the effectiveness of a *wind mask*. This mask operation works in two steps by:

(1) Calculating the mask – for three days before and after the day in question, determine the e.g., 50th or 75th percentile of power in the 0.03–0.08 Hz band. (The frequency band is chosen as a proxy for wind after studies by Fee and Garcés (2007) and Green et al. (2012), where we choose a similar minimum band but a lower maximum band to reduce overlap with volcanic events.) The mask calculation is performed in the frequency domain, between stages 2 and 3 of pre-processing (section 2.2, main article);

(2) Applying the mask – for each subdivision of the waveform being masked (e.g., 15 minute sections), the power in the 0.03–0.08 Hz band is compared to the reference mask level from (1), and if above the mask level, the amplitude of this section is down-weighted or set to zero. This step takes place prior to step 10 (normalization) in pre-processing.

We find that though the wind mask reduces the prevalence of detected nonvolcanic events (or possibly coherent noise), it also reduces the prevalence of some volcanic events. Thus, we do not incorporate this mask here as part of our processing. As a final note, though the TA does have wind speed sensors at most sites (~70%), such sensors were not available for all sensors on all networks used, so this information was not incorporated for establishing accurate wind-speed to infrasound-amplitude relations at each station (e.g., Bowman, 2005; Woodward et al., 2005; Le Pichon et al., 2009). For future work, alternative wind-noise reduction strategies may include pure-state filters (Olson, 1982; Arnoult et al., 2010), envelope frequency ratios (Sit et al., 2012), Non-Negative Matrix Factorization (Carniel et al., 2014), and signal decomposition using deep learning techniques (Zhu et al., 2019).

S2. Bogoslof Eruption – Onset 12 December 2016

The Bogoslof eruption sequence began on 12 December 2016, but awareness and monitoring by AVO did not begin until the fourth explosion. Notification was prompted by automated infrasound alarms for the Dillingham array, and observations from pilots (Coombs et al., 2018). Retroactive analysis by AVO found that these events were detected by between two or fewer infrasound arrays (e.g., Figure S3). Results summarized in Figure 5 (main article) and Figures S3–S12 show that these weakly infrasonic events were detected with RTM using the presented algorithm. However, as discussed in the main article and supplemental material, results vary with parameter choices. To illustrate, Figure S2 shows DFs for the only parameter and station combinations from section S4 (4 of 24) that showed the 12 December 2016 event. Specifically, these parameter sets involve AGC1 with linear and Nth-root stacking (N = 2).

S3. Bogoslof Eruption – Monthly Detector Functions

Detector functions for December 2016 to September 2017 are provided by Figures S3–S12. Information on non-Bogoslof events during this time period, particularly from Cleveland volcano, Alaska, are addressed by section 3.5 (main article) and Table S2.

S4. Bogoslof Eruption – Monthly RTM Statistics

Here we expand upon sections 3.4 and 3.6 of the main article, commenting on semblance and F-ratio stacking methods, as well potential impacts on real-time processing. We also provide ROC classification, event detection and location accuracy results for all combinations of AGC, stacking, and station groups (Figures S13–S16, Tables S3–S10).

Compared with linear stacking or Nth-root stacking, semblance and F-ratio generally have better ROC classification results for events that were detected using AGC1. For AGC2, improvements were only seen for the single sensor stations (Figure S13). For event detection, semblance and F-ratio were poorer overall vs. linear and Nth-root stacking (Figure S14). Location accuracy for those events that semblance and F-ratio detected (Figures S15 and S16) show improvements in some circumstances, though given a lower detection rate, this metric is difficult to weigh the significance of. With the importance of event detection as a minimum standard, we prefer to weight that consideration at the expense of more false positives in this particular case. Thus, we use linear stacking, rather than semblance or F-ratio for the approach in the main article.

Significantly for real-time processing, the stacking methods vary by computational cost, with linear stacking requiring the least operations, followed by Nth-root stacking (for N = 2), then semblance, with F-ratio the most time consuming. In part this cost comes from the explicit need for time windows (tested with 300 s and 600 s durations, with 150 s overlap), rather than relying on the inter-sample spacing used by linear and Nth-root stacking. Given this computational cost, the time-grid resolution for semblance and F-ratio is made poorer to compensate (but does give smaller files). Using variable rather than fixed window lengths to reflect atmospheric multipathing may be advantageous for RTM strategies in this regard (Park et al., 2018). Further, from a detection perspective, long duration events are less sensitive to use of an accurate celerity than short events. Depending on the detection objective, a fixed celerity could be used to save the computational cost of incorporating celerity into the grid search. This would likely come at the expense of location accuracy, though this may not be important if a secondary method is employed which uses the coarse location as a starting point. Tepp (2018) addresses similar concerns for a near-real-time volcanic seismic swarm detector, including at Bogoslof.

S5. Software Resources

Our RTM algorithm (v. 7.13) is written in the Python programming language (v. 3.6.5, Python Software Foundation, https://www.python.org). We explicitly incorporated the following software packages for processing, analysis and plotting:

Circle Draw: Scholtes, J. (2016). Python-custom distance radius with basemap. Available from: https://stochasticcoder.com/2016/04/06/python-custom-distance-radius-with-basemap/

Dill: McKerns, M. M., Strand, L., Sullivan, T., Fang, A., and Aivazis, M. A. G. (2011). Building a framework for predictive science. *Proceedings of the 10th Python in Science Conference*. Available from: https://arxiv.org/pdf/1202.1056

McKerns, M., and Aivazis, M. (2010–). pathos: a framework for heterogeneous computing. Available from: http://trac.mystic.cacr.caltech.edu/project/pathos/wiki.html

FFmpeg: FFmpeg developers. (2016). FFmpeg tool. Available from: https://ffmpeg.org

GDAL: GDAL/OGR developers. (2018). GDAL/OGR Geospatial Data Abstraction software Library. Available from: https://gdal.org

GISMO: Thompson, G., and Reyes, C. (2017). GISMO - a seismic data analysis toolbox for MATLAB. Available from: https://geoscience-community-codes.github.io/GISMO/

GMT: Wessel, P., Smith, W. H. F., Scharroo, R., Luis, J. F., and Wobbe, F. (2013). Generic Mapping Tools: Improved version released. *EOS Transactions, AGU*, 94(45), 409–410. https://doi.org/10.1002/2013EO450001

IPython: Pérez, F., and Granger, B. E. (2007). IPython: A System for Interactive Scientific Computing. *Computing in Science & Engineering*, 9, 21–29. https://doi.org/10.1109/MCSE.2007.53

Matplotlib: Hunter, J. D. (2007). Matplotlib: A 2D Graphics Environment. *Computing in Science & Engineering*, 9, 90–95. https://doi.org/10.1109/MCSE.2007.55

NumPy: Oliphant, T. E. (2006). A guide to NumPy. USA: Trelgol Publishing.

ObsPy: Beyreuther, M., Barsch, R., Krischer, L., and Wassermann, J. (2010). ObsPy: A Python toolbox for seismology. *Seismological Research Letters*, 81(3), 530–533. https://doi.org/10.1785/gssrl.81.3.530

openpyxl: openpyxl developers. (2016). openpyxl tool. Available from https://openpyxl.readthedocs.io/en/stable/

SciPy: Jones, E., Oliphant, E., Peterson, P. et al. (2001–). SciPy: Open Source Scientific Tools for Python. Available from: https://www.scipy.org

[Our RTM code is not currently publicly available. An alternate RTM infrasound tool, partly based on ours, is located here: https://github.com/uafgeotools/rtm]
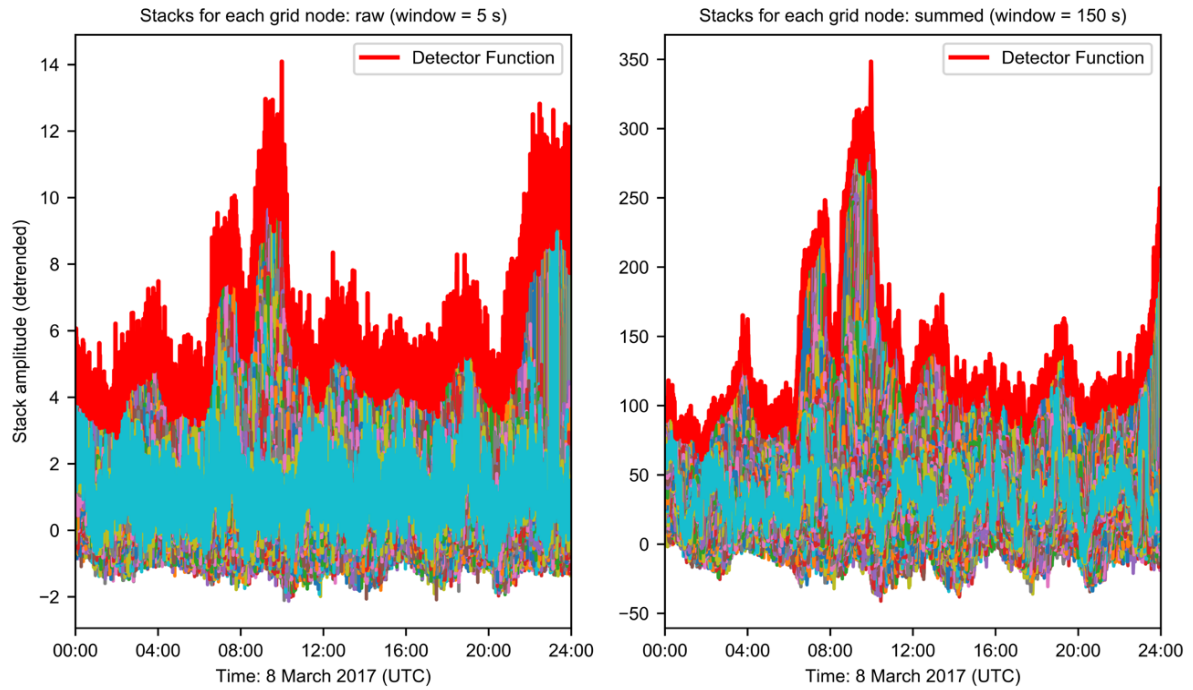
Figure S1. Individual stacks for each grid node in the search area, for the time period covering the 8 March 2017 Bogoslof eruption, using sensors within a radius of 2,000 km. These data are summarized with a detector function (DF) by (left) taking the maximum of all the stacks at each time point (after Walker et al., 2010), shown here as a red line (single-time-window-DF, STW-DF), or (right) taking the maximum sum from a running 150 s window (time-summed-DF, TS-DF). Each point in the DF can be tied to the original stack/grid location that the value came from.
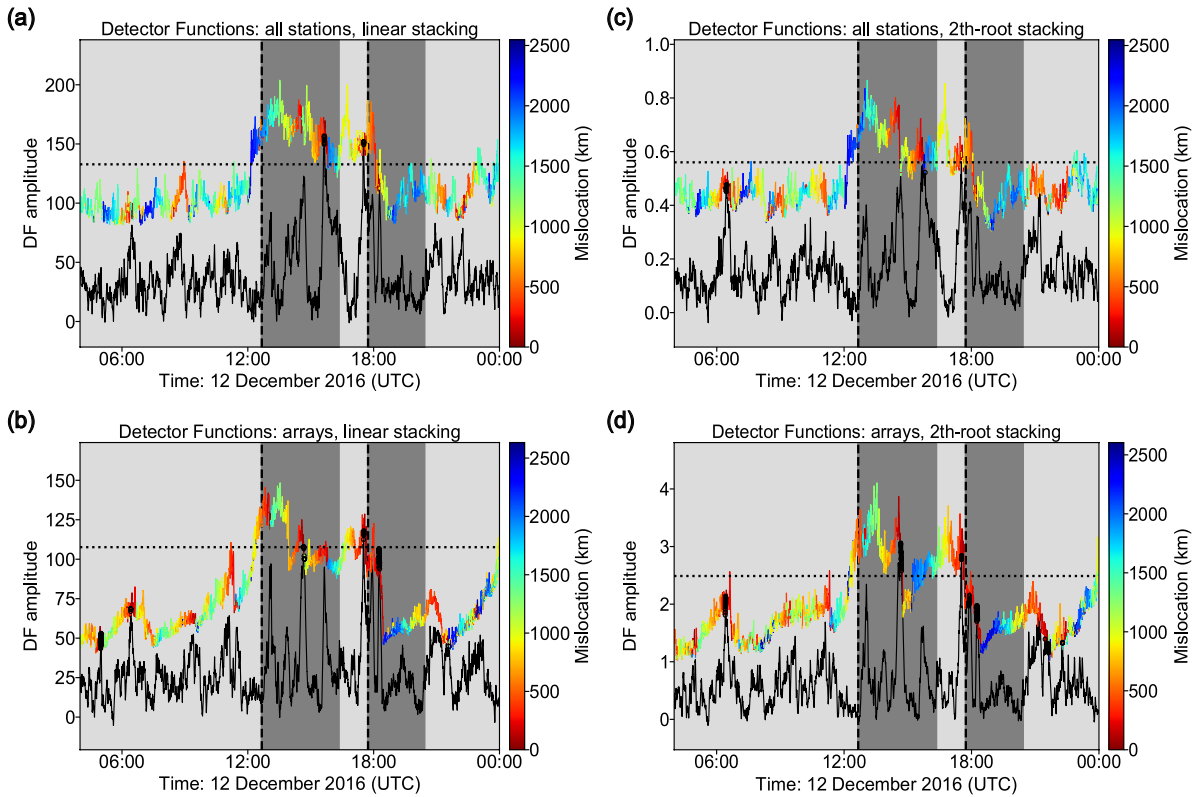
Figure S2. Detector functions (DF) for parameter combinations that identify the Bogoslof eruption sequence onset on 12 December 2016. (a) All sensors, AGC1, linear stacking. (b) Array sensors, AGC1, linear stacking. (c) All sensors, AGC1, Nth-root stacking, N = 2. (d) Array sensors, AGC1, Nth-root stacking, N = 2. Other combinations of sensors, AGC methods, and stacking type did not identify this event above 12.5 dB. Alaska-wide DFs are colored by mislocation and Bogoslof-specific DFs are colored black. The Bogoslof DF is the stack corresponding to the specific trial source location (grid point) at Bogoslof. Matching amplitudes between the two DFs (marked with bold black line segments) indicate zero mislocation. The vertical dashed line is the AVO cataloged event onset, and the dark grey section the period of AVO cataloged infrasound. Horizontal dotted lines earmark the 12.5 dB detection threshold.

Figures S3–S12. (below.) (a) Alaska-wide detector function (DF) whose variation principally reflects eruptions from Bogoslof during the indicated month. DFs use AGC1 and linear stacking (same method as main article) and all available infrasound sensors within 2,000 km of Bogoslof. Colored dots on the second y-axis indicate the number of AVO infrasound arrays were cataloged has having detected infrasound (Lyons et al., 2020; Coombs et al., 2019). These dots are colored as follows: red = detected by both AVO and RTM; blue = detected by AVO only; orange = detected by RTM only; green: no detection by either AVO or RTM. The mislocation to Bogoslof for each DF sample is shaded. The horizontal dashed line is equivalent to 12.5 dB on the Alaska-wide DF. (b) As per (a), though the DF reflects variation specifically at the grid node coincident with the geographic location of Bogoslof (i.e., is equivalent to the stack corresponding to this grid node). Due to the summation process in forming the DFs, DF amplitudes can be higher than the number of normalized waveform envelopes being stacked.
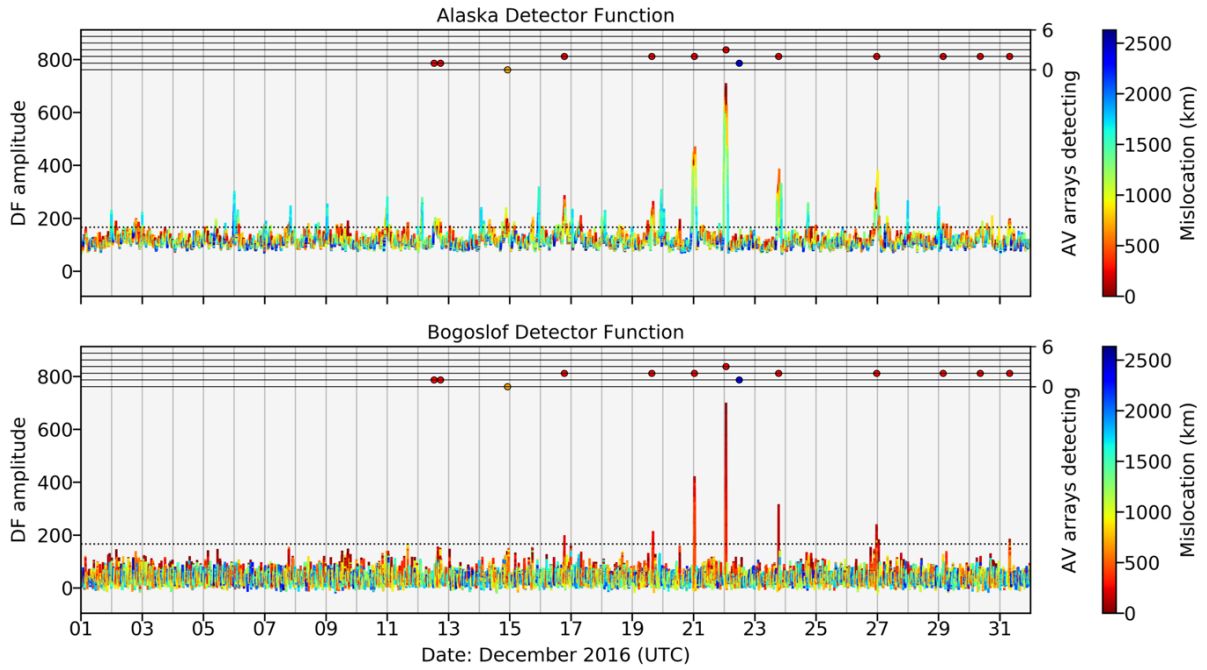
Figure S3.
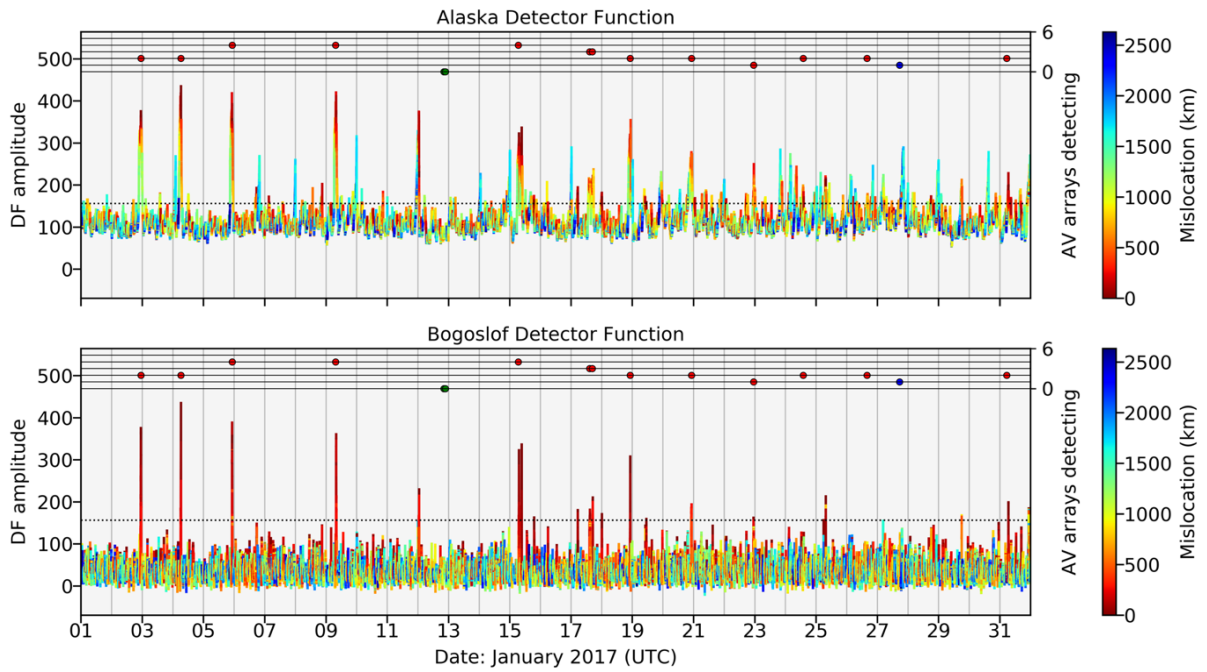
Figure S4.
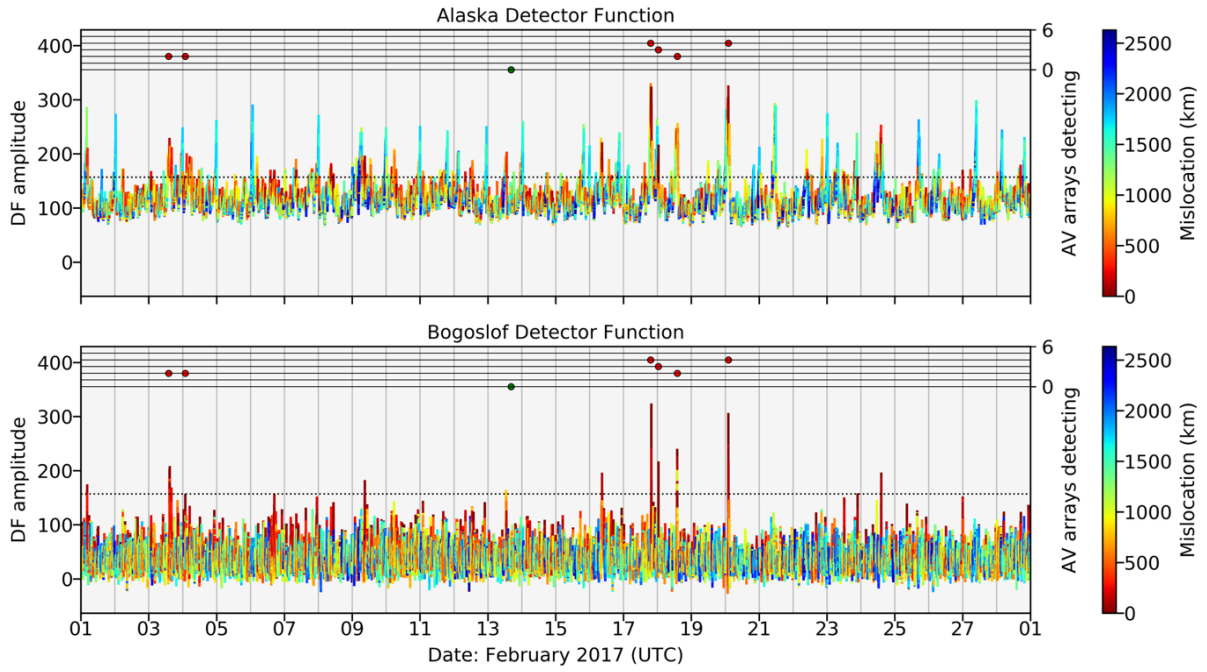
Figure S5.
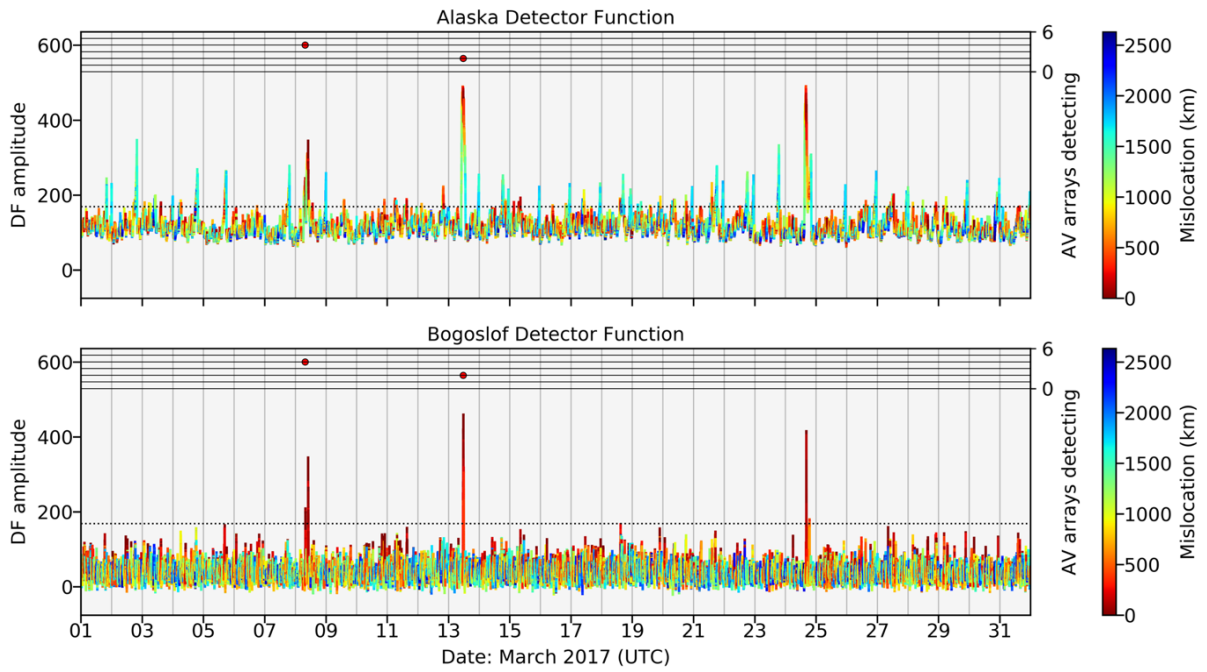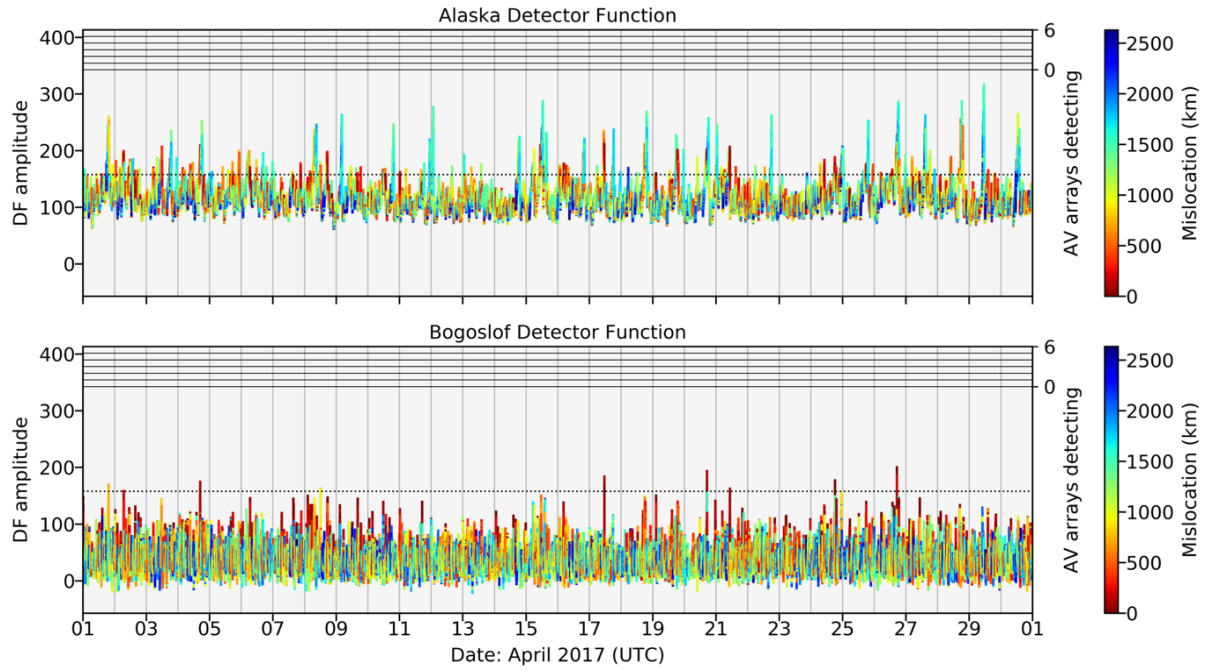
Figure S6.

Figure S7.
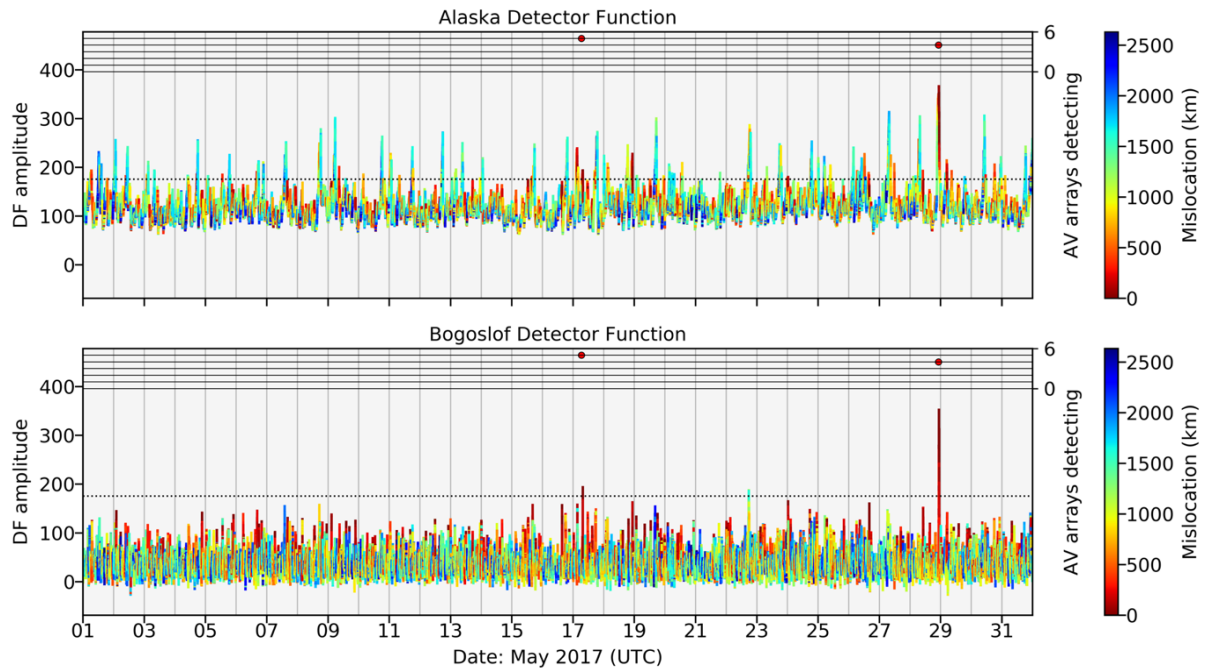
Figure S8.
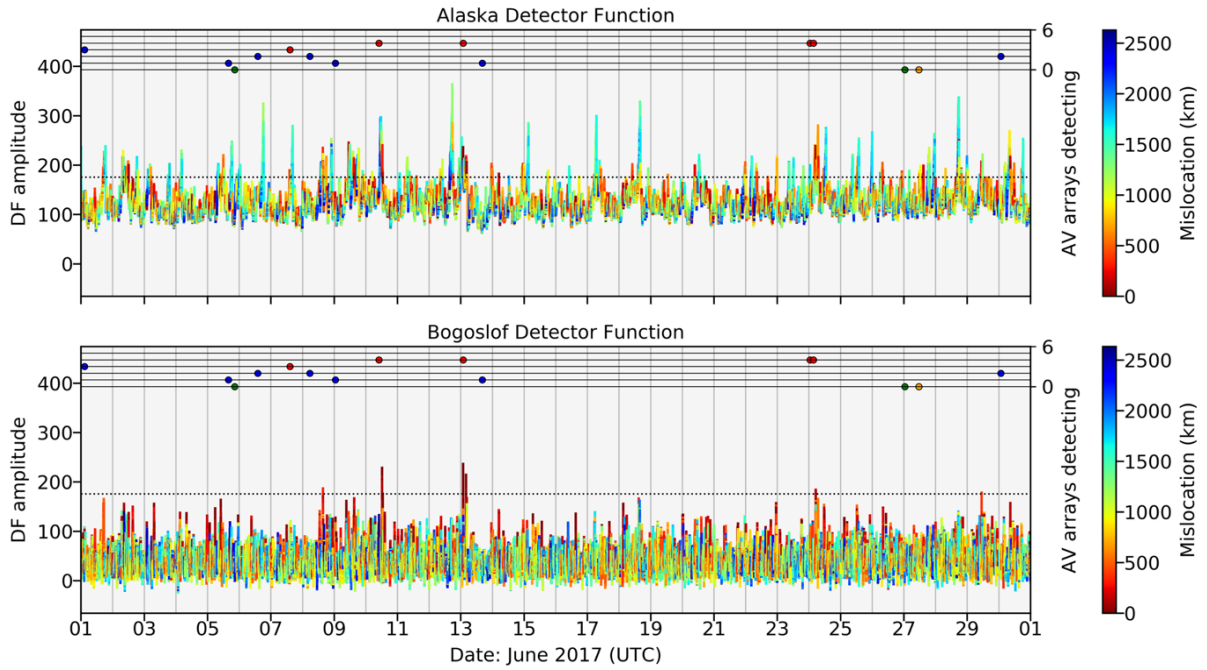
Figure S9.
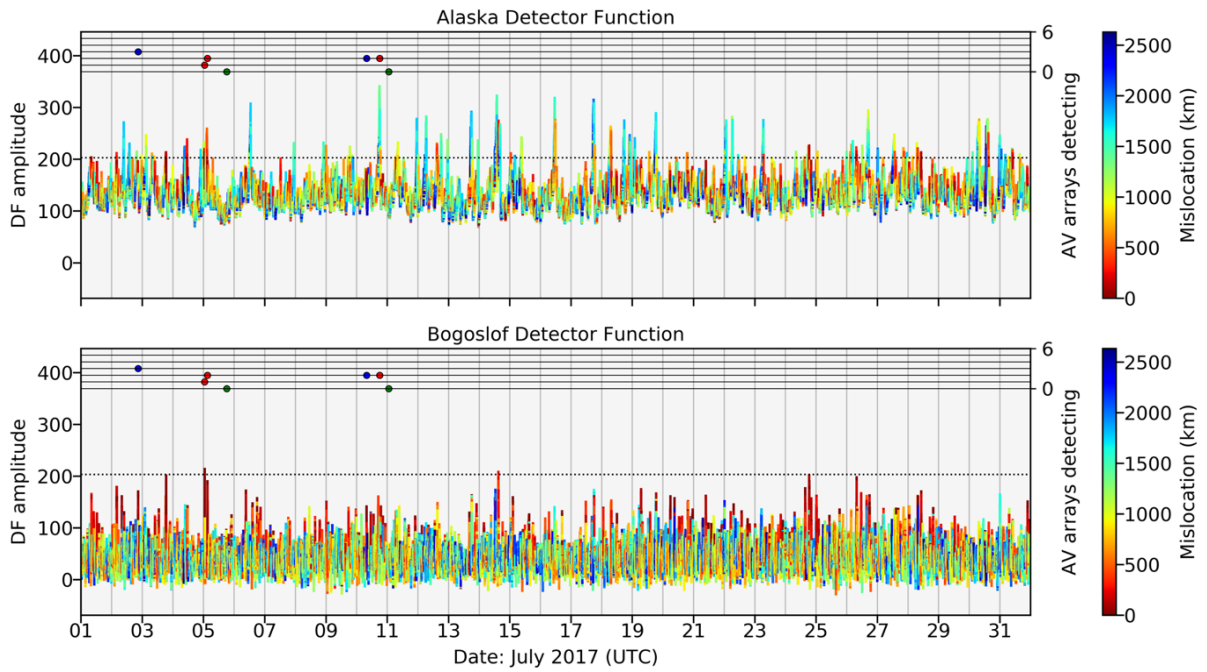
Figure S10.
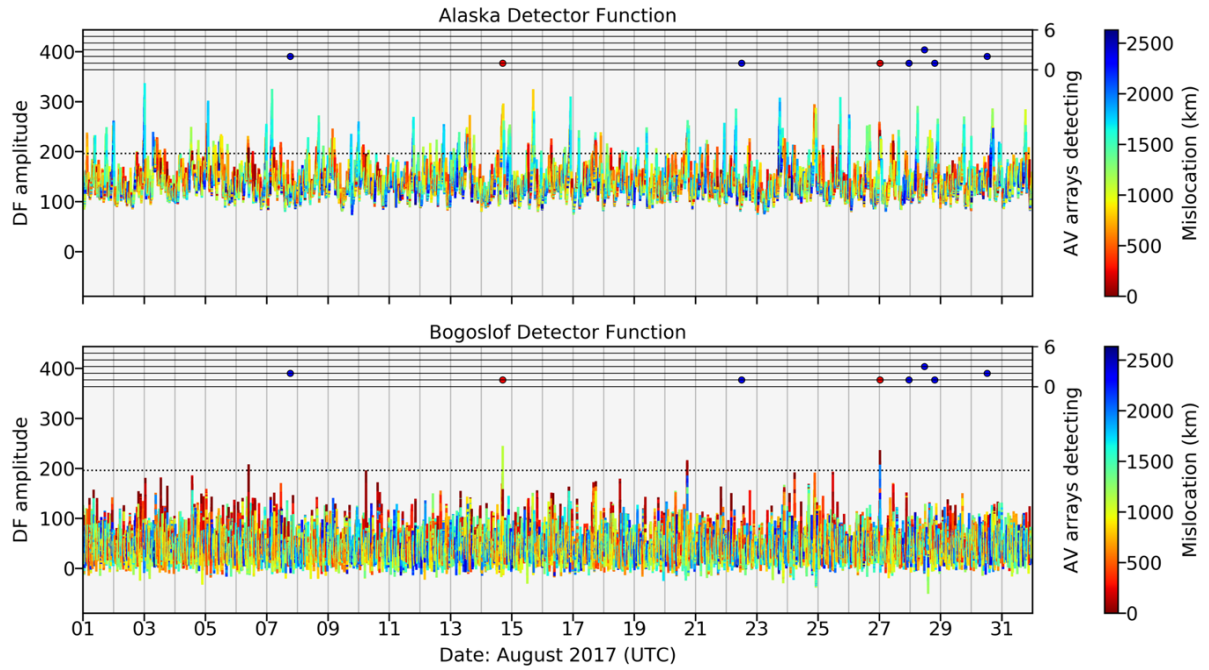
Figure S11.
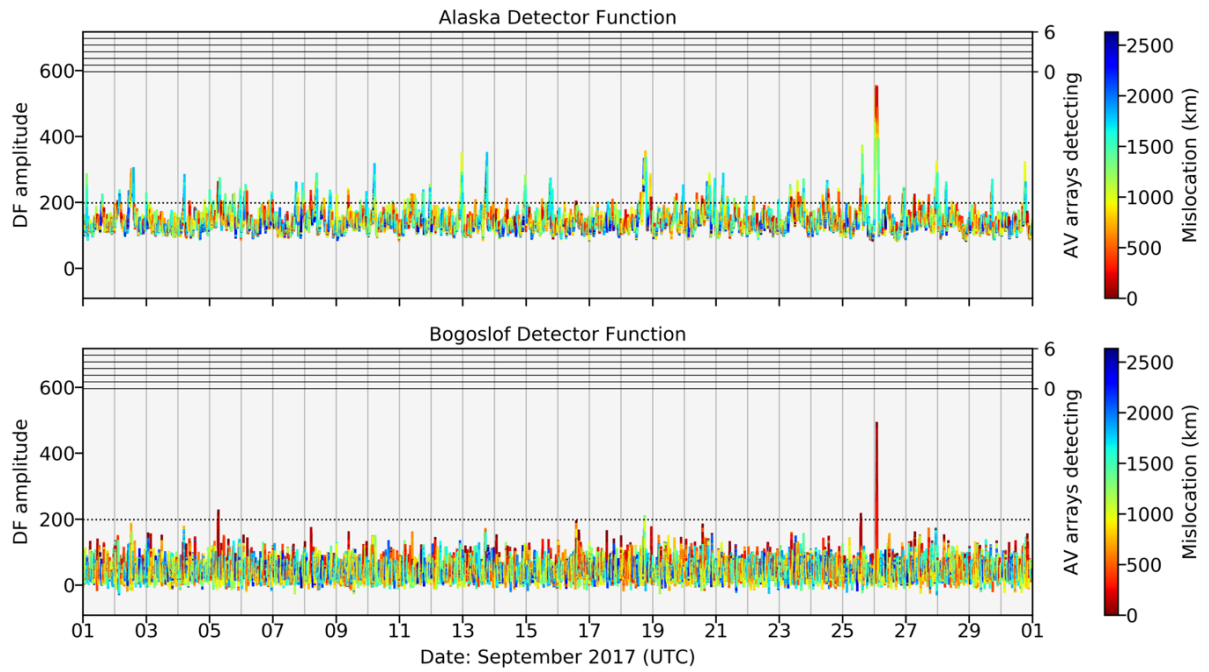
Figure S12.
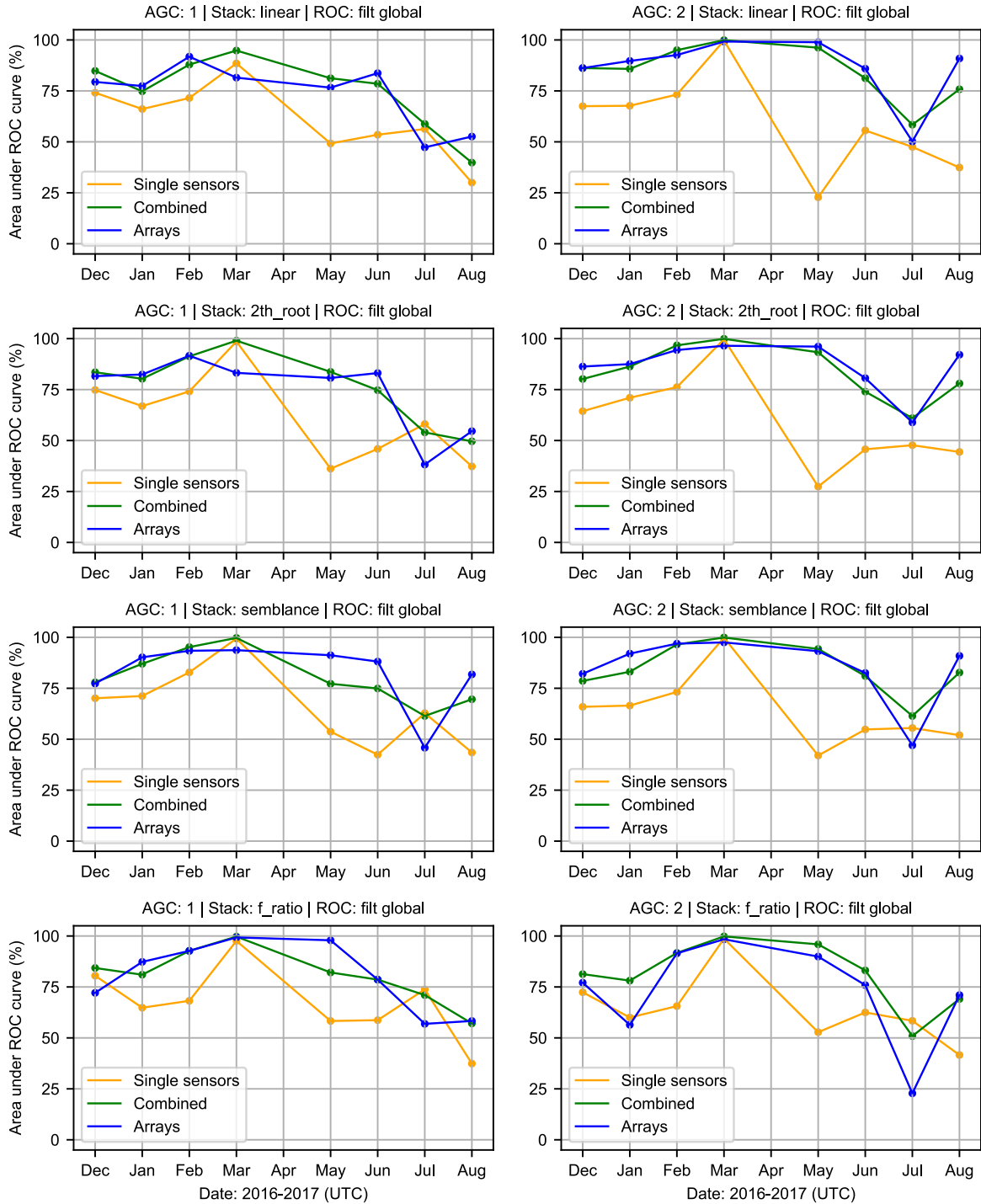
Figure S13. For AVO-cataloged infrasound events from Bogoslof detected by RTM: The area under receiver operating characteristic (ROC) curves are shown for each combination of station selection, automatic gain correction (AGC) type, and stacking method. Semblance and F-ratio stacking methods use 300 s windows, with 150 s overlap. Events were cataloged for every month except April 2017. Absence of markers for a particular month here indicates no detections by the approach. Data values are contained in Tables S3–S10. The term *global* refers to Alaska-wide detector functions. The term *2th_root* refers to Nth-root stacking with N = 2.
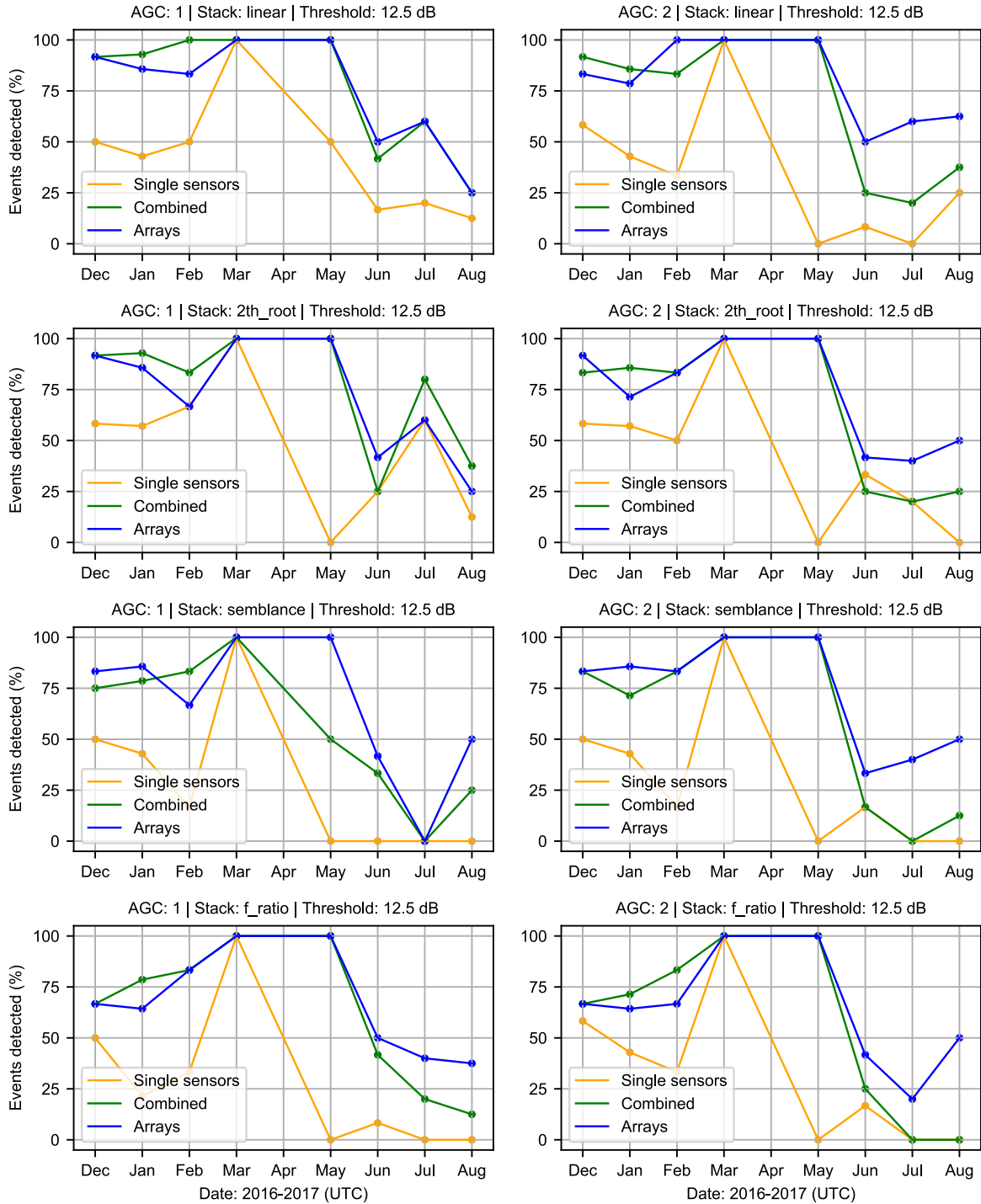
Figure S14. As for Figure S13 but showing event detection rates. As per section 3.4 of the main article, a detection allows for a ±15-minute margin around the AVO cataloged infrasound observation period.
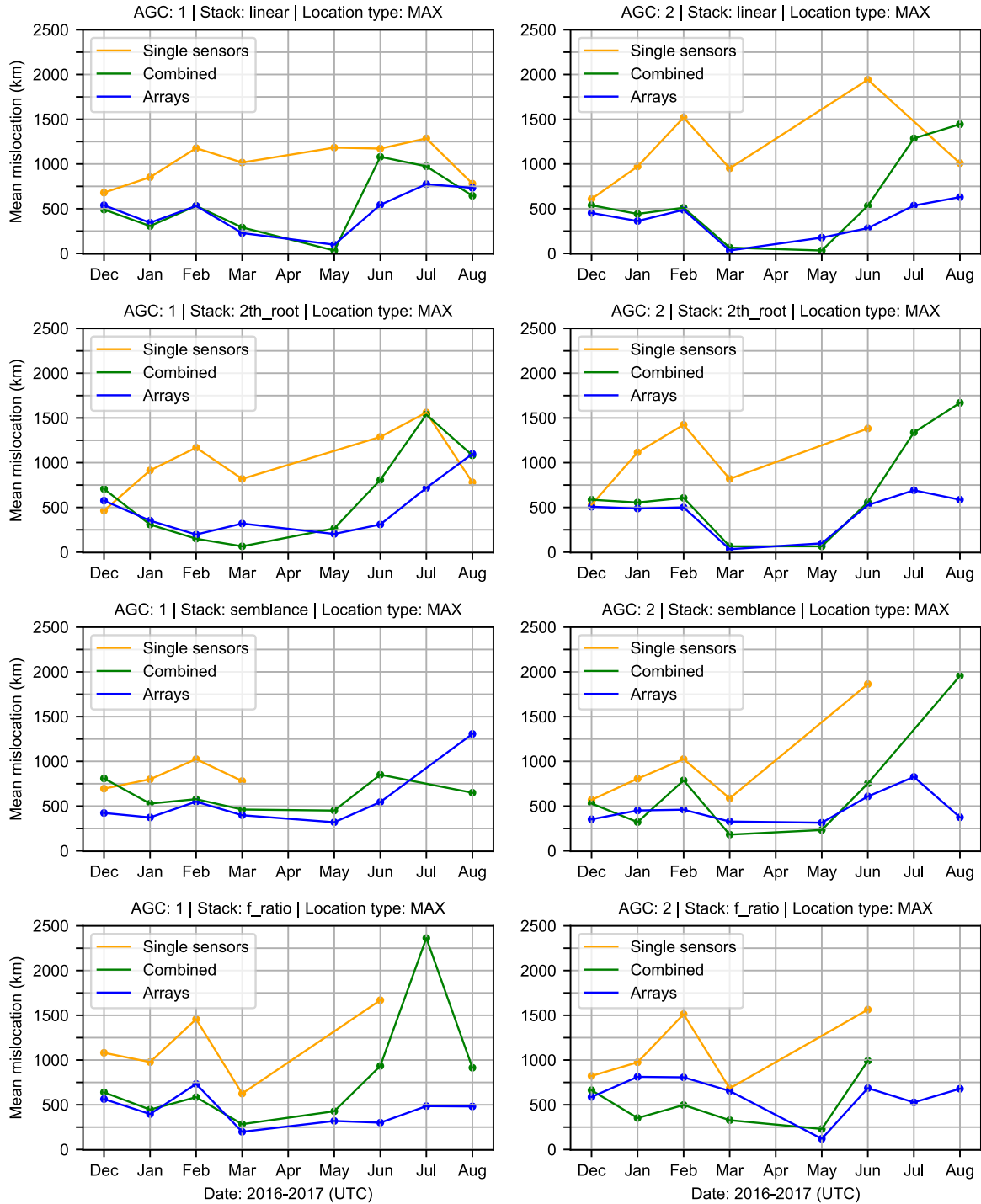
Figure S15. As for Figure S13 but showing mean MAX mislocations of detected events. As per section 3.4 of the main article, a detection allows for a ±15-minute margin around the AVO cataloged infrasound observation period.
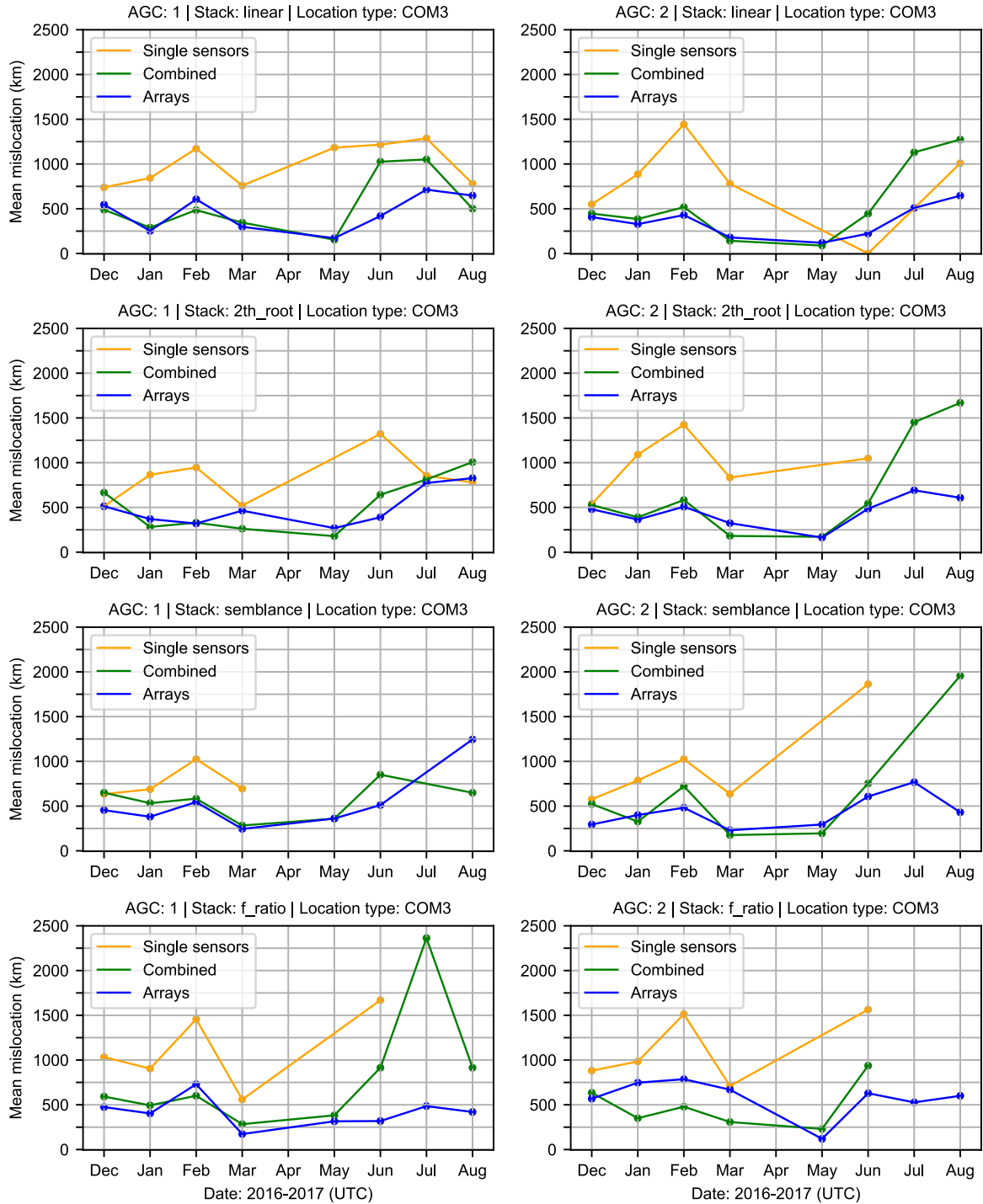
Figure S16. As for Figure S13 but showing mean COM3 mislocations of detected events. As per section 3.4 of the main article, a detection allows for a ±15-minute margin around the AVO cataloged infrasound observation period.

Movie S1. Uploaded separately.

Top panel: Alaska-wide detector function (DF) (colored by mislocation) and Bogoslof-specific DF (colored black) for an eruption at Bogoslof on 8 March 2017. The Bogoslof DF is the stack corresponding to the specific trial source location (grid point) at Bogoslof. Similar amplitudes between the two DFs indicate low mislocation with respect to Bogoslof. Final location estimates for events are performed only on the high amplitude values of the peak (process not shown here). See section S1.5, supplemental material, and section 2.5 (main article) for further information on location methods. Data is from all available infrasound sensors within 2,000 km of Bogoslof. The vertical dashed line is the AVO cataloged event onset, and the dark grey section the period of AVO cataloged infrasound. The horizontal dotted line earmarks the 12.5 dB detection threshold.

Middle panel: Variation in mislocation from Bogoslof for each DF sample.

Bottom panel: Time-slice through stack information where the color-scale represents the amplitude of time-aligned data stacks at each grid location. The corresponding time in each DF is indicated by the moving red dashed marker in the top and middle panels. Time stamps are also provided in the map title. A yellow star marks the grid node with the highest stack amplitude at each time step. Sensors are shaded red proportional to stack contribution for the corresponding source time. Circles are at 500 km spacing, centered on Bogoslof.

Movie S2. As for Movie S1, but using only infrasound array sensors.

Movie S3. As for Movie S1, but using only single sensor stations.

Table S1. Uploaded separately. Notes on Selected RTM Processing Parameters.
Note: Primarily based on linear stacking with AGC1 (section S1.2), using all available sensors.

Table S2. Uploaded separately. RTM Observations for a Selection of non-Bogoslof Volcanic Eruptive Events from December 2016–2018.
Note: For each event, we test with AGC1 and AGC2 linear stacking methods using all sensors as described previously, as well as with array-only configurations. Eruption times, durations, plume information, event sizes and other characteristics from are from Alaska Volcano Observatory (2019) and KVERT, Institute of Volcanology and Seismology FEB RAS (2019). This table is referred to in section 3.5 of the main article.

Tables S3–S10. (below.) Detection and Location Statistics for Bogoslof Eruption Sequence.
Note 1: Events considered are those cataloged by AVO as having detectable infrasound.
Note 2: April 2017 had no AVO cataloged events.
Note 3: As per section 3.4 of the main article, a detection allows for a ±15-minute margin around the
          AVO cataloged duration period.
Note 4: The term *global* refers to Alaska-wide detector functions.
Note 5: The term *2th_root* refers to Nth-root stacking with N = 2.
Note 6: The mean values in the tables do not account for different sample sizes and so should only be
used as relative rather than absolute measures of performance.

AUC: Area under receiver operating characteristic (ROC) curves.
EVD: Event detection proportion.
MAX: Mean mislocation using MAX method.
COM3: Mean mislocation using COM3 method.

AGC: 1 | Stack: linear | ROC: filt global | Location: SNR global | Threshold: 12.5 dB															
Time period	All sensors				Arrays				Single sensors				Mean			
	AUC (%)	EVD (%)	MAX (km)	COM3 (km)	AUC (%)	EVD (%)	MAX (km)	COM3 (km)	AUC (%)	EVD (%)	MAX (km)	COM3 (km)	AUC (%)	EVD (%)	MAX (km)	COM3 (km)
2016-12	85	92	491	488	79	92	539	545	74	50	680	739	371	239	219	359
2017-01	75	93	306	290	77	86	344	253	66	43	852	843	236	141	153	225
2017-02	88	100	532	485	92	83	531	606	72	50	1177	1172	368	266	229	355
2017-03	95	100	290	345	82	100	228	298	88	100	1016	759	223	160	160	224
2017-04	N/A	N/A	N/A	N/A	N/A	N/A	N/A	N/A	N/A	N/A	N/A	N/A	N/A	N/A	N/A	N/A
2017-05	81	100	33	154	77	100	98	172	49	50	1183	1183	111	116	61	101
2017-06	78	42	1080	1026	84	50	543	418	54	17	1172	1216	549	181	394	529
2017-07	59	60	974	1051	47	60	775	713	56	20	1286	1286	628	274	363	615
2017-08	40	25	644	500	53	25	733	647	30	12	780	780	424	242	233	415
Mean	75	76	544	542	74	74	474	457	61	43	1018	997	N/A	N/A	N/A	N/A

Table S3.

AGC: 1 | Stack: 2th_root | ROC: filt global | Location: SNR global | Threshold: 12.5 dB															
Time period	All sensors				Arrays				Single sensors				Mean			
	AUC (%)	EVD (%)	MAX (km)	COM3 (km)	AUC (%)	EVD (%)	MAX (km)	COM3 (km)	AUC (%)	EVD (%)	MAX (km)	COM3 (km)	AUC (%)	EVD (%)	MAX (km)	COM3 (km)
2016-12	84	92	706	666	82	92	576	513	75	58	464	514	442	229	291	433
2017-01	80	93	308	282	82	86	352	370	67	57	913	865	238	182	154	230
2017-02	91	83	150	330	92	67	197	320	74	67	1168	946	206	165	97	198
2017-03	99	100	65	262	83	100	320	464	99	100	818	522	227	216	88	227
2017-04	N/A	N/A	N/A	N/A	N/A	N/A	N/A	N/A	N/A	N/A	N/A	N/A	N/A	N/A	N/A	N/A
2017-05	84	100	266	179	81	100	204	269	36	0	N/A	N/A	155	150	134	128
2017-06	75	25	807	642	83	42	309	390	46	25	1288	1322	342	166	298	325
2017-07	54	80	1537	812	38	60	718	773	58	60	1561	854	528	297	552	530
2017-08	50	38	1081	1007	55	25	1098	827	37	12	780	780	718	306	381	706
Mean	77	76	615	522	74	71	472	491	62	47	999	829	N/A	N/A	N/A	N/A

Table S4.

| AGC: 1 \| Stack: semblance \| ROC: filt global \| Location: SNR global \| Threshold: 12.5 dB | | | | | | | | | | | | | | | |
| Time period | All sensors | | | | Arrays | | | | Single sensors | | | | Mean | | | |
	AUC (%)	EVD (%)	MAX (km)	COM3 (km)	AUC (%)	EVD (%)	MAX (km)	COM3 (km)	AUC (%)	EVD (%)	MAX (km)	COM3 (km)	AUC (%)	EVD (%)	MAX (km)	COM3 (km)
2016-12	78	75	809	650	77	83	423	455	70	50	695	634	384	202	321	374
2017-01	87	79	528	533	90	86	374	381	71	43	800	688	331	183	228	316
2017-02	95	83	577	583	93	67	550	546	83	17	1025	1025	409	241	242	383
2017-03	100	100	462	284	94	100	398	245	99	100	780	694	260	146	220	260
2017-04	N/A	N/A	N/A	N/A	N/A	N/A	N/A	N/A	N/A	N/A	N/A	N/A	N/A	N/A	N/A	N/A
2017-05	77	50	450	360	91	100	320	362	54	0	N/A	N/A	252	168	201	226
2017-06	75	33	851	851	88	42	545	512	42	0	N/A	N/A	490	211	312	465
2017-07	61	0	N/A	N/A	46	0	N/A	N/A	63	0	N/A	N/A	61	23	31	0
2017-08	70	25	649	649	82	50	1307	1245	44	0	N/A	N/A	675	450	248	652
Mean	80	56	618	558	83	66	559	535	66	26	825	760	N/A	N/A	N/A	N/A

Table S5.

| AGC: 1 \| Stack: f_ratio \| ROC: filt global \| Location: SNR global \| Threshold: 12.5 dB | | | | | | | | | | | | | | | |
| Time period | All sensors | | | | Arrays | | | | Single sensors | | | | Mean | | | |
	AUC (%)	EVD (%)	MAX (km)	COM3 (km)	AUC (%)	EVD (%)	MAX (km)	COM3 (km)	AUC (%)	EVD (%)	MAX (km)	COM3 (km)	AUC (%)	EVD (%)	MAX (km)	COM3 (km)
2016-12	84	67	639	592	72	67	564	474	80	50	1081	1033	413	204	262	402
2017-01	81	79	446	494	87	64	396	403	65	21	977	905	324	190	192	304
2017-02	93	83	585	601	93	83	733	729	68	33	1457	1457	476	302	246	456
2017-03	100	100	284	284	99	100	198	173	98	100	625	559	194	124	160	194
2017-04	N/A	N/A	N/A	N/A	N/A	N/A	N/A	N/A	N/A	N/A	N/A	N/A	N/A	N/A	N/A	N/A
2017-05	82	100	428	382	98	100	319	316	58	0	N/A	N/A	261	171	195	234
2017-06	79	42	934	914	79	50	300	319	59	8	1669	1669	431	146	348	408
2017-07	71	20	2363	2363	57	40	485	485	74	0	N/A	N/A	973	187	826	949
2017-08	57	12	914	914	58	38	481	420	37	0	N/A	N/A	484	164	330	465
Mean	81	63	824	818	80	68	434	415	67	27	1162	1124	N/A	N/A	N/A	N/A

Table S6.

98

| AGC: 2 \| Stack: linear \| ROC: filt global \| Location: SNR global \| Threshold: 12.5 dB | | | | | | | | | | | | | | | |
| Time period | All sensors | | | | Arrays | | | | Single sensors | | | | Mean | | | |
	AUC (%)	EVD (%)	MAX (km)	COM3 (km)	AUC (%)	EVD (%)	MAX (km)	COM3 (km)	AUC (%)	EVD (%)	MAX (km)	COM3 (km)	AUC (%)	EVD (%)	MAX (km)	COM3 (km)
2016-12	86	92	538	446	86	83	453	407	68	58	609	550	328	195	230	319
2017-01	86	86	442	385	90	79	363	328	68	43	972	886	278	168	196	264
2017-02	95	83	511	518	93	100	488	430	73	33	1520	1444	367	202	228	346
2017-03	100	100	65	142	99	100	33	179	100	100	952	779	92	126	88	92
2017-04	N/A	N/A	N/A	N/A	N/A	N/A	N/A	N/A	N/A	N/A	N/A	N/A	N/A	N/A	N/A	N/A
2017-05	96	100	33	88	99	100	177	120	23	0	N/A	N/A	121	106	52	88
2017-06	81	25	533	445	86	50	283	222	56	8	1942	0	270	111	213	245
2017-07	58	20	1286	1130	50	60	535	509	48	0	N/A	N/A	575	193	464	555
2017-08	76	38	1444	1273	91	62	630	646	37	25	1010	1010	660	258	515	643
Mean	85	68	607	553	87	79	370	355	59	34	1167	778	N/A	N/A	N/A	N/A

Table S7.

| AGC: 2 \| Stack: 2th_root \| ROC: filt global \| Location: SNR global \| Threshold: 12.5 dB | | | | | | | | | | | | | | | |
| Time period | All sensors | | | | Arrays | | | | Single sensors | | | | Mean | | | |
	AUC (%)	EVD (%)	MAX (km)	COM3 (km)	AUC (%)	EVD (%)	MAX (km)	COM3 (km)	AUC (%)	EVD (%)	MAX (km)	COM3 (km)	AUC (%)	EVD (%)	MAX (km)	COM3 (km)
2016-12	80	83	586	527	86	92	507	479	64	58	529	537	372	216	247	364
2017-01	86	86	555	390	88	71	487	364	71	57	1115	1091	321	179	232	311
2017-02	97	83	606	583	94	83	500	507	76	50	1424	1424	393	228	255	378
2017-03	100	100	65	182	96	100	33	324	100	100	818	834	105	174	88	105
2017-04	N/A	N/A	N/A	N/A	N/A	N/A	N/A	N/A	N/A	N/A	N/A	N/A	N/A	N/A	N/A	N/A
2017-05	93	100	65	172	96	100	98	164	27	0	N/A	N/A	121	120	64	90
2017-06	74	25	558	544	81	42	526	485	46	33	1382	1048	381	197	215	368
2017-07	61	20	1338	1452	59	40	692	692	48	20	N/A	N/A	735	257	475	721
2017-08	78	25	1669	1669	92	50	586	608	44	0	N/A	N/A	778	242	588	752
Mean	84	65	680	690	87	72	429	453	60	40	1054	987	N/A	N/A	N/A	N/A

Table S8.

AGC: 2 | Stack: semblance | ROC: filt global | Location: SNR global | Threshold: 12.5 dB															
Time period	**All sensors**				**Arrays**				**Single sensors**				**Mean**			
	AUC (%)	EVD (%)	MAX (km)	COM3 (km)	AUC (%)	EVD (%)	MAX (km)	COM3 (km)	AUC (%)	EVD (%)	MAX (km)	COM3 (km)	AUC (%)	EVD (%)	MAX (km)	COM3 (km)
2016-12	79	83	529	523	82	83	353	295	66	50	569	576	318	153	226	309
2017-01	83	71	321	327	92	86	451	400	66	43	806	788	287	188	158	274
2017-02	96	83	787	722	97	83	460	482	73	17	1025	1025	426	221	315	400
2017-03	100	100	182	176	98	100	328	230	100	100	586	637	201	142	127	201
2017-04	N/A	N/A	N/A	N/A	N/A	N/A	N/A	N/A	N/A	N/A	N/A	N/A	N/A	N/A	N/A	N/A
2017-05	94	100	233	196	93	100	314	294	42	0	N/A	N/A	201	162	125	170
2017-06	81	17	753	753	82	33	608	607	55	17	1864	1864	481	236	280	459
2017-07	61	0	N/A	N/A	47	40	826	768	56	0	N/A	N/A	444	272	48	413
2017-08	83	12	1956	1956	91	50	375	431	52	0	N/A	N/A	805	178	686	777
Mean	85	58	680	665	85	72	464	438	64	28	970	978	N/A	N/A	N/A	N/A

Table S9.

AGC: 2 | Stack: f_ratio | ROC: filt global | Location: SNR global | Threshold: 12.5 dB															
Time period	**All sensors**				**Arrays**				**Single sensors**				**Mean**			
	AUC (%)	EVD (%)	MAX (km)	COM3 (km)	AUC (%)	EVD (%)	MAX (km)	COM3 (km)	AUC (%)	EVD (%)	MAX (km)	COM3 (km)	AUC (%)	EVD (%)	MAX (km)	COM3 (km)
2016-12	81	67	662	635	77	67	587	568	72	58	822	881	434	237	267	427
2017-01	78	71	352	350	56	64	812	747	60	43	975	984	413	292	159	402
2017-02	92	83	498	479	92	67	807	786	66	33	1512	1512	459	320	210	440
2017-03	100	100	328	308	98	100	654	669	99	100	684	710	354	289	175	354
2017-04	N/A	N/A	N/A	N/A	N/A	N/A	N/A	N/A	N/A	N/A	N/A	N/A	N/A	N/A	N/A	N/A
2017-05	96	100	230	230	90	100	120	120	53	0	N/A	N/A	149	103	127	117
2017-06	83	25	991	937	76	42	686	629	62	17	1564	1564	569	243	365	547
2017-07	51	0	N/A	N/A	23	20	527	527	58	0	N/A	N/A	289	183	39	264
2017-08	69	0	N/A	N/A	71	50	679	600	42	0	N/A	N/A	374	224	46	340
Mean	81	56	510	490	73	64	609	581	64	31	1111	1130	N/A	N/A	N/A	N/A

Table S10.

Chapter 3. Improving Detection And Localization Of Explosive Volcanism in Alaska via Infrasound Noise Reduction: Backprojection and Array Processing Applications

This chapter has been submitted in this form to *Geophysical Journal International*.

Co-authors are R. S. Matoza[1], D. Fee[2], M. M. Haney[3], and J. J. Lyons[3].

[1]Department of Earth Science and Earth Research Institute, University of California, Santa Barbara, California, USA, [2]Wilson Alaska Technical Center, Alaska Volcano Observatory, Geophysical Institute, University of Alaska Fairbanks, Alaska, USA, [3]U.S. Geological Survey Volcano Science Center, Alaska Volcano Observatory, Anchorage, Alaska, USA

Abstract

The recent deployment of a relatively dense regional infrasound network in Alaska offers a novel opportunity to remotely study multiple erupting volcanoes each year, which together exhibit a range of sizes, durations, and styles. This network comprises many former stations from the EarthScope Transportable Array (2014–2021), those operated by the Alaska Volcano Observatory, and others. Such events provide a unique validation data set to examine the ability of different network configurations and processing strategies to detect, locate, and characterize remote volcanic eruptions. Due to the often long distances between stations and the volcanoes in the region, notable limitations to detection and location schemes come from anisotropic atmospheric propagation, and low signal-to-noise (SNR) conditions, with microbaroms and wind being the dominant contamination sources. Here we focus on improving data processing to reduce noise and therefore enhance signal detection and source location accuracy using backprojection and array processing approaches. Additional evaluation metrics include SNR changes, distortion, need for manual data labeling, and computational cost. We compare a range of techniques that separate signals and noise in the spectral domain, including within the same frequency band. Examples include block thresholding, non-negative matrix factorization, and data-adaptive Wiener filtering. Such noise reduction on individual waveforms (i.e., pre-stack) can improve many basic analyses, given that SNR enhancements do not rely on combining traces (i.e., co-stack strategies) in order to improve coherence and isolate events. We further compare results of the pre- and co-stack methods, as well as combinations of both techniques. Denoising effects vary significantly between algorithms, with performance typically proportional to the original SNR of the data, and inversely proportional to the spectral and temporal overlap of signals and noise. Data from the 2016–2017 submarine and subaerial Bogoslof eruption

sequence, as well as synthetics, provide a basis for the analysis. Our primary findings are that reducing the amplitude of microbaroms, as well as their coherence between sensors, benefits array processing by simultaneously limiting background clutter and enhancing the number of detected volcanic event arrivals. Wind noise reduction has little effect on these results, but does improve waveform and backprojection SNR.

1. Introduction

Between 2016 and 2021, seven different volcanoes erupted in Alaska, spanning both a wide geographical area, and a range of explosive and effusive behaviors (Figure 1). Notable among these was the December 2016 to August 2017 eruption of Bogoslof, which produced seventy explosive eruptions (e.g., Coombs et al., 2019). With some plumes reaching over 10 km in elevation at this isolated island, hazards to passing aircraft were a pressing concern. An absence of on-ground instrumentation meant that all observations were made remotely, including using seismicity, satellite imagery, lightning detection, and infrasound. Infrasound refers to acoustic waves with frequencies below 20 Hz, the typical lower threshold of human hearing. Volcanic explosions radiate infrasound through the atmosphere, where it can propagate for thousands of kilometers (e.g., Matoza et al., 2011a). This makes infrasound a useful tool for remote detection and location of volcanoes such as Bogoslof, and others in Alaska. The arrival of the EarthScope Transportable Array (TA) in Alaska, beginning in 2014 (Figure 1), was unprecedented in terms of having a large, dense, regional seismoacoustic network close to a volcanic arc. The TA complemented sparsely spread infrasound stations already in place, operated by the Alaska Volcano Observatory (AVO). From 2019–2021, as the TA's mission wound down, many sites were transferred to other operators such as the Alaska Earthquake Center (AEC), with the remaining sites

removed entirely. In this paper we continue to refer to the TA, as that was the network in

place during the eruption being assessed.
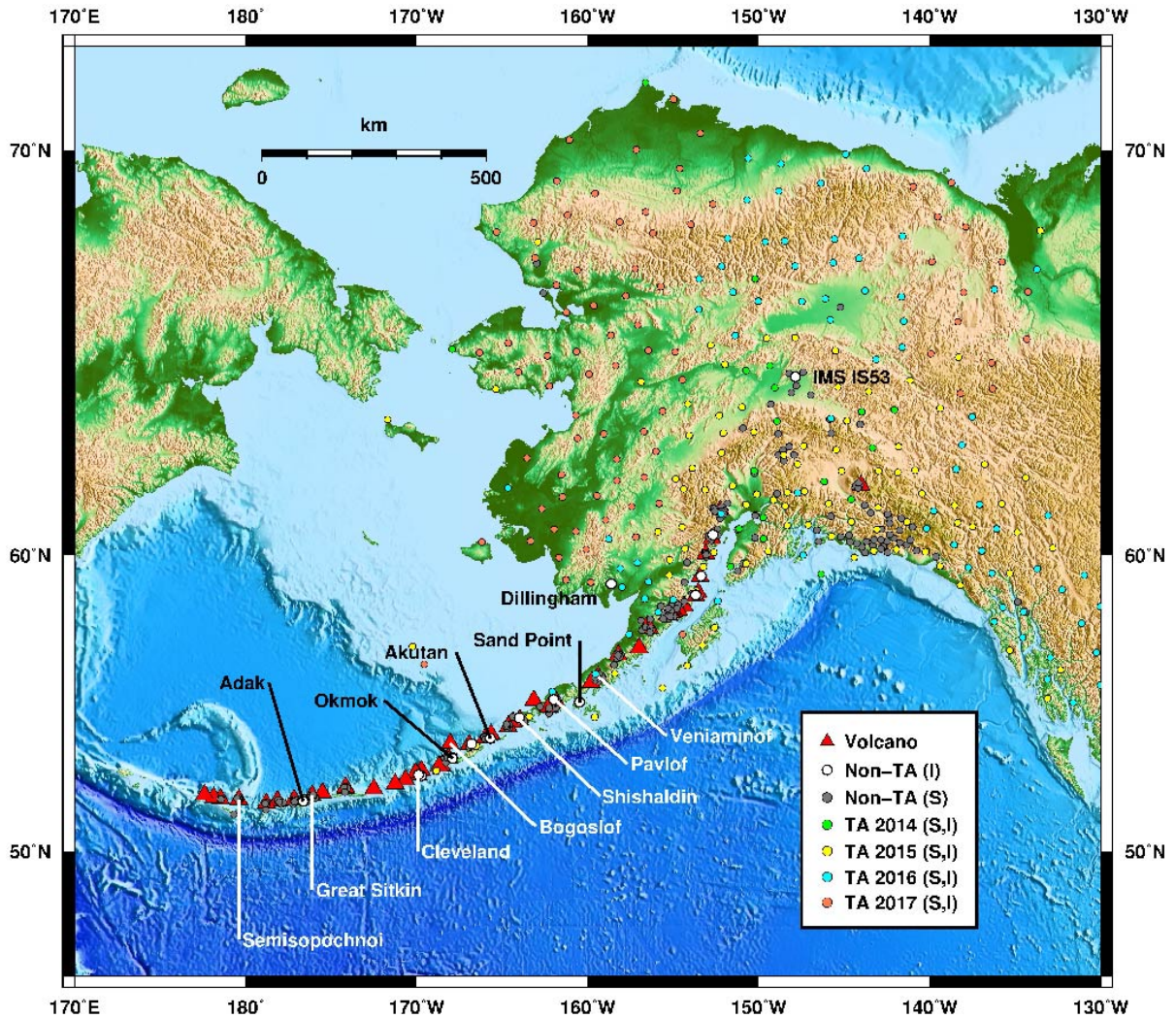
Figure 1. Locations of volcanoes with eruptions since 2016, and available seismic (S) and infrasound (I) data in Alaska during the course of the Bogoslof eruption (2016–2017). Infrasound arrays that are referenced in this study are labelled in black, as well as volcanoes that have erupted since 2016 in white (Mount Cleveland volcano also has an infrasound array). Since 2020, several additional infrasound arrays have been installed by the Alaska Volcano Observatory in the Aleutian Islands. The quantity of TA stations varied through the eruption, with installations migrating westward. Some TA stations were removed entirely starting in 2021, while others have been adopted by existing regional networks.

In previous work we explored using the TA and regional infrasound stations for detection and location of explosive eruptions in the Aleutian Arc and Kamchatka, Russia (Sanderson et al., 2020a). We found that a simple envelope-based backprojection technique, and automated event identification process, was able to capture up to 85% of the infrasound generating events from Bogoslof that were catalogued by AVO (Coombs et al., 2019). Notable limitations to the scheme come from anisotropic atmospheric propagation, and low signal-to-noise (SNR) conditions, with wind being the dominant noise source. Here we focus on improving waveform data processing to reduce noise, thereby enhancing signal detection and source location accuracy. Signals from Bogoslof often have similar character to microbaroms (ocean noise) and wind, providing a strong challenge for signal separation. In part this is due to attenuation and remote detection, but also due to the often submarine nature of the eruptions (e.g., Lyons et al., 2019).

In this study we extend our focus from a backprojection location technique (reverse time migration, RTM), to include array processing. Both strategies work on the principle of beamforming (stacking) signals from different sensors according to an acoustic velocity model, such that constructive and destructive interference improves the amplitude of acoustic arrivals, and decreases non-acoustic noise sources such as wind. Wind noise is a common problem that can make beamforming ineffective for three principal reasons: (1) in array processing, local wind turbulence (among other factors) can reduce the coherence of signals of interest between the array elements; (2) in RTM, wind affects the amplitude of traces which are typically normalized prior to stacking; and (3) again in RTM, a common approach is to take envelopes of waveforms before stacking, with this smoothing effect reducing the impact of destructive interference. One of our aims, therefore, is to explore how wind noise

can be removed from our data prior to beamforming, and whether this removal provides benefits to detection and location strategies. [Appendix 1 describes early work on this topic.]

A second natural phenomena that impacts infrasound records are microbaroms. These are acoustic arrivals generated by nonlinear wave-wave, and wave-shore interaction, with a spectral peak between 0.1–0.5 Hz (e.g., Bowman et al., 2005). This frequency range overlaps with the majority of the Bogoslof events (e.g., Fee et al., 2020; Lyons et al., 2020), more noticeably at remote stations where attenuation has reduced higher frequency components. Microbaroms are detectable worldwide due to their low frequencies, and there are many potential source areas (Landès et al., 2012; Matoza et al., 2013). In Alaska, the primary origin and strength of microbaroms varies over the course of the year, such that backazimuth of the microbaroms and volcanoes may periodically coincide. Being acoustic arrivals, microbaroms often constructively add during beamforming (depending on the algorithm and spatial extent of the source region). Such directional interference can cause false alarms and missed detections in monitoring applications (e.g., Matoza et al., 2011b). This pervasiveness leads to microbaroms being the main source of so-called clutter (Ceranna et al., 2019; Mialle et al., 2019). Consequently, we also aim to see if reducing microbaroms improves array processing and RTM performance.

To our knowledge there is limited prior literature on denoising individual infrasound traces, as SNR enhancement usually comes through beamforming. These denoising methods enable a waveform to be separated into signal and noise components, enabling manipulation of either. This contrasts with classification approaches that identify time periods of signals and noise, but do not modify the signal. One recent development is a study by Carniel et al. (2014), with the supervised approach employing statistical foreground activity detection, non-negative matrix factorization (NMF), and Wiener filtering to reduce wind noise

affecting volcanic tremor. Another recent study, by Williams et al. (2020), shows how denoising infrasound traces could improve the number of volcanic eruption detections made during array processing by reducing microbaroms. This approach is based on semi-supervised adaptive spectral subtraction using non-local means. Finally, Cook et al. (2021) combine a wind noise detection and compensation technique based on the characteristic spectral shape of wind noise in the presence of a windscreen, using synthetic sources in the low-audio range. These approaches do not currently exist as open source tools, and are very limited in terms of test cases, factors we aim to improve on. Many contemporary signal separation techniques stem from developments more commonly seen in the audio, music, and image processing industries going back some decades (e.g., Boll, 1979). Seismology has also had some recent developments in denoising single traces, using statistical threshold and machine learning based techniques (e.g., Cabras et al., 2012; Langston and Mousavi, 2018; Zhu et al., 2019; Jiang et al., 2020). Approaches such as seismoacoustic coherence weighting (e.g., Matoza and Fee, 2014; Fee et al., 2017; Ichihara et al., 2021) take advantage of co-located sensors and air-to-ground coupled signals. Median filters can be effective for removing (or keeping) impulsive signals and white Gaussian noise (e.g., Bednar, 1983).

To remove unwanted wind noise and microbaroms from our data, we examine several existing open source data decomposition tools. The approaches span fully supervised (training with signals and noise), semi-supervised (training with noise only), and unsupervised classes. The methods can be applied to a single trace, however, without need for large training data sets. Our analysis covers several kinds of volcanic events, station types, and source-station distances. We aim to identify how well these kinds of trace denoising approaches are beneficial in terms of detecting and locating events under these different but common circumstances. As with any realistic implementation of a processing

workflow, there is no one optimal method or set of parameter choices, particularly with such a large number of free parameters (e.g., Withers et al., 1998; Mialle et al., 2019). For evaluation criteria here, we use metrics like SNR, distortion, and phase changes, which are particularly relevant for meeting the goals of the project.

The organization of the paper is as follows: First we describe the typical characteristics of Bogoslof infrasound, wind noise, and microbarom clutter, as well as how hardware characteristics can affect these observations. Next, we review the data decomposition methods used for isolating signals of interest, and then the array processing and RTM schemes used for detecting and locating events. Finally, we present our results which show that microbarom reduction primarily improves array processing by not only reducing clutter, but also by enhancing event detections, particularly in the band previously dominated by microbaroms. Some methods only reduce microbarom amplitude, whereas others also reduce residual microbarom inter-sensor similarity and thus detectability. Wind noise reduction does not strongly affect array processing performance, but does improve SNR for backprojected data, thereby helping improve event identification.

2. Data and Station Characteristics

The geological, geochemical, and geophysical nature of the Bogoslof eruption sequence is presented in a special journal issue (Waythomas et al., 2019), following several prior publications (e.g., Coombs et al., 2018, and references therein). Of particular relevance here are those studies which address the infrasound character of the eruptions, including Haney et al., (2018), Wech et al. (2018), Lyons et al. (2019), Haney et al. (2020), and Schwaiger et al. (2020). Infrasound records of the eruptions persist from minutes to hours, with the frequency range of the eruptions spanning from below 0.1 Hz, to more than 10 Hz

(as recorded at the nearby Okmok array), depending on whether the eruption is at a submarine or subaerial stage (Fee et al., 2020; Lyons et al., 2020). Higher frequency components are attenuated with distance. For eruption catalog information, we refer to Coombs et al. (2019), who include which infrasound arrays made observations, as well as detection start and stop times. Lyons et al. (2020) have a differing record of which arrays recorded events in some instances. Differences in detection rates between sources may be due to different array processing methods and thresholds (section 3.4). We include notes in the supplemental material on some of these differences, as well as other potential improvements to catalogs. All dates here are in Coordinated Universal Time (UTC).

Wind noise nominally has a spectrum with amplitude inversely proportional to frequency. This slope largely reflects the inertial subrange of the turbulence spectra, produced by atmospheric eddies of varying wavenumber and kinetic energy (e.g., Raspet et al., 2006). How wind noise presents at, and affects the stations in Alaska, can vary drastically due to hardware differences, location, and time of year. In this study, we evaluate data from all infrasound sensors within 2,500 km of Bogoslof, including the TA, an array which is part of the International Monitoring System (IMS IS53), and six arrays operated by AVO (Figure 1). The AVO operated array locations and station codes are as follows: Akutan (AKS), Adak (ADKI), Cleveland (CLCO), Dillingham (DLL), Okmok (OKIF), and Sand Point (SDPI). Infrasound sensors generally have a flat response from 0.01 or 0.1 Hz to 50 Hz, and four to 8 elements per array. During the eruption, ADKI, DLL, IS53, and OKIF had either domes or pipe systems acting to reduce higher frequency wind noise through spatial averaging (Dixon et al., 2019; Lyons et al., 2020). As the remaining majority of stations have limited wind noise reduction hardware in the form of basic diffusers (Busby and Aderhold, 2020), detection capability is particularly affected, and efforts to reduce wind noise must be

done post-recording. Snow cover can also act as a lowpass filter (Adam et al., 1998). Stations away from coasts, and forested sites are typically less windy. Sources closer to stations will have limited path attenuation, and so broader frequency ranges will be recorded. Proximal stations without wind noise reduction hardware will often have relatively similar eruption and wind noise characteristics.

3. Methods

Here we introduce the techniques employed to prepare data, and to separate the events of interest from microbaroms and wind noise. We also describe the array processing and RTM strategies used to detect and locate events. Figure 2 provides an overview of these stages, with parameters and program links given in the supplemental material. The processing workflow is similar to those of e.g., Cabras et al. (2012), and Carniel et al. (2014), who begin with removal of persistent background sources, and then subdivide the remaining data into signals and noise.
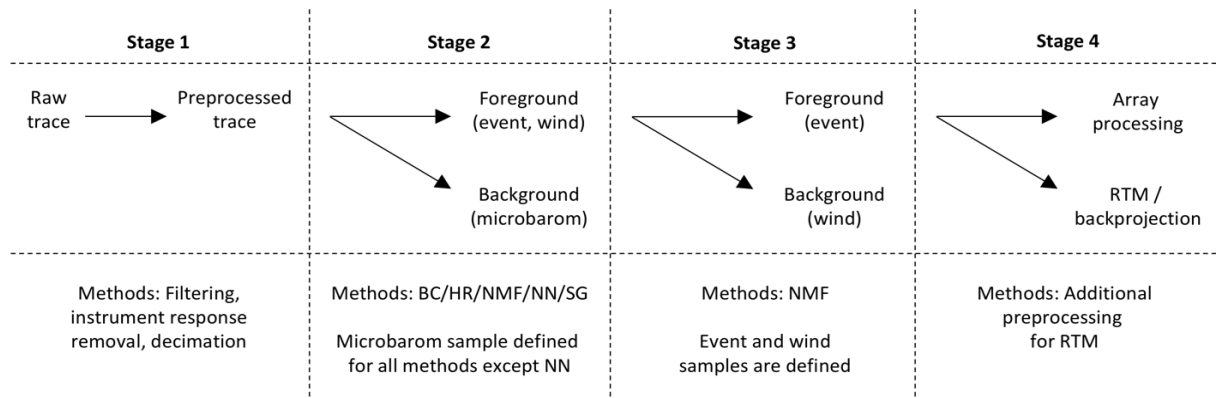
Figure 2. Summary of processing steps in denoising data prior to array processing and backprojection. Stage 1 is basic data preparation, stage 2 removes the microbarom, and stage 3 removes the wind noise. BC: BCseis; HR: Harmonic Regeneration; NMF: Non-negative Matrix Factorization; NN: Nearest-neighbour filtering; SG: Spectral gating.

3.1. Preprocessing

We preprocess all traces via the following steps: (1) taper the waveform, (2) filter above 0.01 Hz, (3) remove instrument responses using a water level at 35 dB, and (4) down-sample to 20 Hz after applying an anti-aliasing filter. These parameters are used to limit amplification of very low frequency noise, and ensure workable computational processing times by limiting the sample rate, while retaining dominant event and noise frequencies (up to 10 Hz). This preprocessing is termed stage 1 of the methodology sequence (Figure 2). For local networks, where event spectra deviate from background noise at higher frequencies than the examples here, use of the full sample rate may be beneficial.

3.2. Microbarom Removal

Stage 2 of the workflow is to remove microbarom signals from the remaining data, which comprises potential events of interest, as well as high amplitude intermittent wind noise. In this study we compare five different methods to evaluate some of the advantages and disadvantages of each. For all methods except for nearest-neighbor filtering, a section of microbarom must be labeled as a reference. It is also possible to use a microbarom profile from an archive, or use a synthetic spectral representation. This can be useful in instances where a trace does not have a viable microbarom-only section. Brief descriptions of the five methods follow, and we refer the reader to the references cited for further details. Several methods overlap in procedure, and thus are not wholly independent concepts. Parameter choices are those that result in similarly reduced microbarom spectral amplitudes. For each method, it is possible to reduce the microbarom amplitude further, but this can be at the expense of the event waveform.

Even when local winds are minimal, infrasound spectra will still typically present with a turbulence-induced negative slope, superposed with a microbarom peak. Stage 2

methods using a noise reference window will inevitably encompass both aspects of the ambient infrasound, unless some prior compensation is applied (e.g., Cook et al., 2021). Consequently, while this stage removes the microbarom as primarily intended, persistent atmospheric effects are also reduced. In this paper we will refer to both components of this lower-noise ambient state as the microbarom to avoid confusion with more prominent wind noise. Acronyms for the following methods are included in Table 1 for reference.

Table 1. List of acronyms that appear repeatedly in the paper, and what they refer to. Additional acronyms are only defined at the time of their introduction in the paper.

Acronym	Definition	Category
ADKI	Adak infrasound array	Stations
AGC1	Automatic Gain Control method 1	Backprojection
AGC2	Automatic Gain Control method 2	Backprojection
AKS	Akutan infrasound array	Stations
AVO	Alaska Volcano Observatory	Stations
BC / BCseis	Block Choice seismic analysis	Denoising
CLCO	Cleveland volcano infrasound array	Stations
DF	Detector Function	Backprojection
DLL	Dillingham infrasound array	Stations
HR / HRNR	Harmonic Regeneration Noise Reduction	Denoising
IMS	International Monitoring System	Stations
IS53	IMS station IS53	Stations
NMF	Non-negative Matrix Factorization	Denoising
NN	Nearest-Neighbor analysis	Denoising
OKIF	Okmok infrasound array	Stations
PMCC	Progressive Multi-Channel Correlation	Array processing
PSD	Power Spectral Density	Characteristics
PWS	Phase Weighted Stacking	Backprojection
RTM	Reverse Time Migration	Backprojection
SDPI	Sand Point infrasound array	Stations
SG	Spectral Gating	Denoising algorithms
SI-SDR	Scale-Invariant Signal to Distortion Ratio	Characteristics
SNR	Signal to Noise Ratio	Denoising algorithms
TA	EarthScope Transportable Array	Stations
UTC	Coordinated Universal Time	Reference time

3.2.1. Block choice (BC)

Block thresholding is the practice of adjusting the power in the time-frequency blocks formed via spectral transformation of data. We use the BCseis (Block Choice Seismic Analysis) program to implement this technique (Langston and Mousavi, 2018). This method incorporates wavelet transforms, making it unique among the tools described here. First, higher-order statistical tests are applied to the blocks in order to remove Gaussian noise. Next, the spectral representation is sharpened by concentrating energy around instantaneous frequencies. Signals and remaining noise are then separated using thresholds derived from generalized cross-validation (evaluating models with resampled data) and a Wiener filter. The operation of BCseis requires choosing a spectral resolution parameter, which has a considerable effect on the computation time (section 5.1). We find little first-order waveform difference between the lowest two settings (one and four voices), but that time-frequency representations of one voice data are noticeably coarse. Consequently, for analysis here, we use four-voice data, which remains practical for large data sets.

3.2.2. Harmonic Regeneration (HR)

Harmonic regeneration noise reduction (HRNR; Plapous et al., 2006) is the final part of this data-adaptive method. For each time step, the current a posteriori SNR (ratio of noisy signal power and noise power), and a priori SNR (ratio of clean signal power and noise power) from the previous step are used to determine the new a priori SNR and spectral gain required for a clean signal. Noise is removed using a Wiener-type filter, and following additional gain control, HRNR reduces harmonic distortion in the result.

3.2.3. Non-Negative Matrix Factorization (NMF)

NMF is the process of factorizing a matrix **X** into two other matrices, **W** and **H**. In our case, **X** is a spectrogram. **W** is composed of basis vectors, also known as dictionary elements, representing the spectral amplitude at each frequency. **H** is a matrix of activations, also known as weights or gains, representing when the basis vectors occur. There are many popular NMF algorithms that perform this task, and here we use the Kullback-Leibler application by Bryan et al. (2013). To ensure the preprocessed trace is split into a foreground (components of interest) and background (undesired elements, typically noise), the basis vectors in **W** are pre-grouped into two sets, one set based on the frequency characteristics of the microbarom sample, and the other set based on everything else in the trace. The initial state of **H** is randomized. The individual time series are then reconstructed by using a masking filter to downweigh the undesired spectral elements. We did not have success when keeping **W** randomized, i.e., exploring whether the data naturally falls into two groups. Without pre-grouping, the resulting components of **W** and **H** have no ordering, necessitating some type of rule-based clustering mechanism. Given the large frequency overlap between Bogoslof events, wind noise, and microbaroms, effective clustering rules would be difficult to design.

3.2.4. Nearest-Neighbor Filtering (NN)

For this technique, no noise region needs to be specified, making the method fully unsupervised (McFee et al., 2015). The process first filters a time-frequency representation of the data by replacing blocks with the median properties of those nearby (i.e., neighbors), thereby discarding variable elements, and keeping repetitive ones such as the microbarom. This resulting matrix is then used as a background reference in a square-root-based Wiener filter, retaining only the event and wind noise elements. One of the key parameters is to

specify the number of nearest-neighbors being aggregated. Given that some of the Bogoslof events have durations of several hours, it is necessary in these cases to make this particular parameter quite large in order to ignore such events. The consequence, however, is that processing slows down considerably (section 5.1). Another limitation is that for periods of persistently high winds, this method may extract some of the wind noise components, not just the microbarom.

3.2.5. Spectral Gating (SG)

Noise gating is the practice of only passing signals through a system that are above a particular amplitude. For this technique, we use the implementation of Sainburg and Amr (2019). This method operates by masking trace elements that have lower power frequency components than thresholds based on the statistics of the designated noise-only section. A filter smooths the mask before being applied to the data. The mask application is via direct multiplication with the data spectrogram. This approach potentially leads to more artifacts than seen with masking procedures such as a Wiener filter. There are several similarities with the BC tool, but here the approach is simpler, and operates with a Fourier transform.

In prior work (Sanderson et al., 2020b), we explored the impact of several unsupervised algorithms on microbarom and wind noise for RTM applications. This included spectral gating, but by treating the entire trace as the reference from which to determine the average noise from, rather than a manually identified region as here. Other unsupervised techniques assessed by Sanderson et al. (2020b) included spectral subtraction, adaptive foreground detection, and frequency-sorted NMF. These techniques performed inconsistently for the wide range of source-station distances and station hardware, with limited benefit to RTM detection and location. Consequently, we have focused more here on semi-supervised approaches, which can benefit from the specific nature of each station.

3.3. Wind Noise Removal

After the preprocessed trace has had the microbarom removed by any of the five methods in section 3.2, a second decomposition step separates out the wind noise in stage 3 (Figure 2). Stage 3 uses NMF, regardless of the stage 2 technique. This selection follows from finding that the non-NMF stage 2 methods are relatively ineffective at removing wind noise while leaving the events intact. In part this is due to limited training options, but also that threshold-based methods that use high wind noise as a reference, will inevitably remove relatively low amplitude events. Here we take a fully supervised approach where we label an example wind section, as well as the event section using eruption catalogs. This approach is appropriate for effective separation as volcanic jetting (i.e., explosions like jet engines) and wind noise are often superficially similar in terms of waveforms and spectral content (e.g., Matoza et al., 2011a). The effectiveness of the wind noise removal also depends on how similar wind characteristics are at different times of day, as the amplitude and frequency range can change. Selecting a region of high amplitude wind noise generally ensures higher noise reduction levels. Scaling the amplitude of the basis vectors has the effect of adjusting the degree to which wind noise is removed. For simplicity, here we do not perform any such scaling. Notably, we find that a semi-supervised approach of only labeling the event can slightly improve wind noise reduction when compared to when both the event and wind are selected, but sometimes this is at the expense of event fidelity. Also, by not including a wind label, the option of basis vector scaling is unavailable. A semi-supervised approach of only labeling wind performs less well than the fully supervised case, doubling the wind noise amplitude in the foreground of stage 3 (results not shown). This latter approach may be useful in automated classification systems, where the characteristics of the microbarom and wind noise are generally well established, but the nature of events are not. Here, we are

focusing on the benefits of denoising using as much prior knowledge as possible, leaving integration into a classification system to future work.

The full signal separation sequence is illustrated in Figure 3. The 31 January 2017 Bogoslof event was chosen as an example given the low amplitude activity hidden by the microbarom, transition from subaqueous explosions to subaerial jetting behavior (Fee et al., 2020), and varying spectral overlap between the event and multiple wind bursts. In stage 2, the stage 1 preprocessed trace (Figure 3, first row) is operated on using NMF to separate out the microbarom background from any remaining arrivals in the foreground (Figure 3, second and third rows). The blue-line bracketed region in the top plot is used as a relatively clean microbarom sample. Next, we separate the stage 2 foreground into a new foreground-background pair (stage 3), containing predominantly event and wind noise components respectively (Figure 3, fourth and fifth rows). The yellow and green bracket regions on the third row of Figure 3 are those designated as representative of event and wind noise characteristics for this second NMF process. The decomposition strategies are not perfect, however, and desired or undesired components may or may not pass between stages, depending on how similar they are to each other. For instance, the example in Figure 3 shows effective microbarom isolation and removal in stage 2, whereas some wind noise remains in the foreground by stage 3. In part this is due to the frequency content of the wind at the start, middle, and end of the day varying considerably. Consequently, additional processing may be able to remove the very low frequency wind noise components that coincide with the event. However, this could be challenging given the similarity between the non-jetting parts of the event, which include very low frequencies, and this midday wind noise. What is considered to be mid-day wind noise here is somewhat speculative given the timing relative to the eruption, and dissimilar frequencies to wind later in the day. However,
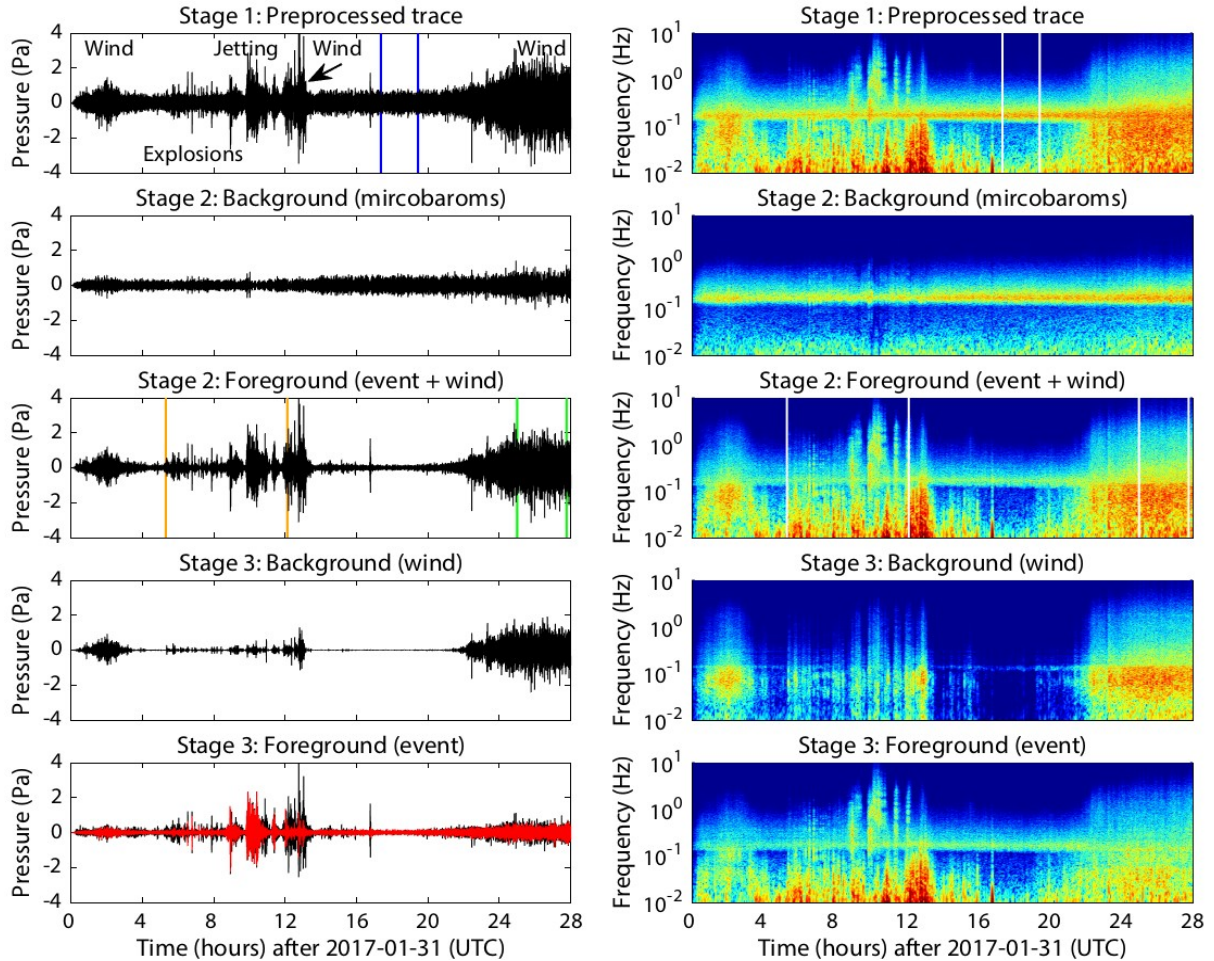
Figure 3. Denoising stages applied to infrasound records of the Bogoslof eruption on 31 January 2017. Data are from OKIF channel 1. In this example we use NMF for both stage 2 and stage 3 separation steps. Data segments designated during processing are bracketed on the left-hand side on the appropriate traces as follows: microbarom (blue), event (orange), wind (green). The event timing is provided by the infrasound statistics in the AVO catalogue (travel time corrected). In the bottom panel, the red trace is the underlying black trace filtered >0.1 Hz, removing some very low frequency wind elements. The righthand side shows the corresponding spectral content. Here, the brackets are in white only for clarity. Warmer colours in the spectrogram indicate relatively high power. The microbarom is effectively removed in stage 2, with much of the wind at the beginning and ends of the day removed in stage 3. Wind during the middle of the day largely remains as it differs in nature to that used as a reference.

the semi-coherent arrivals have apparent velocities on the order of 10 m/s, with beamforming

suggesting arrivals are from the northwest and southeast, and so an eruption related

phenomenon seems unlikely. Although gravity waves may have such velocities, we do not

further speculate on such a source here. Such a variable wind noise spectra is not

unprecedented, given that different kinds of turbulence produce different spectral

118

characteristics (e.g., Walker and Hedlin, 2010; Cook et al., 2021). Spectral analysis of the infrasound suggests that a volcanic jetting episode occurs during the final mid-day wind burst, ending at ~13:09. This would extend the catalogued infrasound activity by an hour, aligning more with the seismic end time (13:30) provided by Fee et al. (2020).

In Figure 4a, we compare the first-order performance of each stage of the signal separation methods, using infrasound records of the 31 January 2017 Bogoslof eruption, recorded at OKIF. Each individual stage 2 method effectively removes the majority of the microbarom, and the common stage 3 (NMF) method significantly reduces the wind noise to low levels. The degree of wind noise reduction during stage 2, which aims to only remove microbaroms, varies slightly between methods. Minor deviations in the microbarom dominated portion of the signal are primarily shown by the grey (stage 2) BC trace, which retains some impulsive components. For the event portion, NN performs relatively poorly on preserving the initial impulses. To indicate the processing combinations in this paper, where only stage 2 is performed, we use the relevant acronym, and if stage 3 is also performed, we use "+ NMF" as a suffix.

As it is not possible to know exactly what this event looks like noise-free, it is challenging to say which of the signal separation methods shown in Figure 4a are best at preserving the original waveform from this illustration alone. As noted in the section introduction, the noisy/original data beam in Figure 4b cannot be used as an indicator of the true signal, given that the microbaroms remain after beamforming. For the beam effective velocity and backazimuth, we use mean values from array processing results (section 3.4) during the eruption (333 m/s and 347°). This backazimuth differs from the true direction (352°), likely due to deflection of the arrivals by crosswinds. Such deviations from true are common for many Bogoslof explosions, at OKIF, as well as at the other arrays. Figure 4b

does illustrate, however, that wind noise is reduced by beamforming without any additional denoising steps, but much more so when beamforming denoised traces. In section 5, however, for a more impulsive and discrete Bogoslof explosion, we use metrics such as cross-correlation, phase changes, and the signal to distortion ratio to more systematically measure waveform alteration under different noise conditions.
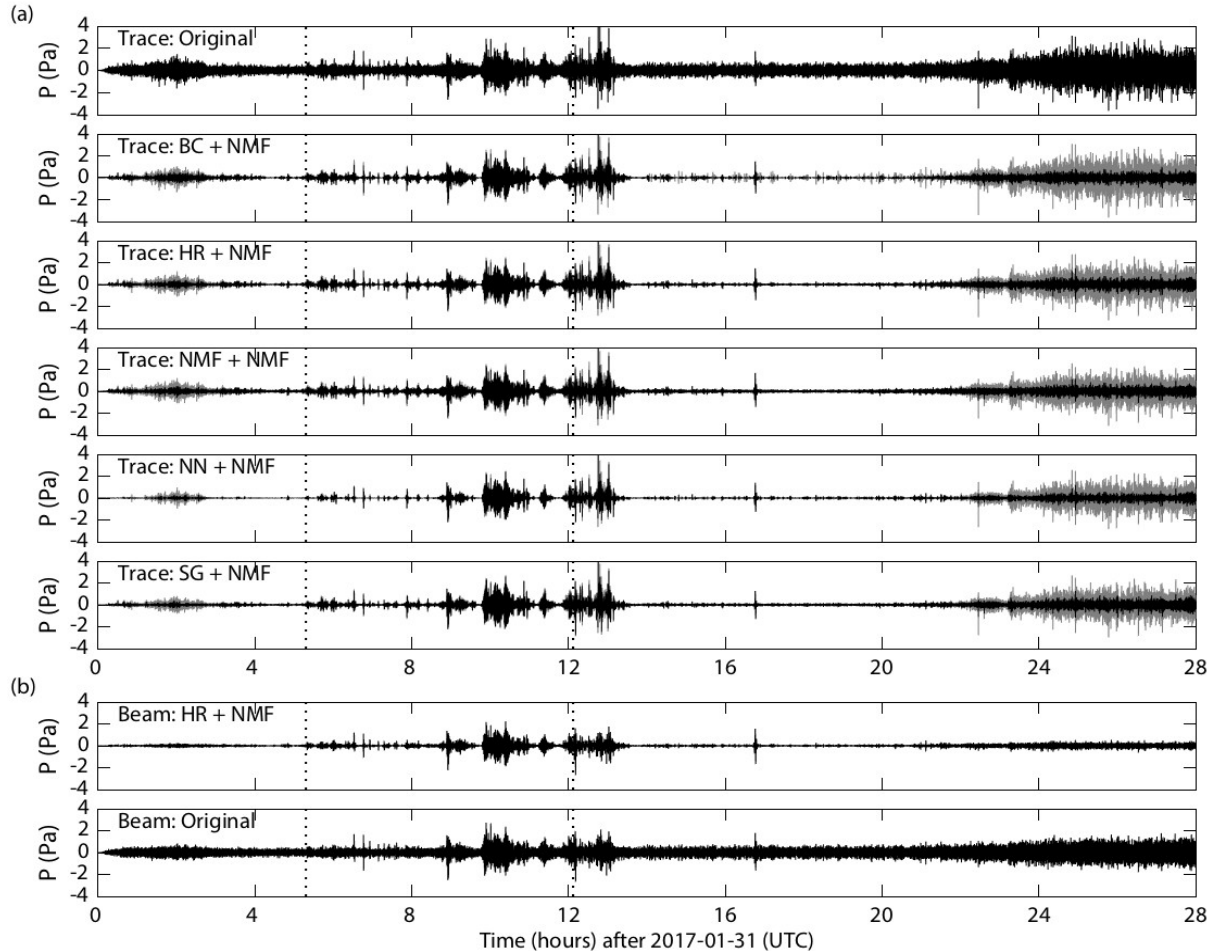
Figure 4. (a) Comparing first order differences between the original non-separated waveform (top), and each signal separation method (stage 1 = grey, and stage 2 = black, P = pressure). Data are from the 31 January 2017 Bogoslof eruption, recorded at OKIF (channel 1). Dotted lines mark the duration of the infrasound from the event in the AVO catalogue (travel time corrected). The mean stage 2 SNR is 18.6 dB after denoising and 6 dB beforehand, representing a 310% increase in SNR. This calculation uses the marked microbarom period in Fig. 3 as a noise estimate, and the event section from 09:45-10:30 for the signal component. (b) Array beams for noisy traces, and for denoised (HR + NMF) traces. To a first order, resulting waveforms after stage 2, or stage 3, are similar between methods. Denoised beams have higher SNR than original beams during the non-windy parts as microbaroms do not destructively interfere.

Another useful processing evaluation metric is comparing the power spectral density (PSD) of each segment of the labeled data section at each stage of the processing. By doing this, we are able to establish whether signal separation is occurring as intended under different conditions. For example, Figure 5 compares PSDs for two of the stage 2 and 3 combinations from Figure 4, where we choose two widely contrasting examples for illustration. For the microbarom labeled time section (Figures 5a and 5d), both methods similarly reduce the microbarom peak from their original levels (stage 1, blue trace) to those in the stage 2 foreground (purple), when compared at ~0.2 Hz. This is by design to keep the methods generally comparable. However, the shape of the resulting spectra is quite different, with the sharper NN peak demonstrating higher attenuation away from the center. Further, after applying NMF in stage 3, Figure 5a shows a frequency split in the peak of the residual microbarom between the foregrounds (green) and background (yellow), whereas those in Figure 5d are more similar. During the wind segment (Figures 5b and 5e), many profiles are similar, with differences resulting from the initial stage 2 separation. Here BC has a relatively sharp stage 2 background peak (red) compared to NN, meaning that the original wind noise (blue) is relatively unaltered in the stage 2 foreground (purple), except around 0.2 Hz. An ideal case is consistent removal of the microbarom (and other persistent sources) through the trace, which neither method does a good job of here. In terms of the event portion we see that after stage 2, the BC background (Figure 5c, red) has the desired shape (i.e., like that in Figure 5a), indicating that the foreground (purple) has been adjusted appropriately. In contrast, for NN (Figure 5f), overcompensation has occurred due to the broader profile microbarom extracted (red), particularly at frequencies < 0.1 Hz. Despite having removed most of the microbarom in stage 2, stage 3 inadvertently reduces the microbarom further, particularly in Figure 5c. To a first-order for this event, the BC, HR, and
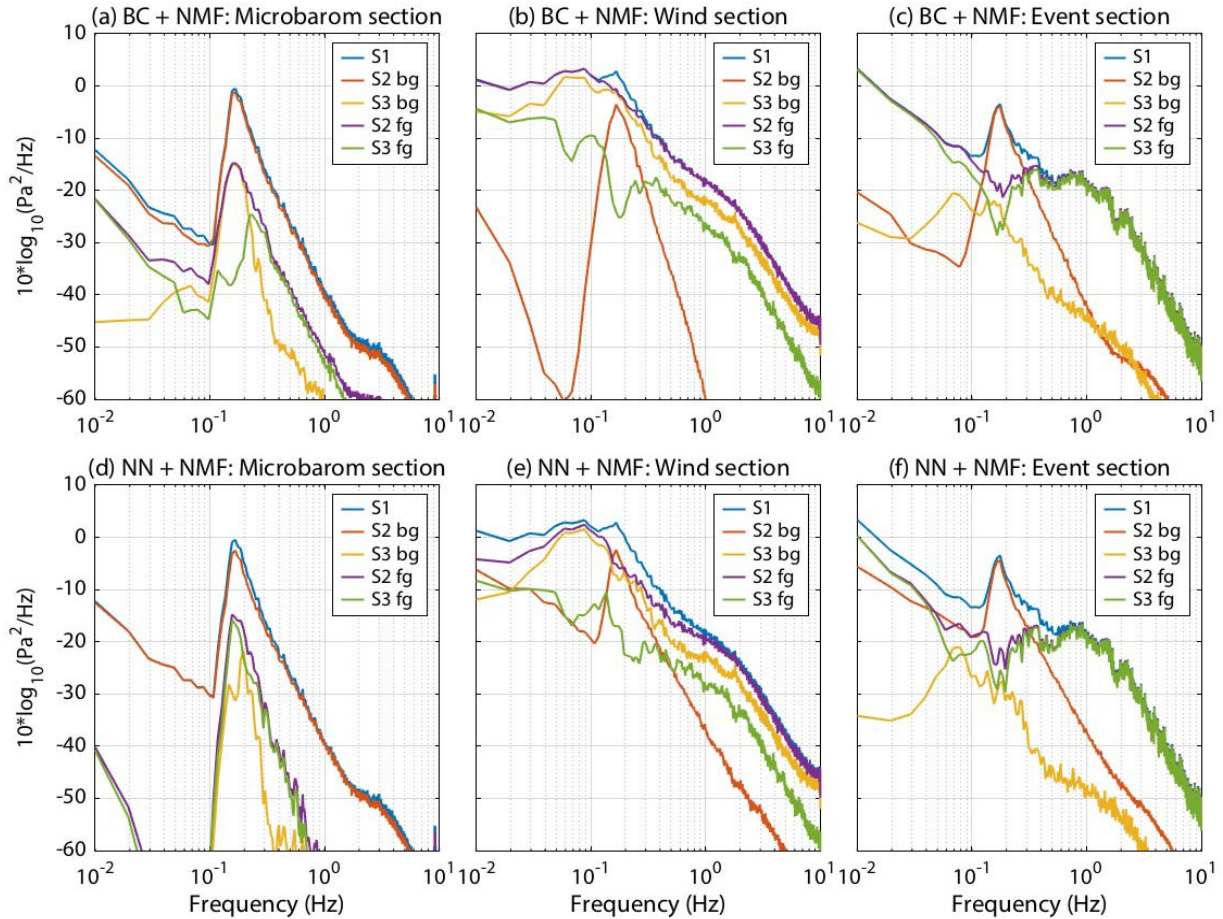
Figure 5. Examples of contrasting Power Spectral Density (PSD) estimates for labelled data segments at each processing stage (S). Fg and bg refer to the foreground and background respectively. Even though denoised traces using different methods may appear similar to a first order (Fig. 4), there may be subtler, but important differences in the frequency domain. Here we see for instance that microbarom removal in stage 2 is not evenly removed in different parts of the traces, and also that residual microbaroms may be re-split during stage 3. (a–c) PSDs for BC in stage 2, and NMF in stage 3. (d–f) PSDs for NN in stage 2, and NMF in stage 3.

NMF methods have similar PSDs, with NN contrasting the most to these, and SG sharing

characteristics of these endmembers. For other events and parameter combinations, however,

results can vary. PSD analysis showed minimal differences between performing a single

NMF operation to simultaneously separate microbaroms, wind noise, and events, and the

two-step NMF + NMF approach described thus far. For consistency and ease of comparison

with the other stage 2 approaches, we retain use of the two-step process.

3.4. Array Processing

For array processing, we use the progressive multi-channel correlation software, PMCC (Cansi, 1995; Le Pichon et al., 2010). PMCC searches in time-frequency space for coherent plane-wave arrivals that have similar wavefield parameters on multiple three element subarrays. As the three element combinations are of varying size, the array is sensitive to a wide range of frequencies, which reduces spatial aliasing. Where four element arrays such as OKIF have four subarrays and an aperture of ~100 m, the eight-element array, IS53, has 56 subarrays, and an aperture of ~2 km. PMCC groups detections of similar arrivals into families, for which the corresponding time-frequency blocks are called pixels. Output wavefield parameters from the processing include backazimuth, apparent velocity, mean frequency, and maximum amplitude (~waveform peak to peak). PMCC configuration parameters are supplied in the supplemental material, which includes a threshold to only detect acoustic arrivals (apparent velocities 250–500 m/s). Trace denoising occurs prior to running PMCC.

AVO infrasound array processing for the Bogoslof eruption was performed using a least-squares beamforming algorithm (Olson and Szuberla, 2005) incorporating the mean of the cross-correlation maximum (MCCM; e.g., Haney et al., 2018; Lyons et al., 2020) as a detection metric. Declaration of a detection is based on specific thresholds which cannot be directly reproduced with PMCC. As mentioned in section 2, use of variable parameters over time have led to slightly different published catalogs on the Bogoslof eruption (e.g., Coombs et al., 2019; Lyons et al., 2020). As we show in section 4, given the range of acoustic sources around Alaska and often great source-receiver distances, it is possible that some detections are coincidental rather than eruption related, and equally that some eruptions can be hidden.

3.5. Backprojection

Backprojection, also known as RTM, describes a delay and stack grid search approach for locating events. For each trial source location on a grid, appropriate sections of waveform envelopes from the surrounding stations are extracted according to a velocity model, then aligned and stacked. To take some account of the different atmospheric paths, our simple backprojection scheme performs the spatial grid search for a range of fixed celerities (range/time, 250–350 m/s), and then retains the highest amplitude from all stacks at each time step to form a detector function (DF). The grid node which gives the highest amplitude in the DF is typically assumed to be the event source. Details of the basic data preprocessing, detection, and location methodologies can be found in Sanderson et al. (2020a), from which we use the "time-summed-DF" approach. This involves applying a running summation window to each stack before the DF is calculated. This tends to improve location accuracy and event classification rates, at the expense of event detection sensitivity.

For regional source location, backprojection of direct infrasound is an uncommonly applied tool when compared to backazimuth-yielding methods. In part this is due to the rarity until recently of sufficiently dense infrasound networks with single stations, such as the TA. Backprojection using arrays is also possible however (e.g., Shani-Kadmiel et al., 2018). Air-to-ground coupling recorded on seismometers has also been used as a proxy for infrasound in backprojection schemes (e.g., Walker et al., 2010).

For RTM, we will address two topics. Firstly, whether denoising traces prior to stacking ("pre-stack") is beneficial to event detection and location. Secondly, we will compare linear stacking to three advanced stacking techniques from seismology, namely: (1) phase-weighted stacking (PWS; Schimmel and Paulssen, 1997), (2) robust stacking (Pavlis and Vernon, 2010), and (3) selective stacking (Yang et al., 2020). We refer to these methods

as "co-stack" signal enhancement strategies. Each of these methods, though differing in implementation, ultimately penalize traces that do not share common waveform elements, and thus noise is reduced. We explored some further stacking-based methods such as pure-state filtering (e.g., Samson and Olson, 1981), auto-covariance filtering (Nakata et al., 2015), and a technique using singular value decomposition-based Wiener filters (Moreau et al., 2017). The computational time for these approaches, however, was not balanced by the performance level for the Bogoslof data set. Nth-root stacking, semblance, and F-statistic function stacking were previously found to not be advantageous vs. linear stacking for Bogoslof data (Sanderson et al., 2020a).

Data is processed in the same way as for array processing, i.e., the workflow in Figure 2. For each trace, we label event sections according to catalog onsets and expected delay times to each station, based upon a mean celerity derived from record section inspection. These steps keep with the intention of focusing on the degree to which trace-based denoising improves RTM results, rather than incorporating an automated feature classification scheme. Sample microbarom and wind noise sections are picked manually.

4. Results

To illustrate some of the capabilities of the denoising processes, we use both array processing and RTM detection and location approaches. We focus on the 15 January, 31 January, and 8 March 2017 Bogoslof eruptions, as well as on a longer period covering a series of explosions.

4.1. Array Processing

In Figure 6 we show PMCC processing results for the 31 January event, and compare the results of the original (noisy) data, and denoised data using BC + NMF.

Figure 6a shows 24 hours of beamed data from OKIF and a summary of PMCC detections, plotted as backazimuth vs. time vs. frequency. In the original data, the microbarom presents as largely continuous detections to the southeast. The BC processing removes the large majority of the microbarom detections, particularly the earlier section which had a slightly lower amplitude than the reference section (Figure 3). Scaling plotted microbarom detections by amplitude would reduce the clutter further. Another persistent signal migrates from ~67° to ~62° over the course of the day (the ~5–8 Hz detections in Figure 6a). High-frequency arrivals often point to anthropogenic sources. However, at OKIF, the microbarom packets typically grade to higher frequencies away from the azimuthal center, with these marginal detections having lower quality detection statistics. Consequently, this is likely an artifact due to non-optimal processing parameters for the array geometry. Post-processing thresholds can filter these lower quality detections. Other arrays variously show fewer or no such anomalies.

Figure 6b shows a close-up of only those detections likely associated with the eruption. The denoised data has more PMCC detections, as well as lowering the minimum frequency range of those detections into that previously occupied by the microbarom. The mean frequency of the families is also lower as a consequence. It should be noted that the corner frequency of the OKIF instruments was 0.1 Hz, limiting correct representation of < 0.1 Hz arrivals despite deconvolution of the instrument response. The azimuthal distribution of the denoised arrivals are slightly more dispersed than in the original data, potentially due to distortion during processing rather than reflecting improved accuracy. Notable features from results for the other methods include NN + NMF further extending the detection frequency range (at times to 0.01 Hz), whereas NMF + NMF doesn't appear to affect the frequency range.

126
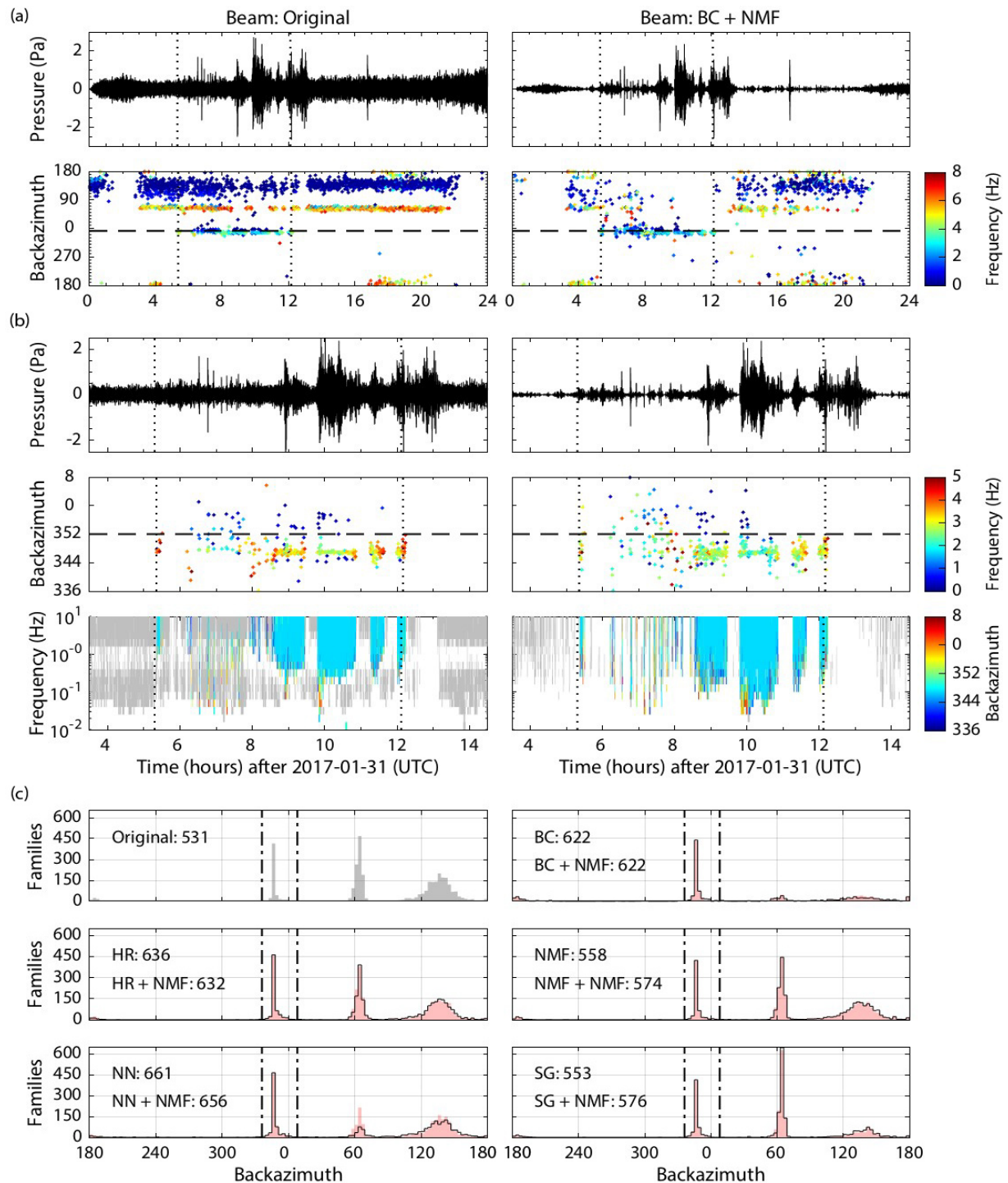
Figure 6. PMCC processing results for the 31 January 2017 Bogoslof eruption, for noisy (left) and BC + NMF denoised data (right), recorded at OKIF. Denoising methods generally increase the number of event detections, and reduce both microbarom detections and microbarom amplitude. (a) 24-hour view of results. Beams are aligned according to the means of the backazimuths and velocities from PMCC detections within ±16° of true (352°). Each point on the backazimuth vs. time plot represents a PMCC family color-coded by mean frequency. Vertical dotted lines demark the catalogued infrasound period (travel time corrected). The horizontal dashed line indicates the true backazimuth. (b) Close-up view of the eruption period. In the frequency vs. time plots, pixels are color-coded by frequency if the detections are ±16° of true. Pixels from

other azimuths are grey, and white means no pixels. (c) Histograms showing OKIF PMCC detection statistics for the 31 January 2017 Bogoslof eruption for each denoising method combination (stage 2 shaded, stage 3 outlined). The first peak is for the eruption, the second peak is likely due to a processing artefact, and the third peak is for microbaroms. Vertical dashed lines demark ±16° limits around the true backazimuth to Bogoslof from OKIF, which are used to calculate frequency totals provided in the subplot titles, and as per Fig. 6(b). Values shown are the number of families detected within ±16° of true.

The summary of the PMCC results for the different denoising techniques in Figure 6c shows some significant variation in terms of detection of the different activity. As noted for Figure 6a, BC effectively removes much of the microbarom (as does SG) and related artifacts (which SG preserves). For the other methods, the number of microbaroms detected is not greatly reduced, even though the amplitude of the microbaroms are. As the PMCC threshold parameters do not include amplitude, the lack of microbaroms detections for BC and SG indicate that such arrivals are not simply made sufficiently small, but rather the waveforms are made incoherent via denoising. Compared to the results for the noisy data, all denoising methods increase the numbers of families for the eruption. NN increases eruption detections the most, by ~24.5% vs. the original data.

In Figure 6a, gaps occurring in the microbarom align with increases in wind noise. We find that if stage 3 is performed without stage 2, there is a minimal (4%) uptick in detected microbaroms. This is an important result as it suggests limited value for array processing by removing wind noise in this way, i.e., few new detections will be found. The picture is more complex when combining stage 2 and 3, however, with microbarom families decreasing by an additional 20% during stage 3 for BC + NMF, for example, and increasing by 7% for SG + NMF (Figure 6c). Equally Figure 6c shows some minor (< 5%) variation for event detections between stage 2 and 3.

To assess denoising performance on event location using multiple arrays, we apply an automated cross-bearings approach with the IMS-vASC algorithm (Matoza et al., 2017). IMS-vASC uses a grid search to tally the number of intersecting backazimuths over time.

There are two output layers which we use here. Firstly, the during layer, which is the map of total intersecting pixels for the day of the event in question. Secondly, the cleaned layer, which retains only those areas of the during layer that have a specific ratio (here, > 1.5) when compared to the average pixel counts in those areas for the days preceding the eruption. The idea of the cleaned layer is to remove persistent background sources like microbaroms, thereby retaining prominent transient events. In Figure 7, we compare two events using original and BC-denoised data. BC provides a compromise between strong microbarom reduction and moderate increases in event detection (Figure 6). The 31 January event uses two prior days for the cleaned grid calculation, and the 8 March event uses one prior day. These short prior durations are not ideal to provide background averages, but are constrained by the rapid movement of the dominant microbarom sources. During these prior periods, gaps in array detections are common due to wind noise. Consequently, the estimates of the background noise sources are not particularly robust here. As the prior days do not contain any events, it is not possible to apply stage 3 processing to the data, and so this step isn't applied to the during-layer results either.

For the 31 January event (Figures 7a–7f), all five AVO arrays have clear PMCC detections, with OKIF detecting the most (Figure 6). Consequently, the event location is constrained accurately, but a nearby microbarom source dominates the mapped results for the unprocessed data in the during layer (Figure 7a), as well as the cleaned layer (Figure 7b). As the event and microbarom do not share a common backazimuth at any of the arrays, separating these sources in backazimuth-frequency space is straightforward (Figure 7c). For the BC data, however, the microbarom is much reduced for the during layer (Figure 7d), and further still in the cleaned layer (Figure 7e). Now the Bogoslof eruption is the only
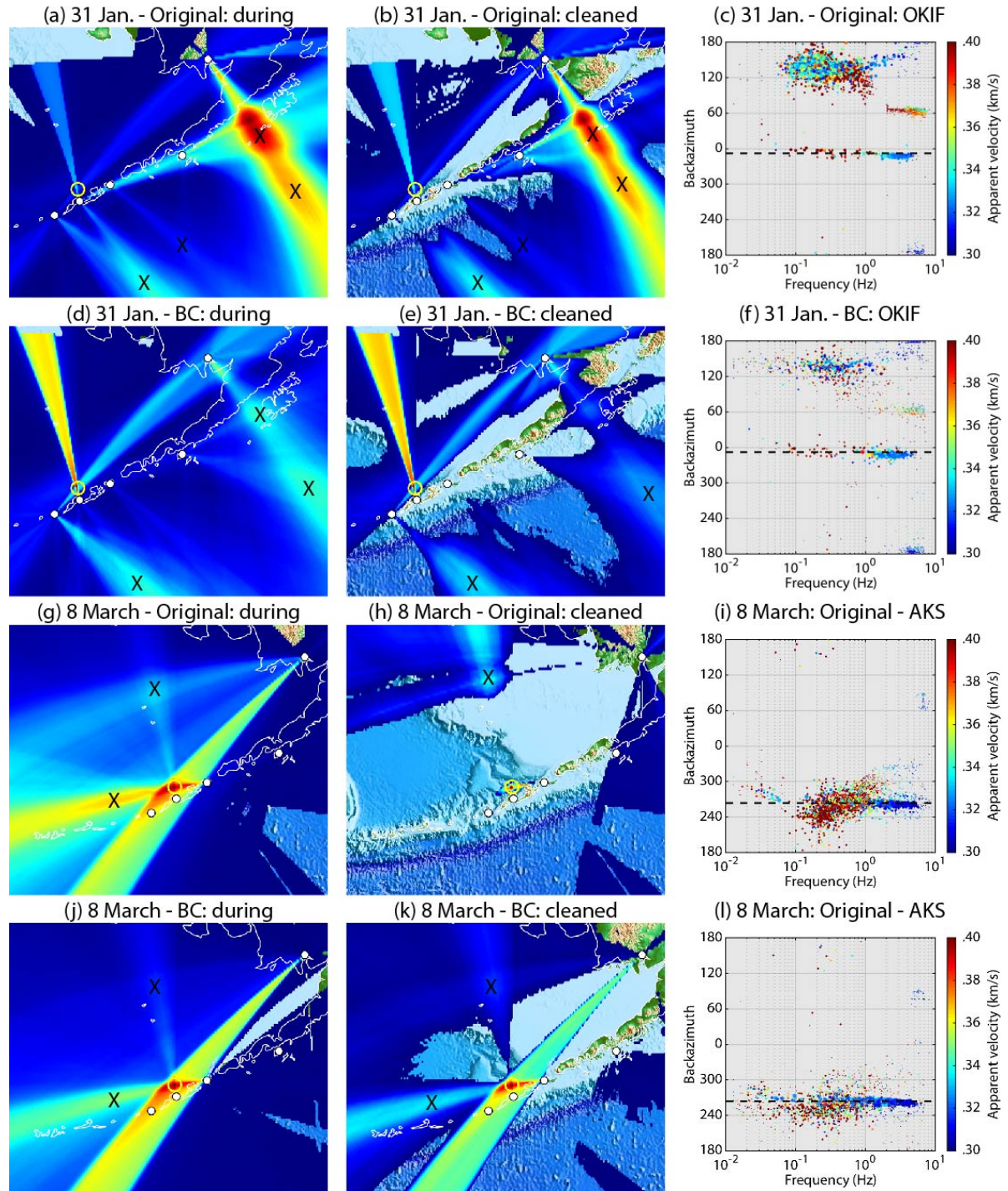
Figure 7. Mapping array cross-bearings using IMS-vASC. Reducing microbarom clutter can help isolate events of interest. This reduction can be done via data denoising and/or removing longer-term background average cross-bearing values. (a) During-grid layer, for the 31 January 2017 Bogoslof event, using unprocessed (noisy) data. Warmer colours indicate higher numbers of overlapping backazimuths, normalized for each plot. Infrasound arrays are marked with white circles, historically active volcanoes as red triangles, with Bogoslof enclosed by a yellow ring. Xs mark source areas of microbaroms. The grid resolution is 0.1°. (b) Cleaned-grid layer for data in (a). (c) Amplitude-scaled scatter plot of the frequency and backazimuth for each detection at OKIF (the true backazimuth is marked with a dashed line). (d-f) As for (a-c), but using BC processed data. (g-l) As for (a-f), but for the 8 March 2017 Bogoslof event. Data in (l) are from AKS.

prominent source. This provides an example where the denoising process provides an improvement over layer cleaning, useful in cases where there is limited prior data. Results for the noisy data can be improved significantly if the minimum number of pixels to count a station in intersection is set to 100 instead of 10 (as used in Figure 7), while also requiring each station to contribute. Detections by all five arrays is a rare occurrence however, and so such a constrained strategy cannot generally be relied upon. As crosswinds variously deviate arrivals from their true backazimuth, we use a 5° tolerance. For reference, Coombs et al. (2019) report only OKIF and SDPI detecting this event, whereas Lyons et al. (2020) list AKS, CLCO, and OKIF.

For the 8 March event (Figure 7g–l), only three AVO arrays have clear PMCC detections (AKS, DLL, OKIF). SDPI has some detections coincident with Bogoslof during the event window, but these are removed during denoising, so it's uncertain from this analysis alone whether these arrivals are event related. As the primary microbarom source in this example shares a backazimuth with Bogoslof for most arrays, there is typically an overlap in backazimuths between event and microbarom detections. Coupled with less detecting arrays, the source location is less precise (e.g., Figure 7g vs. 7a). Following layer cleaning, the noisy data provides a narrowed-down source location (Figure 7h). The scatter plot in Figure 7i shows the backazimuth overlap for the microbarom and event at the AKS array. For the BC data, the microbarom source in the during layer is slightly reduced (Figure 7j), but otherwise there is not a great change apparent. For the cleaned layer however (Figure 7k), there is only a modest reduction in background elements. This implies that many areas from the during layer had ratios > 1.5 compared to the prior layer for the BC data. Incidentally, if the ratio is changed from 1.5 to 3, then no event is detected at Bogoslof for the noisy-data clean layer, but still is for BC, suggesting the denoised data is a more robust

result. This is also reflected by limiting the during period to the event itself, rather than the whole day, where for the denoised data, the maximum overlapping pixel count around Bogoslof is ~8% higher than without denoising (when comparing cleaned layers). In terms of backazimuth vs. frequency, the event is clearer following denoising, and with an extended lower frequency range (Figures 7i and 7l). For this event Coombs et al. (2019) note the same detecting arrays as above (including SDPI), while Lyons et al. (2020) list AKS and OKIF.

A longer-term example using DLL array data illustrates some of the benefits of denoising more explicitly. Figure 8 shows how several Bogoslof eruptions become much clearer in the array processing results once microbaroms are reduced. This example uses microbarom removal processing only, without any explicit wind noise reduction. Three of the eruptions in Figure 8, one on 14 December 2016, and two on 12 January, did not meet the published cataloguing criteria for infrasound detection (Coombs et al., 2019; Lyons et al., 2020). The first two of these events are detectable using PMCC, however, with less confidence for the third. Some eruptions, however, become less detectable with processing, such as on 16 and 29 December. In terms of the methods compared in Figure 8, SG shows the events most clearly by reducing the number of detections as well as amplitude. BC also reduces detection numbers, but those have less diminished amplitudes. This is due to BC leaving residual microbarom spikes in the foreground, despite having similar time-average PSD peak values as the other methods. Although using NMF in stage 3 would reduce these spikes (Figure 3), it's not possible to apply stage 3 consistently to those days where events didn't occur (~40% of Figure 8). Notably, a group of detections at ~18:22 15 December has a backazimuth similar to that of an eruption on the day prior. The SDPI array also detected these arrivals ~25 minutes earlier, with a backazimuth also coincident with Bogoslof. This time delay is reasonable if Bogoslof was the source. Nearer arrays to Bogoslof such as OKIF

and AKS (Figure 1) do not show corresponding detections, although shadow zones with high

transmission loss in the 300 km around Bogoslof were typical of the time (Schwaiger et al.,

2020). There is, however, no other known evidence that this was an eruption.
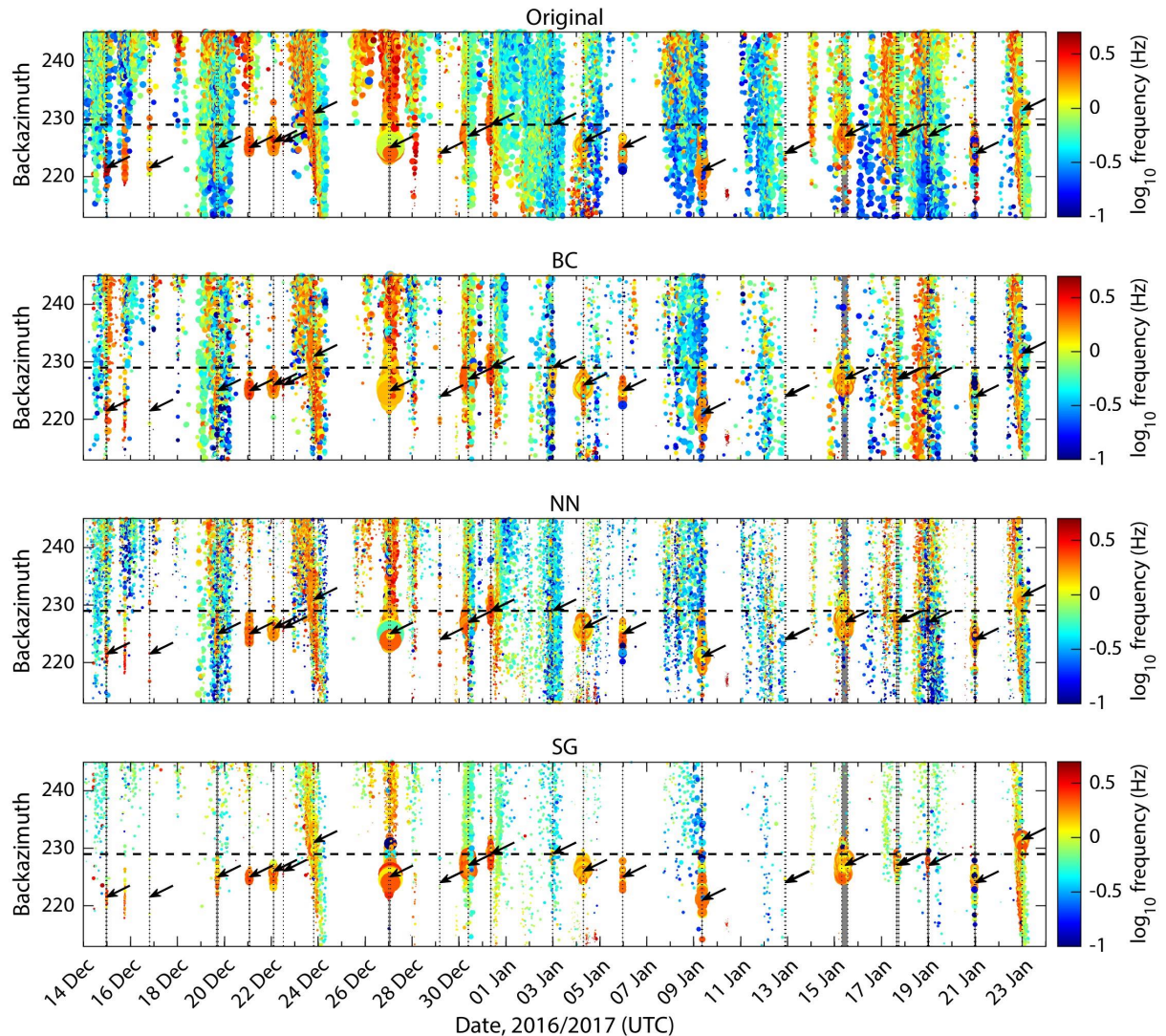
Figure 8. PMCC processing results for the period of 14 December 2016 to 24 January 2017, for noisy, BC, NN, and SG denoised data, recorded at DLL. Detections are scaled by amplitude, and coloured by frequency on a log axis to help distinguish events from the microbarom. A minimum threshold of 50 pixels per family ensure only high-quality detections are displayed. Some small detections may not be visible at the figure resolution. AVO catalogued eruption periods are shaded by vertical grey bars and bound by dashed lines, using a mean stratospheric celerity of 300 m/s to calculate travel times. In this specific case, eruption end times are taken as the latest recorded seismicity, infrasound, or lightning occurrence. Clusters of detections likely associated with these catalogued events are marked with arrows. The arrow positions are the same for all panels despite small variations in backazimuths. Other plot details as per Fig. 6. The microbarom is generally much reduced in the denoised data in terms of detections and amplitude, allowing catalogued and potentially uncatalogued eruptions to be seen more easily (highlighted with arrows).

4.2. Backprojection

We now turn our attention to backprojection, and whether removing the microbarom and wind noise elements from traces can improve detection and location capabilities. We focus on the 15 January 2017 eruption due to its complex nature with four main pulses, and traces typically having poor signal to noise ratios, with clear waveforms only at AV.MSW (located 82 km east of Bogoslof) and DLL. This event was entirely submarine, indicated by the relatively low mean frequency content compared to that of 31 January (Fee et al., 2020).

For the base denoising method, we choose the SG approach as it one of the fastest to compute (section 5.1). As each technique produces similar envelopes to a first-order (Figure 4), we anticipate that the following results are representative of the other systems. We also assess the effects of changing the lower frequency limit from 0.01 Hz, to 0.1 Hz, 0.2 Hz, and 0.35 Hz. For this event, we focus on discussing results from the linear and robust stacking methods, as PWS and selective stacking performed relatively poorly regardless of several parameter and processing combinations. For other events, relative performance may differ (Sanderson et al., 2020b).

Generally, we find that denoising helps improve the SNR of the 15 January event (Figure 9). Removing the microbarom only provides a modest improvement (results not shown), whereas incorporating wind noise removal provides a more noticeable effect. For this latter case, denoising tends to become less impactful as the lower frequency limit increases, indicating that high-pass filtering out wind noise components has a net benefit in this case despite removal of some of the event elements. We also tend to find a greater SNR improvement from high-pass filtering (i.e., 0.01 Hz noisy vs. 0.35 Hz noisy), than by denoising (0.01 Hz noisy vs. 0.01 Hz denoised), as Figure 9 illustrates.
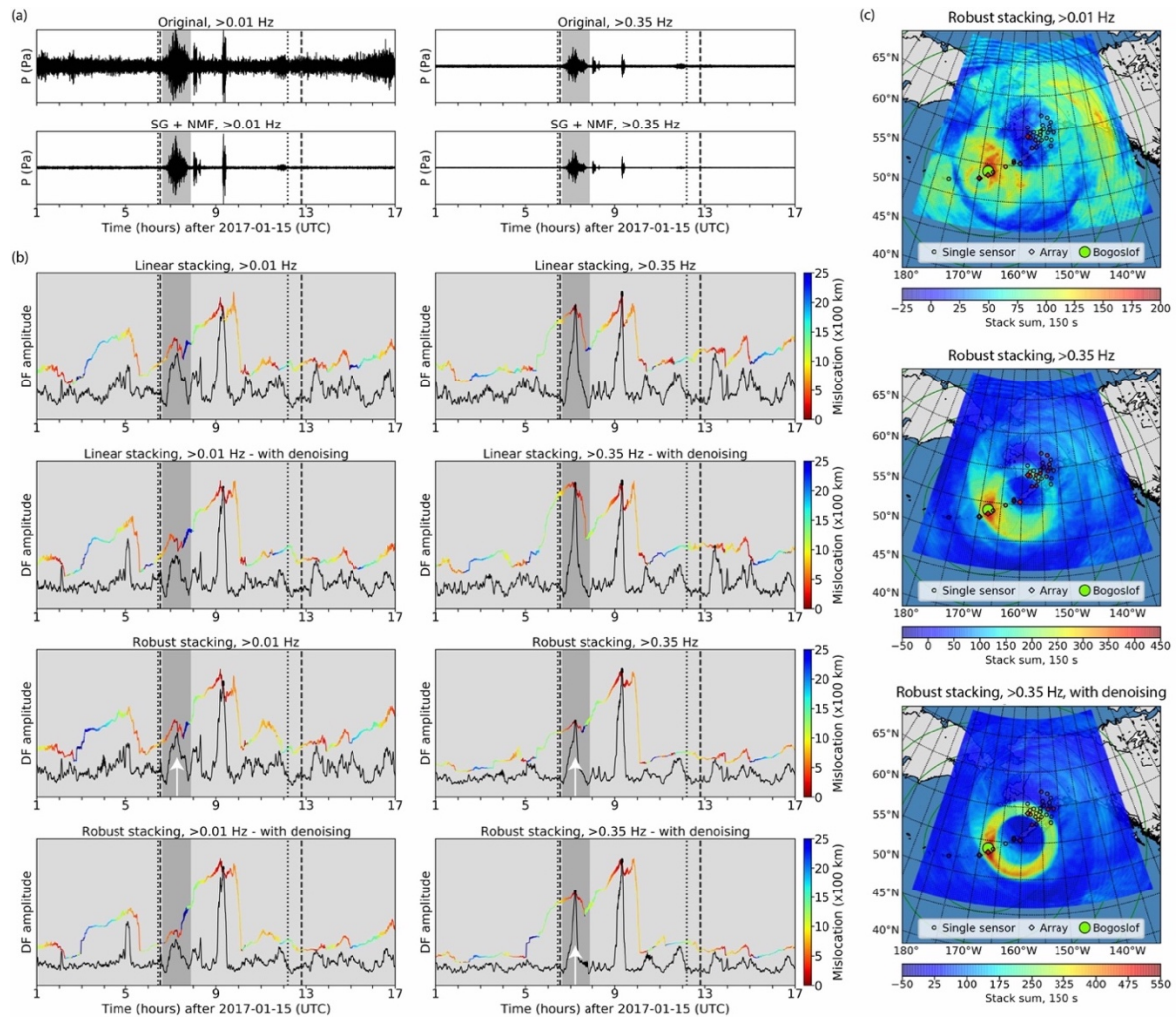
Figure 9. Examples of the effects of stacking, denoising, and filtering, using Bogoslof event on 15 January 2017. Although denoising slightly improves SNR, high-pass filtering has more of an effect. (a) Beams for DLL, with differing high-pass filters. Each panel is scaled ± 1.5 Pa. The vertical dotted lines demark infrasound activity based on PMCC analysis. Vertical dashed lines demark seismic activity in the AVO catalogue, and the grey shaded area spans the catalogued infrasound activity. Infrasound travel times have been corrected for using a celerity of 320 m/s. (b) DFs (coloured lines) all using AGC1. Black lines are stacks of traces assuming Bogoslof is the source. Mislocation is the distance of the corresponding grid node from Bogoslof. Intersections of the Bogoslof stack and DF imply those parts of the DF represent the true source location. Data are from 37 stations (53 channels) within 1,250 km of Bogoslof. Grid spacing is 0.2° latitude, 0.4° longitude. Arrows indicate the times of the maps in (c). (c) Time slices through stacks at the times of arrows shown in (b). The colour scale represents the amplitude of time-aligned data stacks at each grid location. Sensors are shaded red proportional to stack contribution. Circles are at 500 km spacing.

these assessments are based on overall trends when also evaluating three different RTM

preprocessing strategies, two of which involve different kinds of automatic gain control

(referred to as AGC1, and AGC2; Sanderson et al., 2020a). AGC has the effect of

regularizing signal amplitudes, and so can enhance weak event arrivals, but can also increase weak windy sections instead. Consequently, DF shapes may not directly reflect those of the original waveforms recorded. There are some parameter combinations that go against the general trends, such as AGC2 performing best when the lower frequency limit is 0.1 Hz. AGC2 is also the only method that resolves the second event pulse, although the overall SNR is poorer than the examples in Figure 9.

Evaluating the sharpness of the DF peaks is also important, as location estimates are performed on the samples making up the tops of each peak. If the samples happen to represent grid nodes far from the source, then the mislocation value (source distance error) will be high. In this respect, the ≥ 0.35 Hz results are better than those for ≥ 0.01 Hz data, and with mixed results for the noisy vs. denoised data. Location accuracy and peak sharpness is also affected by the azimuthal coverage of detecting stations. Map slices of the stack results in Figure 9c show the distribution of the stations within a 1,250 km radius around Bogoslof, which are biased to the east. Only a subset of these stations contributes positively to the stacks, as indicated by the shading of each station (fewer arrivals occur beyond 1,250 km). These map slices correspond to the first pulse in the eruption, marked by arrows in Figure 9b. This pulse varies in amplitude and shape between parameter configurations, similarly reflected in map form. The smallest and least prominent pulse does locate in the Bogoslof area, but the energy is more distributed than the other cases. For the noisy vs. denoised maps at ≥ 0.35 Hz, the former case is less sharp overall, but there is less smearing of the highest values. Ring features in these maps indicate a dominant impact by the SDPI array at the center of the ring.

Our evaluation of the 15 January event suggests that the eruption onset occurred 13 minutes prior to that listed in the catalog, i.e., at 06:27, rather than 06:40 This stems from

aligning SG-denoised DLL infrasound waveforms and PMCC results with travel-time corrected seismic data (Figure 10). The seismic stations, AV.OKER and AV.MAPS are ~55 km southwest, and ~75 km southeast of Bogoslof respectively. Although the catalog eruption start time is based on multiple types of data, this time matches that given by the catalog infrasound origin, which itself assumes a 340 m/s celerity (used for all events).
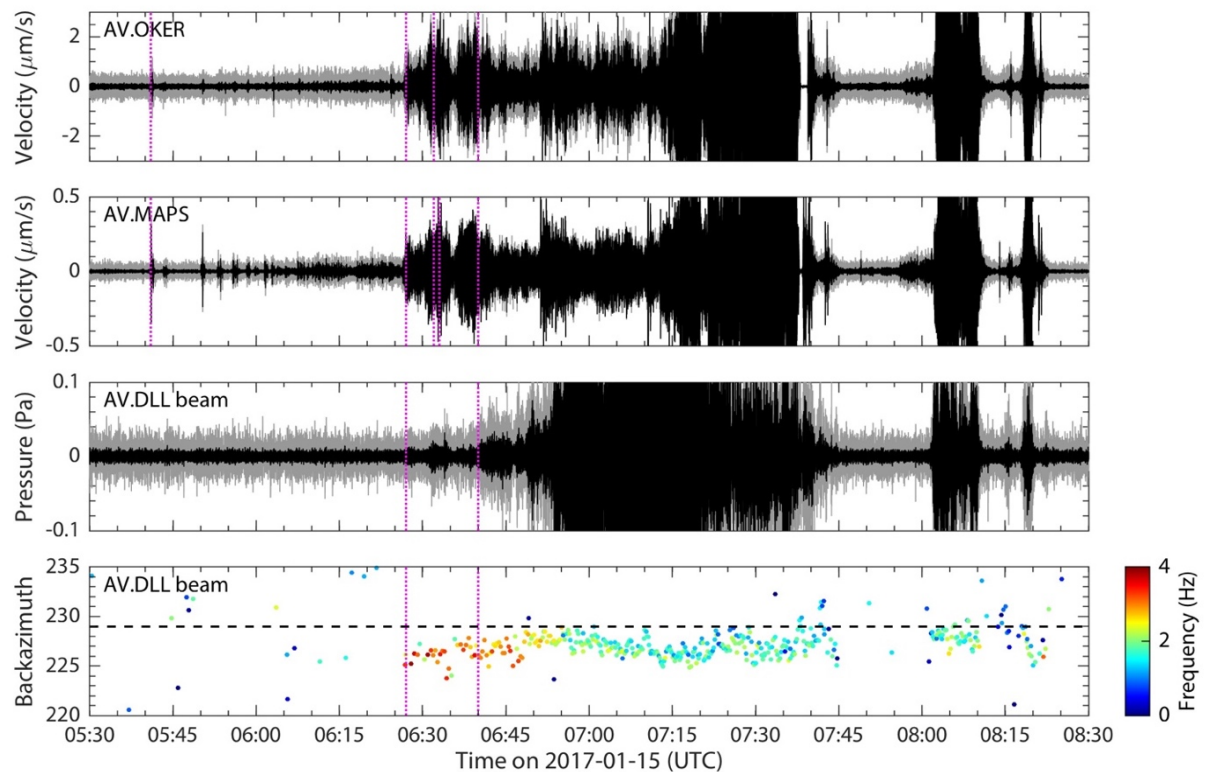
Figure 10. Comparing indicators of the eruption onset for the 15 January Bogoslof event using seismic data from AV.OKER and AV.MAPS (1–20 Hz waveforms), and infrasound data from AV.DLL (>0.35 Hz waveforms, and PMCC results). Data have been travel-time corrected, and clipped to emphases smaller features. For waveforms, grey traces are instrument corrected and filtered, with black traces the SG-denoised versions. Denoising helps show waveform features previously buried in background noise, as well as reducing microbarom presence in the PMCC results. Vertical dotted magenta lines indicate the following, and which include some conflicts: 1) 05:41: precursory seismic swarm onset (Tepp and Haney, 2019); 2) 06:27: explosion seismic onset at AV.OKER (Searcy and Power, 2020), with our analysis of the corresponding onset at AV.MAPS, and our estimate of the explosions and infrasound onset; 3) 06:32: end of precursory seismic swarm (Tepp and Haney, 2019), and catalogued explosion seismic onset (Coombs *et al.*, 2019); 4) 06:33: explosion seismic onset at AV.MAPS (Searcy and Power, 2020); 5) 06:40: catalogued onsets for explosion and infrasound (Coombs *et al.*, 2019).

Adjusting this celerity to 320 m/s, a best-fit value from the RTM results, would change the eruption onset by less than three minutes when also assuming a surface travel path, meaning that celerity alone cannot explain the onset time discrepancy. Our suggested revised eruption onset of 06:27 matches the reported explosion seismic onset at AV.OKER of ~06:27 (Searcy and Power, 2020), and slightly prior to that at AV.MAPS of ~06:33. Our assessment of the AV.MAPS data indicates an earlier onset similar to that of AV.OKER (Figure 10). Prior to the eruption, precursory seismicity occurs (from 05:41), with discrete events merging intro low amplitude tremor. Tepp and Haney (2019) mark the end of this precursory activity at 06:32, the same time used as the eruption seismic onset by Coombs et al. (2019) for the AVO catalog. Thus, there is some uncertainty regarding the transition from precursory to eruptive behavior using the seismicity alone, but integration of the infrasound analyzed here points toward an eruption nearer to 06:27 than 06:40. Separately, as the catalogued infrasound duration is based on OKIF, which didn't record the eruption well, the listed duration is only 76 minutes. At DLL however, PMCC shows the eruption continued until at least 12:11 (accounting for travel time), approaching six hours from the onset (but still prior to the catalogued seismic end time of 12:48). Given the low amplitude of the start and end of the eruption, as well as azimuthally coincident microbaroms, denoising helps with accurately identifying these features in the data.

5. Discussion

Infrasound is becoming an increasingly popular tool for volcano monitoring, at local, regional, and global scales. Microbaroms are largely an inescapable aspect of such recordings (e.g., Matoza et al., 2013; Matoza et al., 2019), and such clutter may inhibit clear detection of eruptions when viewed as waveforms, spectrograms, or in array processing

results. This extends to other events like chemical blasts, where expected frequency spectra for yields of ~0.1–10 kT overlap with the microbarom band (e.g., Green and Bowers, 2010). This is a potential issue for the IMS infrasound network, which is designed with such activity in mind. Wind noise also manifests in infrasound recordings, and may disrupt coherent records of signals of interest, depending on the wind speed. In this paper we present a preliminary investigation of several open source denoising tools and techniques as applied to the Bogoslof shallow-submarine eruption sequence, which produced dominant frequencies that overlapped both wind noise and the microbarom. Although these styles of eruption are uncommon, remote monitoring involves attenuation of higher frequencies with distance, and that such denoising techniques have wide applicability. In the following, we review our main findings, and explore some subtleties which may affect denoising performance.

5.1. Microbarom Clutter

We find that all the stage 2 methods increase the number of PMCC detections associated with eruptions, particularly where the mean family frequency overlaps the microbarom (Figure 6). PMCC results also show that even where the amplitude of the microbarom is reduced to similar levels by the different methods (Figure 4), that there can be along-trace variability during the event and wind sections (Figure 5). Additionally, the microbarom detectability in PMCC can be quite variable. For instance, whereas all methods affect the amplitude of detections, BC and SB perform best in terms of reducing microbarom detections entirely (Figure 6c), allowing events of interest to be more easily distinguished for arrays where the microbarom shares a backazimuth with the volcano (Figure 8). Backazimuth estimates often disperse by a few degrees from the noisy data estimates, but given crosswind advection is typical, it is difficult to establish the relative accuracy. During the nine-month Bogoslof eruption, AKS, DLL, and IS53 were the only arrays with

139

microbarom backazimuth conflicts. With more infrasound stations added since 2017, such conflicts have increased. Incidentally, PMCC does not always resolve similar concurrent signals arriving from different directions. Thus, for large, low frequency events like that of 8 March 2017, the microbarom has the appearance of stopping during the event, and so the event appears relatively clearly in time-series at the aforementioned arrays without any denoising. Our results also highlight several instances where the current AVO catalog for Bogoslof can be improved by: (1) extending the reported infrasound duration of some events, with that of 15 January for example appearing to start ~13 minutes earlier than reported, and lasting several hours longer; (2) increasing the number of arrays that made detections, with e.g., those on 14 December and 12 January detected at DLL despite no catalogued infrasound at any array; (3) potentially detecting additional events (e.g., 15 December), though these currently lack supporting evidence. Section S2 of the supplemental material provides additional examples. Care should be taken with interpretation however, as the array processing of microbarom signals can result in artifacts that may be of similar frequency and backazimuth to eruptions. Such findings and event vs. microbarom vs. artifact discrimination are typically facilitated by denoising processing.

We also find that the denoising methods can sometimes decrease the detectability of events, along with the microbarom, thus potentially negatively impacting any event catalogs and/or duration estimates. Some examples of these events are shown in Figure 8 for SG processed data (16 and 29 December). Although these events may appear dubious as detectable at all given the dispersed backazimuths, there are distinct groups of detections that are separate from the microbarom (centered off figure at ~270°) at the exact travel-time adjusted catalog range. From closer inspection, the SG PMCC results show about 1/3 less detections vs. the unprocessed data for these events, but more notably, the amplitudes are

much smaller. These two events are very weak, and largely indistinguishable from background even after denoising. At least here, the BC approach has an advantage. Similar behavior may occur for traces used during RTM processing. Other stage 2 approaches may also have particular weaknesses, such as those outlined for NN in section 3.2.4. The nature of NN makes it more suitable for situations where events are short and wind is sporadic. Otherwise the untrained nature of the technique makes it challenging to effectively remove only the microbarom in an effective and computationally efficient way.

To assess alteration to denoised signals under different noise conditions, we begin by taking a high SNR Bogoslof signal from OKIF at ~02:38 20 February 2017 as a reference, and bury it in progressively higher amplitude microbaroms, then assess how well that contamination is removed. The microbarom sample is taken from ~06:12 the same day, and scaled between 1 and 100 times its original amplitude. This type of event has its peak frequency in the microbarom range, presenting a strong denoising challenge. The results in Figure 11a are based on comparing the reference and the denoised result during the marked 30 s event section. For methods which require a noise reference, we use a section 15-45 s prior to the event. For SNR calculations, we use a section 15-45 s after the event. For some metrics such as the correlation coefficient, each method performs relatively similarly, with values only dropping below 0.8 where the original SNR was < 2 dB. In terms of maximum amplitude, there is more variety, with most deviations occurring where the original SNR is < 5 dB. In terms of SNR for denoised traces, NMF provides little advantage for this event (unlike that in Figure 4), with NN improving SNR the most. Finally, we present scale-invariant signal-to-distortion ratio (SI-SDR) values (Le Roux et al., 2018), where the distortion is essentially the residual between the original signal and the denoised version.
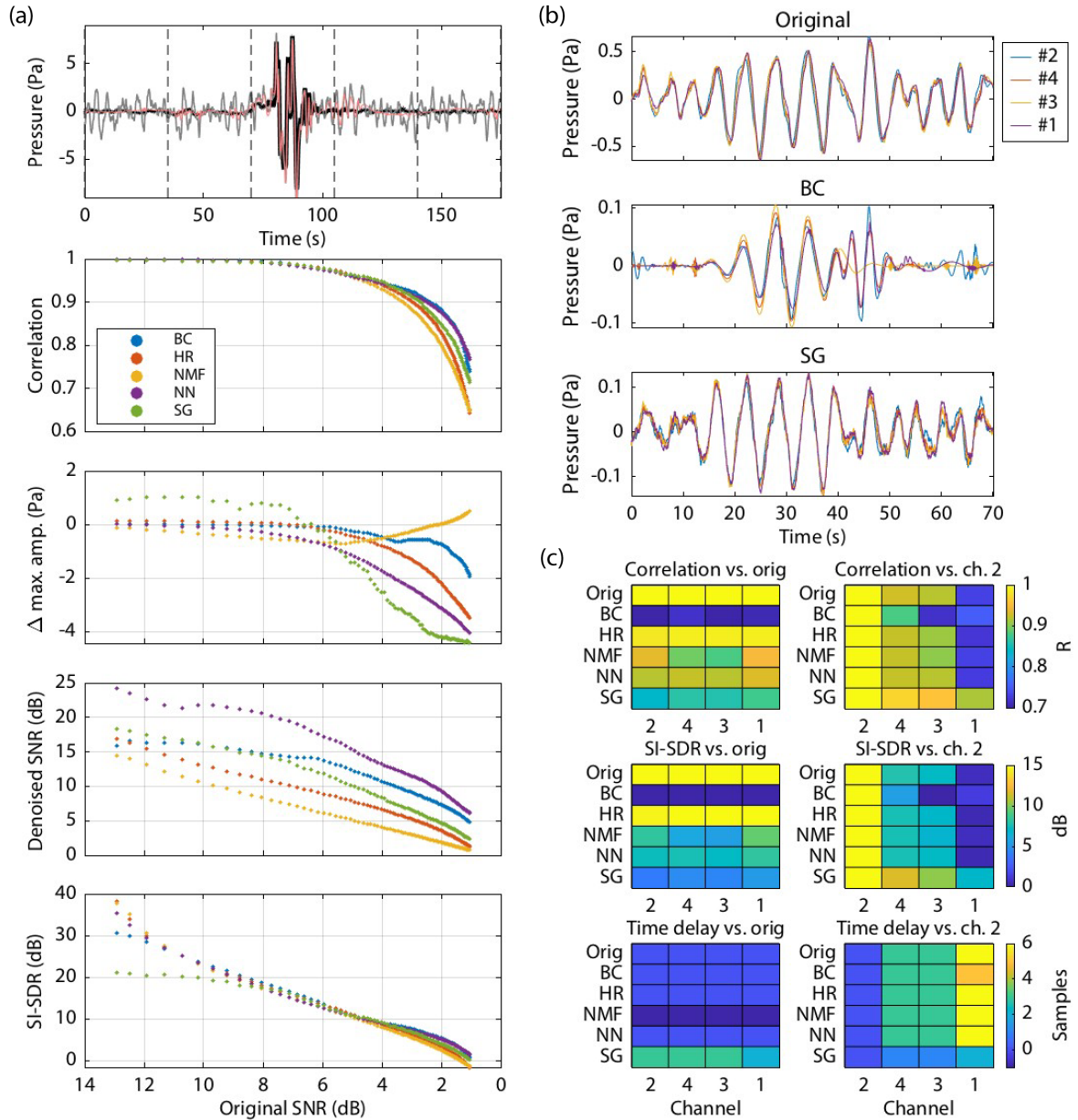
Figure 11. Evaluating the impact of denoising methods, including under different noise conditions. (a) A high SNR Bogoslof event trace from ~02:38 20 February 2017 is contaminated by progressively higher noise levels. Top panel: Example waveform processing for OKIF channel 1: Black trace – high SNR reference waveform; Grey trace – black trace with microbarom added (scaled by a factor of 30), giving an original SNR level of ~4 dB; Red trace – denoised grey trace (using BC). Dashed lines mark periods 0–35 s, 70–105 s, 140–170 s, respectively indicating data sections respectively used for microbarom labelling in denoising methods that require this, the event, and noise used in SNR calculations. Panels 2–5: Correlation coefficient, change in maximum amplitude, SNR of denoised trace, SI-SDR. Generally, denoising performance degrades as added noise increases, but there are wide differences in terms of denoised performance. (b) Example microbarom data prior to, and after denoising using BC and SG methods, showing variable noise reduction and phase changes. Data also from OKIF. (c) Comparing denoised to original data from (b) for each OKIF channel using correlation, SI-SDR, and time delay metrics. The left panels compare each denoised channel to its original counterpart, whereas the right panels compare each channel to channel 2 within the same processing scheme. Channels are arranged left to right by increasing distance from the microbarom source. This data shows that BC and SG methods produce residual microbaroms that will be more difficult to detect due to their more distorted and time-shifted signals.

Here, results are generally similar, except for SG, and are affected by the aforementioned amplitude change. We find that for this short event, particularly at higher noise levels, the denoising can be sensitive to spectral windowing parameters, the amount of data before and after the event, the microbarom section used as an overlay, and how that overlay aligns with the reference waveform. In the supporting material, we repeat the same tests for three synthetic event signals that have similar and dissimilar frequency content to the microbarom. Denoising performance is enhanced in the latter case, particularly at lower initial SNR.

To get an initial insight into why the BC and SG approaches reduce microbarom clutter to a much higher degree compared to HR, NMF, and NN (Figure 6), we examine the distortion of the microbarom in the stage 2 foreground (Figures 11b and 11c). This is relevant as simply reducing the amplitude of the microbarom will not significantly change the number of detections. There appear to be three primary factors: (1) SG processed traces have relatively high changes to the interchannel delay times, when compared to the noisy data. These several sample adjustments can mean that the apparent velocity PMCC calculates is no longer in the acceptable acoustic range, and so a pixel is not generated; (2) BC and SG processed channels show relatively low correlation and more distorted components vs. the noisy data equivalents, suggesting that traces are less likely to meet PMCC wavefield parameter thresholds; (3) BC data often has a low correlation between its own traces. Not all microbarom packets exhibit this behavior during processing however, with yet to be determined factors dictating how microbaroms are split between foreground and background.

An important aspect of choosing a stage 2 processing method is computational efficiency, particularly for real time applications and/or processing large data sets. The following run times and memory use values are those required to process 24 hours of 20 sample per second data with a single core 3.1 GHz processor. For the Fourier transform

based methods, here we use 2048 FFT points, and 75% overlap of 2,048 sample windows. BC uses four voices as stated previously. BC: 213 s, 12.5 GB; HR: 7.5 s, 0.3 GB; NMF: 5.5 s, 0.55 GB; NN: 258 s, 0.9 GB; SG: 2.6 s, 0.1 GB. We use the same parameters between methods to allow for direct comparison, but this may not always be ideal. For example, NN has a more even along-trace foreground/background separation with 50% overlap. As mentioned in section 3.2.4, for NN, speed can be increased by reducing the number of nearest-neighbors, appropriate for cases where events and noise are shorter in duration than the cases presented here. The five wavelet options included with BCseis can also make a noticeable difference to results. For instance, when using a Shannon, rather than the Morlet wavelet, ~9% more detections are found for the event in Figure 6, including during some of the gaps between pulses. Also, for Figure 8, events on 23 December and 22 January are noticeably clearer with the Shannon wavelet. However, waveform distortion was relatively high for several test events, and so not pursued here.

5.2. Wind Noise

We find that wind noise reduction has little effect on improving signal or clutter detectability in array processing results (Figure 6). Whereas PMCC is capable of detecting signals with SNR < 1, at high wind speeds infrasound arrivals become very poorly correlated and hard to resolve. For RTM, wind noise removal provides more benefits using robust stacking than linear stacking for the 15 January event. For both stacking types, high-pass filtering provides a greater net benefit, however. Microbarom removal has a relatively small impact here, but may be more important where the majority of stations have very low initial SNR. The RTM processing parameters are primarily tuned for noisy linear stacking, whereas other parameters may work better depending on the configuration. Similarly, the effects of tuning parameters for the stacking methods could be explored. AGC to some extent undoes

the wind noise reduction, but results are still better with AGC, than without. As with stage 2 processing, there is a wide variation on the computation times for stacking methods, with the python-based PWS implementation taking 230 times longer than linear for each stacking operation. Although PWS performed poorly here, and could not justify the computation time, improvements may be seen when using a realistic propagation model to improve the alignment of arrivals and thus SNR (e.g., Shani-Kadmiel et al., 2018).

A potential factor in how well stage 3 denoising works is that as the SNR and frequency content of signals typically decrease with distance, event characteristics may change relative to noise, depending on propagation conditions, the local site environment (vegetation, topography, snow), and station design. We analyze the 8 March Bogoslof eruption, which was one of the best spatially recorded, with arrivals evident at 36 different stations within a 2,500 km radius. Of these, we use 25 stations which have relatively low winds coincident with the event. Figure 12a shows some contrasting arrivals at stations at increasing distance from Bogoslof, with progressive attenuation of higher frequencies with distance generally evident. OKIF, being the closest array, shows the event frequency range extending to at least 0.05 Hz. The wind noise at the start and end of the day is mostly < 0.1 Hz, but does extend higher. Wind noise at the DLL array, however, generally does not exhibit these higher frequencies, with the TA.TCOL station being similar in this regard. These two stations are some of the few sites in this study that are in dense tree cover, with the wind noise reduction pipes at DLL also playing a part. Nearby stations retain the higher wind noise frequencies seen at OKIF, and to a greater extent at TA.L27K, which is much more typical for TA stations. TA.L27K has a relatively poor wind noise reduction levels compared to the other stations shown, with relatively similar event and wind spectra.
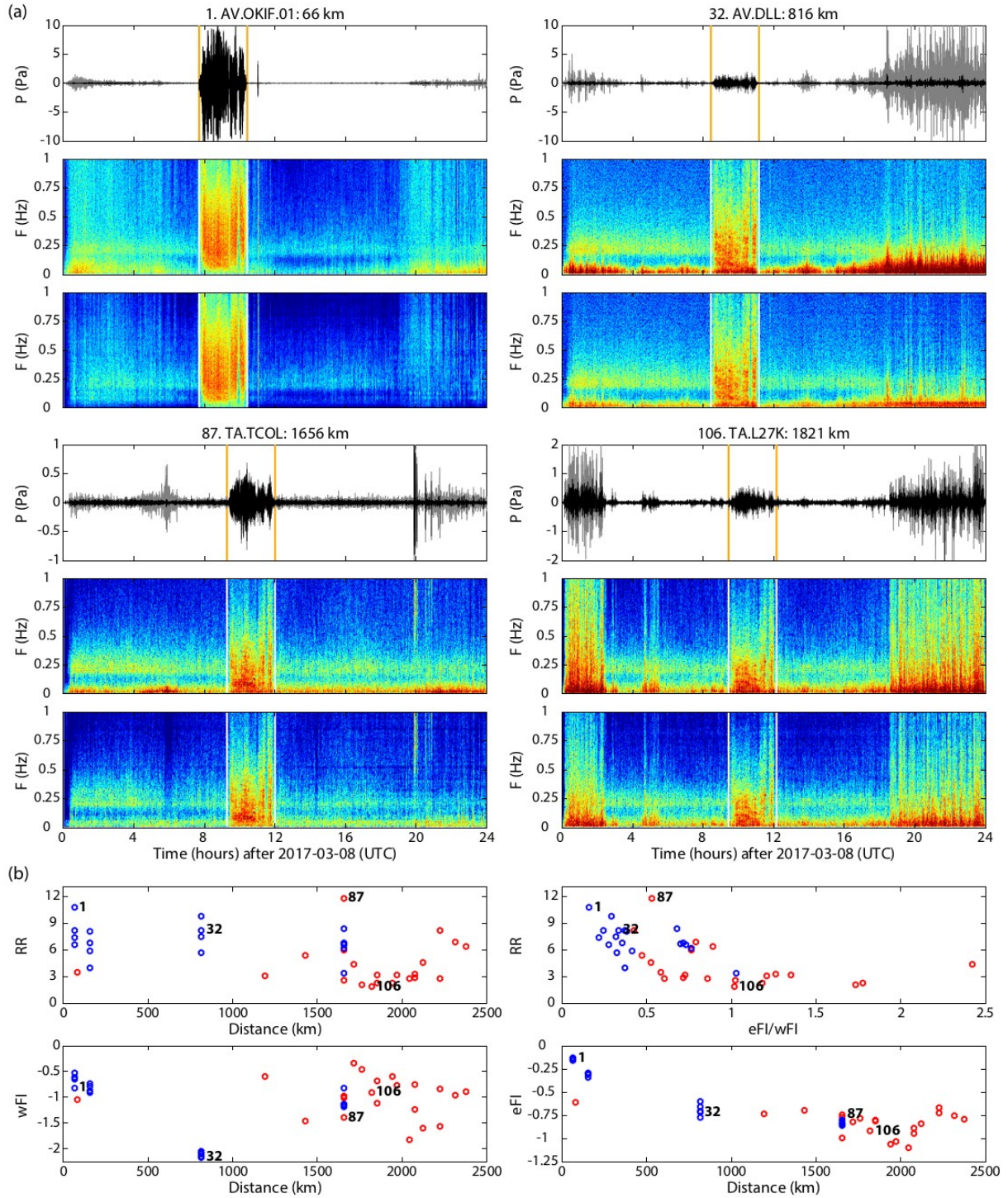
Figure 12. Assessing the effect of the relative frequency content of wind and eruptions on NMF performance. Higher SNR improvements are seen where the events have a higher frequency index relative to the wind, rather than only requiring a difference between the two. (a) Examples of stage 2 (grey) and stage 3 (black) waveforms from the 8 March 2017 Bogoslof eruption, with respective spectrograms shown below. Subplot titles include the station number in terms of distance from Bogoslof (not all stations shown), the corresponding distance, and the station code. Vertical bars mark the continuous infrasound phase of the eruption, according to the AVO catalogue, adjusting for a 280 m/s celerity. For each station, wind occurs primarily at the beginning and ends of the day. The upper end of each spectrogram color scale has been

adjusted such that the event portions appear to have similar maximum values. This enables more direct comparison given the different amplitudes of the signals, particularly regarding attenuation of the higher frequencies. TA.TCOL contains some non-wind noise which is not removed. P = Pressure, F = frequency. (b) Plots showing how the RR, wFI, and eFI values vary with distance, using blue for array elements, and red for non-array stations. RR is also plotted against eFI/wFI. The stations from part (a) are marked.

As NMF depends on the spectral content of the training examples, we hypothesize that dissimilar wind noise and event characteristics will produce better wind noise reduction in stage 3. As metrics, first, we implement the Frequency Index (FI) concept of Buurman and West (2006) as follows: $FI = \log_{10}(A_{upper}/A_{lower})$, where A_{lower} is the mean spectral amplitude from 0.01–0.25 Hz, and A_{upper} is the same for 0.25–1.0 Hz. This division uses the microbarom center as the division point. In the following, eFI refers to the FI value for the event sample, and wFI for the wind noise sample. Figure 12b shows that eFI generally decreases with distance indicating attenuation of higher frequencies, with wFI displaying some of the variation seen in Figure 12a. To measure how well NMF affects SNR, we compare changes in event to wind noise amplitude ratios. For this we define a second metric, $RR = (e_3/w_3)/(e_2/w_2)$, where e and w are the root-mean-square amplitudes of event and wind noise samples, and 2 and 3 are stage 2 and 3 of the processing. Higher RR values indicate better wind noise reduction. In terms of whether RR depends on eFI/wFI, i.e., how similar the event and wind noise spectra are, there isn't a clear picture. For instance, RR does vary for eFI/wFI < 1, but not above. RR values are generally higher for arrays than for non-array stations, likely due to the closer source proximity and presence of more sophisticated wind noise reduction systems. Some variation for metrics exists within arrays, reflecting slight differences between elements, even at 100 m apertures. A caveat to eFI-dependent results in Figure 12b, and more generally, is that when using 0.01 Hz as a lower filter bound, many stations will have some degree of wind noise during the event (e.g., three of four stations in Figure 12a). This could make signal separation harder if there is less difference between the

event and wind noise. For the culled events in Figure 12, however, noise reduction is generally better if using 0.01 Hz rather than 0.05 Hz, or 0.1 Hz. For these high-passed results, there is much less RR differentiation between stations.

A caveat to the analysis of Figure 12, is that the SNR of the unprocessed data varies between stations, which, as Figure 11 shows, is a factor influencing the SNR of denoised signals. In the supporting material, we evaluate stage 3 noise reduction for the same synthetic event signals as for stage 2, using two sources of wind noise that each do, and do not overlap with the events. Briefly, these results indicate improved denoising performance for: (1) non-overlapping events and wind noise, (2) wind noise samples from an array rather than TA station, and (3) events that are relatively high frequency compared to the wind noise. As for the stage 2 denoising, in future work we aim to expand the range of events analyzed with such methods in order to understand their suitability and best method of application.

6. Conclusions

By evaluating five different methods, we find that persistent background clutter such as the microbarom can be reduced effectively in infrasound data without any training, but more consistently with training. The BC and SG methods perform best in this regard. Separating wind noise from events on the other hand is more challenging, and good separation at most TA stations is only possible by training on both the wind noise and the event using NMF. Training solely on the wind noise usually provides only a moderate improvement over the original signal. At AVO and IMS arrays, the wind noise character typically differs from the events significantly due to hardware and/or source proximity, and as such, separating signals from wind noise is easier. It is likely that some training is a fundamental aspect of a general wind noise reduction scheme, as unsupervised

foreground/background separation techniques are not well suited to this task. Microbarom reduction primarily benefits PMCC array processing by enhancing signal detection in the microbarom range, and also removing surrounding clutter in cases of a shared backazimuth. Wind noise reduction explored here does not appreciably affect array processing results, however. In contrast, RTM benefits mainly from wind noise reduction due to significant trace amplitude modulation, and less so from microbarom removal. We also find that PMCC can be a useful tool for helping to refine existing Bogoslof eruption catalogs in that PMCC clearly detects infrasound from several catalogued events previously reported to have no infrasound records, or otherwise for specific arrays. The onsets and duration of some events also warrant re-evaluation based on our observations, which are enhanced via denoising.

In this study we focus largely on the extent to which denoising can improve SNR when using semi-supervised and fully supervised processing. We implement open source denoising methods that can be applied to a single trace. This approach promotes accessibility and flexibility, as not all data sets will contain the thousands of records potentially necessary to produce reliable dictionaries. Infrasound noise reduction on individual waveforms can likely improve results from many analysis types aside from detection and location strategies, and should be an area of future study for the community. Even for simply viewing waveforms and spectrograms, microbarom (or microseism) removal is generally useful by increasing fidelity, but particularly benefits identification and presentation of weakly detected events at remote distances. More broadly, trace-based noise reduction can increase the value of isolated infrasound sensors in places where an array, or noise reducing hardware such as a wind dome, is impractical.

7. Future Directions

Developing a "one scheme fits all data sets" signal enhancement strategy is a challenging task due to potentially high variability in signal and noise character, even at the same infrasound station over the space of a few hours. Signals will be affected by source style and duration, anisotropic radiation, atmospheric structure, wind direction, and the type of recording sensor. Due to time-varying multipathing, eruption signals may not be consistent between stations, nor even at the same station from a repeating source. Noise predominantly comes from wind, which presents differently depending on location, station design, as well as wind speed and the types of turbulence produced. Dominant wind noise frequencies may change by a few Hz, rather than being confined < 0.1 Hz. Microbaroms are often an undesirable element in infrasound data, but are not noise, given they are coherent acoustic arrivals. The strength and peak frequency of the microbarom will vary at a station over the course of a year with the seasons and stratospheric wind direction. The Bogoslof data set, and other active Alaskan volcanoes more generally, provide an excellent opportunity to evaluate the relative performance of new denoising schemes, for which here, we have only begun. The increasing numbers of infrasound sensors being installed in Alaska will facilitate this task.

Developing dictionaries accounting for the wide range of source, path, and site conditions across a diverse region like Alaska is a central issue. Certainly, excluding the event aspect reduces the complexity of the objective, in that training only with noise and microbarom samples permits the cleaned data to contain both volcanic and nonvolcanic signals. Incorporating adaptive data processing (included with e.g., HR) can be an important aspect of real-time monitoring, where the data may be in small chunks, aggregated, or otherwise not fit existing dictionaries. Such real-time use is affected by processing runtime,

and travel-time-latency, which for infrasound can be e.g., 15 mins at a range of 300 km. We suggest a combination of stage 2, 3, and 4 type approaches that sufficiently balance speed and effectiveness in reducing noise while preserving signals. For RTM, it is computationally more efficient to enhance SNR during pre-stack processing than during stacking itself, as each denoising operation is only performed once per trace, rather than per grid node. There are more grid nodes than traces in a typical scenario.

Although we describe and present results from several denoising methods here, and have evaluated many more (e.g., Sanderson et al., 2020b), this only scratches the surface of the field. For instance, Müller (2015) explains how in cases of music, approaches should vary for cases of multiple instrument separation, harmonic/percussive separation, and voice separation. Though not volcanic acoustic examples, they demonstrate that different techniques may be needed depending on the nature of the data, even without any noise present. At the geophysics cutting edge, diverse machine learning techniques are helping to rapidly advance the fields of signal classification and signal denoising, a combination of which will enhance automated volcano event detection and location practices. A popular core technique for both areas is the artificial neural network, with implementations using various degrees of supervision and training (e.g., Zhu et al., 2019; Jiang et al., 2020; Novoselov et al., 2020; Son et al., 2020). Fortunately, open source tools are becoming more available for the community to implement and further develop, with some applied to volcanic seismic data such as tsfresh (Christ et al., 2018; Dempsey et al., 2020), PICOSS (Bueno et al., 2020), and those comprising the VULCAN.ears project (Moreno et al., 2020).

Acknowledgments

Data Availability

For the study period, we downloaded TA, AEC, IMS, and GSN data from the IRIS DMC (https://www.iris.edu/, network codes TA, AK, IM, and II); AVO station data were obtained from the USGS Winston Wave Server (http://pubavo1.wr.usgs.gov:16023/menu, network code AV). Station location information, and instrument responses came from the IRIS DMC, but certain parameters have been adjusted, as detailed in the supplemental material. The supplemental material also includes comments on AVO catalogs for Bogoslof, as well as data processing, analysis, and plotting tools.

References

Adam, V., Chritin, V., Rossi, M., and Van Lancker, E. (1998). Infrasonic monitoring of snow-avalanche activity: What do we know and where do we go from here? *Annals of Glaciology,* 26, 324–328. https://doi.org/10.3189/1998AoG26-1-324-328.

Bednar, J. B. (1983). Applications of median filtering to deconvolution, pulse estimation, and statistical editing of seismic data. *Geophysics*, 48, 1598–1610. https://doi.org/10.1190/1.1441442

Boll, S. (1979). A spectral subtraction algorithm for suppression of acoustic noise in speech. *ICASSP'79 / IEEE international conference on acoustics, speech, and signal processing*, 4, 200–203. https://doi.org/10.1109/ICASSP.1979.1170696

Bowman, J. R., Baker, G. E., and Bahavar, M. (2005). Ambient infrasound noise. *Geophysical Research Letters*, 32, L09803. https://doi.org/10.1029/2005GL022486

Bryan, N. J., Sun, D., and Cho, E. (2013). See NMF software in the supplemental material.

Bueno, A., Zuccarello, L., Díaz-Moreno, A., Woollam, J., Titos, M., Benítez, C., Álvarez, I., Prudencio, J., and De Angelis, S. (2020). PICOSS: Python Interface for the Classification of Seismic Signals. *Computers & Geosciences*, 142. https://doi.org/10.1016/j.cageo.2020.104531

Busby, R. W., and Aderhold, K. (2020). The Alaska Transportable Array: As Built. *Seismological Research Letters,* 91(6), 3017–3027. https://doi.org/10.1785/0220200154

Buurman H., and West, M. E. (2006). Seismic precursors to volcanic explosions during the 2006 eruption of Augustine Volcano. In: J. Power, M. Coombs, and J. Freymueller (Eds), *The 2006 eruption of Augustine Volcano, Alaska* (pp. 41–57). https://doi.org/10.3133/pp17692

Cabras, G., Canazza, S., Montessoro, P. L., and Rinaldo R. (2010). The restoration of single channel audio recordings based on non-negative matrix factorization and perceptual suppression rule. In: H. Pomberger, F. Zotter, and A. Sontacchi (Eds.), *Proceedings of the 13th International Conference on Digital Audio Effects (DAFx-10)*, Graz, Austria (pp. 458-465).

Cabras G., Carniel R., and Jones J. (2012). Non-negative Matrix Factorization: an application to Erta 'Ale volcano, Ethiopia. *Bollettino di Geofisica Teorica ed Applicata,* 53(2), 231-242. https://doi.org/10.4430/bgta0056

Cansi, Y. (1995). An automatic seismic event processing for detection and location: The P.M.C.C. method. *Geophysical Research Lett*ers, 22(9), 1021–1024. https://doi.org/10.1029/95GL00468

Carniel, R., Cabras, G., Ichihara, M., and Takeo, M. (2014). Filtering wind in infrasound data by non-negative matrix factorization. *Seismological Research Letters*, 85(5), 1056–1062. https://doi.org/10.1785/0220130142

Ceranna, L., Matoza, R., Hupe, P., Le Pichon, A., and Landès, M. (2019). Systematic array processing of a decade of global IMS infrasound data. In: A. Le Pichon, E. Blanc, and A. Hauchecorne (Eds.), *Infrasound monitoring for atmospheric studies: Challenges in*

middle-atmosphere dynamics and societal benefits (pp. 471–482). Cham: Springer. https://doi.org/10.1007/978-3-319-75140-5_13

Christ, M., Braun, N., Neuffer, J., and Kempa-Liehr, A. W. (2018). Time series feature extraction on basis of scalable hypothesis tests (tsfresh–a python package). *Neurocomputing*, 307, 72–77. https://doi.org/10.1016/j.neucom.2018.03.067

Cook, M. R., Gee, K. L., Transtrum, M. K., Lympany, S. V., and Calton, M. (2021). Automatic classification and reduction of wind noise in spectral data. *JASA Express Letters*, 1, 063602. https://doi.org/10.1121/10.0005308

Coombs, M. L., Wech, A. G., Haney, M. M., Lyons, J. J., Schneider, D. J., Schwaiger, H. F., Wallace, K. L., Fee, D., Freymueller, J. T., Schaefer, J. R., and Tepp, G. (2018). Short-term forecasting and detection of explosions during the 2016–2017 eruption of Bogoslof volcano, Alaska. *Frontiers of Earth Science*, 6, 122. https://doi.org/10.3389/feart.2018.00122

Coombs, M. L., Wallace, K., Cameron, C., Lyons, J. J., Wech, A., Angeli, K., and Cervelli, P. (2019). Overview, chronology, and impacts of the 2016–2017 eruption of Bogoslof volcano, Alaska. *Bulletin of Volcanology,* 81(11), 1–23. https://doi.org/10.1007/s00445-019-1322-9

Dempsey, D. E., Cronin, S. J., Mei, S., and Kempa-Liehr, A.W. (2020). Automatic precursor recognition and real-time forecasting of sudden explosive volcanic eruptions at Whakaari, New Zealand. *Nature Communications,* 11, 3562. https://doi.org/10.1038/s41467-020-17375-2

Dixon, J. P., Stihler, S. D., Haney, M. M., Lyons, J. J., Ketner, D. M., Mulliken, K. M., Parker, T., and Power, J. A. (2019). Catalog of earthquake parameters and description of seismograph and infrasound stations at Alaskan volcanoes—January 1, 2013, through December 31, 2017. *U.S. Geological Survey Data Series*, 1115. https://doi.org/10.3133/ds1115

Fee, D., Haney, M. M., Matoza, R. S., Van Eaton, A. R., Cervelli, P., Schneider, D. J., and Iezzi, A. M. (2017). Volcanic tremor and plume height hysteresis from Pavlof Volcano, Alaska. *Science*, 355(6320), 45–48. https://doi.org/10.1126/science.aah6108

Fee, D., Lyons, J., Haney, M., Wech, A., Waythomas, C. F., Diefenbach, A. K., et al. (2020). Seismo-acoustic evidence for vent drying during shallow submarine eruptions at Bogoslof volcano, Alaska. *Bulletin of Volcanology,* 82(1), 1–14. https://doi.org/10.1007/s00445-019-1326-5

Freidlander, F. G. (1946). The diffraction of sound pulses. I. Diffraction by a semi-infinite plane. *Proceedings of the Royal Society London A*, 186, 322–344. http://doi.org/10.1098/rspa.1946.0046

Green, D. N., and Bowers, D. (2010). Estimating the detection capability of the International Monitoring System infrasound network. *Journal of Geophysical Research*, 115, D18116. https://doi.org/10.1029/2010JD014017

Haney, M. M., Van Eaton, A. R., Lyons, J. J., Kramer, R. L., Fee, D., and Iezzi, A. M. (2018). Volcanic thunder from explosive eruptions at Bogoslof volcano, Alaska. *Geophysical Research Letters*, 45, 3429–3435. https://doi.org/10.1002/2017GL076911

Haney, M. M., Van Eaton, A. R., Lyons, J. J., Kramer, R. L, Fee, D., Iezzi, A. M., Dziak, R. P., Anderson, J. F., Johnson, J. B., Lapierre, J. L., and Stock, M. (2020). Characteristics of thunder and electromagnetic pulses from volcanic lightning at Bogoslof volcano, Alaska. *Bulletin of Volcanology*, 82(15). https://doi.org/10.1007/s00445-019-1349-y

Ichihara, M., Yamakawa, K., and Muramatsu, D. (2021). A simple method to evaluate the seismic/infrasonic energy partitioning during an eruption using data contaminated by air-to-ground signals. *Earth, Planets and Space* (in review). https://doi.org/10.21203/rs.3.rs-707480/v1

Jiang, J., Stankovic, L., Stankovic, V., and Pytharouli, S. (2021). Automatic detection and classification of microseismic events from super-sauze landslide using convolutional neural networks. Abstract [S052_0009] presented at *2020 Fall Meeting, AGU.*

Landès, M., Ceranna, L., Le Pichon, A., and Matoza, R. S. (2012). Localization of microbarom sources using the IMS infrasound network. *Journal of Geophysical Research*, 117, D06102. https://doi.org/10.1029/2011JD016684

Langston, C. A., and Mousavi, S. M. (2018). Adaptive seismic denoising based on the synchrosqueezed-continuous wavelet transform and block-thresholding. *Air Force Research Laboratory final technical report,* AFRL-RV-PS-TR-2018-0074.

Le Pichon, A., Matoza, R., Brachet, N., and Cansi, Y. (2010). Recent Enhancements of the PMCC Infrasound Signal Detector. *Inframatics*, 26.

Le Roux, J., Wisdom, S., Erdogan, H., and Hershey, J. (2019). SDR – Half-baked or Well Done? *2019 IEEE International Conference on Acoustics, Speech and Signal Processing (ICASSP)*, pp. 626–630. https://doi.org/10.1109/ICASSP.2019.8683855

Lyons, J. J., Haney, M. M., Fee, D., Wech, A. G., and Waythomas, C. F. (2019). Infrasound from giant bubbles during explosive submarine eruptions of Bogoslof volcano, Alaska. *Nature Geoscience*, 12(11), 952–958. https://doi.org/10.1038/s41561-019-0461-0

Lyons, J. J., Iezzi, A. M., Fee, D., Schwaiger, H. F., Wech, A. G., and Haney, M. M. (2020). Infrasound generated by the 2016–17 shallow submarine eruption of Bogoslof volcano, Alaska. *Bulletin of Volcanology*, 82(19). https://doi.org/10.1007/s00445-019-1355-0

Matoza, R. S., and Fee, D. (2014). Infrasonic component of volcano-seismic eruption tremor. *Geophysical Research Letters*, 41, 1964–1970. https://doi.org/10.1002/2014GL059301

Matoza, R., Fee, D., Green, D., and Mialle, P. (2019). Volcano infrasound and the International Monitoring System. In: A. Le Pichon, E. Blanc, and A. Hauchecorne (Eds.), *Infrasound monitoring for atmospheric studies: Challenges in middle-atmosphere dynamics and societal benefits* (pp 1023–1077). Cham: Springer. https://10.1007/978-3-319-75140-5_33

Matoza, R. S., Landès, M., Le Pichon, A., Ceranna, L., and Brown, D. (2013). Coherent ambient infrasound recorded by the International Monitoring System. *Geophysical Research Letters*, 40. https://doi.org/10.1029/2012GL054329

Matoza, R. S., Le Pichon, A., Vergoz, J., Herry, P., Lalande, J.-M., Lee, H.-I., et al. (2011a). Infrasonic observations of the June 2009 Sarychev Peak eruption, Kuril Islands: Implications for infrasonic monitoring of remote explosive volcanism. *Journal of*

Volcanology and Geothermal Research, 200, 35–48. https://doi.org/10.1016/j.jvolgeores.2010.11.022

Matoza, R. S., Vergoz, J., Le Pichon, A., Ceranna, L., Green, D. N., Evers, L. G., et al. (2011b). Long-range acoustic observations of the Eyjafjallajökull eruption, Iceland, April–May 2010. *Geophysical Research Letters*, 38, L06308. https://doi.org/10.1029/2011GL047019

McFee, B., Raffel, C., Liang, D., Ellis, D. P. W., McVicar, M., Battenberg, E., and Nieto, O. (2015). librosa: Audio and music signal analysis in python. *Proceedings of the 14th Python in Science Conference*, 18–25. https://doi.org/10.25080/Majora-7b98e3ed-003

Mialle, P., Brown, D., Arora, N., and colleagues from IDC (2019). Advances in operational processing at the International Data Centre. In: A. Le Pichon, E. Blanc, and A. Hauchecorne (Eds.), *Infrasound monitoring for atmospheric studies: Challenges in middle-atmosphere dynamics and societal benefits* (pp. 209–248). Cham: Springer. https://doi.org/10.1007/978-3-319-75140-5_6

Moreau, L., Stehly, L., Boué, P., Lu, Y., Larose, E., and Campillo, M. (2017). Improving ambient noise correlation functions with an SVD-based Wiener filter. *Geophysical Journal International*, 211(1), 418–426. https://doi.org/10.1093/gji/ggx306

Moreno, G. C., Carniel, R., Lesage, P., and Mendoza Pérez, M. A. (2020). geoStudio and liveVSR - software supporting "VULCAN.ears" project (MSCA - IF - 20126, No.[749249]), *Zenodo*. http://doi.org/10.5281/zenodo.4305100

Müller, M. (2015). *Fundamentals of Music Processing – Audio, Analysis, Algorithms, Applications* (489 p.). Cham: Springer. https://doi.org/10.1007/978-3-319-21945-5

Nakata, N., Chang, J. P., Lawrence, J. F., and Boué, P. (2015). Body wave extraction and tomography at Long Beach, California, with ambient-noise interferometry. *Journal of Geophysical Research: Solid Earth*, 120, 1159–1173. https://doi.org/10.1002/2015JB011870

Novoselov, A., Balazs, P., and Bokelmann, G. (2020). Separation and denoising of seismically-induced ground-motion signals with dual-path recurrent neural network architecture. Abstract [S052_0007] presented at *2020 Fall Meeting, AGU*.

Olson J. V., and Szuberla, C. A. L. (2005). Distribution of wave packet sizes in microbarom wave trains observed in Alaska. *Journal of the Acoustical Society of America*, 117, 1032–1037. https://doi.org/10.1121/1.1854651

Pavlis, G. L., and Vernon F. L. (2010). Array processing of teleseismic body waves with the USArray. *Computers & Geosciences*, 36, 910–920. https://doi.org/10.1016/j.cageo.2009.10.008

Plapous, C., Marro, C., and Scalart, P. (2006). Improved signal-to-noise ratio estimation for speech enhancement. *IEEE Transactions on Audio, Speech, and Language Processing*, 14(6), 2098–2108. https://doi.org/10.1109/TASL.2006.872621

Raspet, R., Webster, J., and Dillon, K. (2006). Framework for wind noise studies. *Journal of the Acoustical Society of America*, 199, 834–843. https://doi.org/10.1121/1.2146113

Samson, J. C., and Olson, J. V. (1981). Data-adaptive polarization filters for multichannel geophysical data. *Geophysics*, 46, 10, 1423–1431. https://doi.org/10.1190/1.1441149

Sainburg, T., and Amr, K. (2019). See NoiseReduce software in the supplemental material.

Sanderson, R. W., Matoza, R. S., Fee, D., Haney, M. M., and Lyons, J. J. (2020a). Remote detection and location of explosive volcanism in Alaska with the EarthScope Transportable Array. *Journal of Geophysical Research: Solid Earth*, 125, e2019JB018347. https://doi.org/10.1029/2019JB018347 [Dissertation chapter 2]

Sanderson, R. W., Matoza, R. S., Fee, D., Haney, M. M., and Lyons, J. J. (2020b). Infrasonic backprojection with the EarthScope Transportable Array in Alaska: Improving detection and localization of explosive volcanism via noise reduction. Abstract [S001-0013] presented at *2020 Fall Meeting, AGU*. [Dissertation appendix 2]

Schimmel, M., and Paulssen, H. (1997). Noise reduction and detection of weak, coherent signals through phase-weighted stacks. *Geophysical Journal International*, 130(2), 497–505. https://doi.org/10.1111/j.1365-246X.1997.tb05664.x

Schwaiger, H. F., Lyons, J. J., Iezzi, A. M., Fee, D., and Haney, M. M. (2020). Evolving infrasound detections from Bogoslof volcano, Alaska: Insights from atmospheric propagation modeling. *Bulletin of Volcanology*, 82(27). https://doi.org/10.1007/s00445-020-1360-3

Searcy, C. K., and Power, J. A. (2020). Seismic character and progression of explosive activity during the 2016–2017 eruption of Bogoslof volcano, Alaska. *Bulletin of Volcanology*, 82(1), 1–15. https://doi.org/10.1007/s00445-019-1343-4

Shani-Kadmiel, S., Assink, J. D., Smets, P. S. M., and Evers, L. G. (2018). Seismoacoustic coupled signals from earthquakes in central Italy: Epicentral and secondary sources of infrasound. *Geophysical Research Letters*, 45, 427–435. https://doi.org/10.1002/2017GL076125

Slad, G. W., and Merchant, B. J. (2016). USGS VDP infrasound sensor evaluation. *Sandia National Laboratories Report*, SAND2016-1902. https://doi.org/10.2172/1331426

Son, S., Seydoux, L., de Hoop, M. V., and Campillo, M. (2020). Detecting and clustering seismic signals with datasets from a single station located in southern California by unsupervised deep learning. Abstract [S052_0005] presented at *2020 Fall Meeting, AGU*.

Tepp, G., and Haney, M. M. (2019). Comparison of short-term seismic precursors and explosion parameters during the 2016–2017 Bogoslof eruption. *Bulletin of Volcanology*, 81(63). https://doi.org/10.1007/s00445-019-1323-8

Thelen, W. A., and Cooper, J. (2015). An analysis of three new infrasound arrays around Kīlauea Volcano. *U.S. Geological Survey Open-File Report*, 2014–1253. https://doi.org/10.3133/ofr20141253

Walker, K. T., and Hedlin, M. A. H. (2010). A review of wind-noise reduction methodologies. In: A. Le Pichon, E. Blanc, and A. Hauchecorne (Eds.), *Infrasound monitoring for atmospheric studies* (pp. 141–182). Dordrecht: Springer. https://doi.org/10.1007/978-1-4020-9508-5_5

Walker, K. T., Hedlin, M. A. H., de Groot-Hedlin, C., Vergoz, J., Le Pichon, A., and Drob, D. P. (2010). Source location of the 19 February 2008 Oregon bolide using seismic networks and infrasound arrays. *Journal of Geophysical Research: Solid Earth*, 115, B12. https://doi.org/10.1029/2010JB007863

Waythomas, C. F., Lyons, J. J., Fee, D., and Wallace, K. L. (2019). The 2016–2017 eruption of Bogoslof volcano, Alaska: preface to the special issue. *Bulletin of Volcanology*, 81(48). https://doi.org/10.1007/s00445-019-1301-1

Wech, A., Tepp, G., Lyons, J., and Haney, M. (2018). Using earthquakes, T waves, and infrasound to investigate the eruption of Bogoslof volcano, Alaska. *Geophysical Research Letters*, 45(14), 6918–6925. https://doi.org/10.1029/2018GL078457

Williams, R. A., Perttu, A., and Taisne, B. (2020). Processing of volcano infrasound using film sound audio post-production techniques to improve signal detection via array processing. *Geoscience Letters*, 7(9). https://doi.org/10.1186/s40562-020-00158-4

Withers, M., Aster, R., Young, C., Beiriger, J., Harris, M., Moore, S., and Trujillo, J. (1998). A comparison of select trigger algorithms for automated global seismic phase and event detection. *Bulletin of the Seismological Society of America*, 88(1), 95–106. https://doi.org/10.1785/BSSA0880010095

Yang, X., Bryan, J., Okubo, K., Jiang, C., Clements, T., and Denolle, M. A. (2020). Optimizing the stacking of noise correlation functions, submitted to *Geophysical Journal International*.

Zhu, W., Mousavi, S. M., and Beroza, G. C. (2019). Seismic signal denoising and decomposition using deep neural networks. *IEEE Transactions on Geoscience and Remote Sensing*, 57(11), 9476–9488. https://doi.org/10.1109/TGRS.2019.292677

Supplemental Material

The following contains information on: (1) adjustments made to the AVO metadata available through the IRIS DMC; (2) synthetic noise reduction tests; (3) discrepancies between, and within, published Bogoslof eruption catalogs; (4) software resources; and (5) software parameters employed.

S1. Station Metadata Modifications

Here we detail changes made to IRIS DMC sourced metadata for use in this paper:

S1.1. Station Names and Locations

For simplicity in this paper, we refer to the Okmok infrasound array as OKIF, which is the current Okmok infrasound array name at the IRIS DMC. The nature of the Okmok metadata is complicated, however. Firstly, at the time of the Bogoslof eruption in 2016/2017, the array did not have a particular unifying acronym, with the channels named OK01–OK04 BDF given there were only four sensors. This remained true until July 2018, when two additional channels were added, and the array was designated as OKIF. At this same time, all the instruments were changed to another type, and channel codes changed from BDF to HDF, without any change in sample rate. This series of events has led to multiple sets of overlapping metadata on IRIS, as well as other servers, some of which is currently inconsistent. Here we use the following coordinates for Okmok channels 1–4, values which come from internal AVO documentation. These values are more precise versions of those listed for OKIF 01–04 HDF at the IRIS DMC. Based on PMCC analysis, these coordinates are more accurate than those listed for OK01–04 BDF at IRIS. We have not evaluated the OKIF 01–04 BDF values in detail as ch.1 is specified to be 130 m from its expected location.

Channel name, latitude, longitude
  > Okmok channel 1: +53.41083004, -167.914267
  > Okmok channel 2: +53.41001901, -167.913663
  > Okmok channel 3: +53.40998297, -167.914996
  > Okmok channel 4: +53.41029796, -167.914317

For further Okmok metadata details, please refer to, e.g.:
  > Dixon et al. (2019), Lyons et al. (2020)
  > http://ds.iris.edu/mda/AV/OK01/
  > http://ds.iris.edu/mda/AV/OKIF/01/BDF/ and /HDF/
  > http://130.118.181.39:16023/menu (USGS server from which most AVO array data was obtained)

For the Cleveland array metadata, we take IRIS DMC information from /AV/CLCO1/ etc., rather than /AV/CLCO/.

S1.2. Instrument Responses

At the time of writing, we find that the several of the instrument responses available from the IRIS DMC for the AV network during the Bogoslof eruption period (12 December 2016 to 30 August 2017) are not internally consistent and/or consistent with other records of

what these responses should be and/or data inspection. Consequently, we make the following adjustments here, where (1) 'gain' indicates the datalogger gain, $S(d)$, in SEED Stage 2 is changed from 30 (IRIS DMC) to 1 (here), and (2) 'frequency' indicates the frequency of sensitivity, f_s, in SEED Stage 0 is changed from 0.05 Hz (IRIS DMC) to 1 Hz (here).

ADAK: Metadata not available on IRIS, but has the same sensor and datalogger configuration as at OK01-4 BDF.

ADKI: Frequency

AKS: Gain, frequency

CLCO: Frequency. Poles and zeros in the IRIS DMC instrument specifications are for a Chaparral 25X. The instrument type is, however, a VDP-5 (Lyons *et al.*, 2020). Consequently, we use the appropriate poles and zeros given by Thelen and Cooper (2015) (specified for the VDP-10, but are the same for the VDP-5). We set the A_0 normalization factor to 157.2165 to appropriately scale the response. Poles and zeros are provided by Thelen and Cooper (2015) in units of Hz, whereas considering these values to be in rad/s (without conversion) gives the reported flat response of 0.0125 to 25 Hz. This flat response is also demonstrated by Slad and Merchant (2016). Consequently, we take the reported units of the poles and zeros to be rad/s rather than Hz in this case.

DLL: From 5 May 2017 to at least 30 August 2017 (the end of the eruption sequence), channels 2 and 5 have amplitudes half those of other channels, without a mitigating factor in the instrument response information. Consequently, these data are scaled to match the other traces. From the start of the eruption on 12 December 2016, to 5 May 2017, channel 3 was not functioning, and consequently unused.

DFR: Metadata not available on IRIS. As the data is poor quality throughout the Bogoslof eruption sequence, and the data only used for RTM which includes normalization, we do not remove the instrument response for DFR.

MSW: Gain, frequency

OKIF: Gain, frequency. Response information taken from OK01–4 BDF, see section S1.1.

PN7A, PS1A, PS4A, PV6A: Frequency

SDPI: Frequency. The IRIS DMC specification given for the VDP-10 instrument contains an extra zero, so this is removed to match the specifications given by Thelen and Cooper (2015). We also set the A_0 normalization factor to 157.2165, rather than 1.56115, to appropriately scale the response. Poles and zeros from Thelen and Cooper (2015) are taken to have been reported in rad/s rather than Hz, as outlined for CLCO.

SSLN: Metadata not available on IRIS. As with DFR, we do not remove the instrument response, and the data is normalized during RTM pre-processing.

S2. Synthetic Noise Reduction Tests

This section follows from Figure 11, which explores how well different denoising schemes perform depending on the signal to noise ratio of the original data. Details of the methodology are provided in section 5.1. Here we combine synthetic signals with scaled microbaroms, as well as with scaled wind noise. The synthetic waveforms are: 1) a shocked pressure pulse (Friedlander, 1946), with a broad spectra that peaks at 1 Hz; 2) a 0.2 Hz exponentially decaying signal; and 3) a 2.0 Hz exponentially decaying signal (Figure S1). Amplitudes are scaled to ~7.9 Pa, similar to the event in Figure 11. These signals are chosen to be similar to, and in contrast to the peak frequency of the microbarom (~0.2 Hz). Similarly, these signals have varying degrees of spectral overlap with the two wind samples borrowed from Figure 12. One wind sample is from AV.DLL, with the station using wind noise reduction pipes to reduce higher frequency noise. The other wind sample is from TA.L27K, which uses a simple diffuser, and retains more of the higher frequencies (Fig A1).
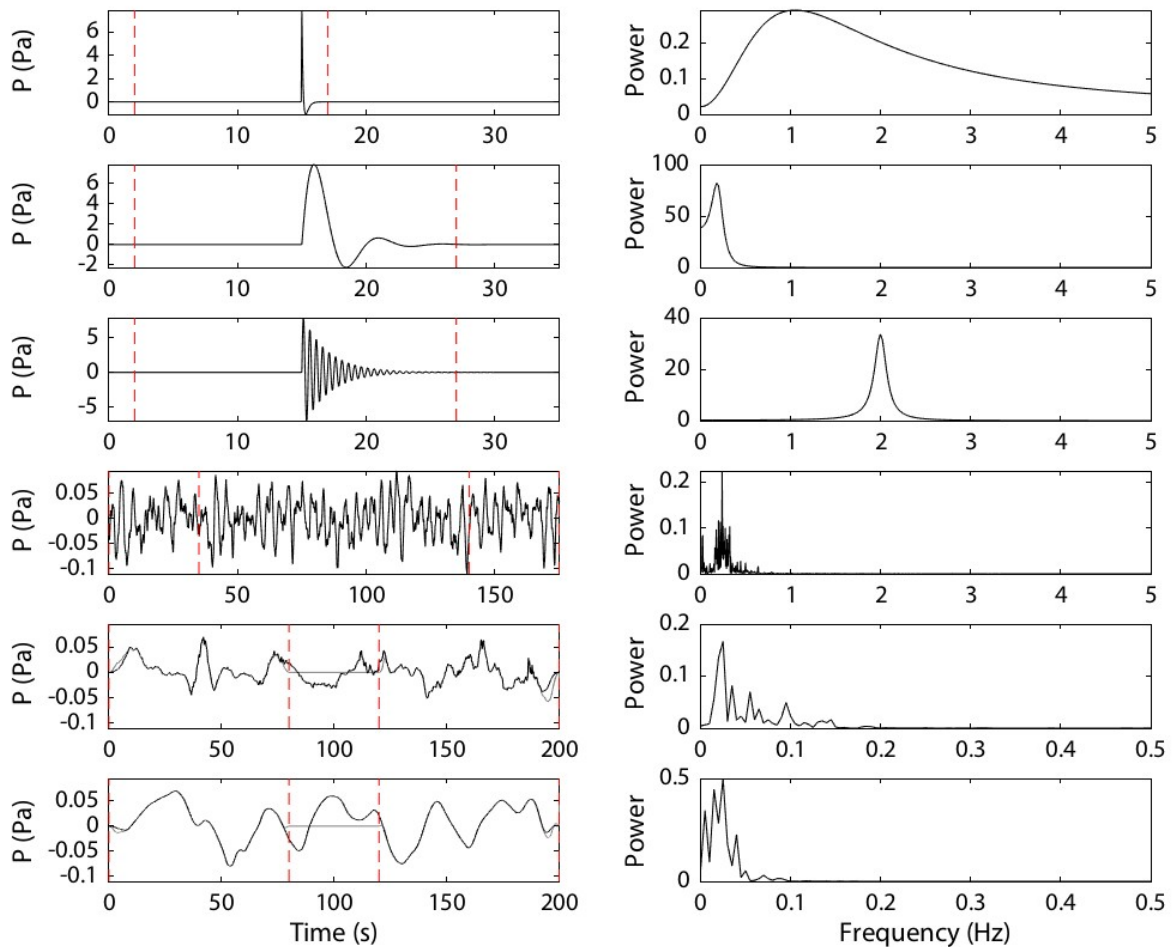
Figure S1. Waveforms and power spectra for synthetic event signals (rows 1–3), microbarom sample (row 4), and wind samples (rows 5–6). Wind in row 5 is from AV.L27K, and wind in row 6 is from AV.DLL. Each wind waveform shows the continuous sample in black, and a version where the center is zeroed out in order to create a discontinuous version (grey). Differences at the edges are due to applied tapering. Red vertical dashed lines show the time limits used for calculations. The microbarom sample is the same as that from Figure 11. Wind traces have already undergone stage 2 processing with the SG (spectral gating) method.

These wind samples are both scaled to have an initially similar amplitude to the microbarom sample, before all of the noise samples are scaled from 1 to 100 times in order to change the SNR. Two wind data formats are assessed: 1) continuous wind samples that overlap with the synthetic events, and 2) wind samples that are zeroed in the middle so that there is no noise overlap with the event, where wind only occurs at the end of the traces. For the wind noise reduction, the event labelling window is set to start prior to the actual event onset (here by 13 s). This approach produces improved results when compared to having the window start right at the onset. This may relate to reduced tapering of the impulsive onsets of the events during processing. The expanded window does, however enable calculations to incorporate any acausal distortion prior to event onsets. Due to the lower frequency of the wind compared to the microbarom, longer time windows are used for calculations.
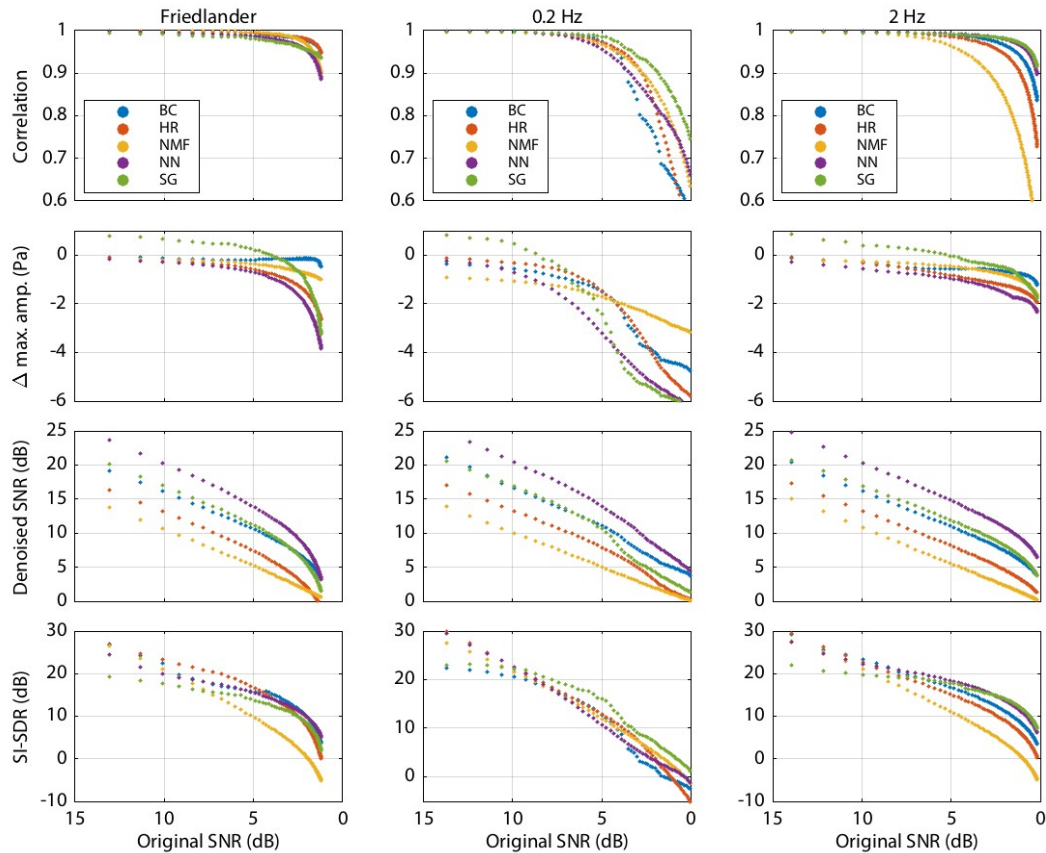
Figure S2. Evaluating the impact of denoising methods on removing the microbarom component from data, under different initial signal to noise conditions. Panels show the correlation coefficient, change in maximum amplitude, SNR of the denoised trace, and SI-SDR.

For the microbarom removal evaluation in Figure S2, we find generally similar results between the Friedlander pulse, and the 2 Hz signal. Both show decreasing statistical parameters as the original SNR decreases. The relative performances between methods are also similar for each event type. For the 0.2 Hz signal, which has a very similar frequency content to the microbarom, denoising performance is consistently worse than the other two cases, particularly where the original signal is below ~7–8 dB SNR. The results for the 0.2 Hz event are similar to those in Figure 11, where the Bogoslof explosion was also predominantly low in frequency.

For the wind removal results in Figure S3, there is a more complex picture than for the microbaroms. In terms of correlation, the discontinuous wind samples do not drop off, even at very low SNR. At 0.2 Hz and 2 Hz, the DLL continuous wind results decay at relatively high SNR compared to L27K. These results are also reflected in the maximum amplitude plots, where the original amplitude is maintained in the discontinuous wind noise case. For the overlapping wind however, the maximum amplitude diverges with lower original SNR. In terms of the SNR of the denoised data, the DLL results are better than those for L27K, with the greatest difference at 0.2 Hz, though with all data sets having a net SNR improvement. This suggests that the wind-noise spectral differences between the two stations is impactful, with the lower frequency noise at DLL easier to remove. This type of result was also presented in Figure 12. For the SI-SDR metrics, again we find better performance for the discontinuous wind samples, with little drop off even at low original SNR. The different synthetic events here produce somewhat similar results, but the 0.2 Hz signal has noticeably lower SI-SDR than in the other two cases, indicating higher distortion. This may be due to the dominant frequency being closest to the frequencies contained by the wind.
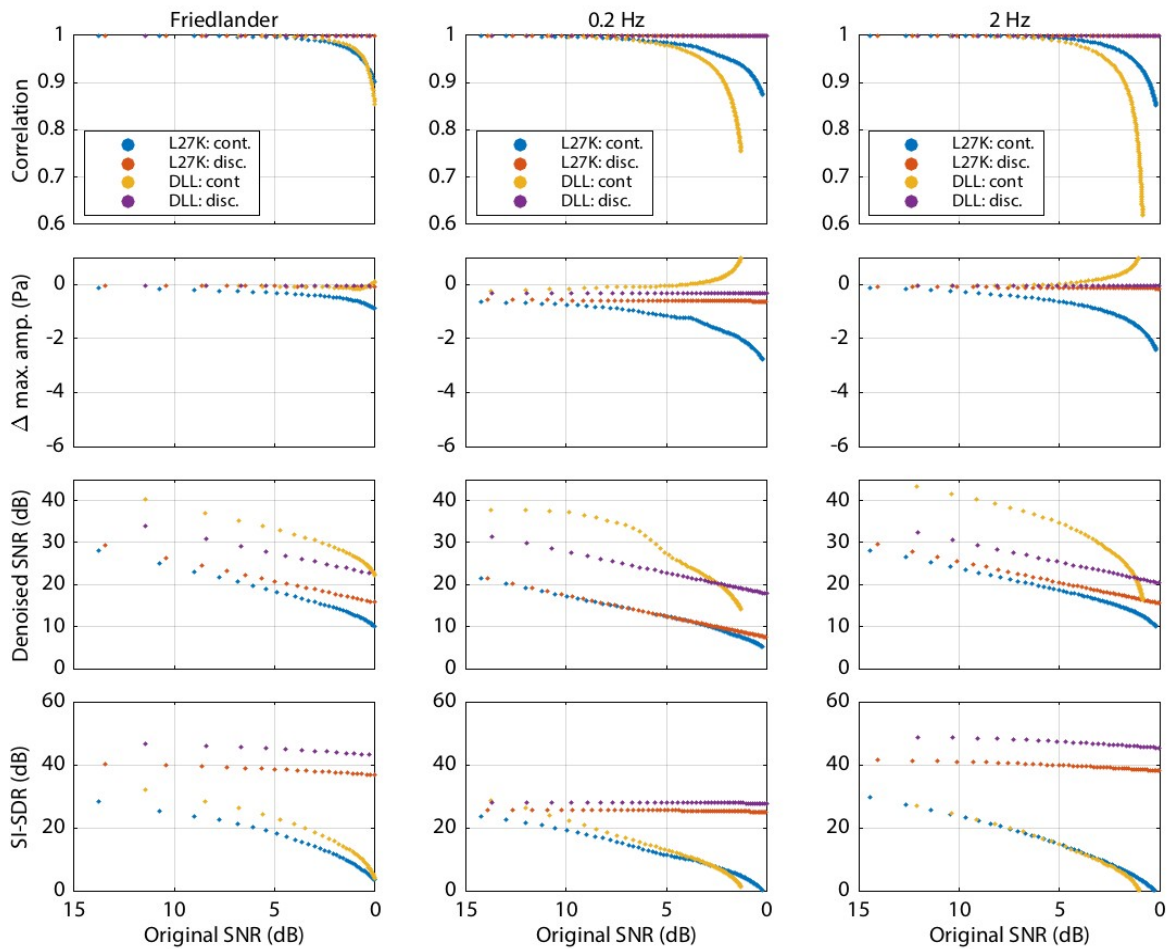
Figure S3. As for Figure S2, but for wind. In this case, NMF is the only method applied, however. The four data sets plotted are for combinations of stations TA.L27K, and AV.DLL, and whether the wind noise is continuous through the synthetic events, or only at the ends of the traces (discontinuous).

S3. Catalog Discrepancies

Here we mainly provide some comments on differences in reported infrasound observations between publications detailing infrasound records from Bogoslof, as well as potential conflicts within those reports. We anticipate that these comments can provide a useful reference when working with Bogoslof infrasound data. In the following, T1 refers to Table 1 from Coombs et al. (2019), ESM1 refers to Electronic Supplementary Material 1 from Coombs et al. (2019), F3 refers to Figure 3 from Lyons et al. (2020), and DS2 to Data Set 2 from the supporting information by Wech et al. (2018). Comments on known differences between infrasound observations in this study and the above references are provided within the main article, and not reiterated here.

ESM1 states that infrasound results are based on processing parameters used by Lyons et al. (2019), whereas T1 (also from Coombs et al., 2019) refers to parameters by Lyons et al. (2020). Table S1 below shows differences in array detections, including between T1 and F3, which should be identical for OKIF (see events 15 and 47).

In ESM1, events 21, 22, 27, 30, 31, 34, 41, 46, and 70 are listed as 'nd' (no detection) for 'Infrasound detection duration' (at OKIF), even though OKIF is listed as a detecting array. In relation to S1.1, ESM1 refers to the Okmok array as OK0 and OKO, rather than OKIF.

ESM1 determines several eruption onsets based on back-propagated infrasound arrivals, using a fixed celerity of 340 m/s. This celerity may not be accurate for all events, depending on factors like atmospheric temperature, ray paths, wind speed and direction etc. The impact on eruption start times would be more pronounced where timing is based on DLL (21/70 events), rather than OKIF, with differences of up to 10 minutes possible from those reported.

There are eight instances in ESM1 of infrasound being registered prior to the given eruption onset times (which are based on multiple types of data) listed in Table S2. It's uncertain if this infrasound represents some kind of pre-eruptive degassing, or whether the eruption onset times need re-evaluation. E.g., for 10 June, ESM1 gives an infrasound onset of 08:27, and an eruption onset of 09:58. ESM2 from Coombs et al. (2019), notes "*This event started with discrete explosions detected on the Okmok infrasound array as early as 8:27, but intensifying from 11:18 to 11:38*". PMCC suggests an infrasound start time of 07:33, approximately an hour earlier than the above source.

For event 29, the seismic activity time period is given by ESM1 as 05:20 to 07:23, whereas Fee et al. (2020) describe seismic activity continuing to ~13.30.

At DLL, F3 notes there is 'no data' for several events (#s 37, 38, 57–59, 63–65). Full data is available, however, for events 37, 38, and 63–65. This data is recently available from IRIS, but previously also from the Wilson Alaska Technical Center. We do not intend here to reassess all events for all arrays with PMCC, but do note that events 37, 38, 63, and 64 are clearly detectable at DLL with PMCC. ESM1 also logs event 37 and 38 at DLL.

Table S1. Comparing reported detections for arrays in Wech et al. (2018) (DS2), Coombs et al. (2019) (T1, ESM1), and Lyons et al. (2020) (F3). Arrays are ordered within each group by distance from Bogoslof from left to right. Not all arrays were operating at all times (see Lyons et al., 2020, and comments above regarding DLL data availability).

Event	DS2 OKIF	T1 OKIF	ESM1 OKIF	ESM1 AKS	ESM1 CLCO	ESM1 SDPI	ESM1 ADKI	ESM1 DLL	F3 OKIF	F3 AKS	F3 CLCO	F3 SDPI	F3 ADKI	F3 DLL
1		X	X						X					
2	X	X	X						X					
3					X	X								
4		X	X			X			X					
5						X		X						
6						X		X						X
7	X	X	X		X			X	X					X
8								X						
9						X		X						X
10						X		X						X
11						X		X						
12						X		X						X
13						X		X				X		X
14					X			X						
15		X				X		X						X
16	X	X	X		X	X		X	X					X
17	X	X	X		X	X		X	X					X
18														
19														
20		X	X		X	X		X	X					X
21			X			X		X						X
22			X			X		X						X
23						X		X				X		
24	X	X	X					X	X					X
25								X						X
26		X	X					X	X					X
27			X					X						
28	X	X	X						X					
29	X	X	X			X			X	X	X			
30			X					X						
31			X					X						
32														
33	X	X	X			X		X	X	X	X			X
34			X	X				X		X				X
35				X				X						X
36	X	X	X	X		X		X	X	X				
37	X	X	X	X		X		X	X	X				
38		X	X					X?	X					
39	X	X	X	X	X	X		X	X	X	X			
40	X	X	X	X		X		X	X	X				
41			X		X			X						
42		X	X						X					
43														
44		X	X		X				X					
45	X	X	X	X	X				X		X			
46			X		X						X			
47		X		X							X			
48	X	X	X	X	X		X		X	X			X	
49	X	X	X	X	X	X			X	X	X		X	X
50		X	X						X	X				
51	X	X	X	X	X	X			X				X	X
52	X	X	X	X	X	X			X	X				X
53														X
54											X			
55	X	X	X	X					X	X				
56		X	X	X	X				X	X				
57	X	X	X						X					
58	X	X	X				X		X					
59														
60	X	X	X	X					X					
61	X	X	X	X					X					
62														
63	X	X	X		X				X	X	X			
64				X						X				
65		X	X						X	X				
66	X	X	X						X	X				X
67	X	X	X						X					
68	X	X	X	X	X				X	X				X
69	X					X				X				
70			X		X						X			X

Table S2. Entries from ESM1 where the infrasound onset is given as prior to the eruption onset (UTC times).

Event	Infrasound onset	Eruption onset
15	06:16	06:19
26	13:48	13:51
28	17:22	17:25
34	00:32	00:34
35	13:57	14:00
41	02:43	02:44
48	08:27	09:58
63	17:39	18:21

S4. Principal Software Resources

We explicitly incorporated the following software packages for processing, analysis and plotting:

BCSeis: A GUI and set of inline functions for performing various non-linear thresholding operations using the Continuous Wavelet Transform (http://www.ceri.memphis.edu/people/clangstn/software.html).

> Langston, C. A., and Mousavi, S. M. (2018). Adaptive seismic denoising based on the synchrosqueezed-continuous wavelet transform and block-thresholding, *Air Force Research Laboratory final technical report* AFRL-RV-PS-TR-2018-0074. Available at: https://apps.dtic.mil/dtic/tr/fulltext/u2/1061053.pdf

BSSEval: Stöter, F.-R., and Liutkus, A. (2019). Audio source separation evaluation metrics (https://github.com/sigsep/bsseval)

> Vincent, E., Gribonval, R., and Févotte, C. (2006). Performance measurement in blind audio source separation, *IEEE Transactions on Audio, Speech and Language Processing*, 14, 4, 1462–1469.

Circle Draw: Scholtes, J. (2016). Python-custom distance radius with basemap (https://stochasticcoder.com/2016/04/06/python-custom-distance-radius-with-basemap/).

Dill: Serialization and deserialization of built-in python types (https://github.com/uqfoundation/dill)

> McKerns, M., and Aivazis, M. (2010–). pathos: a framework for heterogeneous computing. (https://uqfoundation.github.io/project/pathos).

> McKerns, M. M., Strand, L., Sullivan, T., Fang, A., and Aivazis, M. A. G. (2011). Building a framework for predictive science. *Proceedings of the 10th Python in Science Conference* (https://arxiv.org/pdf/1202.1056).

IPython: A rich architecture for interactive computing in multiple programming languages (https://ipython.org/).

> Pérez, F., and Granger, B. E. (2007). IPython: A System for Interactive Scientific Computing. *Computing in Science & Engineering*, 9, 21–29. https://doi.org/10.1109/MCSE.2007.53

GDAL: GDAL/OGR developers (2018). GDAL/OGR Geospatial Data Abstraction software Library (https://gdal.org)

GISMO: Thompson, G., and Reyes, C. (2017). GISMO - a seismic data analysis toolbox for MATLAB (https://geoscience-community-codes.github.io/GISMO/).

GMT: Generic Mapping Tools (https://www.generic-mapping-tools.org/).

> Wessel, P., Smith, W. H. F., Scharroo, R., Luis, J. F., and Wobbe, F. (2013). Generic Mapping Tools: Improved version released. *EOS Transactions, AGU*, 94, 45, 409–410. https://doi.org/10.1002/2013EO450001

IMS-vASC: Combined infrasound signal association and source location using a brute-force, grid- search, cross-bearings approach (https://github.com/rmatoza/ims_vasc).

> Matoza, R. S., Green, D. N., Le Pichon, A., Shearer, P. M., Fee, D., Mialle, P., and Ceranna, L. (2017). Automated detection and cataloguing of global explosive volcanism using the International Monitoring System infrasound network. *Journal of Geophysical Research: Solid Earth,* 122, 2946–2971. https://doi.org/10.1002/2016JB013356

Librosa: Music and audio analysis, music retrieval systems (https://librosa.org/doc/latest/auto_examples/plot_vocal_separation.html)

> McFee, B., Raffel, C., Liang, D., Ellis, D. P. W., McVicar, M., Battenberg, E., and Nieto, O. (2015). librosa: Audio and music signal analysis in python. *Proceedings of the 14th Python in Science Conference,* 18–25. https://doi.org/10.25080/Majora-7b98e3ed-003

Matplotlib: A comprehensive library for creating static, animated, and interactive visualizations in Python (https://matplotlib.org/).

> Hunter, J. D. (2007). Matplotlib: A 2D Graphics Environment. *Computing in Science & Engineering*, 9, 90–95. https://doi.org/10.1109/MCSE.2007.55

NMF: Bryan, N. J., Sun, D., and Cho, E. (2013). Single-Channel Source Separation Tutorial Mini-Series (https://ccrma.stanford.edu/~njb/teaching/sstutorial/)

NoisePy: A high-performance python tool for ambient-noise seismology (https://github.com/mdenolle/NoisePy).

> Jiang, C., and Denolle, M. NoisePy: a new high-performance python tool for seismic ambient noise seismology. *Seismological Research Letters*, 91, 3, 1853–1866. https://doi.org/10.1785/0220190364

NoiseReduce: Sainburg, T., and Amr, K. (2019): Noise reduction in python using spectral gating (speech, bioacoustics, time-domain signals). (https://github.com/timsainb/noisereduce)

NumPy: Oliphant, T. E. (2006). A guide to NumPy. USA: Trelgol Publishing (https://numpy.org/).

ObsPy: A Python Toolbox for seismology/seismological observatories (https://docs.obspy.org/).

> Beyreuther, M., Barsch, R., Krischer, L., and Wassermann, J. (2010). ObsPy: A Python toolbox for seismology. *Seismological Research Letters,* 81, 3, 530–533. https://doi.org/10.1785/gssrl.81.3.430

Openpyxl: Openpyxl developers. (2016). A Python library to read/write Excel 2010 xlsx/xlsm/xltx/xltm files (https://openpyxl.readthedocs.io/en/stable/).

Pisces: Pisces: A practical seismological database library in Python (https://github.com/LANL-Seismoacoustics/pisces).

> MacCarthy, J. K., and Rowe, C. A. (2014). Pisces: A Practical Seismological Database Library in Python, *Seismological Research Letters,* 85, 4, 905–911. https://doi.org/10.1785/0220140013

PMCC: Progressive Multichannel Correlation (PMCC) software. Access is administered by CEA/DASE/LDG, France, and not publicly available.

> Cansi, Y. (1995). An automatic seismic event processing for detection and location: The P.M.C.C. method. *Geophysical Research Lett*ers, 22, 9, 1021–1024. https://doi.org/10.1029/95GL00468

RTM: Our Reverse Time Migration (RTM) code (v. 7.13+) is not currently publicly available, but we include supporting software resources in this list. An alternate RTM infrasound tool, partly based on ours, is located here: https://github.com/uafgeotools/rtm

SciPy: Jones, E., Oliphant, E., Peterson, P., et al. (2001–). SciPy: Open Source Scientific Tools for Python (https://www.scipy.org).

Subaxis - Subplot: Grinsted, A. (2020). Create axes in tiled positions (https://www.mathworks.com/matlabcentral/fileexchange/3696-subaxis-subplot).

WienerNoiseReduction: Scalart, P. (2020). Wiener filter for noise reduction and speech enhancement (https://www.mathworks.com/matlabcentral/fileexchange/24462-wiener-filter-for-noise-reduction-and-speech-enhancement).

> Plapous, C., Marro, C., and Scalart, P. (2006). Improved signal-to-noise ratio estimation for speech enhancement. *IEEE Transactions on Speech and Audio Processing*, 14, 6, 2098–2108. https://doi.org/10.1109/TASL .2006.872621

S5. Software Parameters

Details on parameter choices for each processing method are provided below to enable reproducibility. These parameters were determined from tests using multiple stations and events. Some codes were modified to be able to output extracted noise, as well as extracted signals. We use the stated Fourier transform parameters for all processing except for Figure 11, where due to the short event and poorer results for some methods with the standard parameters, we use 512 FFT points, a window length of 512 samples, and a hop size of 32. This suggests that some of the shorter events in Figure 8 may benefit from non-default Fourier parameters.

S5.1. Block Choice (BC)

The following are parameters for the BCseis_process function in BCseis v.1.2:

```
% Wavelet parameters
   params.wavelet_type = "morlet";
   params.nvoices = 4;

% Band pass/block parameters
   params.nbpblck = 0;
   params.scale_min = 1;
   params.scale_max = 1000;
   params.bthresh = 0.0;

% Noise Determination parameters
   params.nnbnd = 1;
   params.tstrn = round((t1)/FS); % Seconds
   params.tfinn = round((t2)/FS); % Seconds

% Noise and/or Signal Threshold parameters
   params.noisethresh = 1; % 1 to retain signal, 0 to retain noise
   params.signalthresh = 0; % 0 to retain signal, 1 to retain noise
   params.nsig = 2.25;

% Signal to Noise function parameters
   params.nsnr = 0;
   params.nsnrlb = 1.0;
```

For voices = 4, we chose the Morlet wavelet based on the balance of the following observations:
   1. *morlet*: Event and extracted noise amplitude OK, correct polarity, uneven + gappy spectrograms
   2. *mhat*: Event and extracted noise amplitude too big, correct polarity, clipped spectrograms at high frequencies
   3. *shannon*: Event amplitude too big, extracted noise amplitude OK, partly correct polarity, OK spectrograms
   4. *hhat*: Event and extracted noise amplitude OK, correct polarity, uneven + clipped + vertically gappy spectrograms

S5.2. Harmonic Regeneration (HR)

The following are parameters for the WienerNoiseReduction.m file (version October 2020):

    NFFT = 2048; % FFT points
    SP = 0.25; % shift percentage
    wl = 2048; % window length, samples
    alpha = 0; % parameter in a priori SNR calculation

The WienerNoiseReduction code by default scales the output trace to be the same amplitude as the input trace. There are instances where this result may not be desirable however, e.g., if the highest amplitude of the input trace is an element that is being removed. We find that instead, scaling the output by a factor of 2 produces an improved result.

S5.3. Non-Negative Matrix Factorization (NMF)

The following are parameters for the scriptcomplete.m file in NMF code III:

    K = [25 25]; % number of basis vectors
    supervised = [1 1]; % binary vector specifying what is supervised
    MAXITER = 30; % total number of iterations to run

    FFTSIZE = 2048; % FFT points
    HOPSIZE = 512; % hop length, samples
    WINDOWSIZE = 2048; % window length, samples

S5.4. Nearest-Neighbor Filtering (NN)

The following are parameters for the plot_vocal_separation.py file:

    n_fft = 2048 # FFT points
    hop_length = 512 # hop length, samples
    win_length = 512 # window length, samples
    nn_filter width = 2 # frame comparison parameter

    margin_i = 0.75 # mask parameter
    margin_v = 1.75 # mask parameter
    power = 2 # mask parameter

S5.5. Spectral Gating (SG)

The following are parameters for the noisereduce.py file, also see example at https://timsainburg.com/noise-reduction-python.html:

    n_grad_freq = 10 # how many frequency channels to smooth over with the mask
    n_grad_time = 1 # how many time channels to smooth over with the mask

    n_fft = 2048 # FFT points
    win_length = 2048 # window length, samples
    hop_length = 512 # hop length, samples

    n_std_thresh = 1.5 # how many sdevs > than the mean dB of the noise (at each freq. level)
                       to be considered signal
    prop_decrease = 0.7 # to what extent should you decrease noise (1 = all, 0 = none)

S5.6. Progressive Multi-Channel Correlation (PMCC)

The PMCC (Cansi, 1995; version 4.3.c1) initialization files for each array are uploaded separately. For each station, a unique configuration file and a common filter-bands file are required. Full descriptions of the file formats are included in PMCC software documentation (not included here). Configuration files: <array_name>.ini. Filter file: filters.ini (applies to all stations, assumes 20 Hz sample rate). DLL has two configuration files: One is for five channels, covering 12 December 2016 to 5 May 2017, and one is for six channels, covering May 2017 to 30 August 2017. The difference is indicated in the respective file names.

S5.7. Reverse Time Migration (RTM)

Parameters are the same as those described in Sanderson et al. (2020a).

Chapter 4. A Pilot Experiment on Infrasonic Lahar Detection at Mount Adams, Cascades: Ambient Infrasound and Wind-Noise Characterization at a Quiescent Stratovolcano

This chapter appeared in this form in:

[1]Department of Earth Science, University of California, Santa Barbara, California, USA
[2]Earth Research Institute, University of California, Santa Barbara, California, USA

Abstract

Erosion, hydrothermal activity, and magmatism at volcanoes can cause large and unexpected mass wasting events. Large fluidized debris flows have occurred within the past 6,000 years at Mount Adams, Washington, and present a hazard to communities downstream. In August 2017, we began a pilot experiment to investigate the potential of infrasound arrays for detecting and tracking debris flows at Mount Adams. We deployed a telemetered four-element infrasound array (BEAR, 85 m aperture), ~11 km from a geologically unstable area where mass wasting has repeatedly originated. We present a preliminary analysis of BEAR data, representing a survey of the ambient infrasound and noise environment at this quiescent stratovolcano. Array processing reveals near continuous and persistent infrasound signals arriving from the direction of Mount Adams, which we hypothesize are fluvial sounds from the steep drainages on the southwest flank. We interpret observed fluctuations in the detectability of these signals as resulting from a combination of (1) wind-noise variations at the array, (2) changes in local infrasound propagation conditions associated with atmospheric boundary layer variability, and (3) changing water flow speeds and volumes in the channels due to freezing, thawing, and precipitation events. Suspected mass movement events during the study period are small (volumes $< 10^5$ m^3 and durations < 2 min), with one of five visually confirmed events detected infrasonically at BEAR. We locate this small event, which satellite imagery suggests was a glacial avalanche, using three additional temporary arrays operating for five days in August 2018. Events large enough to threaten downstream communities would likely produce stronger infrasonic signals detectable at BEAR. In complement to recent literature demonstrating the potential for infrasonic detection of volcano mass movements (Allstadt et al., 2018), this study highlights the practical and computational challenges involved in identifying signals of interest in the expected noisy background environment of volcanic topography and drainages.

1. Introduction

Massive fluidized debris flows (lahars) originating from the upper slopes of volcanoes can occur without warning. Historically and recently, lahars have buried entire villages near volcanoes, with great loss of life (e.g., Pierson et al., 1990; Major et al., 2018). These potentially devastating, fast-moving flows pose an ongoing threat to people living in low-lying areas along drainages emanating from volcanoes. The study presented here is sited on Mount Adams in the Cascade Range of the Pacific Northwest, where large lahars have occurred within the past 6,000 years and are a significant ongoing hazard to communities downstream (Griswold et al., 2018).

It is possible to detect the early stages of catastrophic lahars, and so potentially warn people to seek higher ground before the lahar arrives, but most endangered populations do not have lahar detection systems. Reviews of monitoring strategies for lahar and debris flows are provided by Arattano and Marchi (2008), Pierson et al. (2014), Stähli et al. (2015), Allstadt et al. (2018), and Hürlimann et al. (2019). Infrasound sensor arrays record acoustic waves propagating through the atmosphere at frequencies below the threshold of human hearing (< 20 Hz) (Fee and Matoza, 2013; De Angelis et al., 2019; Matoza et al., 2019). Many kinds of surface mass movements at volcanoes (e.g., rockfalls, pyroclastic flows, and lahars) are known to produce distinctive infrasound signals (e.g., Allstadt et al., 2018, and references therein).

To investigate the potential of infrasound for detecting and tracking lahars at Mount Adams, we conducted a pilot experiment. Since August 2017, we have operated a four-element telemetered infrasound array (SB.BEAR), located ~11 km from a hydrothermally weakened and unstable zone above the White Salmon and Avalanche Glaciers, where historical mass wasting has originated and future events are expected (Finn et al., 2007;

Figures 1a and 1b). In August 2018, we temporarily deployed three additional three-element arrays (PHAB, CHIP, and RAIN), to help corroborate and locate signals recorded at BEAR. BEAR is scheduled for removal in August 2021.

This article is organized as follows: First, we outline some of the relevant geological hazards at Mount Adams and the nature of the stations used in the study. Next, we describe our data-processing methods and the anticipated acoustic character of mass movement signals. Analysis of the ambient infrasound (e.g., Matoza et al., 2013) and noise environment (e.g., Brown et al., 2014) follows, including wind–noise impacts and arrivals likely of fluvial origin. This analysis focuses first on the long-term records from BEAR and then on insights contributed by the temporary infrasound arrays. We identify several event types in the data and isolate events that are candidates for mass movements. The timing, location, and character of a glacial avalanche is assessed in detail.

1.1. Study Area

Mount Adams, one of the largest Cascade volcanoes, last erupted 540–2,500 years ago (Hildreth and Fierstein, 1995; Scott et al., 1995) and has since continued to have active fumaroles near its summit (Hildreth and Fierstein, 1995; Vallance, 1999). Explosive eruptions that fragmented the core of the mountain, and hydrothermal activity that has altered the volcanic material to soft, low-strength hydrous minerals, together have produced 1.8 km^3 of weak, unstable material in a bowl-shaped volume centered under the summit (Finn et al., 2007). Water saturation within this rotten core volume increases potential for slope failure and generation of hazardous lahars (Finn et al., 2007). Additional nonmagmatic forcing factors are snow loading, fracturing due to ice formation, pore pressure changes, erosion, and earthquakes (Vallance, 1999).
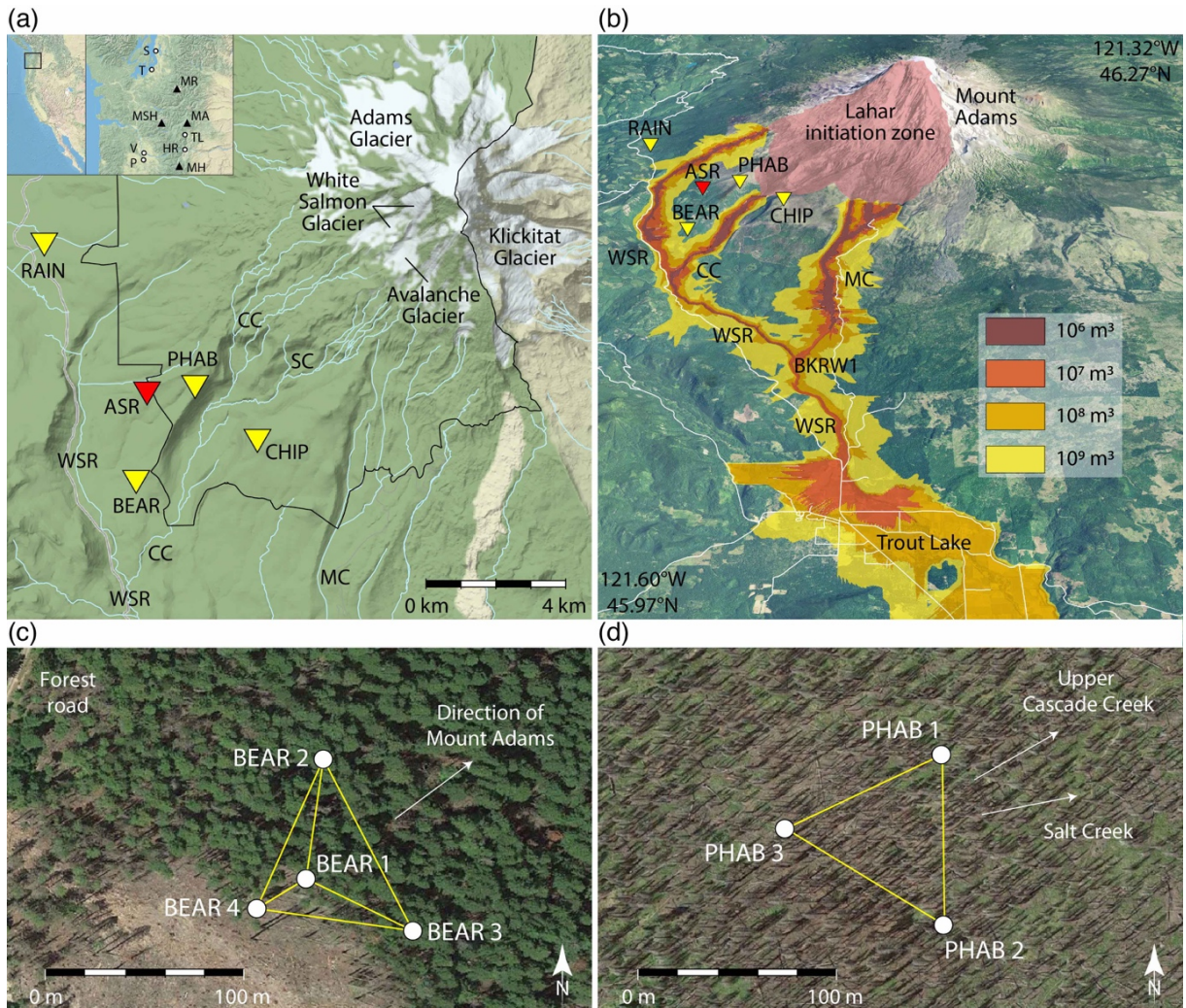
Figure 1. Important features in the Mount Adams study area. (a) The main panel gives an overview of the stations, glaciers, drainages, and wilderness boundary (black line). Insets are regional maps, showing nearby volcanoes and urban areas. (b) Modeled lahar inundation extents in the White Salmon River Valley (modified from Griswold et al., 2018). BKRW1 is a U.S. Forest Service weather station. (c) Geometry of the four subarrays at BEAR. (d) Geometry of PHAB (no subarrays). CC, Cascade Creek; HR, Hood River; MA, Mount Adams; MC, Morrison Creek; MH, Mount Hood; MR, Mount Rainier; MSH, Mount St. Helens; P, Portland; S, Seattle; SC, Salt Creek; T, Tacoma; TL, Trout Lake; V, Vancouver; WSR, White Salmon River.

A large lahar, associated with eruptions ~6,000 years ago, flowed more than 40 km down the White Salmon River drainage (Vallance, 1999). At the current location of Trout Lake, Washington, 27 km south of Mount Adams, the lahar left deposits up to 20 m thick and spread out to form the present floor of the Trout Lake Valley. Figure 1b gives an indication of the path of the 6.6×10^7 m^3 flow. Another smaller lahar, ~250 years ago, reached the location of the town and formed a deposit up to 4 m thick (Vallance, 1999;

Griswold et al., 2018). There is currently no evidence to suggest that this recent lahar was triggered by an eruption or unrest.

Continued instability of the Mount Adams summit region is demonstrated by recurring debris flows and lahars, with lengths of up to 3 km on subdecadal timescales (Norris, 1994; Scott, 2010; Allstadt et al., 2017; Lloyd, 2018) and up to 8 km during the past 100 years (Vallance, 1999). Ultimately, it would be desirable to detect these small-to-moderate-sized events, because larger slope failures are expected to initiate similarly.

2. Methodology

The equipment, data processing, and anticipated event characteristics for this study are described in the following. Infrasound arrays typically consist of at least three microbarometer pressure-sensing elements arranged spatially on the ground with an aperture of ~50–100 m, connected to a single digitizer and telemetry system (e.g., Garcés et al., 2003; Matoza et al., 2007). Siting arrays close to volcanoes with direct line of sight to the upper slopes facilitates rapid detection and localization of acoustic signals from surface events, but this must be balanced with other logistics, including site-noise (e.g., Matoza et al., 2007).

Mass wasting infrasound may be identified based on multiple signal features, but this is still an active area of research (Allstadt et al., 2018). Array processing helps significantly by providing direction-of-arrival information from one or more arrays, with changes in back azimuth and inclination angle (a measure of altitude) over time indicating a moving source (Ulivieri et al., 2011; Johnson and Palma, 2015; Marchetti et al., 2015; Thüring et al., 2015; Bosa et al., 2020). Array processing is also critical in identifying these coherent infrasonic signals within incoherent wind noise, because wind-noise waveforms can superficially resemble mass movement signals (Matoza et al., 2019). Similar methods have been

investigated for mass movement events in nonvolcanic settings (e.g., Adam et al., 1998; Yount et al., 2008; Leng et al., 2017; Moore et al., 2017; Johnson et al., 2019; Marchetti et al., 2019). We build on these studies to investigate the potential for real-time lahar detection at Mount Adams, considering realistic ambient infrasound and noise conditions near the drainages of this quiescent stratovolcano.

2.1. BEAR Array

BEAR is our long-term infrasound array at Mount Adams. Siting an array close to the primary drainages from the unstable southwest flank presumably enhances the potential for mass movement detection. The Gifford Pinchot National Forest covers the broader region, however, with much of Mount Adams itself designated a wilderness zone (Figure 1a). Long-term installations inside the wilderness boundary are heavily restricted; consequently, site locations close to likely source zones on the upper slopes are limited. The resulting design and location of the BEAR array still allows for real-time data acquisition, and minimization of permit issues.

Four Hyperion IFS-3111 infrasound sensors comprise the BEAR array, which has an aperture of 85 m (Figure 1c). Each sensor has a high-frequency shroud for wind-noise reduction. These sensors provide a frequency response within 3 dB from 0.01 to 100 Hz, low self-noise floor (≤ 0.1 mPa), and high dynamic range (120 dB). Valve boxes cover the sensors to provide basic protection from animals and snow accumulation. Wind-noise attenuation domes (e.g., Raspet et al., 2019) were not deployed due to the potential for crushing by the winter snowpack. A technical issue led to limited sensor sensitivity through 28 September 2017, after which performance was nominal. All dates and times provided are in Coordinated Universal Time (UTC). Further information on station siting and design is provided in the supplemental material available to this article.

2.2. Temporary Infrasound Arrays

The temporary infrasound arrays at PHAB (Figure 1d), CHIP, and RAIN were deployed between 26 and 31 August 2018, to provide azimuthal coverage of anticipated signal sources on the southwest side of Mount Adams as well as other noise sources in the area. Data from these temporary arrays were recorded locally with no telemetry link. Respective array apertures are ~80, ~75, and ~70 m. PHAB and CHIP were located on ridgetops on either side of the main drainage within the Mount Adams Wilderness (Figure 1), with RAIN located at a lower altitude, and in denser forest to the west of Mount Adams.

At each temporary array, the Chaparral Model 60-UHP infrasound sensors sit within foam wind filters, but are otherwise exposed to the atmosphere. Sensor performance specifications are comparable to those at BEAR, except for the greater self-noise floor here (~25 mPa), and lower dynamic range (109 dB).

2.3. Seismic Data

To detect seismicity at Mount Adams, the Pacific Northwest Seismic Network (PNSN) maintains a single-component short-period seismic station UW.ASR on Stagman Ridge (Moran, 2005), 2.5 km from our infrasound array (Figures 1a and 1b). As debris-laden rivers are also strong generators of seismicity (e.g., Hsu et al., 2011; Tsai et al., 2012; Roth et al., 2016; Walsh et al., 2020), seismic data can help corroborate ambiguous infrasound signals or otherwise clarify when our stations are not detecting known events. Unfortunately, station ASR had impaired sensitivity for ~75% of 2017–2019 (Natalie Chow, Designer and Program Coordinator, PNSN, written comm., 2020). Many time intervals contain only electronic noise or have the sensor response focused between 10 and 30 Hz. Observations of five seismogenic mass movement events at Mount Adams between 1983 and 2012 are

presented by Norris (1994) and Allstadt et al. (2017). These events were recorded on regional stations to distances of 183 km.

2.4. Data Processing

The array processing scheme is described in the following, as are expected event characteristics. We use the progressive multi-channel correlation (PMCC) array processing algorithm (Cansi, 1995; Le Pichon et al., 2010; Matoza et al., 2013) as a first step to analyze the infrasound waveform data. PMCC estimates parameters of coherent plane waves at the array, including back azimuth, apparent velocity, signal frequency, and F-statistic (akin to the signal-to-noise ratio [SNR]). The PMCC maximum amplitude estimates are approximately equal to the peak-to-peak amplitude values of the corresponding time series. Apparent velocity (v_{app}) values from PMCC can be used to infer wavefront incidence angles above the horizontal, $\theta_H = \cos^{-1}(v_{int}/v_{app})$, by assuming an intrinsic adiabatic velocity, $v_{int} \approx \sqrt{(403 \cdot T)}$. T is the temperature in Kelvin.

PMCC searches in time–frequency space for plane-wave arrivals consistent across multiple subarrays with similar wavefront properties. This approach helps reduce uncertainty in cases of spatial aliasing (Cansi and Le Pichon, 2009; Marty, 2019). The four-element BEAR array has four possible subarrays (three-sensor triads that are subsets of the full array) (Figure 1c). An array bandwidth of ~0.3–8 Hz balances wavefield estimation accuracy and spatial aliasing ambiguity (Garcés, 2013). Higher-frequency events may be well resolved if signals are clear, short, and broadband (Garcés, 2013; de Groot-Hedlin et al., 2014). We include data up to 50 Hz in this study (i.e., low audio), a range that is important for identifying small acoustic sources. For simplicity here, the term infrasound is used to include this extended frequency band.

Wavefront similarity is indicated by a low consistency value, that is, the sum of the time delays between array elements. A successful search will result in a record of the wavefield parameters for that time window and frequency-band combination—termed a pixel. Related pixels are then grouped into families, with higher pixel counts indicating more robust results. PMCC is an efficient array processing method, making it suitable for real-time applications. One day of typical BEAR data (100 samples per second) requires ~2.5 hours to process on a 3.1 GHz processor.

2.4.1. Signal Characteristics

To identify potential events at Mount Adams, we look for transient signals in the raw waveform data, together with coherent array processing results that arrive from an appropriate azimuth range with an acoustic velocity. We also examine signal amplitude, robustness of the detection family, and changes in back azimuth indicative of moving sources. Anticipated lahar signal properties include emergent, broadband seismoacoustic waveforms, which last from tens of minutes to hours in duration. For lahars capable of reaching up to 20 km, amplitudes of 2.5 Pa may be expected at a distance of 4 km during the peak of the event (equivalent to 10 Pa at 1 km), although, this is a value based on limited observations (Johnson and Palma, 2015). Waveform durations from the collapse, fall, and flow of consolidated or unconsolidated material would likely be from tens of seconds to several minutes (Allstadt et al., 2018, and references therein). Onsets could be emergent or impulsive according to the mode of initiation, with most energy concentrated from 1 to 10 Hz, depending on volume and composition. Amplitudes for such events can vary considerably, with reduced pressure observations of 1 Pa at 1 km for small rockfalls and ice avalanches (e.g., Havens et al., 2014; Johnson and Ronan, 2015), to 110 Pa at 1 km for very large avalanches (Allstadt et al., 2017). Machine-learning-based classification and location

schemes are increasingly being applied to mass wasting monitoring applications (e.g., Allstadt et al., 2018; Ye et al., 2019; Liu et al., 2020; Wenner et al., 2020).

When analyzing waveforms alongside PMCC results, denoising steps help to isolate signals of interest. Here, we apply two denoising tools on a case-by-case basis to time-delayed beams during postprocessing. First, BCseis (Langston and Mousavi, 2018), which uses an adaptive block thresholding approach in the frequency domain, and (2) an iterative Wiener filter (Plapous et al., 2006), which minimizes the difference between noise-contaminated signals and a designated noise-only section to isolate the signals of interest.

3. Results

Our results include characteristics of background infrasound from the long-term BEAR infrasound array, and records of mass wasting and other activity. Data from both the temporary infrasound arrays and BEAR are used to isolate some of the sources of the coherent background arrivals and to locate and model a glacial avalanche.

3.1. BEAR Array

3.1.1. Background Signals

Array processing results from BEAR reveal near-continuous and persistent infrasound signals arriving from the direction of Mount Adams (back azimuths 30°–65°; Figure 2a), which we hypothesize result from turbulent fluvial processes, such as rapids and waterfalls (e.g., Johnson et al., 2006; Huang et al., 2008; Schmandt et al., 2013; Feng et al., 2014; Ronan et al., 2017; Anderson et al., 2019) in the steeper upper portions of the Cascade Creek and Salt Creek drainages. Observed fluctuations in the detectability of these signals over time likely result from a combination of: (1) variation in wind-noise levels at the array (e.g., Woodward et al., 2005; Matoza et al., 2011), (2) changes in local infrasound

propagation conditions associated with atmospheric boundary layer variability (e.g., Fee and Garcés, 2007; Matoza et al., 2009; Wilson et al., 2015; Kim et al., 2018), and (3) changing flow speeds in the channels (assuming the infrasound is fluvial in origin). By covering the infrasound sensors, higher snowpacks are expected to reduce wind noise, as well as increase the attenuation of signals of interest, particularly, at higher frequencies (Adam et al., 1998). The number of detections from the 30° to 65° azimuth range is highest during the summer (May–August; Figures 2b and 2c), consistent with an increase in glacial meltwater flow. Winter (November–February) detections for this direction may relate to increased flow from rainfall and rain-on-snow melting during storms (Figures 2d and 2e). Corresponding mean signal frequencies are typically 3–20 Hz throughout the year—a similar range to whitewater features described by Anderson et al. (2019). In the 30°–65° azimuth range, apparent velocities are 330–360 m/s, indicating low incident angles and local signal sources. The time periods designated as summer and winter are derived from Figure 2a, being equal length and equally spaced periods that exhibit distinct characteristics.

The BEAR array also records seasonally dependent 3–20 Hz signals in almost all directions disjoint from Mount Adams (Figure 2). It is likely that this wide distribution of detections is also tied to high-gradient streams and waterfalls, which cover the region. An initial analysis (presented in the supplemental material) shows similar temporal trends for PMCC detection quantities and regional river discharge. The story is complex, given the variable input of rainfall and snow melt in the disparate watersheds, as well as fluctuating atmospheric conditions. In addition, waterfalls each have their own seismoacoustic signature based on height, plunge style, topographic directivity, and flow volume (Burtin et al., 2008; Díaz et al., 2014; Anderson et al., 2019). Future work with additional weather and hydrological sensors would help untangle the factors directing this fluvial infrasound.
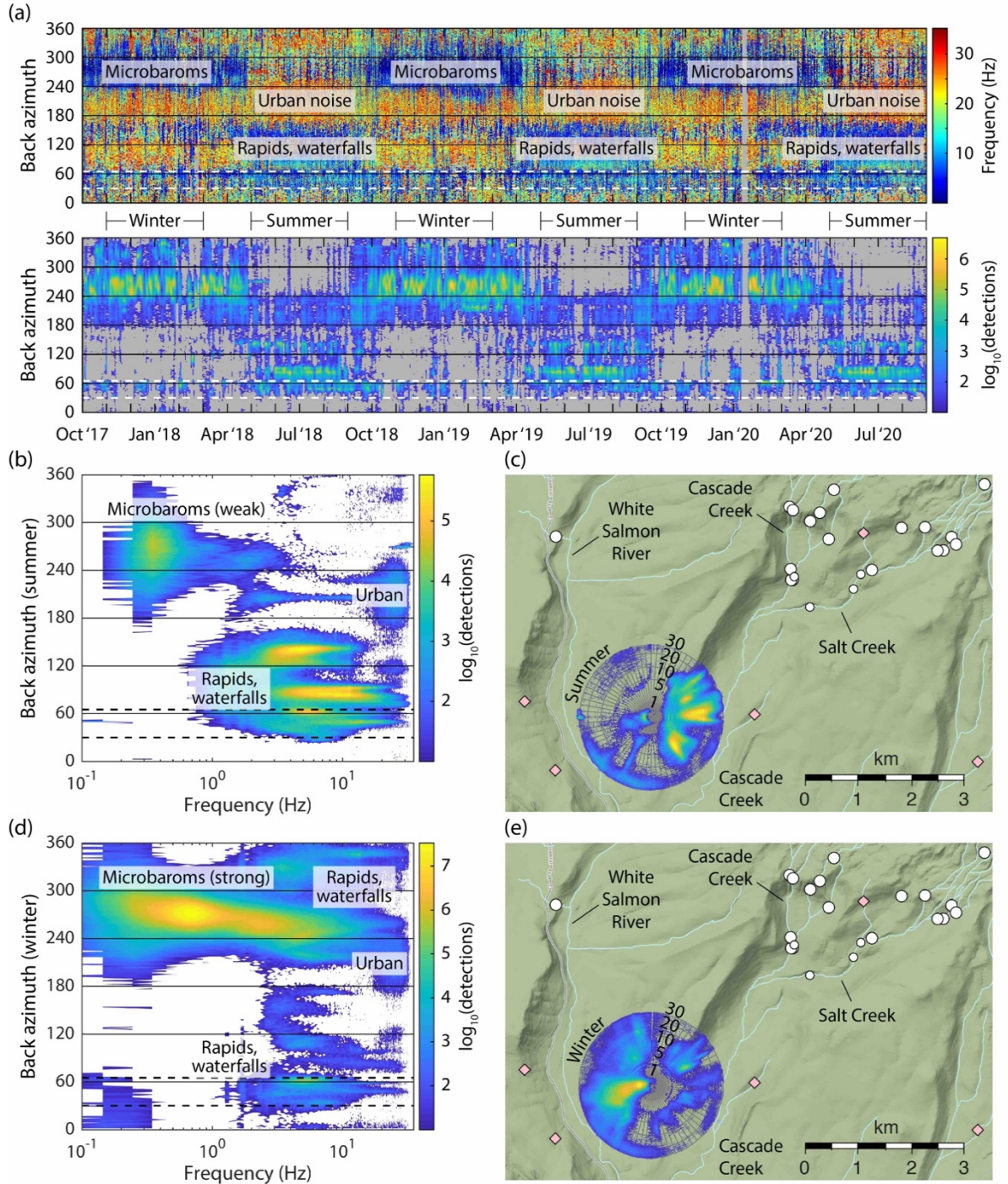
Figure 2. Seasonal trends in infrasound detections, illustrating distinct source types and locations. (a) Progressive multi-channel correlation (PMCC) results at BEAR, plotted as back azimuth versus time. The top panel is color coded by family mean frequency, and the bottom panel is color coded by the log number of detections in the top panel. Bin sizes are one day in time and 0.1 Hz in frequency. Gray indicates < 10 detections. White-dashed lines bracket the back-azimuth range to the upper Cascade Creek and Salt Creek basins (colored black in panels b,d). (b) 2D histogram of summer detections (May–August). Bin sizes are 1.0° in azimuth and 0.1 Hz in frequency. Absence of color indicates < 10 detections. (c) Polar 2D histogram for summer detections, with higher frequencies at increasing radius. The positions of waterfalls 5–10 m and > 10 m in total height are marked with small and large circles, with selected high-gradient streams as diamonds. Panels (d,e) are the same as panels (b,c), but for winter detections (November–February).

184

The most dominant feature of the PMCC processing results is the coherent background infrasound from the Pacific Ocean (microbaroms) during the winter. Wave–wave interaction primarily generates such signals, typically resulting in a peak between 0.1 and 0.5 Hz (Bowman et al., 2005). Wave–shore interaction may contribute frequencies up to 20 Hz (Garcés et al., 2006), although, significant attenuation would be expected at this distance. During the summer, microbarom signals are infrequently observed (Figure 2c) due to the change in dominant stratospheric wind direction from eastward blowing to westward blowing (Le Pichon et al., 2009), as well as a decrease in storm activity.

Another dominant feature in the PMCC results is persistent year-round higher-frequency signal content in the low-audio range (20–50 Hz), likely of anthropogenic origin from passing aircraft and surrounding urban areas (Matoza et al., 2007; Campus and Christie, 2010, and references therein; Pilger et al., 2018). The corresponding source directions are predominantly from south to southwest (a range covering Hood River, Portland, and Vancouver) (Figure 1a).

Figure 3 shows probabilistic power spectral density (PSD) plots (McNamara and Buland, 2004) for the time periods covered by Figure 2. The principal differences between the summer and winter periods are in the 0.1–10 Hz band, with a much wider range in noise level during the summer and a prominent microbarom peak in the winter. These spectra span the full range of global noise models (Bowman et al., 2007; Brown et al., 2014).

3.1.2. Mass Wasting and Other Activity

Having characterized the background infrasound at BEAR, we next examine records from BEAR (and ASR), at times of reported or imaged mass movements at Mount Adams. We then filter the PMCC results to isolate additional mass wasting candidates and other event types.
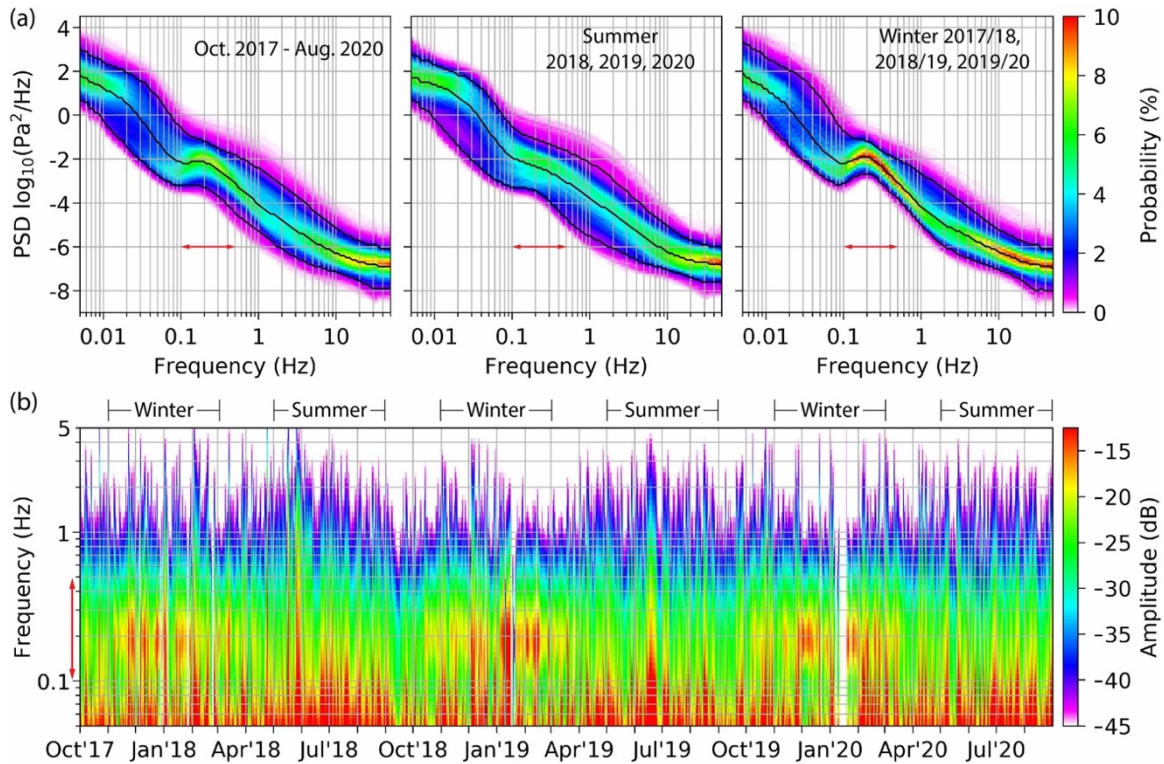
Figure 3. Seasonal trends in ambient infrasound, reflecting stronger microbaroms in winter and higher wind noise in summer. (a) Probabilistic power spectral density (PSD) estimates of BEAR (channel 1) infrasound data for (1) the whole study period, (2) summers, and (3) winters. These time periods correspond to those in Figure 2. All parameters follow those by McNamara and Buland (2004). Time windows used to estimate the PSDs are 1 hr long with 50% overlap and a 10% cosine taper. The color scheme indicates the percentage of counts in each amplitude–frequency bin out of the total count at that frequency. Bins are 1 dB by 1/8 of an octave, with powers averaged over a full octave. Black lines are the 5th, 50th, and 95th percentiles for the data in each plot. Red arrows indicate the range of the microbarom peak (0.1–0.5 Hz). (b) The temporal evolution of the PSD for the whole study period.

3.1.2.1. Search for Signals Associated with Witnessed Small Events

Table 1 lists notable events at Mount Adams between June 2017 and August 2020, as witnessed by local observers or identified in available satellite imagery. Satellite images are four-band PlanetScope Scenes (3 m resolution, see Data and Resources), which were visually inspected only during time frames indicated to be of interest by local witness reports or seismoacoustic data. The table includes debris flows, glacial movements, and changes in river character, which may indicate potential upstream debris flows in the preceding hours. Since the installation of BEAR, there have been five visually confirmed mass movements: two in 2017, and one each in 2018, 2019, and 2020. This number is likely an underestimate.

186

Table 1. Witnessed accounts of physical processes at Mount Adams from 2017 to 2020 which may have produced seismoacoustic signals, and brief notes on any corresponding geophysical data. The "timing" column gives a window during which the event may have occurred (or did) given the observations in the "time constraints" column. All times are UTC. Seismometer response was impaired < 10 Hz during events from 2017–2018, and impaired at all freqs for the 2019 event. PMCC, Progressive Multi-Channel Correlation.

Timing	Location	Description	Infrasound (BEAR)	Seismic (ASR)	Time constraints
18:12:07 3 June 2017 – 18:12:40 4 June 2017.	Battlement Ridge to Klickitat Glacier, SE Mount Adams.	Debris flow ~1.6 km long, 400,000 m³ (Darryl Lloyd, written comm., 2017).	Not installed.	Most likely candidate a broadband envelope at 21:01 3 June, duration 5 minutes.	Satellite images on 3 (not seen) and 4 June (seen). In-person observation on 6 June (Darryl Lloyd, written comm., 2017).
~5–11 Sep. 2017.	Below summit onto White Salmon and Avalanche Glaciers.	Debris flow from ~3,350 to 2,750 m elevation.	Not fully operating. No clear signals.	Frequent emergent and impulsive events. Sustained signal 4 Sep. 13:00–22:00.	White Salmon River muddy on 6 Sep. In-person view on 11 Sep. Unclear in satellite images.
19:30–20:00 15 Sep. 2017.	Above Horseshoe Meadows, SW Mount Adams.	"Rockslide" sounds.	Not fully operating. No clear signals.	Elevated seismic signals from 19:35 to 20:35.	Noises reported by hikers.
~10–11 July 2018.	White Salmon River in Trout Lake.	Muddy flow.	No strong candidate signals. Persistent noise.	Sustained noise. Several prominent impulsive events.	In-person observation on 11 July. Satellite images show minor snow melt.
20–27 July 2018, possibly earlier, or as late as 5 Aug. 2018.	White Salmon Glacier headwall onto Avalanche Glacier.	Small debris flow from ~3,600 to 2,700 m elevation, 1.4 km distance (Darryl Lloyd, written comm., 2018).	Strong diurnal wind noise. Few robust candidate signals. Broadband impulses from ~22:00 4 Aug. to ~03:00 5 Aug. during an intense storm are consistent with thunder. Some back azimuths during the storm coincide with nearby water turbulence.	Frequent impulsive events amidst diurnal noise. Candidate signals at 16:37 21 July, and 14:36 27 July. Clear broadband signals during storm ~22:00 4 Aug. to ~03:00 5 Aug.	In-person observations on 20 July (potentially not seen), 27 July (potentially seen) and 5 Aug. (seen). Unclear in satellite images.
~28–30 July 2018.	White Salmon River in Trout Lake.	Muddy flow.	Few clear events with no strong candidate signals, noisy background.	Long noisy periods (only some diurnal), frequent events, no standout candidates.	In-person observation on 29 and 30 July. Satellite images show some snow melt.
8–9 Aug. 2018.	White Salmon Glacier.	Noises heard.	Prominent event at 20:22 9 Aug., but PMCC metrics inconsistent with a local origin. Otherwise few clear events.	Frequent impulsive events, more commonly during daytime when hot. Includes remote event at 20:22 9 Aug.	Noises reported by hikers. Satellite images show widening crevasses on the upper White Salmon Glacier 8–10 Aug.
21:34:54 24 Aug. – 18:29:25 28 Aug. 2018.	White Salmon Glacier.	Ice/snow avalanche (not witnessed in person).	Clear impulsive broadband arrivals on all four infrasound arrays ~16:01 28 Aug.	~16:01 28 Aug. 2018 event is just above background seismically.	Satellite images on 24 (not seen) and 28 Aug. (seen).
22:48–23:08 28 Aug. 2018.	White Salmon Glacier.	Noises heard.	Strong background noise, no clear signals, but several viable PMCC detections.	Impulsive signals 22:37–22:45 (earlier than observations).	In-person observation. Satellite images show no significant glacier changes.
8–15 June 2019.	Below summit onto Avalanche Glacier.	Debris flow from ~3,400 to 2,800 m elevation, 900 m distance.	Strong diurnal wind noise. PMCC shows two potential detections at ~03:28 12 June, but metrics aren't robust.	Potentially a series of four pulses at 17:49 11 June, duration 1.5 mins.	In-person view on 8 June (not seen) and 15 June (seen). Satellite images on 11 June (not seen) and 15 June (seen).
~22:30 4 July 2020.	Above Stagman Ridge, SW Mount Adams	"Avalanche" sounds.	No distinct waveforms or potential PMCC detections.	No distinct waveforms.	Noises reported by hikers. Unclear in satellite images.
~01:45 31 Aug. 2020. May extend before/after by a few hours.	Above tree line on SW Mount Adams, toward Williams Mine	Rockslide	No distinct waveforms or potential PMCC detections during +/- 2 hours.	Few distinct waveforms during +/- 2 hours. Large impulsive glitch-like signal at 01:08.	In person view during event. Unclear in satellite images.

In cold months in particular, the mountain often is hidden by clouds, and human access is limited, making visual observations of events difficult. All observed events took place from June to September, when temperatures are relatively warm, snow is melting, and the greatest potential for instability occurs (e.g., Mills, 1991). The 28 August 2018 event is the only entry from Table 1 for which we could find clearly attributable seismoacoustic signals. The main complications are: (1) relatively small amplitude events; (2) poor knowledge of the timing of the events; (3) coherent array detections (clutter) regularly coming from the expected azimuths; (4) waveform characteristics are likely weak and emergent, and superficially similar to wind noise; (5) unknown local propagation conditions; and (6) limited numbers of stations and data types. In conclusion, few obvious waveforms correspond to the events of Table 1, because these events likely are at or below station detection thresholds.

To illustrate the previous issues, Figure 4 shows selected processing results for the speculated time period of the July 2018 debris flow event. Data types include PMCC processing results (back azimuth, cross-correlation, maximum amplitude, each color coded by family mean frequency), filtered beamformed data, and spectral content over time. Diurnal winds are expected to present with power inversely proportional to frequency, but, notably here, the relative power in each band is inconsistent over time. The wind bursts interrupt the higher-frequency background PMCC detections in Figure 4 (with similar observations by Matoza et al., 2009; Green et al., 2012; the time series in Figures 2 and 3 also show a similar relation between PMCC detection gaps and wind bursts). Lower-frequency detections are more continuous, particularly, on 20 and 21 July. The next section shows that there are no clear detection candidates for the July 2018 debris flow when considering appropriate PMCC wave parameter combinations.
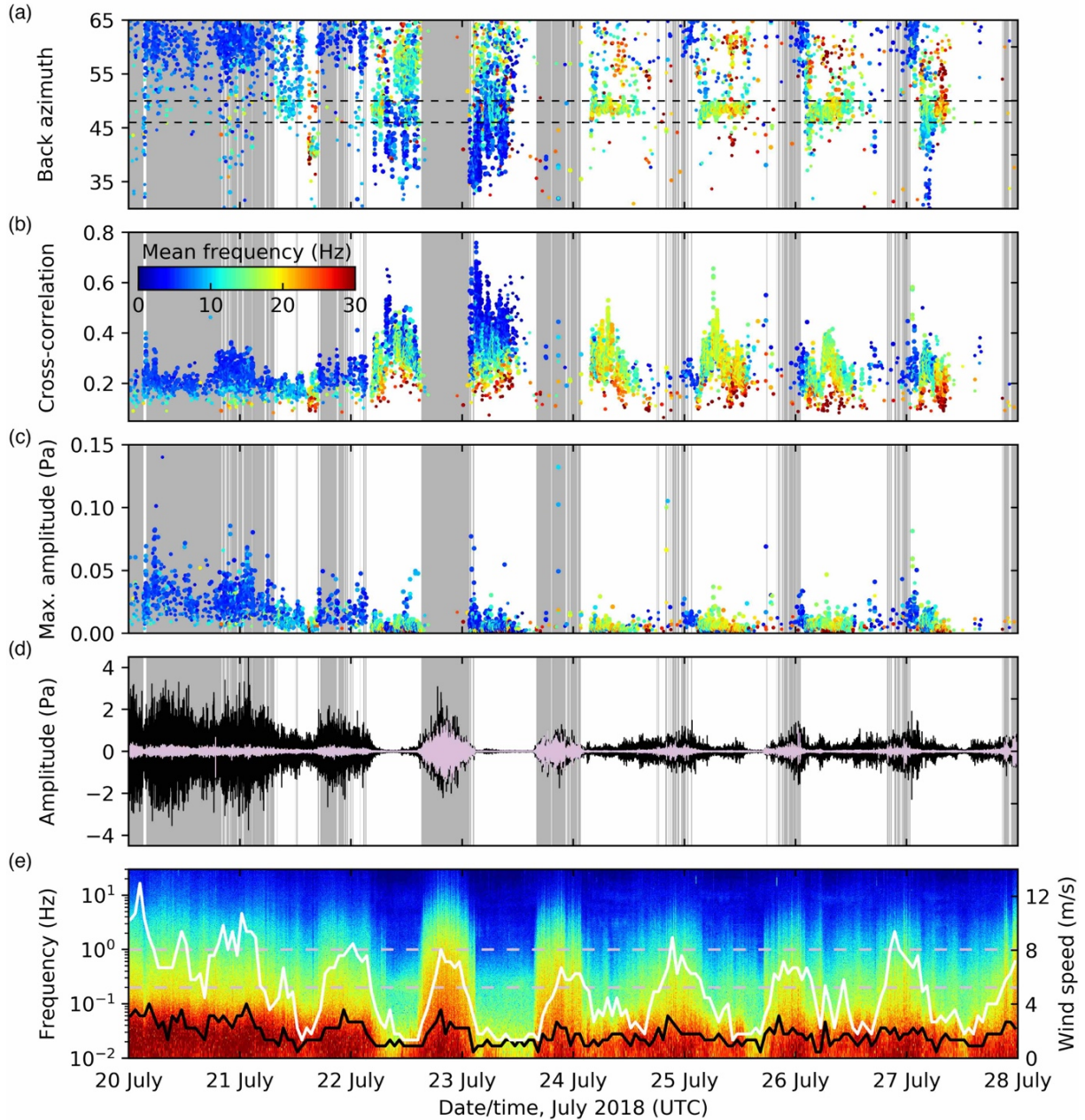
Figure 4. BEAR infrasound analysis for period spanning speculated occurrence of a debris flow at Mount Adams (as per eye witness details in Table 1), showing how wind noise can affect event detectability. (a–c) PMCC results limited to those detections with back azimuths from 30°–65°, which covers the majority of Mount Adams. Horizontal dashed lines cover the expected event back-azimuth range. Detections are color coded by family mean frequency. Incoherent wind noise from 0.2 to 1.0 Hz correlates well with gaps in high-frequency PMCC detections, with background shading applied if the PSD sum from 0.2 to 1.0 Hz exceeds 0.6 Pa^2/Hz (5.5 min bins). d) Beamformed infrasound for a back azimuth of 48° and apparent velocity of 350 m=s, values appropriate to sources traversing the Avalanche Glacier. Waveforms are filtered before beamforming as follows: 0.01–0.2 Hz (black trace) and 0.2–1.0 Hz (purple trace). (e) A spectrogram of unfiltered beamformed infrasound, with dashed lines at 0.2 and 1.0 Hz. PSD is plotted on a log scale. Mean wind speed (solid black line) and maximum wind speed (solid white line) are from the U.S. Forest Service station at BKRW1 (Fig. 1b). Characteristics of signals from debris flows are either absent (no events occurred) or cannot be easily identified with such analysis.

189

3.1.2.2. Distilling and classifying automatically detected signals

Following our search for signals associated with known mass movements, we now aim to identify instances of such events on the upper slopes of Mount Adams for which we do not have first-hand accounts. We isolate possibly associated PMCC detections by requiring positive SNRs (F-statistic ≥ 1.5, peak-to-peak amplitude ≥ 0.1 Pa), appropriate locations (back azimuth 40°–55°, apparent velocity 330–360 m/s), with reasonable thresholds (number of pixels ≥ 35, cross-correlation ≥ 0.6). We also limit results to those with mean frequency ≥ 5 Hz to avoid some fluvial detections. Since August 2017, there have been 36 events matching these criteria. PMCC processing results for these events are included in the supplemental material. Such events do not, however, coincide with those in Table 1, other than that on 28 August 2018. This remains the case with no minimum amplitude (which gives 444 detections).

Using the presumed waveform characteristics (the Data Processing section; Allstadt et al., 2018) as well as weather data (from Ventusky, see Data and Resources), we classify 12 of the 36 events as mass wasting candidates. Durations range from 20 to 90 s, with amplitudes up to ~0.22 Pa. In the example in Figure 5a, ASR first registers the direct seismic arrival at 7 s and then an acoustic component as a ground-coupled airwave (GCA) at 37 s. BEAR records the direct airwave ~5.4 s later. The acoustic arrival times and PMCC back azimuth (44.3°) indicate a source region at ~2,000 m elevation (assuming a velocity of 333 m/s, appropriate for a mean path temperature of 2 °C). The corresponding origin time would be ~14 s and may relate to the broadband seismic component. Eleven of the twelve mass movement candidates have similar back azimuths (42°–46°), spanning the White Salmon Glacier. The remaining event aligns with the Avalanche Glacier headwall (46°–49°), from which multiple debris fans indicate minor ongoing rockfall. In the next section, we more

190

fully analyze the 28 August 2018 event, which was detected by the three temporary infrasound arrays, in addition to BEAR, and is the only one of these mass movement candidate events to clearly appear in satellite imagery.
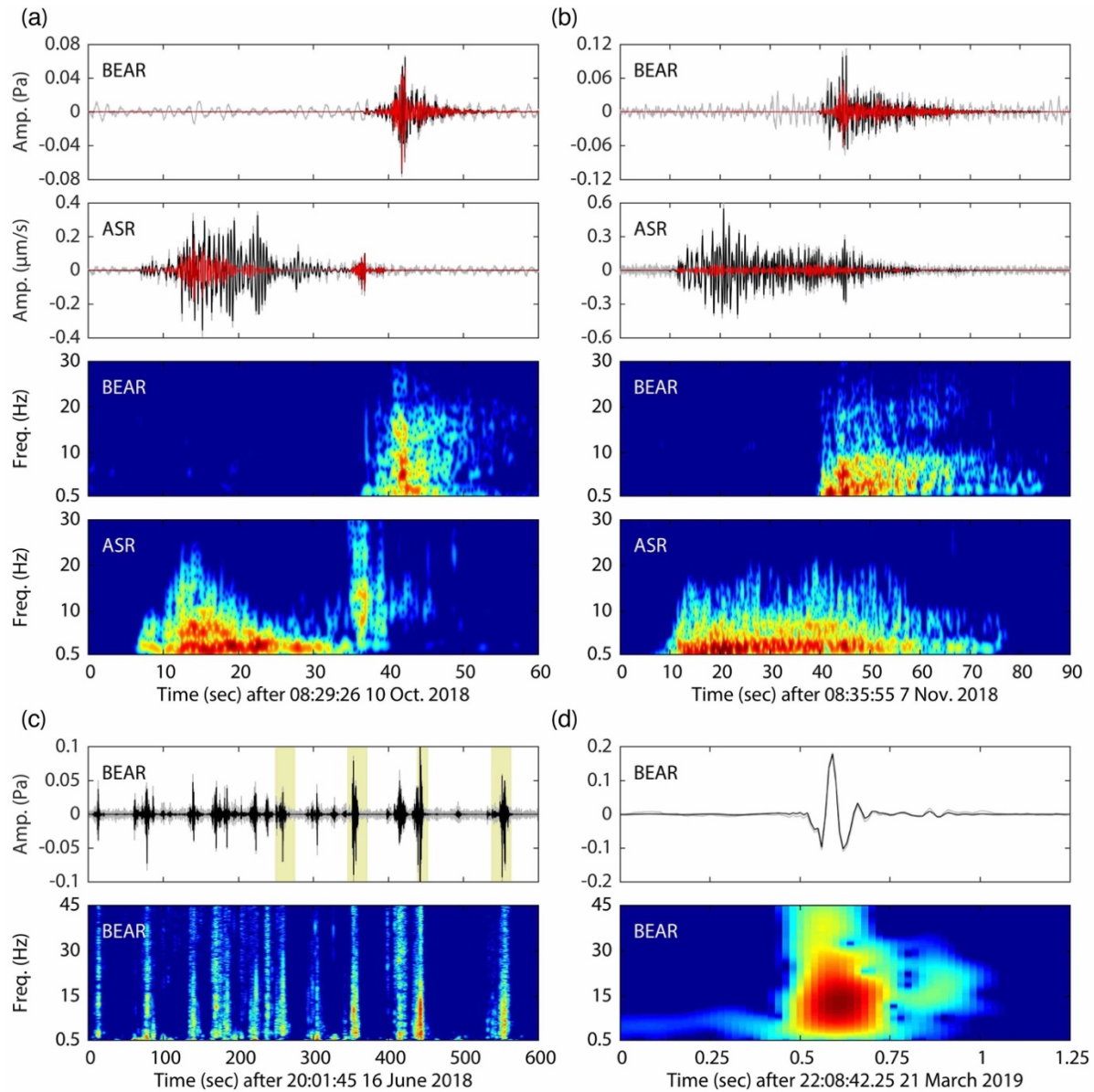

Figure 5. Examples of several event types that have back azimuths coincident with Mount Adams. (a) Potential mass wasting event from 10 October 2018 recorded at BEAR and ASR. A ground- coupled airwave (GCA) arrives at ASR at ~37 s. (b) A potential mass wasting event from 7 November 2018. Any GCAs at ASR are unclear in this case. (c) Thunder events at BEAR. Yellow-highlighted signals are those that coincidentally met the PMCC event parsing criteria. (d) Impulsive event example from 21 March 2019, possibly caused by an icequake or tree fall. In all figure parts, gray traces are > 0.5 Hz, black traces are denoised using BCseis, and red traces are black traces > 4 Hz. Infrasound traces have been beamformed using back azimuth and apparent velocity values from PMCC. The spectrogram plots PSD on a log scale, with warm colors indicating relatively high values and cold colors indicating relatively low values.

We interpret 18 of the 36 events as thunder (e.g., Farges and Blanc, 2010), occurring as part of sequences. Each instance typically has an erratic waveform 10–30 s in duration with an amplitude < 1 Pa (Figure 5c), although, events of up to 4 Pa and > 60 s have been recorded. Spectra tend to be even and broadband, though some spectra peak < 10 Hz, perhaps indicating relatively distant sources (Bass, 1980; Assink et al., 2008). When ASR is operational, thunder is typically registered via weak GCAs, with arrival times relative to BEAR dictated by the back azimuth. The absence of direct seismic arrivals for these events reduces the probability of these events being mass movements. Few of the hundreds of these thunder signals remain after parsing the PMCC detections; thus, our simple PMCC bulletin selection criteria are useful for an initial basic data screening. A more robust set of discriminators may be required, however, because the character of thunder can vary widely (e.g., Johnson et al., 2011; Liu et al., 2015; Marchetti et al., 2019; Haney et al., 2020), and repeated surges of fluidized debris flows may produce similar sets of signals (e.g., Kogelnig et al., 2014; Liu et al., 2015).

The remaining six events are impulsive with short codas, lasting 0.5–3 s, and spanning 3–30+ Hz in frequency. Four of the examples have negative first motions (Figure 5d). These events may be icequakes (comparable to those described by Lombardi et al., 2019, with Richardson et al., 2012, and Allstadt and Malone, 2014, being other useful references) or possibly large tree-fall events. We rule out electromagnetic interference, given the acoustic travel times, general absence of thunderstorms, and similar amplitudes on each sensor (vs. Haney et al., 2020). Gun shots are also unlikely, as such signals are typically ≪ 0.5 s in duration (e.g., Maher and Shaw, 2008).
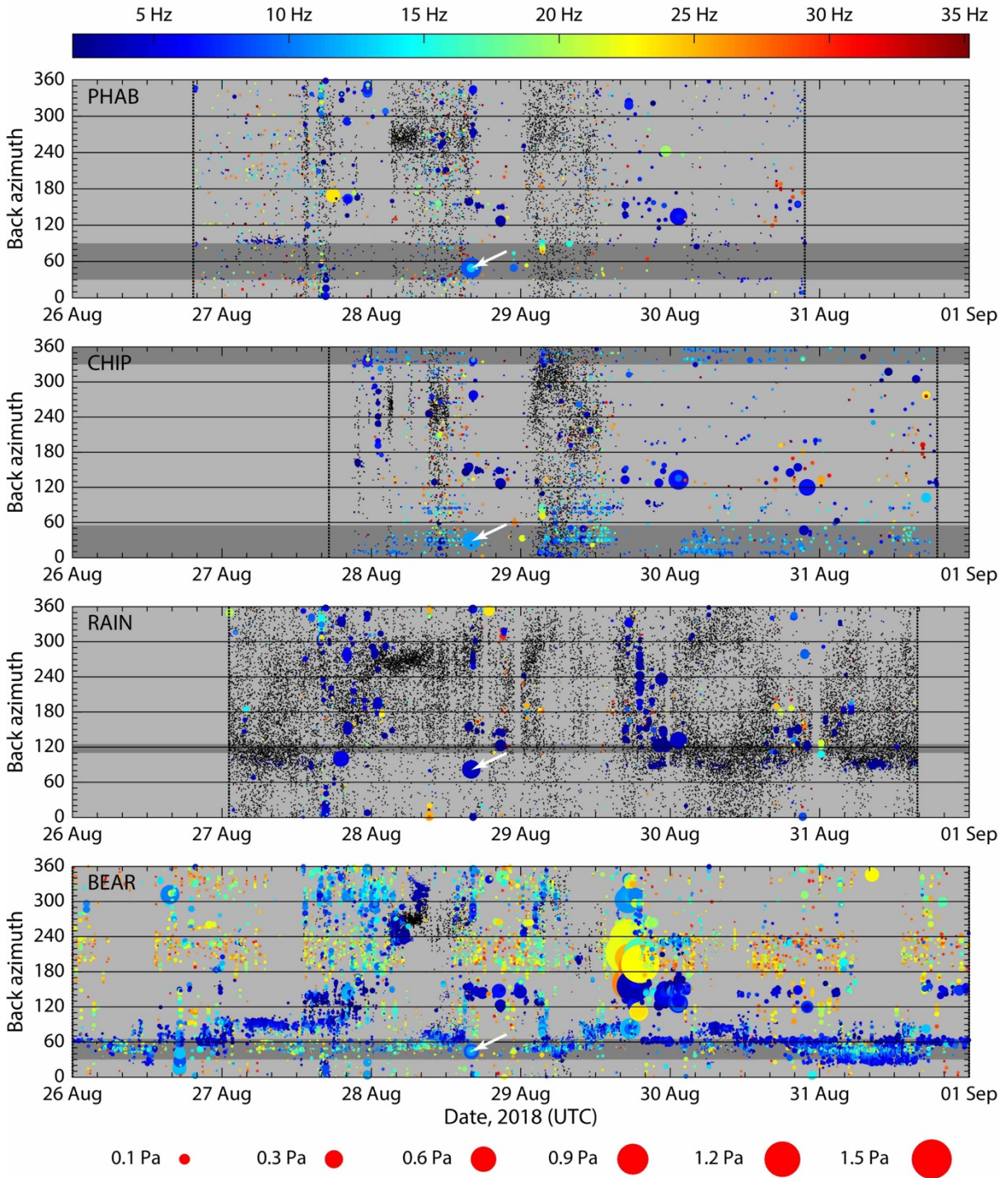
Figure 6. PMCC results from (a) PHAB, (b) CHIP, (c) RAIN, and (d) BEAR for 26–31 August 2018, showing highly variable detection sensitivity. Detections ≥ 2 Hz are scaled according to the maximum amplitude for each family and colored according to mean family frequency. Detections <2 Hz are shaded black and not scaled. Back azimuths are clockwise from north. Darker gray bars encompass the azimuth range of the upper basins of Cascade Creek and Salt Creek for each station (Fig. 1a). Vertical dotted lines indicate the respective recording periods. At CHIP, a technical issue affected the data quality for the first 3.5 hours, resulting in a gap in the PMCC detections. All these detections are coherent infrasound arrivals, rather than noise, with the majority likely deriving from the numerous turbulent streams and waterfalls in the region. White arrows point to a glacial avalanche (Table 1).

3.2. PHAB, CHIP, and RAIN Arrays

As with the BEAR results earlier, we first address the origins of the background signals recorded by these temporary arrays and then proceed to an example of mass wasting. These results help illustrate the challenges relating to site selection and source characterization.

3.2.1. Background Signals

PMCC detection results for each station are presented in Figure 6, with a focus on identifying any arrivals from the waterfalls located in the upper Cascade Creek and Salt Creek basins (Figures 1 and 2). We retain detections > 2 Hz to limit inclusion of microbaroms. Of the temporary stations, CHIP has the most detections within the back-azimuth band, with PHAB not indicating any sustained signal sources. At RAIN, some sustained detections occur, though in a back-azimuth range of 82–96°, corresponding to the sources either nearby RAIN, or higher up Mount Adams, in the region of the White Salmon and Avalanche Glaciers.

To constrain source locations, we apply an automated cross-bearings approach with the IMS-vASC algorithm (Matoza et al., 2017). IMS-vASC uses a grid search to tally the number of intersecting back azimuths over time. Here, we use a grid resolution of 0.005°. Figure 7 shows sample results, highlighting intersections of ≥ 20 pixels between the nearest station and at least one other station. Other requirements are family frequency ranges of 2–35 Hz and an azimuth tolerance of 2°, to limit results to the principal local sources within ~20 km. Figure 7 also shows the location of waterfalls as well as selected high-gradient streams, each of which may be potential signal sources. Waterfall data are primarily via the Northwest Waterfall Survey (see Data and Resources). We find a general coincidence between these fluvial features and the back azimuths where topography and propagation

194

conditions allow. Line of sight is particularly limited around RAIN, where several falls are behind ridges or in deep canyons. More sources are detected when use of the closest station to the intersection is not required, but the configuration in Figure 7 more clearly outlines the effects of acoustic and topographic features. Drainages on Mount Adams coincide with the most dominant detections as anticipated. Falls with low discharge, such as Swampy Meadow Falls (~0.1 m^3/s), may not be detected, despite being ~15 m in total height. Conversely, unidentified waterfalls may exist beneath the widespread dense tree coverage. Some intersection areas may be coincidental overlaps from temporally distinct events or derive from multiple arrays having similar back azimuths for the same event. An IMS-vASC video in the supplemental material illustrates the episodic directionality of the detections.
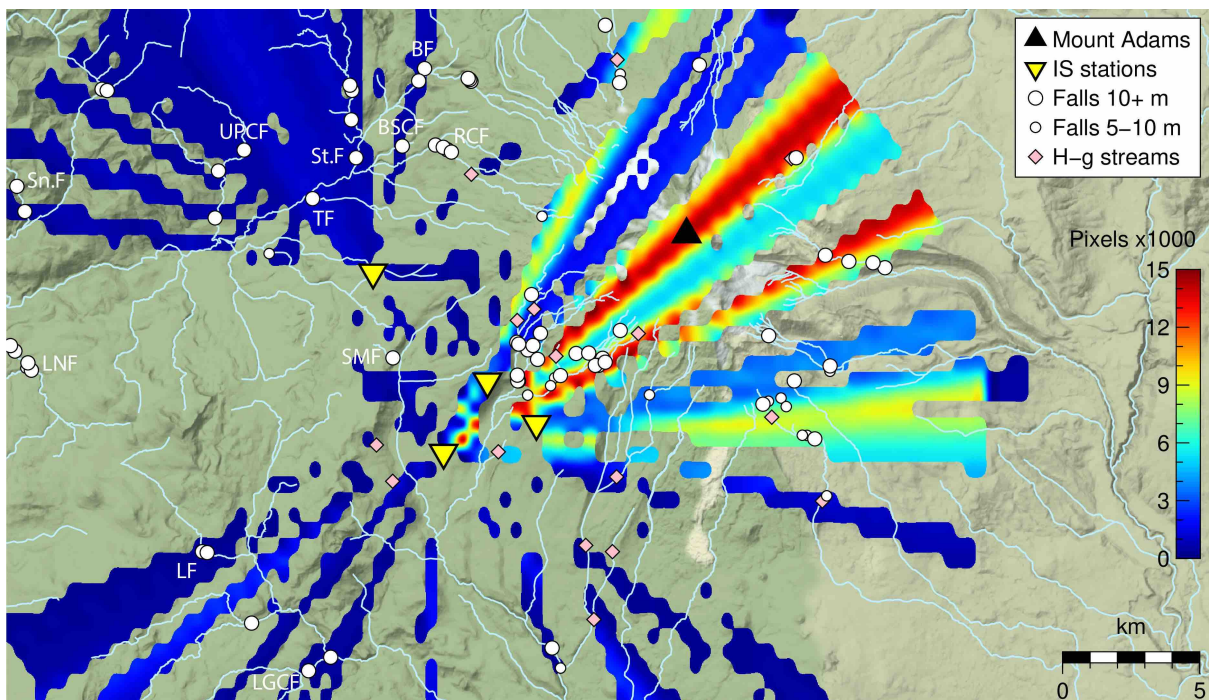

Figure 7. Back-azimuth intersections for 26–31 August 2018 (grid-during layer from IMS-vASC) showing a high coincidence between infrasound arrival directions and turbulent waters. Total pixel counts (> 275) are displayed for a grid square only if the nearest station detects a signal from the appropriate back azimuth, as well as any one other station. The positions of known waterfalls are indicated, along with selected high gradient (H-g) streams that align with IMS-vASC features. Some well-known waterfalls are labeled: BF, Babyshoe Falls; BSCF, Big Spring Creek Falls; LF, Langfield Falls; LGCF, Little Goose Creek Falls; LNF, Little Niagra Falls; RCF, Riley Creek Falls; SMF, Swampy Meadow Falls; Sn.F, Snagtooth Falls; St.F, Steamboat Falls; TF, Twin Falls; UPCF, Upper Pin Creek Falls.

In general, PHAB and CHIP had noticeably few detections, despite proximity to potential signal sources on Mount Adams (Figure 7). We attribute this, in part, to their ridgetop locations, where widespread wildfires had led to sparse vegetation (Figure 1) and relatively high wind noise (Hedlin et al., 2002; Webster and Raspet, 2015). The wildfires meant that more forested sites in proximal areas were unavailable. Gaps in detections, as with BEAR, coincide with increases in wind noise (Figure S3). Variation in proximity to sources, propagation conditions, and station hardware noise floors may also be relevant. The station geometry is also likely to contribute to the detection discrepancy, because BEAR detections fall by ∼50% when using only the outer three sensors. Global Positioning System (GPS) positional accuracy due to tree density (i.e., sensor location error of ∼2–3 m) may also have affected array processing results. Due to the relatively poor detection rates for the temporary stations, we used lower signal association thresholds in PMCC.

3.2.2. Glacial Avalanche

An avalanche occurred on the White Salmon Glacier on 28 August 2018 at ∼16:01, as determined using infrasound and satellite imagery. Analyzing such events in detail helps constrain the detection, location, and modeling capabilities of the arrays. All four infrasound arrays clearly recorded the event for 25 s, despite amplitudes below 0.3 Pa (Figures 6 and 8a and Table 1). The mean frequency of PMCC families ranged from 4 Hz (RAIN) to 12 Hz (CHIP), with the full-frequency range between all sites 0.4–40 Hz. Such results depend on attenuation and SNR for each station. Waveforms begin emergently, are briefly dominated by two low-frequency (0.3–2.5 Hz) impulses, and then decay slowly. The event is preceded by 15 s by two broadband precursory signals (Figure 8a) on all arrays except RAIN. The consistent time delay between precursory and main phases indicates a co-located source.
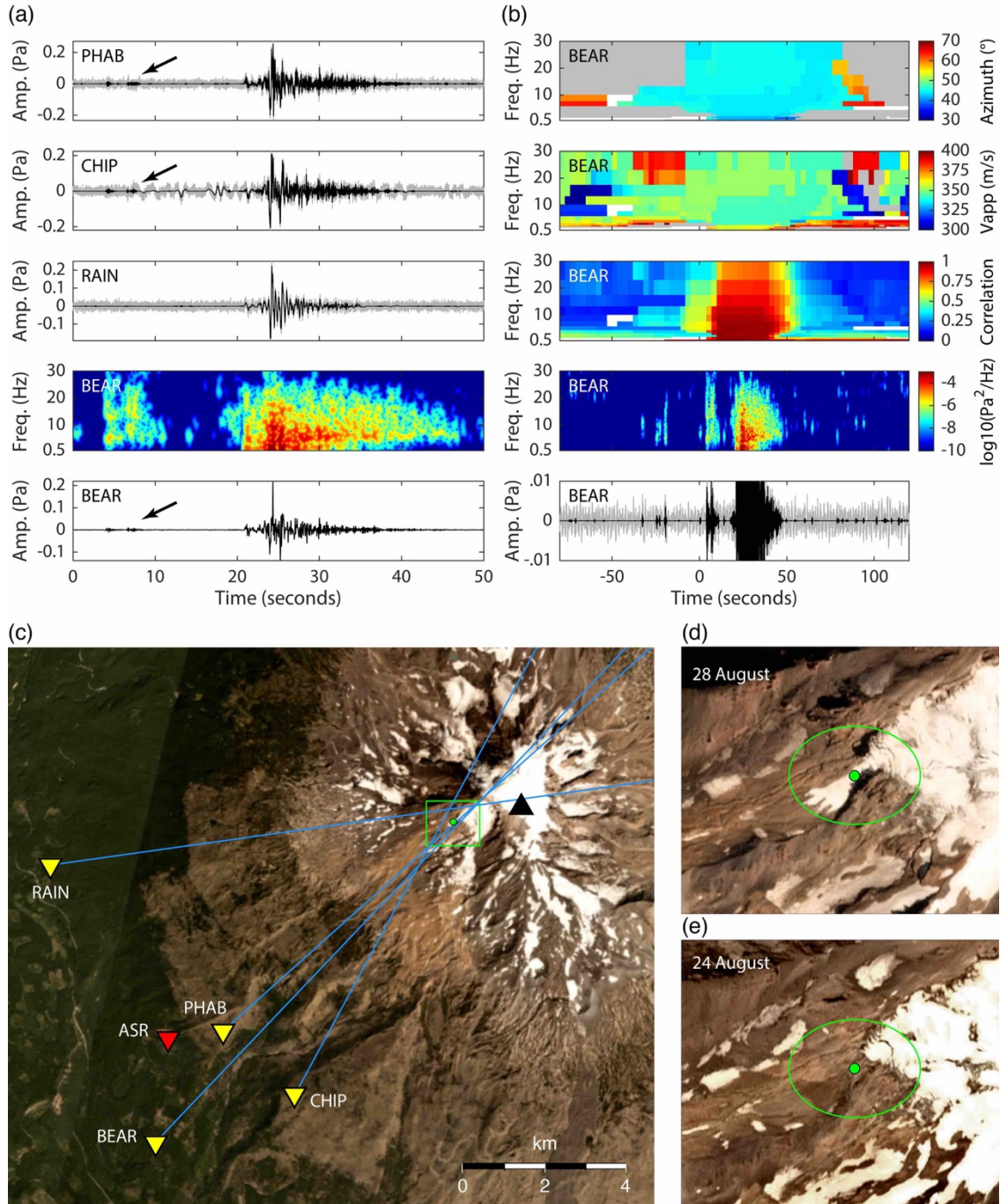
Figure 8. Glacial avalanche signal characteristics, array processing results, and derived location. (a) Beamformed infrasound waveforms from event on 28 August 2018 at ~16:01, for frequencies > 0.5 Hz (gray) and subsequent denoising with a Wiener filter (black). Apparent velocities (v_{app}) and back azimuths used in the beamforming are the means from PMCC families whose maximum frequency is 5 Hz. The spectrogram plots PSD at BEAR using the same scale as that in panel (b). Arrows point to weak precursory infrasound. (b) Expanded timeframe for same event from panel (a), focusing on BEAR data. Back azimuth, v_{app}, and correlation values derive from PMCC statistics. Gray pixels are off-scale; white means no pixels. Waveform clipping helps illustrate the precursory signals prior to 20 s. (c) Triangulation of PMCC back-azimuth values used in panel (a). The marked area around the intersection of back azimuths is expanded in panels (d, e), which also show the mean location provided by the inversion of sensor arrival times as a green dot, and the 95% confidence interval. The images in panels (c, d) are from 28 August 2018 at ~18:29.

Back azimuth and apparent velocity statistics for BEAR show sustained values during the precursory signals and main event (Figure 8b). This consistency extends ~40 s earlier at BEAR, with additional impulsive signals detected (−32 to −18 s in Figure 8b), though these features are not observed at the other arrays. Back-azimuth triangulation places the event at a steep (45°) bluff at the front of the upper White Salmon Glacier (Figure 8c). Back azimuths are determined by averaging PMCC families with maximum frequencies up to 5 Hz. We find that incident angle estimates from each station do not converge on a specific elevation for a source, regardless of modeled mean path temperature or the family frequency range considered. RAIN tends to underestimate the angle, with BEAR overestimating (as is also the case for mass wasting events in Figure 5). Without further calibration, the method has limited application at BEAR, given that errors of a few degrees will give high-elevation uncertainties at remote source-station distances. We also perform an iterative least-squares inversion of the 13 arrival times for the event using the location method of Geiger (1910, 1912), more recently addressed by, for example, Ge (2003), Stein and Wysession (2003), and Havskov and Ottemöller (2010). Altitude is allowed to vary in 10 m steps from 2,500 to 3,800 m, and velocity from 300 to 400 m/s in 2.5 m/s increments. One hundred inversions are performed, randomly perturbing the collective arrival times at each array by 0.15 s, while necessitating the adjustments of PHAB and CHIP be within 0.15 s of each other, given their similar locations. The resulting 95% confidence interval ellipsoid centers at the bluff within the triangulation mesh, spanning 540 m × 400 m horizontally, 934 m vertically (Figure 8d). The mean altitude is ~85 m above the corresponding elevation. Attempting to locate the event with just arrival times from BEAR provides a poor location estimate. Better results may be obtained using alternate location methods for single arrays, for example, Szuberla et al. (2006), Shani-Kadmiel et al. (2018), Green and Nippress (2019), and Shang et al. (2019).

Satellite photographs taken 2.5 hours after the located event show an ~20,000 m² area of glacial avalanche debris from the front of the upper White Salmon Glacier (Figure 8d). Prior to the event, the closest images with clear views are four days prior, without evidence of debris (Figure 8e). Ongoing instability is implied by rockfall debris in the same area at other times of year.

The infrasound signals themselves suggest a mixture of falling and flowing processes (Allstadt et al., 2018, and references therein). The precursory components and emergent onset may reflect the initial detachment and failure stages (Zimmer et al., 2012; Havens et al., 2014; Schimmel et al., 2017). Given the absence of real-time visual observations of the event, a detailed attribution of the infrasound source time function to a specific mass movement sequence is not possible. To a first order, however, we model the source time history as a hemispherical monopole in terms of the mass (M) of air displaced:

$$M(t) = 2\pi r \iint P(t) \, dt^2$$

in which P is the pressure time series and r is the source-station distance (e.g., Lighthill, 2001; Oshima and Maekawa, 2001; Moran et al., 2008). Figure 9 shows that the highest mass values are ~100 kg, equivalent to a sphere of ~6 m diameter (d), assuming an air density of 1 kg/m³. A monopole is applicable when the source is acoustically compact (d ≪ λ/2π, λ is the wavelength) and recorded in the far field (r ≫ λ/2π). Here, d = 6 m, λ = 337.5m at 1 Hz, and r > 7,700 m, thereby reasonably approximating a monopole.

Multiple peaks during the source time function in Figure 9 may indicate repeat collapses from the glacier front. Given the size of the debris fan is much larger than that implied by the mass values in the source time function, we speculate that contributing factors to the discrepancy may be (1) additional events occurred in the preceding four days that went

undetected, (2) low turbulence of the flow front was inefficient in generating infrasound (e.g., Naugolnykh and Bedard, 2002; Mayer et al., 2020), (3) little momentum was built up by the avalanche during the short (~300 m) unconstrained runout on a rough surface, with, for example, Kogelnig et al. (2011) showing a strong correlation between velocity and infrasound pressure for moving sources. Seismically, the event is barely above the background noise, due to an impaired sensor response.
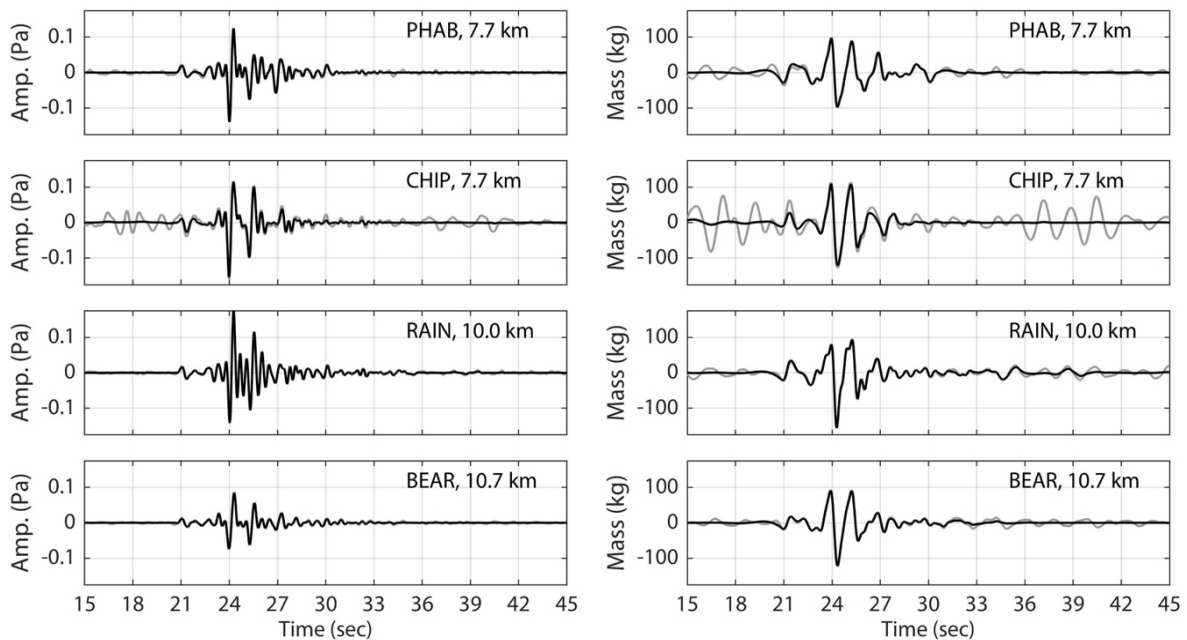

Figure 9. Glacial avalanche infrasound records and their equivalent mass source time functions. (a) Infrasound amplitudes at each array (0.5–3 Hz). Black traces have been denoised with a Wiener filter, gray traces have not. For CHIP, we remove remaining noise from 16 to 19 s by manually editing the spectral content with BCseis. The timescale matches that from Figure 8a. Distances are those between arrays and the mean source location provided by the travel-time inversion. (b) Mass equivalent source time functions for black and gray traces.

4. Discussion

Our study is motivated by the potential of using infrasound to quickly detect, progressively locate, and swiftly alert people about oncoming large lahars, which are both hazardous and relatively infrequent at Mount Adams. To the extent that smaller mass movement events may be precursors or triggers to large events, we are initially aiming in this

study to characterize sources of background noise, and identify thresholds and best methods for event detection using infrasound arrays. During our three-year study, several small debris flows or flow candidates were reported by local observers; however, we did not find signatures of these events in our data (Table 1). In contrast, we identified 12 events at BEAR that are possible candidates for mass movements based upon expected seismoacoustic signal characteristics. With one exception, none of these signals had local reports or other visual data to illuminate associated physical processes. Using additional temporary arrays, in addition to the main BEAR array, we were successful in locating and characterizing a glacial avalanche on the upper White Salmon Glacier. This event was confirmed using before and after satellite images. The corresponding local time for the event was early morning, with low wind typical of the time period improving potential SNR. In general, our results of mass movement observation are primarily limited by (1) infrequent events above the detection threshold of our arrays, (2) a lack of visual observations of activity for those candidate detections we do have, and (3) year-round background sound clutter from the direction of Mount Adams that is unrelated to mass wasting.

To quickly and accurately locate the incipient stages of hazardous lahars from the summit area of Mount Adams with infrasound, it may be beneficial to add permanent arrays nearer to source zones. The limited detection of known mass movements to date implies that improved SNR equipment design (e.g., Albert and Pankow, 2019, 2020) and preprocessing noise reduction strategies (e.g., Williams et al., 2020) would be of use for deployments in these more exposed areas, and where source amplitudes could be relatively low. Given permitting issues, however, potentially desirous solutions like low-cost and low-power telemetered systems that reduce preparation and installation time (e.g., Schimmel et al., 2018; Ye et al., 2019), may prove challenging to implement. We find that when ASR is

correctly operating, some small mass movement events are clearly detectable seismically (Figure 5). Seismic propagation velocities mean that low alarm latency can be achieved at ASR, despite its location outside the wilderness boundary. A sole seismic station, however, has limited effectiveness in a monitoring capacity.

Notably, lahars can grow in volume as they propagate down drainages, which we have shown to be sources of (presumably) fluvial infrasound with many similar signal characteristics. Obvious changes in back azimuth with time can be indicative of flow fronts (e.g., Bosa et al., 2020), but static sound sources can develop during flows at waterfalls, check dams, and due to propagation effects caused by topography (e.g., Johnson and Palma, 2015; Marchetti et al., 2019). For a single array such as BEAR, these scenarios provide a strong challenge for automated signal detection, location, and modeling procedures. For one or more arrays, probabilistic analyses and modeling could potentially help establish confidence levels for detection thresholds for a range of network configurations (e.g., Le Pichon et al., 2009; Green and Bowers, 2010; Tailpied et al., 2013), given a priori assumed lahar source signal properties of amplitude, frequency content, duration, likely locations, and so forth (e.g., George and Iverson, 2014; Johnson and Palma, 2015; Allstadt et al., 2018; Watson et al., 2020). Such models should also account for (1) statistically characterized variations in site noise (wind noise) (e.g., Le Pichon et al., 2009; Green and Bowers, 2010; Brown et al., 2014), (2) local propagation (wind strength and direction, topography, temperature, and attenuation), and (3) variability in background clutter.

A more comprehensive monitoring strategy of Mount Adams could involve focused seismoacoustic and video surveillance of multiple key drainages (Figure 1b) as well as weather sensors, flow gauges, and trip wires, in line with designs for areas of similar concern (e.g., Kogelnig et al., 2014; Liu et al., 2015; Chen et al., 2016; Schimmel and Hübl, 2016;

Moran, 2018; Marchetti et al., 2019). Such diverse instrumentation would likely benefit detection sensitivity, flow-front location accuracy, avoiding false alarms, interpreting physical properties, and also tailoring any alerts to events of particular magnitude.

5. Conclusions

The BEAR infrasound array is the first at Mount Adams and lays groundwork for a system which could potentially detect and track lahars rumbling down the southwest flank. To date, BEAR, as well as three additional temporary arrays in August 2018, have helped meet initial goals by establishing ambient background wind-noise characteristics and likely sources of clutter, as well as successfully locating a small glacial avalanche that was also visible in satellite imagery. This event was one of 12 suspected mass movements detected by BEAR during the study period. Other transient signals recorded include thunder and, possibly, icequakes. SNR, the primary factor controlling lahar detection, is presumably dictated mainly by source proximity, source size, and wind levels. Wind noise precluded detection of several witnessed small debris flows below the summit; however, it is more likely that large events of a hazardous nature would be detectable with the current instrumentation at BEAR and ASR. The drainages themselves appear to create abundant seasonal clutter from fluvial and waterfall infrasound, although, further confirmation of these sources (e.g., using flow-gauge or time-lapse video data) is needed. Characterizing this clutter is imperative for any future robust infrasonic lahar monitoring system, which should be supplemented by additional data types to reduce ambiguity. Novel real-time station designs may be required to meet environmental, budgetary, and logistical challenges in this remote region. Future work with more advanced processing methods may better characterize multiple clutter sources and wind noise, and could enhance signal detectability.

Data and Resources

Infrasound and seismic data are available from the Incorporated Research Institutions for Seismology (IRIS) Data Management Center (DMC) via links in the following citations: BEAR (UC Santa Barbara, 1989); PHAB, CHIP, and RAIN (Matoza and Haymon, 2018); ASR (University of Washington, 1963). Time-lapse camera images from BEAR documenting weather and equipment conditions are available at https://doi.org/10.25349/D9903G. Sensor specifications are published manufacturer values. Waterfall names and sizes derive from Northwest Waterfall Survey (https://www.waterfallsnorthwest.com) and Google Earth. BKRW1 wind and rainfall data are provided by MesoWest (https://mesowest.utah.edu), snow and temperature data by the National Oceanic and Atmospheric Administration (NOAA; https://www.ncdc.noaa.gov), river discharge data by the U.S. Geological Survey (USGS; https://waterdata.usgs.gov/nwis), and event-coincident weather data by Ventusky (https://www.ventusky.com). Satellite images are via Planet Labs (https://www.planet.com). All websites were last accessed in August 2020. The supplemental material for this article includes extended information on detected events, system hardware, weather and hydrology data, as well as tools used for data processing, analysis, and plotting.

Acknowledgments

For their invaluable assistance, the authors wish to thank Seth Moran and Weston Thelen (Cascade Volcano Observatory, U.S. Geological Survey), Deborah Terrion, Erin Black, and Jon Nakae (U.S. Forest Service), Paul Hegarty, Chris Livsey, Sean Maher, Rodrigo de Negri, and R. Pu (UC Santa Barbara), Howard Peavey (independent, technical advice), and Jon Caryl (Mount Adams Tree Service). The authors are appreciative for

References

Adam, V., V. Chritin, M. Rossi, and E. Lancker (1998). Infrasonic monitoring of snow-avalanche activity: What do we know and where do we go from here? *Ann. Glaciol.* 26, 324–328, doi: 10.3189/1998AoG26-1-324-328.

Albert, S., and K. L. Pankow (2019). Comparison of wind noise reduction systems for use in temporary infrasound deployments, *The AGU Fall Meeting*, San Francisco, California, Abstract S41E-0581.

Albert, S., and K. L. Pankow (2020). Temporary wind noise reduction systems for infrasound: Comparison over time and response analysis, *The AGU Fall Meeting*, Abstract S006-01.

Allstadt, K., and S. D. Malone (2014). Swarms of repeating stick-slip icequakes triggered by snow loading at Mount Rainier volcano, *J. Geophys. Res.* 119, no. 5, 1180–1203, doi: 10.1002/2014JF003086.

Allstadt, K. E., R. S. Matoza, A. B. Lockhart, S. C. Moran, J. Caplan- Auerbach, M. M. Haney, W. A. Thelen, and S. D. Malone (2018). Seismic and acoustic signatures of surficial mass movements at volcanoes, *J. Volcanol. Geoth. Res.* 364, 76–106, doi: 10.1016/j.jvol- geores.2018.09.007.

Allstadt, K. E., B. G. McVey, and S. D. Malone (2017). Seismogenic landslides, debris flows, and outburst floods in the western United States and Canada from 1977 to 2017, *U.S. Geol. Surv. Data Release*, doi: 10.5066/F7251H3W.

Anderson, J. F., T. J. Ronan, H. D. Ortiz, D. G. E. Gomes, J. R. Barber, J. B. Johnson, and J. P. McNamara (2019). Whitewater acoustics, *The AGU Fall Meeting*, San Francisco, California, Abstract H53O-2030.

Arattano, M., and L. Marchi (2008). Systems and sensors for debris-flow monitoring and warning, *Sensors* 8, no. 4, 2436–2452, doi: 10.3390/s8042436.

Assink, J. D., L. G. Evers, I. Holleman, and H. Paulssen (2008). Characterization of infrasound from lightning, *Geophys. Res. Lett.* 35, L15802, doi: 10.1029/2008GL034193.

Bass, H. E. (1980). The propagation of thunder through the atmosphere, *J. Acoust. Soc. Am.* 67, 1959–1966, doi: 10.1121/1.384354.

Bosa, A., J. B. Johnson, S. De Angelis, J. J. Lyons, R. P. Escobar-Wolf, A. Roca, and A. Pineda (2020). Tracking secondary lahar flow paths and characterizing pulses and surges using infrasound array networks at Volcán Fuego, Guatemala, *The AGU Fall Meeting*, Abstract V009-03.

Bowman, J. R., G. E. Baker, and M. Bahavar (2005). Ambient infrasound noise, *Geophys. Res. Lett.* 32, L09803, doi: 10.1029/2005GL022486.

Bowman, J. R., G. Shields, and M. S. O'Brien (2007). Infrasound station ambient noise estimates and models 2003–2006, *The 2007 Infrasound Technology Workshop*, Tokyo, Japan, 13–16 November, Abstract 5-5, available at https://l2a.ucsd.edu/local/Meetings/2007_ITW_Japan/Presentations/session_5/Bowman_infrasound_noise_Tokyo_ITW.ppt (last accessed August 2020).

Brown, D., L. Ceranna, M. Prior, P. Mialle, and R. J. Le Bras (2014). The IDC seismic, hydroacoustic and infrasound global low and high noise models, *Pure Appl. Geophys.* 171, 361–375, doi: 10.1007/s00024-012-0573-6.

Burtin, A., L. Bollinger, J. Vergne, R. Cattin, and J. L. Nábělek (2008). Spectral analysis of seismic noise induced by rivers: A new tool to monitor spatiotemporal changes in stream hydrodynamics, *J. Geophys. Res.* 113, no. B05301, doi: 10.1029/2007JB005034.

Busby, R. W., R. L. Woodward, K. A. Hafner, F. L. Vernon, and A. M. Frassetto (2018). The design and implementation of EarthScope's USArray Transportable Array in the conterminous United States and Southern Canada. Retrieved from: http://www.usarray.org/researchers/obs/transportable/l48_ta_report

Campus, P., and D. R. Christie (2010). Worldwide observations of infrasonic waves, in *Infrasound Monitoring for Atmospheric Studies*, A. Le Pichon, E. Blanc, and A. Hauchecorne (Editors), Springer, Dordrecht, The Netherlands, 185–234, doi: 10.1007/978-1-4020-9508-5_6.

Cansi, Y. (1995). An automatic seismic event processing for detection and location: The P.M.C.C. method, *Geophys. Res. Lett.* 22, no. 9, 1021–1024, doi: 10.1029/95GL00468.

Cansi, Y., and A. Le Pichon (2009). Infrasound event detection using the progressive multi-channel correlation algorithm, in *Handbook of Signal Processing in Acoustics*, D. Havelock, S. Kuwano, and M. Vorländer (Editors), Springer, New York, New York, 1425–1435, doi: 10.1007/978-0-387-30441-0_77.

Chen, N.-S., J. I. Tanoli, G.-S. Hu, F.-N. Wang, C. L. Yang, H. T. Ding, N. He, and T. Wang (2016). Outlining a stepwise, multi-parameter debris flow monitoring and warning system: An example of application in Aizi Valley, China, *J. Mt. Sci.* 13, no. 9, 1527–1543, doi: 10.1007/s11629-015-3624-5.

De Angelis, S., A. Diaz-Moreno, and L. Zuccarello (2019). Recent developments and applications of acoustic infrasound to monitor volcanic emissions, *Remote Sens.* 11, no. 11, 1302, doi: 10.3390/rs11111302.

de Groot-Hedlin, C. D., M. A. H. Hedlin, and K. T. Walker (2014). Detection of gravity waves across the USArray: A case study, *Earth Planet Sci. Lett.* 402, 345–352, doi: 10.1016/j.epsl.2013.06.042.

Díaz, J., M. Ruíz, L. Crescentini, A. Amoruso, and J. Gallart (2014). Seismic monitoring of an Alpine mountain river, *J. Geophys. Res.* 119, no. 4, 3276–3289, doi: 10.1002/2014JB010955.

Dzurisin, D., J. W. Vallance, T. M. Gerlach, S. C. Moran, and S. D. Malone (2005). Mount St. Helens reawakens, *Eos Trans. AGU* 86, no. 3, 25–29, doi: 10.1029/2005EO030001.

Farges, T., and E. Blanc (2010). Characteristics of infrasound from lightning and sprites near thunderstorm areas, *J. Geophys. Res.* 115, A00E31, doi: 10.1029/2009JA014700.

Fee, D., and M. Garcés (2007). Infrasonic tremor in the diffraction zone, *Geophys. Res. Lett.* 34, L16826, doi: 10.1029/2007GL030616.

Fee, D., and R. S. Matoza (2013). An overview of volcano infrasound: From Hawaiian to Plinian, local to global, *J. Volcanol. Geoth. Res.* 249, 123–139, doi: 10.1016/j.jvolgeores.2012.09.002.

Feng, H. N., Y. C. Yang, I. P. Chunchuzov, and P. X. Teng (2014). Study on infrasound from a water dam, *Acta Acustica United with Acustica* 100, no. 2, 226–234, doi: 10.3813/AAA.918702.

Finn, C. A., M. Descⁿczcz-Pan, E. D. Anderson, and D. A. John (2007). Three-dimensional geophysical mapping of rock alteration and water content at Mount Adams, Washington: Implications for lahar hazards, *J. Geophys. Res.* 112, no. B10204, doi: 10.1029/2006JB004783.

Garcés, M., J. Aucan, D. Fee, P. Caron, M. Merrifield, R. Gibson, J. Bhattacharyya, and S. Shah (2006). Infrasound from large surf, *Geophys. Res. Lett.* 33, L05611, doi: 10.1029/2005GL025085.

Garcés, M., A. Harris, C. Hetzer, J. Johnson, S. Rowland, E. Marchetti, and P. Okubo (2003). Infrasonic tremor observed at Kīlauea Volcano, Hawai'i, *Geophys. Res. Lett.* 30, no. 20, doi: 10.1029/2003GL018038.

Garcés, M. A. (2013). On infrasound standards, part 1: Time, frequency, and energy scaling, *Inframatics* 2, no. 2, doi: 10.4236/inframatics.2013.22002.

Ge, M. (2003). Analysis of source location algorithms—Part II: Iterative methods, *J. Acoust. Emission* 21, 29–51, available at http://www.aewg.org/jae/JAE-Vol_21-2003.pdf (last accessed August 2020).

Geiger, L. (1910). Herdbestimmung bei Erdbeben aus den Ankunftszeiten, *Nachrichten der Königlichen Gesellschaft der Wissenschaften zu Göttingen, mathematisch-physikalische Klasse* 4, 331–349 (in German).

Geiger, L. (1912). Probability method for the determination of earthquake epicenters from the arrival time only, *Bull. St. Louis Univ.* 8, 60–71, available at http://digitalcollections.slu.edu/digital/collection/catalogs/id/6310/rec/118 (last accessed August 2020).

George, D. L., and R. M. Iverson (2014). A depth-averaged debris-flow model that includes the effects of evolving dilatancy: 2. Numerical predictions and experimental tests, *Proc. Math. Phys. Eng. Sci.* 470, 20130820, doi: 10.1098/rspa.2013.0820.

Green, D. N., and D. Bowers (2010). Estimating the detection capability of the International Monitoring System infrasound network, *J. Geophys. Res.* 115, D18116, doi: 10.1029/2010JD014017.

Green, D. N., R. S. Matoza, J. Vergoz, and A. Le Pichon (2012). Infrasonic propagation from the 2010 Eyjafjallajökull eruption: Investigating the influence of stratospheric solar tides, *J. Geophys. Res.* 117, D21202, doi: 10.1029/2012JD017988.

Green, D. N., and A. Nippress (2019). Infrasound signal duration: The effects of propagation distance and waveguide structure, *Geophys. J. Int.* 216, no. 3, 1974–1988, doi: 10.1093/gji/ggy530.

Griswold, J. P., T. C. Pierson, and J. A. Bard (2018). Modeled inundation limits of potential lahars from Mount Adams in the White Salmon River Valley, Washington, *U.S. Geol. Surv. Open-File Rept.* 2018-1013, doi: 10.3133/ofr20181013.

Haney, M. M., A. R. Van Eaton, J. J. Lyons, R. L. Kramer, D. Fee, A. M. Iezzi, R. P. Ziak, J. Anderson, J. B. Johnson, J. L. Lapierre, et al. (2020). Characteristics of thunder and electromagnetic pulses from volcanic lightning at Bogoslof volcano, Alaska, *Bull. Volcanol.* 82, no. 15, 1–16, doi: 10.1007/s00445-019-1349-y.

Havens, S., H.-P. Marshall, J. B. Johnson, and B. Nicholson (2014). Calculating the velocity of a fast-moving snow avalanche using an infrasound array, *Geophys. Res. Lett.* 41, 6191–6198, doi: 10.1002/2014GL061254.

Havskov, J., and L. Ottemöller (2010). *Routine Data Processing in Earthquake Seismology: With Sample Data, Exercises and Software*, Springer, Dordrecht, The Netherlands, doi: 10.1007/978-90-481-8697-6.

Hedlin, M. A. H., J. Berger, and F. L. Vernon (2002). Surveying infrasonic noise on oceanic islands, *Pure Appl. Geophys.* 159, 1127– 1152, doi: 10.1007/s00024-002-8675-1.

Hildreth, W., and J. Fierstein (1995). Geologic map of the Mount Adams volcanic field, Cascade Range of southern Washington, *U.S. Geol. Surv. Map* I-2460, scale 1:50,000, doi: 10.3133/i2460.

Hsu, L., N. J. Finnegan, and E. E. Brodsky (2011). A seismic signature of river bedload transport during storm events, *Geophys. Res. Lett.* 38, no. 13, doi: 10.1029/2011GL047759.

Huang, C.-J., C.-H. Yeh, C.-Y. Chen, and S.-T. Chang (2008). Ground vibrations and airborne sounds generated by motion of rock in a river bed, *Nat. Hazards Earth Syst. Sci.* 8, no. 5, 1139–1147, doi: 10.5194/nhess-8-1139-2008.

Hürlimann, M., V. Coviello, C. Bel, X. Guo, M. Berti, C. Graf, J. Hübl, S. Miyata, J. B. Smith, and H.-Y. Yin (2019). Debris-flow monitoring and warning: Review and examples, *Earth Sci. Rev.* 199, doi: 10.1016/j.earscirev.2019.102981.

Johnson, J. B., J. Anderson, S. De Angelis, R. P. Escobar-Wolf, J. J. Lyons, H.-P. Marshall, and A. Pineda (2019). On the capabilities of networked infrasound arrays for

investigating rapid gravity-driven mass movements: Lahars and snow avalanches, *The AGU Fall Meeting*, San Francisco, California, Abstract V44B-02.

Johnson, J. B., R. O. Arechiga, R. J. Thomas, H. E. Edens, J. Anderson, and R. Johnson (2011). Imaging thunder, *Geophys. Res. Lett.* 38, L19807, doi: 10.1029/2011GL049162.

Johnson, J. B., J. M. Lees, and H. Yepes (2006). Volcanic eruptions, lightning, and a waterfall: Differentiating the menagerie of infrasound in the Ecuadorian jungle, *Geophys. Res. Lett.* 33, L06308, doi: 10.1029/2005GL025515.

Johnson, J. B., and J. Palma (2015). Lahar infrasound associated with Volcan Villarrica's 3 March 2015 eruption, *Geophys. Res. Lett.* 42, no. 15, 6324–6331, doi: 10.1002/2015GL065024.

Johnson, J. B., and T. J. Ronan (2015). Infrasound from volcanic rockfalls, *J. Geophys. Res. Solid Earth* 120, 8223–8239, doi: 10.1002/2015JB012436.

Kim, K., A. Rodgers, and D. Seastrand (2018). Local infrasound variability related to in situ atmospheric observation, *Geophys. Res. Lett.* 45, 2954–2962, doi: 10.1002/2018GL077124.

Kogelnig, A., J. Hübl, E. Suriñach, I. Vilajosana, and B. W. McArdell (2014). Infrasound produced by debris flow: Propagation and frequency content evolution, *Nat. Hazards* 70, 1713–1733, doi: 10.1007/s11069-011-9741-8.

Kogelnig, A., E. Suriñach, I. Vilajosana, J. Hübl, B. Sovilla, M. Hiller, and F. Dufour (2011). On the complementariness of infrasound and seismic sensors for monitoring snow avalanches, *Nat. Hazards Earth Syst. Sci.* 11, 2355–2370, doi: 10.5194/nhess-11-2355-2011.

Kramer, R., A. Lockhart, A. Rinehart, C. Lockett, and A. Darold (2017). Keep the data flowing: an improved, integrated station design and implementation for Mount Rainier lahar detection and warning, abstract [PE23A-117] presented at the *2017 Scientific Assembly, IAVCEI*, Portland, OR.

Langston, C. A., and S. M. Mousavi (2018). Adaptive seismic denoising based on the synchrosqueezed-continuous wavelet transform and block-thresholding, *Final Technical Rept. AFRL-RV-PS-TR-2018-0074, Air Force Research Laboratory*, https://apps.dtic.mil/sti/pdfs/AD1061053.pdf (last accessed August 2020).

Leng, X.-P., D.-L. Liu, F.-Q. Wei, Y. Hong, and D.-F. Dai (2017). Debris flows monitoring and localization using infrasonic signals, *J. Mt. Sci.* 14, 7, doi: 10.1007/s11629-016-3836-3.

Le Pichon, A., R. Matoza, N. Brachet, and Y. Cansi (2010). Recent enhancements of the PMCC infrasound signal detector, *Inframatics* 26, 5–8.

Le Pichon, A., J. Vergoz, E. Blanc, J. Guilbert, L. Ceranna, L. Evers, and N. Brachet (2009). Assessing the performance of the International Monitoring System's infrasound network: Geographical coverage and temporal variabilities, *J. Geophys. Res. Atmos.* 114, D08112, doi: 10.1029/2008JD010907.

Lighthill, J. (2001). *Waves in Fluids, Second Ed.*, Cambridge University Press, Cambridge, United Kingdom, 524 p.

Liu, D., D. Tang, S. Zhang, X. Leng, K. Hu, and L. He (2020). Method for feature analysis and intelligent recognition of infrasound signals of soil landslides, *Bull. Eng. Geol. Environ*. 43, doi: 10.1007/s10064-020-01982-w.

Liu, D. L., X. P. Leng, F. Q. Wei, S. J. Zhang, and Y. Hong (2015). Monitoring and recognition of debris flow infrasonic signals, *J. Mt. Sci.* 12, no. 4, 797–815, doi: 10.1007/s11629-015-3471-4.

Lloyd, D. (2018). *Ever Wild: A Lifetime on Mount Adams*, RLO Media Productions, Portland, Oregon, 160 p.

Lombardi, D., I. Gorodetskaya, G. Barruol, and T. Camelbeeck (2019). Thermally induced icequakes detected on blue ice areas of the East Antarctic ice sheet, *Ann. Glaciol.* 60, no. 79, 45–56, doi: 10.1017/aog.2019.26.

Maher, R. C., and S. R. Shaw (2008). Deciphering gunshot recordings, *Proc. 33rd International Conf. Audio Engineering Society: Audio Forensics—Theory and Practice*, Paper Number 2, Denver, CO, June.

Major, J. J., T. C. Pierson, and J. W. Vallance (2018). Lahar—River of volcanic mud and debris, *U.S. Geol. Surv. Fact Sheet* 2018-3024, doi: 10.3133/fs20183024.

Marchetti, E., M. Ripepe, G. Ulivieri, and A. Kogelnig (2015). Infrasound array criteria for automatic detection and front velocity estimation of snow avalanches: Towards a real-time early-warning system, *Nat. Hazards Earth Syst. Sci.* 15, no. 11, 2545–2555, doi: 10.5194/nhess-15-2545-2015.

Marchetti, E., F. Walter, G. Barfucci, R. Genco, M. Wenner, M. Ripepe, B. McArdell, and C. Price (2019). Infrasound array analysis of debris flow activity and implication for early warning, *J. Geophys. Res.* 124, no. 2, 567–587, doi: 10.1029/2018JF004785.

Marty, J. (2019). The IMS infrasound network: Current status and technological developments, in *Infrasound Monitoring for Atmospheric Studies: Challenges in Middle-Atmosphere Dynamics and Societal Benefits*, A. Le Pichon, E. Blanc, and A. Hauchecorne (Editors), Springer, Cham, Switzerland, 3–62, doi: 10.1007/978-3-319-75140-5_1.

Martysevich, P. (2017). Interpreting infrasound (IS) data quality issues using power density spectra: categorization of sources of disturbances, abstract [T2-O4] presented at the *2017 Infrasound Technology Workshop*, Tromsoe, Norway.

Matoza, R., D. Fee, D. Green, and P. Mialle (2019). Volcano infrasound and the International Monitoring System, in *Infrasound Monitoring for Atmospheric Studies: Challenges in Middle-Atmosphere Dynamics and Societal Benefits*, A. Le Pichon, E. Blanc, and A. Hauchecorne (Editors), Springer, Cham, Switzerland, 1023–1077, doi: 10.1007/978-3-319-75140-5_33.

Matoza, R. S., M. A. Garcés, B. A. Chouet, L. D'Auria, M. A. H. Hedlin, C. de Groot-Hedlin, and G. P. Waite (2009). The source of infrasound associated with long-period events at Mount St. Helens, *J. Geophys. Res.* 114, no. B04305, doi: 10.1029/2008JB006128.

Matoza, R. S., D. N. Green, A. Le Pichon, P. M. Shearer, D. Fee, P. Mialle, and L. Ceranna (2017). Automated detection and cataloging of global explosive volcanism using the

International Monitoring System infrasound network, *J. Geophys. Res.* 122, 2946–2971, doi: 10.1002/2016JB013356.

Matoza, R. S., and R. M. Haymon (2018). *Mount Adams Temporary Infrasound Arrays [Data set]*, International Federation of Digital Seismograph Networks, doi: 10.7914/SN/8J_2018.

Matoza, R. S., M. A. H. Hedlin, and M. A. Garcés (2007). An infrasound array study of Mount St. Helens, *J. Volcanol. Geoth. Res.* 160, 249–262, doi: 10.1016/j.jvolgeores.2006.10.006.

Matoza, R. S., M. Landès, A. Le Pichon, L. Ceranna, and D. Brown (2013). Coherent ambient infrasound recorded by the International Monitoring System, *Geophys. Res Lett.* 40, 429–433, doi: 10.1029/2012GL054329.

Matoza, R. S., J. Vergoz, A. Le Pichon, L. Ceranna, D. N. Green, L. G. Evers, M. Ripepe, P. Campus, L. Liszka, T. Kvaerna, et al. (2011). Long-range acoustic observations of the Eyjafjallajökull eruption, Iceland, April–May 2010, *Geophys. Res. Lett.* 38, L06308, doi: 10.1029/2011GL047019.

Mayer, S., A. van Herwijnen, G. Ulivieri, and J. Schweizer (2020). Evaluating the performance of an operational infrasound avalanche detection system at three locations in the Swiss Alps during two winter seasons, *Cold Regions Sci. Tech.* 173, doi: 10.1016/j.coldre- gions.2019.102962.

McNamara, D. E., and R. P. Buland (2004). Ambient noise levels in the continental United States, *Bull. Seismol. Soc. Am.* 94, no. 4, 1517–1527, doi: 10.1785/012003001.

Mills, H. H. (1991). Temporal variation of mass-wasting activity in Mount St. Helens crater, Washington, U.S.A., indicated by seismic activity, *Arct. Antarct. Alp. Res.* 23, 417–423, doi: 10.2307/1551683.

Moore, J. R., K. L. Pankow, S. R. Ford, K. D. Koper, J. M. Hale, J. Aaron, and C. F. Larsen (2017). Dynamics of the Bingham Canyon rock avalanches (Utah, USA) resolved from topographic, seismic, and infrasound data, *J. Geophys. Res.* 122, 615–640, doi: 10.1002/2016JF004036.

Moran, S. C. (2005). Seismic monitoring at Cascade volcanic centers, 2004—Status and recommendations, *U.S. Geol. Surv. Sci. Investig. Rept.* 2004-5211, 28 pp., available at https://pubs.usgs.gov/sir/2004/5211/ (last accessed August 2020).

Moran, S. C. (2018). Mitigating volcanic hazards through geophysical monitoring and research, *The 2018 Workshop, IRIS*, Albuquerque, New Mexico, Abstract 4-3.

Moran, S. C., R. S. Matoza, M. A. Garcés, M. A. H. Hedlin, D. Bowers, W. E. Scott, D. R. Sherrod, and J. W. Valance (2008). Seismic and acoustic recordings of an unusually large rockfall at Mount St. Helens, Washington, *Geophys. Res Lett.* 35, L10302, doi: 10.1029/2008GL035176.

Naugolnykh, K., and A. Bedard (2002). A model of the avalanche infrasound radiation, *Proc. 2002 IEEE International Geoscience and Remote Sensing Symposium/24th Canadian Symposium Remote Sensing*, 871–872, doi: 10.1109/IGARSS.2002.1025713.

Norris, R. D. (1994). Seismicity of rockfalls and avalanches at three Cascade Range volcanoes: Implications for seismic detection of hazardous mass movements, *Bull. Seismol. Soc. Am.* 84, no. 6, 1925–1939.

Oshima, H., and T. Maekawa (2001). Excitation process of infrasonic waves associated with Merapi-type pyroclastic flow as revealed by a new recording system, *Geophys. Res. Lett.* 28, no. 6, 1099–1102, doi: 10.1029/1999GL010954.

Pierson, T. C., R. J. Janda, J.-C. Thouret, and C. A. Borrero (1990). Perturbation and melting of snow and ice by the 13 November eruption of Nevado del Ruiz, Colombia, and consequent mobili- zation, flow and deposition of lahars, *J. Volcanol. Geoth. Res.* 41, nos. 1/4, 17–66, doi: 10.1016/0377-0273(90)90082-Q.

Pierson, T. C., N. J. Wood, and C. L. Driedger (2014). Reducing risk from lahar hazards: Concepts, case studies, and roles for scientists, *J. Appl. Volcanol.* 3, no. 16, 1–25, doi: 10.1186/s13617-014-0016-4.

Pilger, C., L. Ceranna, J. O. Ross, J. Vergoz, A. Le Pichon, N. Brachet, E. Blanc, J. Kero, L. Liszka, S. Gibbons, et al. (2018). The European Infrasound Bulletin, *Pure Appl. Geophys.* 175, 3619–3638, doi: 10.1007/s00024-018-1900-3.

Plapous, C., C. Marro, and P. Scalart (2006). Improved signal-to-noise ratio estimation for speech enhancement, *IEEE Trans. Audio Speech Lang. Process.* 14, no. 6, 2098–2108, doi: 10.1109/TASL .2006.872621.

Raspet, R., J.-P. Abbott, J. Webster, J. Yu, C. Talmadge, K. Alberts II, S. Collier, and J. Noble (2019). New systems for wind noise reduction for infrasonic measurements, in *Infrasound Monitoring for Atmospheric Studies: Challenges in Middle-Atmosphere Dynamics and Societal Benefits*, A. Le Pichon, E. Blanc, and A. Hauchecorne (Editors), Springer, Cham, Switzerland, 91–124, doi: 10.1007/978-3-319-75140-5_3.

Richardson, J. P., G. P. Waite, W. D. Pennington, R. M. Turpening, and J. M. Robinson (2012). Icequake locations and discrimination of source and path effects with small aperture arrays, Bering Glacier terminus, AK, *J. Geophys. Res.* 117, F04013, doi: 10.1029/2012JF002405.

Ronan, T. J., J. M. Lees, T. D. Mikesell, J. F. Anderson, and J. B. Johnson (2017). Acoustic and seismic fields of hydraulic jumps at varying Froude numbers, *Geophys. Res. Lett.* 44, 9734–9741, doi: 10.1002/2017GL074511.

Roth, D. L., E. E. Brodsky, N. J. Finnegan, D. Rickenmann, J. M. Turowski, and A. Badoux (2016). Bed load sediment transport inferred from seismic signals near a river, *J. Geophys. Res.* 121, no. 4, 725–747, doi: 10.1002/2015JF003782.

Schimmel, A., and J. Hübl (2016). Automatic detection of debris flows and debris floods based on a combination of infrasound and seismic signals, *Landslides* 13, 1181–1196, doi: 10.1007/s10346-015-0640-z.

Schimmel, A., J. Hübl, R. Koschuch, and I. Reiweger (2017). Automatic detection of avalanches: evaluation of three different approaches, *Nat. Hazards* 87, 83–102, doi: 10.1007/s11069-017- 2754-1.

Schimmel, A., J. Hübl, B. W. McArdell, and F. Walter (2018). Automatic identification of Alpine mass movements by a combination of seismic and infrasound sensors, *Sensors* 18, no. 5, 1658, doi: 10.3390/s18051658.

Schmandt, B., R. C. Aster, D. Scherler, V. C. Tsai, and K. Karlstrom (2013). Multiple fluvial processes detected by riverside seismic and infrasound monitoring of a controlled flood in the Grand Canyon, *Geophys. Res. Lett.* 40, no. 18, 4858–4863, doi: 10.1002/grl.50953.

Scott, W. E. (2010). Mount Adams—Summary of current volcanic, hydrologic, and hazard issues, *The 2010 Klickitat-White Salmon Science Conf.*, The Dalles, Oregon, Abstract 03, available at http://www.ykfp.org/klickitat/SciCon/SciCon10/SciCon10_pdf/03_WScott_KWS_WEB.pdf (last accessed August 2020).

Scott, W. E., R. M. Iverson, J. W. Vallance, and W. Hildreth (1995). Volcano hazards in the Mount Adams region, Washington, *U.S. Geol. Surv. Open-File Rept.* 95-492, doi: 10.3133/ofr95492.

Shang, C., P. Teng, J. Lyu, J. Yang, and H. Sun (2019). Infrasonic source altitude localization based on an infrasound ray tracing propagation model, *J. Acoust. Soc. Am.* 145, no. 6, 3805–3816, doi: 10.1121/1.5110712.

Shani-Kadmiel, S., J. D. Assink, P. S. M. Smets, and L. G. Evers (2018). Seismoacoustic coupled signals from earthquakes in central Italy: Epicentral and secondary sources of infrasound, *Geophys. Res. Lett.* 45, no. 1, 427–435, doi: 10.1002/2017GL076125.

Stähli, M., M. Sättele, C. Huggel, B. W. McArdell, P. Lehmann, A. Van Herwijnen, A. Berne, M. Schleiss, A. Ferrari, A. Kos, et al. (2015). Monitoring and prediction in early warning systems for rapid mass movements, *Nat. Hazards Earth Syst. Sci.* 15, 905–917, doi: 10.5194/nhess-15-905-2015.

Stein, S., and M. Wysession (2003*). Introduction to Seismology, Earthquakes and Earth Structure*, Blackwell, Oxford, United Kingdom, 498 p.

Szuberla, C. A. L., K. M. Arnoult, and J. V. Olson (2006). Discrimination of near-field infrasound sources based on time-difference of arrival information, *J. Acoust. Soc. Am.* 120, no. 3, EL23–EL28, doi: 10.1121/1.2234517.

Tailpied, D., A. Le Pichon, E. Marchetti, M. Ripepe, M. Kallel, L. Ceranna, and N. Brachet (2013). Remote infrasound monitoring of Mount Etna: Observed and predicted network detection capability, *Inframatics* 2, no. 1, 1–11, doi: 10.4236/inframatics.2013.21001.

Tape, C., D. C. Heath, M. G. Baker, S. Dalton, K. Aderhold, and M. E. West (2019). Bear encounters with seismic stations in Alaska and Northwestern Canada, *Seismol. Res. Lett.* 90, no. 5, 1950–1970, doi: 10.1785/0220190081.

Thelen, W. A., K. Allstadt, R. Kramer, C. Lockett, A. B. Lockhart, B. Pauk, and S. C. Moran (2019). Current status of the Mount Rainier (Washington) lahar detection system, abstract [V51K-0254] presented at the *2019 Fall Meeting, AGU*, San Francisco, CA.

Thüring, T., M. Schoch, A. van Herwijnen, and J. Schweizer (2015). Robust snow avalanche detection using supervised machine learning with infrasonic sensor arrays, *Cold Regions Sci. Tech.* 111, 60–66, doi: 10.1016/j.coldregions.2014.12.014.

Tsai, V. C., B. Minchew, M. P. Lamb, and J.-P. Ampuero (2012). A physical model for seismic noise generation from sediment transport in rivers, *Geophys. Res. Lett.* 39, no. 2, doi: 10.1029/2011GL050255.

UC Santa Barbara (1989). UC Santa Barbara Engineering Seismology Network [Data set], International Federation of Digital Seismograph Networks, doi: 10.7914/SN/SB.

Ulivieri, G., E. Marchetti, M. Ripepe, I. Chiambretti, G. De Rosa, and V. Segor (2011). Monitoring snow avalanches in northwestern Italian Alps using an infrasound array, *Cold Regions Sci. Tech.* 69, nos. 2/3, 177–183, doi: 10.1016/j.coldregions.2011.09 .006.

University Of Washington (1963). *Pacific Northwest Seismic Network [Data set]*, International Federation of Digital Seismograph Networks, doi: 10.7914/SN/UW.

Vallance, J. W. (1999). Postglacial lahars and potential hazards in the White Salmon River system on the southwest flank of Mount Adams, Washington, *U.S. Geol. Surv. Bull.* 2161, doi: 10.3133/b2161.

Walsh, B., V. Coviello, L. Capra, J. Procter, and V. Márquez-Ramirez (2020). Insights into the internal dynamics of natural lahars from analysis of 3-component broadband seismic signals at Volcán de Colima, Mexico, *Front. Earth Sci.* 8, 542,116, doi: 10.3389/ feart.2020.542116.

Watson, L. M., J. Dufek, E. M. Dunham, and D. Mohaddes (2020). Computational aeroacoustic simulations of infrasound signals from volcanic eruptions, *The AGU Fall Meeting*, Abstract S006-06.

Webster, J., and R. Raspet (2015). Infrasonic wind noise under a deciduous tree canopy, *J. Acoust. Soc. Am.* 137, no. 5, 2670–2677, doi: 10.1121/1.4919340.

Wenner, M., F. Walter, M. J. Chmiel, Z. Zhang, and B. W. McArdell (2020). Comprehensive exploitation of seismic data at a debris flow torrent—Early warning, hazard assessment, parameter estimation, *The AGU Fall Meeting*, Abstract S025-03.

Williams, R. A., A. Perttu, and B. Taisne (2020). Processing of volcano infrasound using film sound audio post-production techniques to improve signal detection via array processing, *Geosci. Lett.* 7, no. 9, 1–13, doi: 10.1186/s40562-020-00158-4.

Wilson, D. K., C. L. Pettit, and V. E. Ostashev (2015). Sound propagation in the atmospheric boundary layer, *Acoust. Today* 11, no. 2, 44–52, available at https://acousticstoday.org/sound-propagation-in-the-atmospheric-boundary-layer-d-keith-wilson-chris-l-pettit-and-vladimir-e-ostashev/ (last accessed August 2020).

Woodward, R., H. Israelsson, I. Bondár, K. McLaughlin, J. R. Bowman, and H. Bass (2005). Understanding wind-generated infrasound noise, *Proc. 27th Seismic Research Review: Ground-Based Nuclear Explosion Monitoring Technologies*, 866–875, available at https:// www.osti.gov/servlets/purl/1027447 (last accessed August 2020).

Ye, J., Y. Kurashima, T. Kobayashi, H. Tsuda, T. Takahara, and W. Sakurai (2019). An efficient in-situ debris flow monitoring system over a wireless accelerometer network, *Remote Sens.* 11, no. 13, 1512, doi: 10.3390/rs11131512.

Yount, J., A. Naisbitt, and E. D. Scott (2008). Operational highway avalanche forecasting using the infrasonic avalanche detection system, *Proc. 2008 International Snow Science*

Workshop, 265–276, https://arc.lib.montana.edu/snow-science/objects/P__8187.pdf (last accessed August 2020).

Zimmer, V. L., B. D. Collins, G. M. Stock, and N. Sitar (2012). Rock fall dynamics and deposition: An integrated analysis of the 2009 Ahwiyah Point rock fall, Yosemite National Park, USA, *Earth Surf. Process. Landf.* 37, 680–691, doi: 10.1002/esp.3206.

Supplemental Material

Here we provide additional information on station hardware, relative signal and noise levels, processing parameters, and processing results. Figures are referred to in the main article. The relation between hydrological, weather, and PMCC detections is illustrated. We also summarize recent debris flow events and infrasound capability at nearby volcanoes, and list software tools used for processing, analysis, and plotting.

S1. Debris Flow Infrasound from Nearby Volcanoes

In 1980, Mount St. Helens (MSH), located approximately 53 km west by north of Mount Adams, and 84 km northeast of Portland, Oregon, erupted explosively, and generated large lahars along several of its drainages. Fortunately, there were no towns in the paths of the lahars. MSH has since remained magmatically active, with episodic construction of a lava dome on the floor of its caldera (Dzsurisin et al., 2005; Matoza et al., 2007). In 2006, a large rockfall from the dome produced infrasound detected 0.6 km and 13.4 km away at Cascade Volcano Observatory (CVO) stations (Moran et al., 2008). The steep interior walls of the Mount St. Helens crater also provide a source of rockfall unrelated to volcanic activity (Mills, 1991; Norris, 1994). The crater station (CC SEP) continues to operate, currently comprising a single sensor. A new infrasound array operating since November 2018 (CC GUAC) is located in the main drainage, 2.4 km north of the dome. At Mount Rainier, 75 km north-northwest of Mount Adams, a five-station infrasound network comprising two single sensors (CC PR01/2), and three 3-sensor arrays (CC PR03/4/5) form part of the lahar monitoring system (Thelen et al., 2019).

From 04:00–08:00 28 October 2018 Coordinated Universal Time (UTC), CVO identified several debris flows at MSH using seismic and flow/turbidity gauge data during a period of heavy rain (Weston Thelen, written communication, 2018). Though BEAR detected signals from the direction of MSH and Mount Adams during this period, any debris flows occurring at either location are indistinguishable from background data. Analysis is complicated by MSH sharing an azimuth with the Pacific Ocean. At Mount Hood, 85 km south of BEAR, a debris flow occurred at 1730–1845 22 October 2017 UTC (Seth Moran, written communication, 2017). This event produced clear seismicity at station UW.VLL, 10 km north of Mount Hood. At BEAR, no infrasound signals could be associated with this event. The prevailing wind direction was west to east, at 1,000 m altitude reducing the probability of clear detection at BEAR. Thus, we conclude, as expected, that such debris flow infrasound signals are relatively weak and not readily detectable at regional distances (> 15 km). Wind direction information were obtained from Ventusky (see Data and Resources in the main article).

Seismogenic landslides, debris flows, and outburst floods in the western United States and Canada from 1977 to 2017 are detailed by Allstadt et al. (2017).

S2. BEAR Array Siting and Equipment Design

We evaluated potential long-term array sites for BEAR using the following measures: (1) open sky to the south for solar power; (2) line-of-sight to the nearest cell tower at Flattop Mountain, ~7.5 km northwest by west of Trout Lake; (3) abundance of trees for wind-noise suppression; (4) minimizing proximity to obvious noise sources such as busy roads, wind turbines, and turbulent water; (5) gently sloping topography across the array footprint to reduce 3D wavefront and signal distortion effects; (6) minimizing topography between source and station; (7) road access for ease of installation; (8) out of sight for security; (9) snow level affecting station design and maintenance potential; (10) risk and vulnerability to damage from debris flows or flooding.

We identified the eventual BEAR site during reconnaissance in September 2016 as the location that most satisfactorily met the above criteria, while remaining outside the wilderness boundary. A key feature of this site was the treeless open area on a southwest facing slope created by a recent timber-salvage clear cut in forest that was damaged by wildfire in 2012 (Figure S1a). Sensor coordinates are provided in Table S1.

Below, we describe the equipment comprising the BEAR array, which has an aperture of ~85 m. We elaborate on the technical and logistical details to enable future reproducibility and to help motivate technical advances that may be necessary to move to a more robust real-time system. Much of the equipment design rationale comes from a combination of performance required (real-time communication with high data completeness, and signal quality), budgetary constraints, environmental conditions, ability to hand-carry, and minimized alteration of the Gifford Pinchot National Forest. Other station designs used in the region include those operated by the Cascade Volcano Observatory (CVO; Kramer et al., 2017) and the EarthScope USArray Transportable Array (Busby et al., 2014). We include a system diagram as Figure S2.

S2.1. Vault

The station enclosure is a Pelican-Hardigg two-wheel transport case (Figure S1b), which provides an insulated, waterproof, and crush-proof environment for the system electronics. All cables enter via four downward facing ports that are filled with steel wool to keep out small animals. To deal with condensation or leaks, the vault contains desiccant packets, drainage holes, and is elevated slightly off the ground. These existing entries, plus small additional holes, permit venting for the battery in case of unexpected overcharging. Padlocks secure the vault. A thick silver-colored ultraviolet resistant tarpaulin keeps the enclosure cool and provides additional environmental protection. Signs on the vault and sensors explain the purpose of the equipment, provide contact details for further information, and discourage tampering.

S2.2. Sensors

These notes on the sensors at BEAR are supplementary to the main article, where the majority of the information is presented. Valve boxes cover the sensors to provide basic protection from animals and snow accumulation (Figure S1c). The boxes are acoustically open on each end. The power consumption of each sensor is 0.75 W. Sensors are connected to a central digitizer by a shielded cable which runs through unburied polyethylene split flex tubing. Armored cable and/or conduit, as well as cable/conduit burial, may be preferred if budgets and permits allow.

S2.3. Digitizer and Telemetry

A four-channel Kinemetrics Obsidian 4X digitizer records data at 100 samples per second (Figure S1b). State-of-health information are recorded once per second. The data are stored locally and also transmitted in real-time via a Digi WR21 cellular modem using a virtual private network (VPN). Waveforms are retrieved at the University of California, Santa Barbara, with Antelope Environmental Monitoring Software, and then pushed to the Incorporated Research Institutions for Seismology (IRIS) Data Management Center (DMC). The Global Positioning System (GPS) clock and cell antennae (Wilson 314411, ~10 dB gain) are mounted in trees, 4.5 m above ground due to winter snow levels (Figure S1d). Waterproof self-fusing tape covers cable connections. For the cell antenna, high-gauge LMR-400 cable reduces transmission losses. These components use a total of 9.5 W of power; 3.5 W for the digitizer, and 6 W for the modem. This setup provides the ability to remotely access the modem and storage system on the digitizer, enabling reconfigurations and data retrieval following telemetry gaps.

S2.4. Power System

The power system is designed to incorporate year-round solar power, rather than rely on non-rechargeable battery power during the winter. Such a strategy is more cost-effective long-term, and reduces vault size. To this end, six 100 W flexible solar panels are mounted in trees 4.5 m above ground (Figure S1d and 1e). A series-parallel wiring system provides both redundancy and enables use of low-gauge cable runs (10 AWG, UL-4703 rated), while minimizing power loss from voltage drop. MC4 connectors provide waterproof cable joins and termination. Calculations for the array indicate a minimum ~400 W requirement in mid-winter, accounting for factors such as temperature, sun exposure, and snow albedo. Thus, two of the panels provide redundancy in case of shading, physical damage, or other failure. A Victron 100/30 maximum power point tracking (MPPT) solar charge controller regulates power to two Sun Xtender 6 Volt PVX-2240T absorbent glass matt (AGM) deep cycle batteries connected in series. The battery capacity varies with discharge rate and temperature, but can power the system for ~7 days without recharging. To protect the batteries from over-discharge, a low-voltage disconnect (LVD) device cuts power to the data logger and sensors if the battery voltage falls below 11.8 V, and then reconnects once the batteries register above 12.8 V during recharging.

S2.5. System Grounding and Protection

Several features reduce the risk of equipment damage from overloads, lightning, and short circuits. A solar combiner box includes both diodes and fuses, as well as a lightning arrestor. The GPS and cell antenna cable runs also include lightning arrestors. Between the battery and LVD is a fuse, with a breaker between the battery and solar charge controller. Three additional fuses are used for the telemetry equipment, data logger, and sensors. Two 1.2 m ground rods are installed 2.5 m apart. All three lightning arrestors, and all solar panel frames, are directly grounded to these posts with 6 AWG THHN/THWN-2 cable. The data logger, solar charge controller, and negative battery terminal are also grounded via an intermediary busbar. All system components are rated for anticipated current and temperature fluctuations. Conductive grease maintains the performance of electrical connections.

S2.6. Solar Panel Mounting System

Given anticipated snow accumulation and permit restrictions on ground disturbance, solar panels were installed in trees on the edge of the clear cut, with the help of a professional tree service. Panels were attached in pairs to an aluminum frame, and angled for winter exposure. Cables run through split flex tubing. All equipment is fixed to the mounts before winching to ~4.5 m. Ratcheting tie-downs attach the mounts to the trees to avoid long-term tree damage. In addition, anti-bird spikes were added to the tops of the mounts to maintain panel performance. Use of 316 stainless steel bolts and other fittings minimizes corrosion. Part of the rationale for using lightweight flexible solar panels was to facilitate mounting the panels in trees, and also to reduce shipping costs.

S2.7. Cameras

Two cameras monitor BEAR for human and animal activity, snow levels, and icing-up of solar panels. One is a time-lapse camera (Plotwatcher Pro), and one is both a motion and infrared triggered camera (Browning Strike Force HD Pro). The cameras also provide temperature measurements that are more accurate of the environment than the data logger measurements inside the insulated vault. Lithium AA batteries power the cameras, with data written locally to SD cards.

The equipment at BEAR has functioned well and required minimal maintenance since installation despite challenging weather conditions. Data completeness is above 99%, with only brief gaps occurring when solar panels freeze up, and batteries run down. Use of at least one additional battery appears justified. An issue with data quality is the presence of one to two second data gaps and/or overlaps that typically occur several times per day. These features are flagged in output MSEED files as data values larger than the range of the digitizer, and thus easily rectified by the user. We attribute the origin of this timing issue to the GPS clock, which has limited sky coverage due to its location on the edge of a tall forest. Camera footage shows intermittent visits from elk, deer, a mountain lion, and the eponymous local bear. Elk occasionally mark or pull slightly on the tarp covering the station. Only eight people (hunters, hikers, and snowmobilers) passed by the site from Aug. 2017 to Oct. 2019, and without any interference. During a visit in Aug. 2018, we found that one of the sensor covers had been overturned, and that a cable conduit had been slightly damaged, likely attributable to animal activity. Tape et al. (2019) provide an informative study of the effects of animal interaction with different station designs across Alaska.

S3. PHAB, CHIP, and RAIN

These notes on the equipment at PHAB, CHIP, and RAIN are supplementary to the main article, where the majority of the information is presented. The temporary station design (Fig S1f) uses a simple, lightweight setup that can be easily carried. The central recording hub incorporates a DiGOS DATA-CUBE[3] (Type 2) 24-bit digitizer, GPS, breakout box, and 12 V power supply (Figure S1g). Eight D-cell batteries in series provide power. Total power consumption for the station is < 0.5 W when the GPS is in cycle mode. A plastic container and bag keep the recording equipment dry. The sensors connect to the breakout box by means of shielded cables (Figure S1h), although these are ungrounded, along with the rest of the system (leading to spectral noise peaks).

Figure S1. (a) Geometry of the BEAR station (4-element infrasound array) with PMCC subarrays shown in yellow. (b) BEAR Pelican-Hardigg vault containing the data logger, cell modem, solar controller, fuses, and lightning arrestors. (c) Hyperion IFS-3111 infrasound sensors (inset) are covered to provide basic protection from animals and snow accumulation. (d, e) Six 100 W solar panels, GPS and cell antennae mounted in trees on edge of clear-cut. (f) Geometry of PHAB station (3-element array), which has no subarrays. (g) PHAB/CHIP/RAIN central recording hub, including digitizer, GPS, power supply and breakout box to connect to the infrasound sensors. (h) Chaparral Model 60-UHP infrasound sensor (inset) inside foam wind filter, as used at PHAB/CHIP/RAIN.
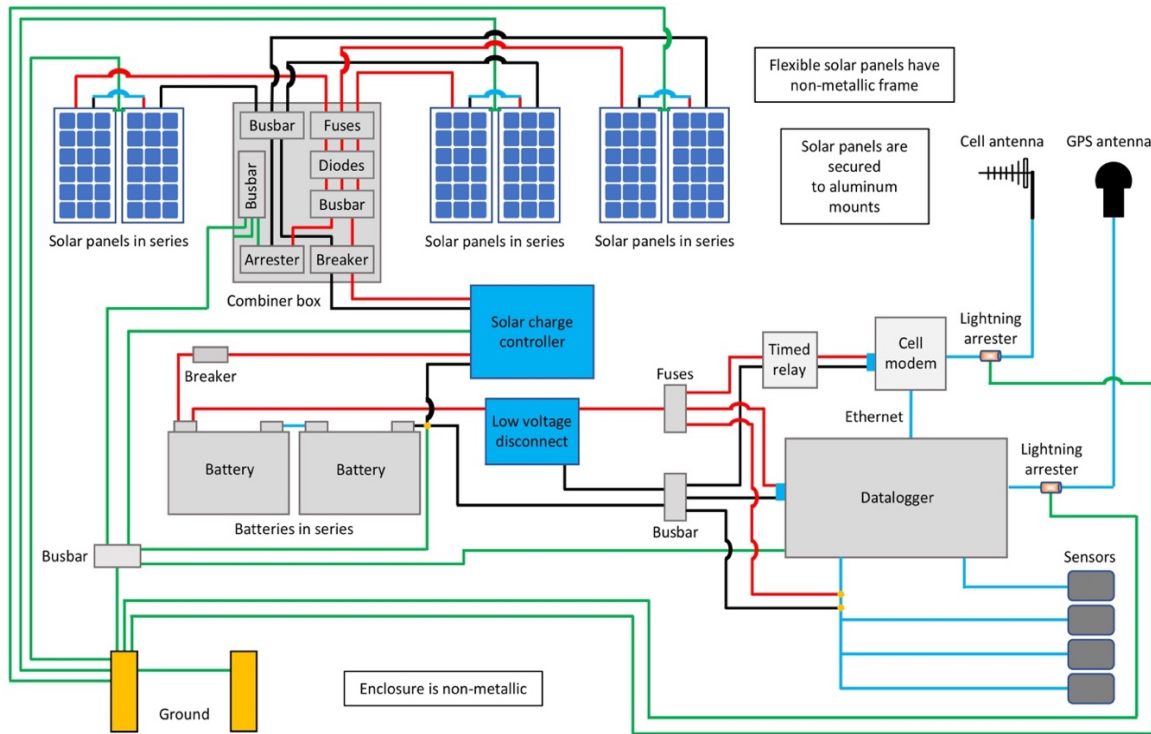
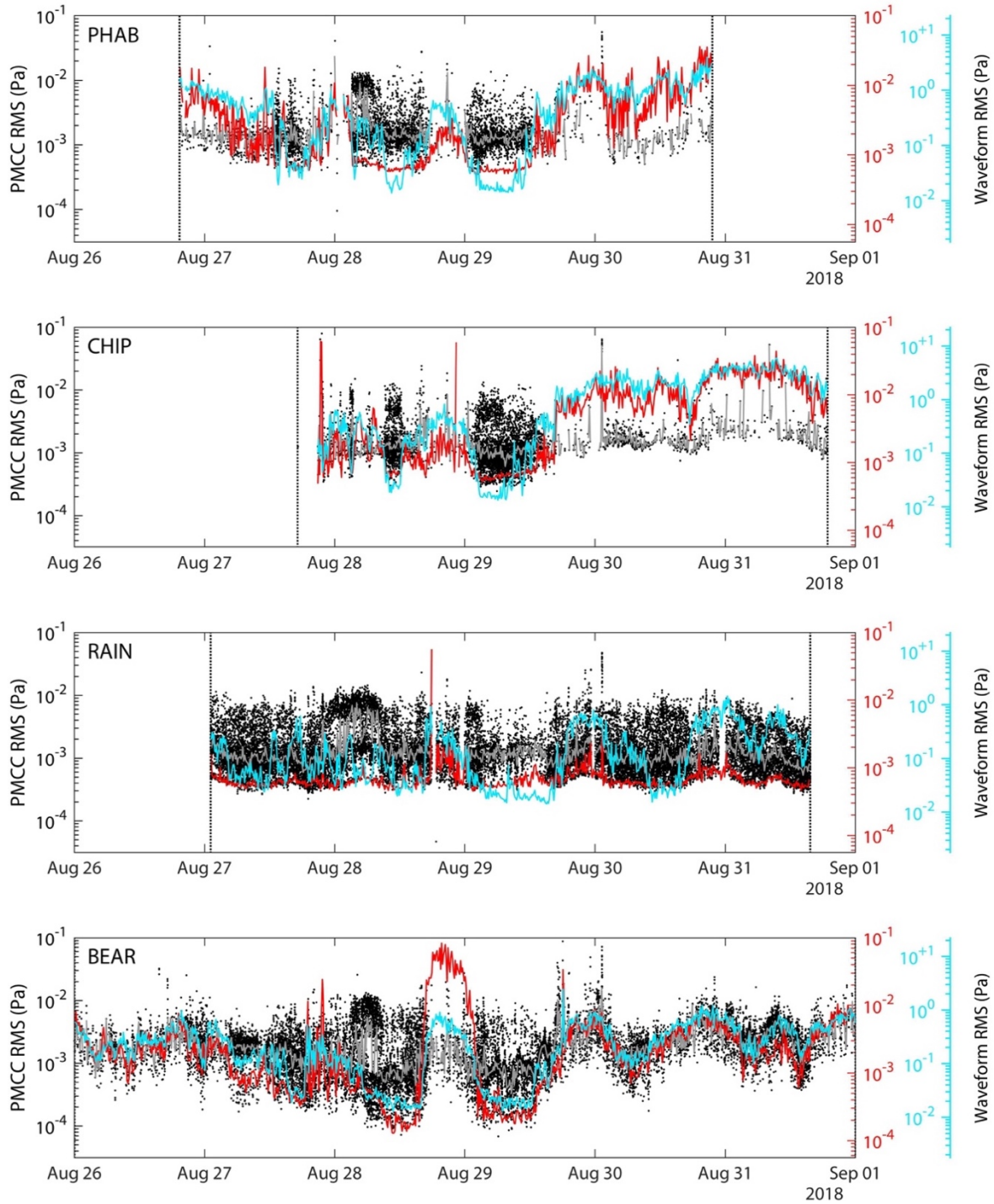**Figure S2.** Schematic of BEAR equipment (not to scale or in physical layout).

Figure S3. Root-mean-square (RMS) amplitudes of signal and noise periods at infrasound arrays. The left axis is for coherent arrivals from Progressive Multi-Channel Correlation (PMCC) processing, with a 10-minute median marked by a gray line. The right axis is for waveforms filtered in two bands which can be indicative of wind noise (0.01–0.5 Hz, blue, Matoza *et al.*, 2011, and 1.2–1.3 Hz, red), again using 10-minute bins. The 0.01–0.5 Hz trace has a range that is two orders of magnitude above the other datasets. The 1.2–1.3 Hz trace provides a much higher anti-correlation between PMCC detections and waveform amplitude at RAIN than in the 0.01–0.5 Hz band. The anti-correlation is slightly lower for CHIP, variable for PHAB, and slightly higher at BEAR, vs. the 0.01–0.5 Hz band. Vertical dotted lines indicate the recording periods. At CHIP, a technical issue affected the data quality for the first 3.5 hours, resulting in a gap in the PMCC detections.

Figure   S4.   (below.)   Probabilistic   power   spectral   density   (PSD)   estimates   of   BEAR (channel 1) infrasound data for each day in Figure S3. All parameters follow those by McNamara and Buland (2004). Time-windows used to estimate the PSDs are 1-hour long with 50% overlap and a 10% cosine taper. The color scheme indicates the percentage of counts in each amplitude-frequency bin out of the total count at that frequency. Bins are 1-dB by 1/8 of an octave, with powers averaged over a full octave. Black lines are the 5th, 50th, and 95th percentiles for the data in each plot. Consistent moderate background noise levels are detected on 26, 27, and 31 August, whereas 28–30 August is marked by low to high background levels.

Regarding Figure S4: There is some temporal variability as to which frequencies change the most in concordance with (assumed) wind speed increase. PSD slopes here contrast with those of e.g., Woodward et al. (2005) who observed consistent slopes regardless of wind speed, even as PSD amplitude increased. Again in contrast to our results, Hedlin et al. (2002) found most variation with wind speed at relatively low frequencies (below 0.5 Hz). The bandwidth of the broad spectral features here do not suggest obvious vault resonance or other technical issues (e.g., Martysevich, 2017). There may be noise amplifying effects > 8 Hz as suggested by Albert and Pankow (2019), however those results were for an inequivalent station design, where the station cover was only open at one end such that less noise averaging occurs by the sensor shroud.

Figure S5. (below.) As for Figure S4, but for the first six days of Fig. 4 in the main article.
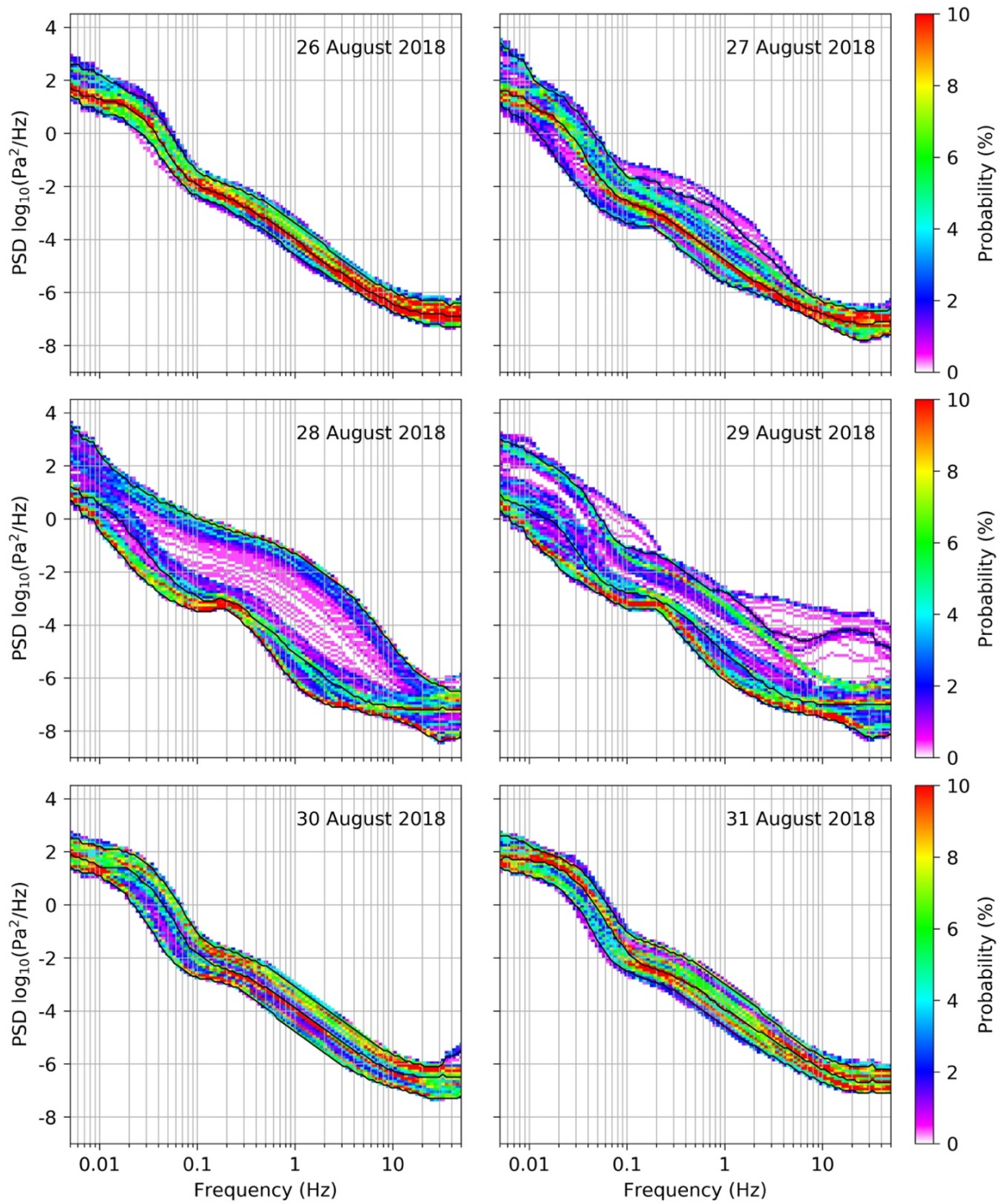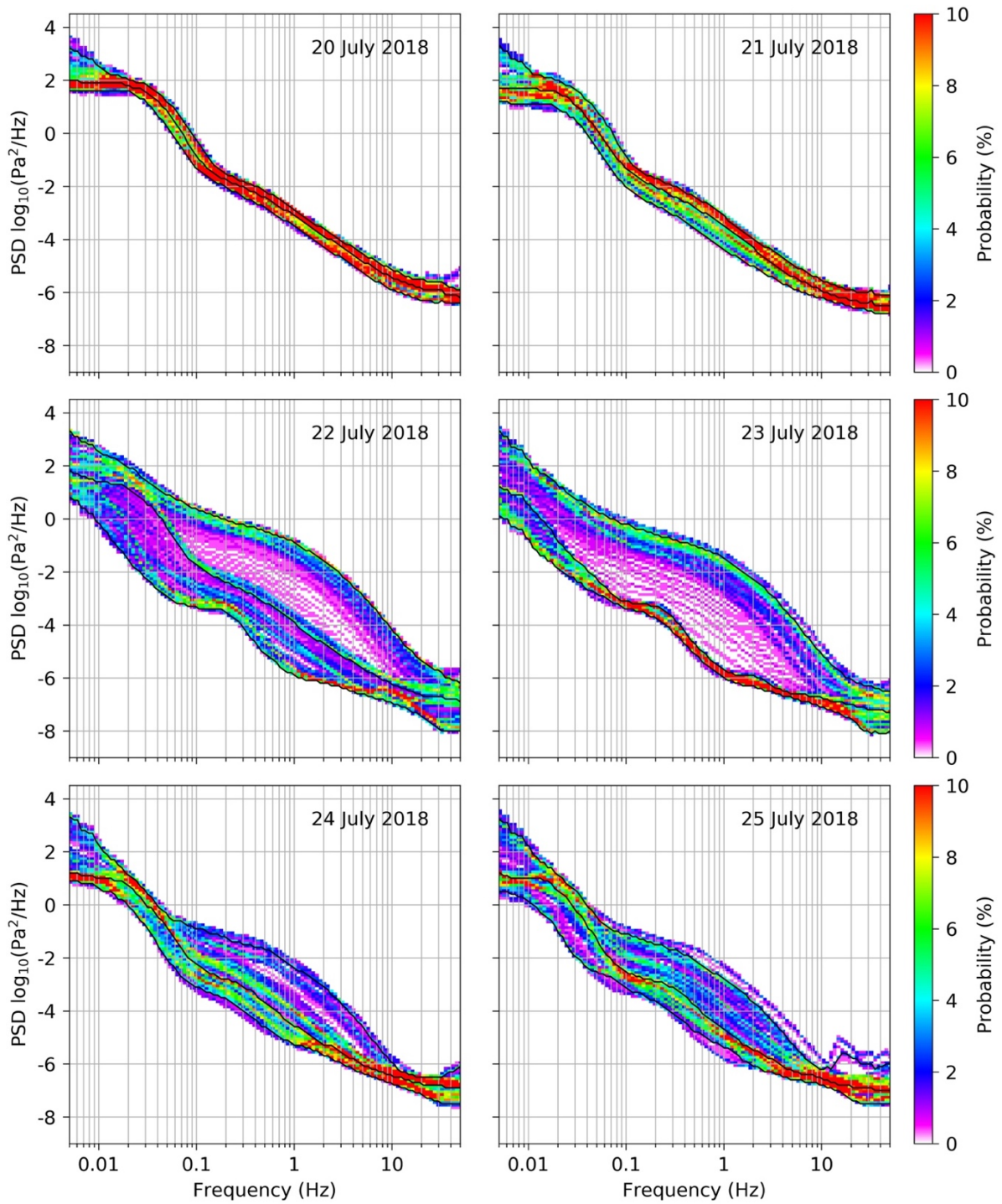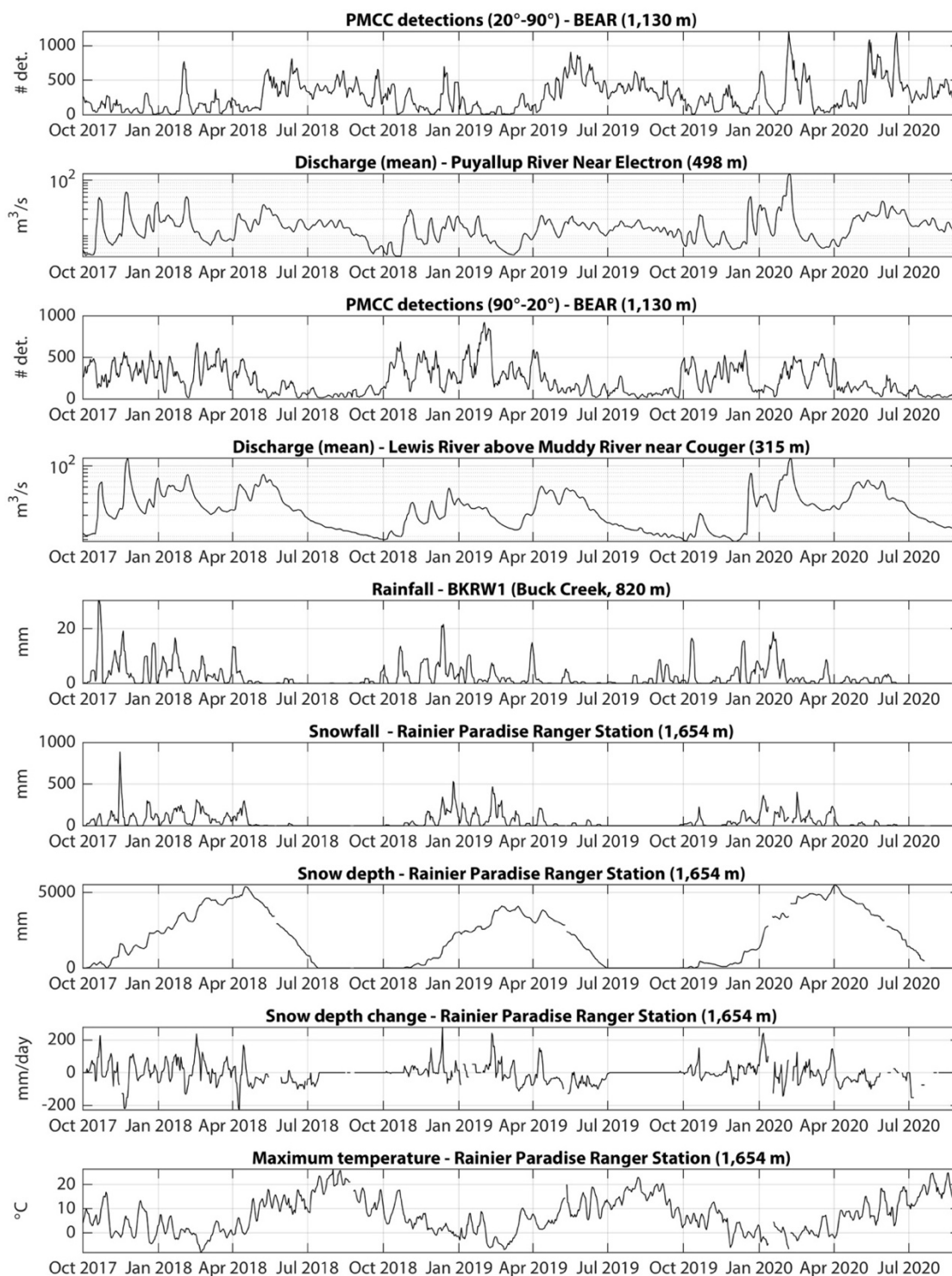
Figure S4.

Figure S5.

Figure S6. Comparing daily PMCC detection totals to daily hydrological and weather information (data sources listed in Data and Resources in the main article). To constrain PMCC detections to those less likely to be associated with microbaroms, mass wasting, and anthropogenic events, we retain detections with mean frequencies of 5–10 Hz. We also require apparent velocities ≤ 360 m/s to increase the likelihood of local sources. Data have been smoothed by taking a 5-day moving average. The elevation above sea level of each station is indicated in the subplot title.

Regarding Figure S6: BKRW1 is 10 km southeast by south from BEAR (Figure 1b in the main article). A sparsity of suitable environmental sensors in the area mean we use two sites close to Mount Rainier (Figure 1b) as analogs for closer stations. The Paradise Ranger Station is 8 km south by east of the 4,392 m summit, and the Puyallup River station is 21 km west by north of the summit. For instance, the elevation of Paradise (1,654 m) gives a better average indication of snow behavior in our study area than such measurements at Trout Lake (~600 m). Further, the Puyallup River gauge is in a small and narrow watershed that predominantly reflects runoff from Mount Rainier, and so is likely a good indicator of runoff from Mount Adams (3,743 m). The Paradise site does record rainfall, but this data, though generally similar to BKRW1, is less complete.

The dominant impacts on river discharge profiles are winter storms and snow melt in spring. Glacial melt from Mount Adams in summer and early autumn is a relatively small contribution that only appears in specific drainages. Fast rises and falls in river discharge typically correlate with sustained rainfall, with snow melt delivering a more gradual rise in response to temperature. We also show discharge from the Lewis River gauge, ~18 km southwest of the area in the top left of Figure 7 in the main article. This gauge collects the cumulative drainage from the waterfalls in this hilly area, with each falls draining a small catchment area. Thus this river gauge is not an ideal measure of flow through the waterfalls themselves. In addition, the gauge collects some runoff from the west side of Mount Adams. The area's relatively limited melt supply and lower average elevation leads to shorter and more pronounced melting periods vs. the Puyallup.

Infrasound cross-spectral coherence and infrasound amplitude have previously been identified as metrics that increase with river discharge so long as there is conversion of hydraulic to acoustic power (e.g., Ronan et al., 2017; Anderson et al., 2019). Rather than discharge itself being important in terms of acoustic observations, it is the ratio of flow speeds (v), to water depth (D) and gravitational acceleration (g), given by the Froude number, $Fr = v/\sqrt{(D \cdot g)}$. Energy conversion is particularly efficient for $Fr > 1.7$, indicating a transition from undular to weak hydraulic jumps (e.g., Ronan et al., 2017).

We use the number of PMCC detections as a proxy for cross-spectral coherence as amplitudes are less useful in this context due to variable and unknown source-station attenuation. The PMCC detections are split into two azimuthal bands: (1) 20°–90°, and (2) 90°–20°. Band 1 covers the waterfalls on Mount Adams above 1,500 m elevation, with Band 2 covering all other azimuths. The PMCC data are compared to the Puyallup River and Lewis River gauges given the rationale outlined above. For Band 1, we find similar PMCC trends with the Puyallup River discharge, though we do not always see direct or even linear proportionality, particularly with rainfall events. (These rainfall events are also recorded at the Lewis River site so are not Puyallup specific). Glacial melt will still feed acoustically powerful waterfalls even during summer. For Band 2, we find a seasonal correlation with the Lewis River discharge, but it is likely that the data still contain many detections that are non-fluvial in origin despite the constraints on frequency and apparent velocity. Wind noise and wind direction can also heavily affect clutter detectability (e.g., Fig. S3), with snow covering the sensors having an increasing effect on higher frequencies.

Table S1. Location coordinates for each sensor in the SB.BEAR, PHAB, CHIP, and RAIN infrasound arrays (latitude, longitude, elevation), as well as for the UW.ASR seismic station. Any revisions of BEAR coordinates will be made available here: http://ds.iris.edu/mda/SB/BEAR/0[1234]/HDF/

	Channel 1	Channel 2	Channel 3	Channel 4
BEAR	+046.130838, -121.605450, 1,129 m	+046.131384, -121.605338, 1,130 m	+046.130600, -121.604757, 1,135 m	+046.130701, -121.605771, 1,125 m
PHAB	+046.154833, -121.584261, 1,479 m	+046.154056, -121.584247, 1,478 m	+046.154496, -121.585278, 1,472 m	N/A
CHIP	+046.140904, -121.561821, 1,581 m	+046.140590, -121.561025, 1,585 m	+046.140075, -121.561711, 1,586 m	N/A
RAIN	+046.190610, -121.638540, 1,222 m	+046.190012, -121.638312, 1,221 m	+046.190035, -121.639050, 1,218 m	N/A
ASR	+046.15259, -121.60164, 1,357 m	N/A	N/A	N/A

Table S2. Uploaded separately. BEAR event detection summary, with PMCC bulletin results meeting the following criteria: back azimuth 40°–55°, mean frequency ≥ 5 Hz, cross-correlation ≥ 0.6, apparent velocity 330–360 m/s, maximum amplitude ≥ 0.1 Pa, number of pixels ≥ 35, and F-statistic ≥ 1.5. The 52 bulletin lines (family summaries) are grouped into 36 individual events based on similar temporal and wave parameter characteristics.

Movie S1. Uploaded separately. Back-azimuth intersections by ≥ 2 stations for 26–31 August 2018 UTC (grid-during layer from IMS-vASC). The association uses PMCC families with maximum and minimum frequencies values between 2 and 40 Hz. The top panel shows intersections within individual one hour time slices. Results are only displayed for a grid node if each array contributes ≥ 10 pixels to that node. The bottom plot is the cumulative stack of all preceding slices. Filled triangles indicate arrays that were active during the entire time window, and unfilled triangles indicate where the arrays were partly active (due to being installed/removed). Known waterfalls, and selected high-gradient streams that align with IMS-vASC features are marked.

PMCC files. The PMCC (Cansi, 1995; version 4.3.c1) initialization files for BEAR, PHAB, CHIP, and RAIN, are uploaded separately. For each station, a configuration file and an additional filter-bands file are required. Although we use the same filter bands for all stations, the filter files vary due to the differing recording rates (100 samples per second at BEAR, 400 samples per second at PHAB, CHIP, and RAIN). Full descriptions of the file formats are included in PMCC software documentation (not included here).

> Configuration files: pmcc_BEAR.txt, pmcc_PHAB.txt, pmcc_CHIP.txt, pmcc_RAIN.txt

> Filter files: filters_BEAR.txt, filters_PHAB_CHIP_RAIN.txt (applies to all three stations)

S4. Software Tools

S4.1. Data Format Conversion

S4.1.1. DATA-CUBE to MSEED

GIPPtools: Software utilities for initial data pre-processing (https://www.gfz-potsdam.de/en/section/geophysical-deep-sounding/infrastructure/geophysical-instrument-pool-potsdam-gipp/software/gipptools/). Retrieved 6/2020.

S4.1.2. MSEED to CSS

Pisces: Pisces: A practical seismological database library in Python (https://github.com/LANL-Seismoacoustics/pisces). Retrieved 6/2019.

> MacCarthy, J. K., C. A. Rowe (2014). Pisces: A Practical Seismological Database Library in Python, *Seis. Res. Lett.* 85, no. 4, 905–911, doi: 10.1785/0220140013.

S4.1.3. SHP to GMT

OGR: GDAL/OGR Geospatial Data Abstraction software Library (https://gdal.org). 6/2018.

S4.2. Data Analysis and Figures

S4.2.1. Non-Native Python Packages

IPython: A rich architecture for interactive computing in multiple programming languages (https://ipython.org/). Retrieved 10/2016.

> Pérez, F., and B. E. Granger (2007). IPython: A System for Interactive Scientific Computing, *Comput. Sci. Eng.* 9, 21–29. doi: 10.1109/MCSE.2007.53.

Matplotlib: A comprehensive library for creating static, animated, and interactive visualizations in Python (https://matplotlib.org/). Retrieved 10/2016.

> Hunter, J. D. (2007). Matplotlib: A 2D Graphics Environment, *Comput. Sci. Eng.* 9, 90–95, doi: 10.1109/MCSE.2007.55.

ObsPy: A Python Toolbox for seismology/seismological observatories (https://docs.obspy.org/). Retrieved 10/2016.

> Beyreuther, M., R. Barsch, L. Krischer, and J. Wassermann (2010). ObsPy: A Python toolbox for seismology, *Seis. Res. Lett.* 81, no. 3, 530–533, doi: 10.1785/gssrl.81.3.430.

S4.2.2. Non-Native MATLAB Functions

BCSeis: Langston, C. A., and S. M. Mousavi (2018). A GUI and set of inline functions for performing various non-linear thresholding operations using the Continuous Wavelet Transform (http://www.ceri.memphis.edu/people/clangstn/software.html). Retrieved 6/ 2020.

> Langston, C. A., and S. M. Mousavi (2018). Adaptive seismic denoising based on the synchrosqueezed-continuous wavelet transform and block-thresholding, *Air Force Research Laboratory final technical report* AFRL-RV-PS-TR-2018-0074. Available at: https://apps.dtic.mil/dtic/tr/fulltext/u2/1061053.pdf. Retrieved 6/2020.

dynamicDateTicks: Deoras, A. (2017). Intelligent dynamic date ticks (https://www.mathworks.com/matlabcentral/fileexchange/27075-intelligent-dynamic-date-ticks). Retrieved 10/2017.

polarPcolor: Cheynet, E. (2020). pcolor in polar coordinates (https://www.github.com/ECheynet/polarPcolor), GitHub. Retrieved January 2020.

Subaxis - Subplot: Grinsted, A. (2020). Create axes in tiled positions (https://www.mathworks.com/matlabcentral/fileexchange/3696-subaxis-subplot).   Retrieved 4/2020.

WienerNoiseReduction: Scalart, P. (2020). Wiener filter for noise reduction and speech enhancement   (https://www.mathworks.com/matlabcentral/fileexchange/24462-wiener-filter-for-noise-reduction-and-speech-enhancement). Retrieved 6/2020.

S4.2.3. Other Packages

Google Earth Pro: 3D Earth representation (https://www.google.com/earth/) with terrain map overlays (http://www.mgmaps.com/kml/). Retrieved 10/2016.

GMT: Generic Mapping Tools (https://www.generic-mapping-tools.org/). Retrieved 7/2017.

> Wessel, P., W. H. F. Smith, R. Scharroo, J. F. Luis, and F. Wobbe (2013). Generic Mapping Tools: Improved version released, *EOS Trans., AGU* 94, no. 45, 409–410, doi: 10.1002/2013EO450001.

IMS-vASC: Combined infrasound signal association and source location using a brute-force, grid-search, cross-bearings approach (https://github.com/rmatoza/ims_vasc). Retrieved 11/2019.

> Matoza, R. S., D. N. Green, A. Le Pichon, P. M. Shearer, D. Fee, P. Mialle, and L. Ceranna (2017). Automated detection and cataloging of global explosive volcanism using the International Monitoring System infrasound network, *J. Geophys. Res. Solid Earth* 122, 2946–2971, doi: 10.1002/2016JB013356.

MUSTANG: Data quality metrics (https://service.iris.edu/mustang/). Last accessed 4/2020.

> Casey, R., M. E. Templeton, G. Sharer, L. Keyson, B. R. Weertman, and T. Ahern (2018). Assuring the quality of IRIS data with MUSTANG, *Seismol. Res. Lett.* 89, no. 2A, 630–639, doi: 10.1785/0220170191.

PMCC: Progressive Multichannel Correlation (PMCC) software. Access is administered by CEA/DASE/LDG, France, and not publicly available.

> Cansi, Y. (1995). An automatic seismic event processing for detection and location: The P.M.C.C. method, *Geophys. Res. Lett.* 22, no. 9, 1021–1024, doi: 10.1029/95GL00468.

QGIS: Open Source Geospatial Foundation Project (http://qgis.org). Retrieved 1/2020.
Layers:
    (1) Background: ESRI National Geographic USA Topography
    (2) Background: Google Satellite
    (3) Background: Stamen Terrain
    (4) Rivers: http://download.geofabrik.de/north-america/us/washington.html
    (5) Wilderness boundary: https://wilderness.net/visit-wilderness/google-earth.php

Chapter 5. Conclusions

This dissertation focuses on the remote detection and location of volcanic processes, principally using infrasound. These low frequency acoustic waves enable observation of phenomena like eruptions and mass movements that may not be possible through techniques such as seismology and satellite imaging, due to attenuation and line of sight issues respectively. The relatively recent adoption of infrasound as a tool in volcanology, and more significantly, the increase in the distribution of infrasound sensors, means that there is still a great scope for improving data collection, signal processing, and analysis techniques. Here, three largely independent projects address some of the outstanding questions and challenges in these fields, and contributing to the body of knowledge on best practices for remotely studying volcanoes with infrasound. In the following, outcomes of the three principal chapters of the dissertation are synthesized, with emphasis given to the principal results, conclusions, and implications. Some limitations of the research are also presented, along with recommendations for future work.

1. Chapter 2

Chapter 2 examines how the recent introduction of a dense regional seismoacoustic network to Alaska can aid in the detection and location of explosive volcanic eruptions. This deployment of the EarthScope Transportable Array (TA) supplements several existing local infrasound arrays operated by the Alaska Volcano Observatory (AVO). These local arrays, with supporting information from seismicity, satellite imagery, lightning detection, and others, were used to catalog 70 explosions during 2016 and 2017 from Bogoslof, a remote volcano located in the Aleutian Islands (Coombs et al., 2019). Infrasound from this well-characterized eruption sequence serves as the primary data set in the development and

calibration of a simple envelope-based reverse time migration (RTM) scheme. This method uses a grid search approach to identify source locations based upon the relative amplitude of stacked data at each grid node. Success of the RTM algorithm and associated parameter choices are characterized using receiver operating characteristic curves, detection rates of cataloged events, and location accuracy. Up to 85% of the 61 Bogoslof infrasound events cataloged by AVO are detectable by RTM, but performance varies significantly depending on the implementation, stations used, and time of year. Identification and location of events with RTM is improved by combining the TA with other sensors in the region; however, individually, the TA typically performs worse than the AVO arrays. For the TA, the high inter-sensor spacing, low azimuthal coverage, high source-stations distances, and higher wind noise levels likely explain this result. The latter aspect is influenced significantly by the use of simpler wind noise reduction systems when compared to the AVO stations. Several eruptions from the nearby Mount Cleveland volcano were also recorded several times across the region, whereas those from further afield in Kamchatka proved more difficult to detect. Ground to air coupling from several earthquakes, as well as a bolide were readily recorded, however (appendix 1). Seasonal variability in dominant wind direction affects detection capability, with infrasound more clearly recorded by downwind stations. In the winter months, winds tend to blow from the Aleutians toward the network, whereas in the summer the reverse is true, underpinning the importance and need for high azimuthal coverage of potentially active volcanoes. For the remote (> 250 km range) observation of volcanic explosions, previous studies have used relatively sparse regional or global networks. This study has, for a dense regional network, demonstrated some of the benefits and limitations for detecting and locating both explosive volcanic, and nonvolcanic sources.

Real time applications can require different implementation considerations than when using data archives. Data transmission from stations to servers is relatively quick compared to the rate at which elastic waves (infrasound, seismic) propagate. Thus signs that an eruption is occurring could be determined from the nearest few stations to the source before the elastic waves have travelled to the further stations in the network (i.e. acting as an early warning system). With data from these proximal sensors, it may be possible to derive a very coarse location and then refine it as the wavefront reaches additional, further stations. This would avoid using a spatio-time grid over a wide region, the resolution of which largely determines RTM runtime, and less so the number of stations. This iterative location process could also be simulated and assessed in advance of implementation using synthetic or pre-recorded data. Equally, for data archives, fine grids can be applied to only those areas for which an initial coarse grid search indicates potential sources. A finer grid spacing, though providing a more precise location and higher computation time, does not necessarily increase the accuracy of the solution. A key element which contributes to source location accuracy is the relative position of stations and sources, such as azimuthal coverage. During the time period spanning the Bogoslof eruption, the majority of volcanoes of interest in Alaska were outside the margins of the TA and the network run by AVO. This geometry leads to spatio-temporal error ellipses, and smearing of location estimates along the source-network axis (Cochran and Shearer, 2006; Koper et al., 2012; Meng et al., 2012). The complexities of atmospheric propagation, changeable stratospheric wind directions, and often high noise levels mean that typically only a small subset of stations clearly detect eruptions in Alaska, accentuating issues related to the source-station distribution.

An averaged (e.g., Morton and Arrowsmith, 2014) or up-to date atmospheric propagation model (e.g., AVO-G2S, Schwaiger et al., 2019) that allows for anisotropy and

wind conditions can help refine the accuracy of candidate location estimates provided by RTM processing. Relatively realistic source-station travel times can then be calculated using a forward-model propagation code. The modeled arrival times from points within the potential source areas are either then compared with the observed arrival times to identify the best fit, or used to adjust waveform alignment in a second round of RTM. Whereas such a step can be computationally time consuming for more realistic models, it may be required for reasonably accurate location of events, particularly given the high density of volcanoes in Alaska. Being able to reasonably account for transmission loss would permit more insight into remote source magnitudes (e.g., Marchetti et al., 2019a). Potential alternative methods that stem more from the existing workflow include: (1) allowing for different celerities between each station and grid node at each time step, rather than using a single value; and (2) stacking representative information from windows that increase in duration with distance to account for wavefield separation within waveguides (e.g., Green and Nippress, 2019).

Other methods that can help confirm, or be used in place of RTM, are those that identify sources through triangulation of back-azimuth estimates, derived from array-processing type algorithms (e.g. Olson and Szuberla, 2008). The existing infrasound arrays operated by AVO can be used for this purpose, but the infrasound sensors in the TA can also be co-opted by treating each group of three sensors as a mini-array (e.g., de Groot-Hedlin and Hedlin, 2015). This latter strategy avoids some of the aforementioned atmospheric propagation issues that affect methods combining traces recorded across large regions, such as RTM. Li et al. (2018) present a somewhat hybrid method that incorporates both stacking and local similarity aspects. Since the Bogoslof eruption begun in 2016, several more infrasound arrays have been added to the region, significantly improving the azimuthal coverage, and thereby improving the capacity for accurate detection and location, with lower

warning latency. The wider distribution of sensors also permits strategies that use sub-network approaches for location estimates (e.g., e.g., Xu et al., 2009).

Aside from volcanoes, there are several other sources of infrasound in Alaska which can be studied, and used for testing and developing detection algorithms, and establishing factors which affect signal detectability. These include rocket launches, earthquakes, bolides, storms, mine blasts, and so forth. Many of these types of events, and others, were recorded by the Transportable Array while it was traversing the continental US (TA Infrasound Reference Event Database, http://ds.iris.edu/ds/products/infrasound-taired/). Comparing observations to existing models for source radiation, wavefield propagation, and air-to-ground coupling are other areas of potential exploration. Using coherence of infrasound and air-to-ground coupled waves at stations that incorporate both seismic and infrasound sensors can help improve SNR as well as location strategies by appropriately weighting data where coherence is high, rather than low (e.g., Fee et al., 2017; appendix 1).

Potential future work avenues to improve upon the existing RTM scheme include stacking other forms of the data than the temporal envelopes used presently, which may better exploit characteristics of the data and improve SNR. Such functions might include short-term average / long-term average (STA/LTA) ratios (e.g., Grigoli et al., 2014), cross-correlation, potentially with one-bit signal conversion (e.g., Ruigrok et al., 2017; appendix 1), envelope frequency ratios (Sit et al., 2012), or kurtosis (e.g., Langet et al., 2014). The RTM code architecture itself also has room for improvement, particularly from a run-time and file size perspective. Use of alternate coding languages for the main time sinks, and new file formats (e.g., ASDF; Krischer et al., 2016) may improve these particular areas. Finally, establishing the interaction of different processing parameters on detector function behavior is an important objective, with an aim to make configuration setups more intuitive.

2. Chapter 3

Chapter 3 explores the question of whether reducing noise and clutter in volcanic infrasound data through signal preprocessing can improve event detectability and location accuracy. This chapter follows partly from findings in chapter 2 which showed that one of the limitations to using TA data were the often low SNR conditions. This chapter continues with RTM assessments, and further introduces array processing results from AVO stations. Data again come from the Bogoslof eruption sequence, as well as synthetic events. Five denoising algorithms are evaluated using metrics for SNR changes, distortion, need for manual data labeling, computational cost, and time-varying detection rates. These methods can isolate and reduce the amplitude of microbaroms in the data, thereby increasing detection of eruption signal components within the corresponding frequency band (~0.1–0.5 Hz). Impacts of this are primarily seen in the array processing results. Another benefit is events becoming clearer through removal of the microbarom clutter in cases of a shared back azimuth. These two factors typically help to improve event identification and location capabilities. Algorithm performance varies between methods, with denoised SNR varying by as much as 10 dB. Use of the PMCC array-processing algorithm highlights where infrasound was detected for several time period or arrays, but had not previously been registered in catalogs developed using other processing methods and threshold levels. Establishing robust event onsets and durations is critical for such catalogs, which subsequent studies may depend on (e.g., chapter 2). Clarity of event limits is typically enhanced via denoising. For wind noise, its relative character to events depends on source station-receive distance, station hardware, vegetation, snow levels, and local wind conditions. This makes for highly variable denoising effectiveness from site to site. Performance is also typically proportional to the original SNR of the data, and inversely proportional to the spectral and temporal overlap of

signals and noise. These findings also apply to microbaroms. Reducing wind noise does not significantly increase the detectability of non-noise elements during such periods, and thus has limited applications for array processing. For RTM, microbarom removal has relatively little effect on stacked SNR, whereas wind removal either through trace denoising or high-pass filtering has more of an impact.

A focus of this study has been exploring the use of open-source denoising methods that can be applied to a single trace prior to any analytical scheme. This approach acts as an alternative to SNR improvement through beamforming or stacking traces. One advantage is computational run-time. For RTM in particular, denoising each trace prior to the grid search stage is often more efficient than using elaborate nonlinear stacking operations for each node of a fine-mesh grid. Another asset of a single-trace based approach is the flexibility that comes with not needing any additional data in order to denoise a waveform. This has applicability to experiments with small data sets where constructing extensive training schemes is not possible. Deployments that have standalone, or widely dispersed sensors can also benefit, as enhancing coherence and event isolation through trace-aggradation is less practical. As infrasound arrays and spatial noise reduction systems can have large footprints, the range of deployment options for single sensors can increase if these kinds of data denoising techniques continue development and become more established in the community. Aside from detection and location strategies, denoising can potentially improve many other kinds of analyses that rely on waveform fidelity, such as source dynamic characterization and quantification, as well as simply viewing and presenting data. Future work expanding upon the range of events and scenarios presented in this paper will be important for understanding application best practices.

There are several additional potential research directions that stem from the work in chapter 3. First, ways to improve the effects of wind noise reduction on RTM processing can be explored further. As stated in chapter 3, high-pass filtering offered improved results compared to wind noise reduction. Automatic gain control (AGC) as part of the processing potentially offset the anticipated improvements made by such denoising. Implementation of AGC was due to results being better with AGC than without for the RTM parameter combinations explored, but there may be an effective configuration for denoised data without AGC. Although non-negative matrix factorization (NMF) was the only method extensively pursued in chapter 3 for wind noise reduction (with several others rejected prior for poor performance), this is an obvious area for development. Particularly, one result was that few additional PMCC detections were made following NMF, but other approaches may prove more fruitful (e.g., Cook et al., 2021). For microbarom denoising, there is room for expansion on making fair comparisons between methods. For instance, parameter choices are based on having consistent spectral amplitudes for the microbarom in the stage 2 foregrounds (e.g., Figure 5, chapter 3). However, other figures show clear differences in performance when using other metrics, such as stage-2 SNR (Figure 11). Although outside of the scope of the study, comparisons between the denoising schemes applied here (prior to PMCC array processing), and schemes that penalize incoherent elements between several pre-aligned traces would be of interest for a few select events (e.g., Samson and Olson, 1981; Nakata et al., 2015). An updated Bogoslof eruption catalog (Coombs et al., 2019) could be generated based on upon such additional analysis, should the processing indicating adjustable onset times, durations, and/or detecting arrays.

One of the central challenges for designing a widely applicable denoising scheme is the highly variable nature of signals and noise, both between stations, and even at the same

station over time. The aforementioned factors dictating wind noise can both affect amplitude, as well as frequency, with a typical dominant frequency < 0.1 Hz not always observed. Similarly, the strength and peak frequency of the microbarom can vary with seasonal storm activity. Signal character may be modulated by source style and duration, anisotropic radiation, as well as time-varying path and site effects. Establishing how these individual effects can impact denoising performance is important for uptake of such tools, with spectral angle (e.g., Ramirez-Lopez et al., 2013) offering an alternative to the frequency-index method in Figure 12. These events may in some cases be similar in nature to either the microbarom or wind, adding another complexity. Exploiting any unique characteristics for each waveform component is therefore critical for successful separation. The methods applied here largely use manual labeling of features to aid in effective denoising, with the scope aimed toward identifying how effective they can be under such supervision. For automated classification and denoising systems, however, the use of dictionaries of a wide variety of potential noise characteristics is likely essential given the variability discussed. Focusing on identifying and removing only the noise, rather than also identifying signals explicitly, may simplify the task, and enable the residual cleaned data to contain a range of both volcanic and nonvolcanic events. As with RTM, real time implementations may require different approaches to when working with already archived waveforms, due to either need for computational efficiency, or the unpredictable and evolving nature of the data. Generally speaking, the goal is a combination of denoising and detection/location processing stages that sufficiently balance speed and effectiveness for the situation at hand. Advances in a variety of machine learning techniques are helping to rapidly develop these kinds of fields. Artificial neural networks commonly underpin the software implementations, which use various degrees of supervision to classify and denoise data (e.g., Zhu et al., 2019; Jiang et al., 2020).

3. Chapter 4

Chapter 4 describes a pilot infrasound experiment from 2017 to 2021 at Mount Adams, WA, to record mass movements and characterize the ambient environmental noise. Hydrothermal alteration and erosion of the summit of this dormant stratovolcano has contributed to mass wasting activity, with the potential for large flows posing a risk to downstream communities (e.g., Finn et al., 2007). Recording small to moderate events that occur on a yearly to decadal scale help establish detection and location capabilities of both recording systems and processing algorithms. Twelve mass movements are identified in data from the long-term infrasound array, based on array processing results, and spectral analysis. Seismic data from an existing nearby station helps to corroborate some of these events, which can generate transient ground vibrations, as well as air-to-ground coupled waves. These small events (volumes $< 10^5$ m^3 and durations < 2 min) were generally not observed visually by eye witnesses, or by satellite. Similarly, several visually observed events were not detected infrasonically. An exception in both cases was a glacial avalanche, which occurred during the deployment of three additional temporary infrasound arrays. The contemporary presence of four stations enabled a precise source location to be determined for the avalanche, which matched visual evidence in satellite imagery. Array processing also reveals near-continuous infrasound signals arriving from most back azimuths around the array, with source activity varying with the time of year. During summer, the predominant direction is toward Mount Adams, coincident with steep drainages and waterfalls on the southwest flank. The other back azimuths also largely coincide with identifiable waterfalls. Fluctuations in this background clutter appears to largely vary with wind-noise levels, individual waterfall characteristics, and water discharge levels. The complex surrounding watershed is affected by a mixture of glaciers, annual snow deposition, precipitation events,

and widely varying temperatures and topography. These factors make a robust analysis of this clutter challenging with the currently available infrasound, weather, and stream data.

Key aspects in whether mass movements can be detected are the source size, source proximity, level of wind noise, and the presence of any other infrasound sources occurring simultaneously. For the events in this study, which are small, and occurring on the order of 5–10 km from sensors, these latter two aspects can be significant. During the day, wind speeds are typically higher, potentially causing events of interest to be masked in the data. The combination of wilderness boundary, and forests either too dense for solar panels, or too sparse for adequate wind mitigation, makes desirable site selections difficult to identify in this area, however. Use of cameras focused on the upper reaches of Mount Adams may have helped capture specific locations of some of the missed events, particularly in the summer when instability is highest and weather clearest. Similarly, confirming that much of the background clutter (microbaroms aside) is produced by local fluvial and waterfall infrasound requires study with additional instrumentation, such as using flow data and imagery at several select sites. As fluidized debris flows (lahars) can traverse these channels, characterizing their normal range of fluvial and infrasonic behaviors is critical, particularly as locations like waterfalls can become dominant sound sources, even in the presence of a moving flow. Reducing microbarom detections using methods described in chapter 3 would help clarify the local data landscape. Additionally, such techniques could potentially remove other clutter from persistent fluvial sources so that only transient changes to these features are highlighted. Exploring alternate array processing algorithms to PMCC would be beneficial, as this algorithm is not optimized to identify more than one source at a time within the same frequency band. Example approaches include root-MUSIC (Rübsamen and Gershman, 2009) and modified applications of CLEAN (Högbom, 1947; den Ouden et al.,

2020). Propagation effects due to topography and wind can also be significant (e.g., Johnson and Palma, 2015; Marchetti et al., 2019b) and needs to be understood better in this region. Better characterization of snow coverage effects on SNR would also significantly help with station and detection system design, particularly given that the limited literature on this topic to date has provided inconsistent results (e.g., Adam, 1998; Bowman et al., 2005; Woodward et al., 2005; Keith et al., 2018).

For large events of a hazardous nature, it is probable that these would be detectable with the kinds of instrumentation and site locations in the study. Activity during the last 100 years has included events up to 8 km long (e.g., Vallance, 1999), with this type of magnitude more likely to be seen in the near term than those of a scale capable of reaching the community of Trout Lake, 22 km south. Probabilistic flow and acoustic propagation modeling can help to establish what kinds of network configurations would be suitable for detecting and tracking such an event, when accounting for factors like flow composition, wind noise levels, and flow path (e.g., Watson et al., 2020; Coco et al., 2021). A future comprehensive monitoring strategy would however not likely rely on infrasound alone, but rather also include additional instrumentation around a few key drainages such as seismometers, video surveillance, flow meters, and trip wires (e.g., Stähli et al., 2015). This range of data types would improve detection sensitivity and flow-front location accuracy, and allow for interpretation of physical properties. With this kind of robust system, false alarms can be minimized, and alerts tailored to events of particular magnitude. Further to a recent review of infrasonic detection of volcano mass movements (Allstadt et al., 2018), this study demonstrates some of the physical and analytical challenges involved in identifying signals of interest in a noisy background environment formed by wind and drainages.

4. Final Remarks

There are several recurring themes in the results from these chapters. These include the limitations of poor SNR and limited sensor distributions, with wind noise and anisotropic atmospheric propagation playing a large part in signal detectability. Wind noise reduction though signal processing is a potentially useful, but still second best scenario compared to careful site selection and hardware designs to limit wind noise being initially recorded. Whereas configurations of pipes and hoses have been traditionally used to this end in high-end arrays (e.g., Marty, 2019), the availability of fabric or metal wind domes are increasing the options available, but their size can sometimes be impractical (e.g., Raspet et al., 2019). Although not widely adopted, optical fiber sensors have also been developed for acoustic detection (e.g., Zumberge et al., 2003), offering effective wind noise reduction, particularly as the sensor length and thus spatial averaging increases. The current range of on-sensor shrouds and diffusers offer relatively poor performance to the above systems, however. With infrasound sensors increasingly beginning formed into standalone networks (e.g., Pilger et al., 2018), or incorporated into existing regional geophysical deployments (e.g., Busby et al., 2018; Le Pichon et al., 2021), and used more commonly in a range of science applications (e.g., Wang and Tanimoto, 2020), ensuring the quality of this data is paramount. Effective wind noise mitigation should be a key aspect in these experiment and deployment designs. Some of these sensors follow a low-power, low-cost, and moderate quality systems, facilitating mass production and testing under a range of scenarios (e.g., Anderson et al., 2017). These efforts are akin to nodal arrays that have become more common in seismology in recent years (e.g., Kiser et al., 2016). As the temporally and spatially evolving velocity structure of the atmosphere affects which stations are able to detect events clearly, wide distributions of sensors are able to both reduce the consequences of poor wavefield sampling

in data analysis. Taking full advantage of these sensors in detecting and locating events of interest, as well as more advanced analyses, often requires use of atmospheric specifications. The ongoing proliferation of open-source propagation and atmospheric modeling codes, as well as the increasing availability of powerful computational resources can ideally make such efforts more routine and commonplace (e.g., de Groot-Hedlin, 2017; Waxler, 2017). Equally, high numbers of sensors are able to highlight where these models still need further development to match predictions and observations (e.g., Green et al., 2018; Fee et al., 2020). In a similar fashion, and as noted for chapter 3, rapid machine learning developments in the fields of automated event and classification, as well as detection and location will facilitate future investigations into the types of questions addressed in this dissertation (e.g., Carniel and Guzmán, 2020, and references therein).

References

Adam, V., Chritin, V., Rossi, M., and Lancker, E. (1998). Infrasonic monitoring of snow-avalanche activity: What do we know and where do we go from here? *Annals of Glaciology*, 26, 324–328. https://doi.org/10.3189/1998AoG26-1-324-328

Allstadt, K. E., Matoza, R. S., Lockhart, A. B., Moran, S. C., Caplan-Auerbach, J., Haney, M. M., Thelen, W. A., and Malone, S. D. (2018). Seismic and acoustic signatures of surficial mass movements at volcanoes. *Journal of Volcanology and Geothermal Research*, 364, 76–106. https://doi.org/10.1016/j.jvol-geores.2018.09.007

Anderson, J. F., Johnson, J. B., Bowman, D. C., and Ronan, T. J. (2017). The Gem infrasound logger and custom-built instrumentation. *Seismological Research Letters*, 89(1), 153–164. https://doi.org/10.1785/0220170067

Bowman, J. R., Baker, G. E., and Bahavar, M. (2005). Ambient infrasound noise. *Geophysical Research Letters*, 32, L09803. https://doi.org/10.1029/2005GL022486

Busby, R. W., Woodward, R. L., Hafner, K. A., Vernon, F. L., and Frassetto, A. M. (2018). *The design and implementation of EarthScope's USArray Transportable Array in the Conterminous United States and Southern Canada*. Retrieved from: http://www.usarray.org/ researchers/obs/transportable/l48_ta_report

Carniel R, and Silvina, R. G. (2020). Machine learning in volcanology: A review. In: K. Németh (Ed.), *Updates in volcanology: transdisciplinary nature of volcano science*. IntechOpen. https://doi.org/10.5772/intechopen.94217

Cochran, E., and Shearer, P. (2006). Infrasound events detected with the Southern California Seismic Network. *Geophysical Research Letters*, 33, L19803. https://doi.org/10.1029/2006GL026951

Coco, M., Marchetti, E., and Morandi, O. (2021). Numerical modeling of infrasound energy radiation by debris flow events. *Pure and Applied Geophysics*, 178, 2301–2313. https://doi.org/10.1007/s00024-021-02759-2

Coombs, M. L., Wallace, K., Cameron, C., Lyons, J. J., Wech, A., Angeli, K., and Cervelli, P. (2019). Overview, chronology, and impacts of the 2016–2017 eruption of Bogoslof volcano, Alaska. *Bulletin of Volcanology*, 81(11), 1–23. https://doi.org/10.1007/s00445-019-1322-9

de Groot-Hedlin, C. (2017). Infrasound propagation in tropospheric ducts and acoustic shadow zones. *The Journal of the Acoustical Society of America*, 142, 1816–1827. https://doi.org/10.1121/1.5005889

de Groot-Hedlin, C. D., and Hedlin, M. A. H. (2015). A method for detecting and locating geophysical events using groups of arrays. *Geophysical Journal International*, 203, 2, 960–971. https://doi.org/10.1093/gji/ggv345

den Ouden, O. F. C., Assink, J. D., Smets, P. S. M., Shani-Kadmiel, S., Averbuch, G., and Evers, L. G. (2020). CLEAN beamforming for the enhanced detection of multiple infrasonic sources. *Geophysical Journal International*, 221(1), 305–317. https://doi.org10.1093/gji/ggaa010

Fee, D., Bishop, J. W., Waxler, R., and Matoza, R. S. (2020). *Infrasound Propagation Working Group (IPWG) report*. Available at: https://watc.alaska.edu/sites/default/files/2021-06/IPWG%20Report_final.pdf

Fee, D., Haney, M. M., Matoza, R. S., Van Eaton, A. R., Cervelli, P., Schneider, D. J., and Iezzi, A. M. (2017). Volcanic tremor and plume height hysteresis from Pavlof Volcano, Alaska. *Science*, 355(6320), 45–48. https://doi.org/10.1126/science.aah6108

Finn, C. A., Desczcz-Pan, M., Anderson, E. D., and John, D. A. (2007). Three-dimensional geophysical mapping of rock alteration and water content at Mount Adams, Washington: Implications for lahar hazards. *Journal of Geophysical Research*, 112, B10204. https://doi.org/10.1029/2006JB004783

Green, D. N., and Nippress, A. (2019). Infrasound signal duration: The effects of propagation distance and waveguide structure. *Geophysical Journal International*, 216(3), 1974–1988. https://doi.org/10.1093/gji/ggy530

Green, D. N., Waxler, R., Lalande, J.-M., Velea, D., and Talmadge, C. (2018). Regional infrasound generated by the Humming Roadrunner ground truth experiment. *Geophysical Journal International*, 214(3), 1847–1864. https://doi.org/10.1093/gji/ggy232

Grigoli, F., Cesca, S., Amoroso, O., Emolo, A., Zollo, A., and Dahm, T. (2014). Automated seismic event location by waveform coherence analysis. *Geophysical Journal International*, 196(3), 1742–1753, https://doi.org/10.1093/gji/ggt477

Högbom, J. (1974). Aperture synthesis with a non-regular distribution of interferometer baselines. *Astronomy and Astrophysics Supplement*, 15, 417–426.

Jiang, J., Stankovic, L., Stankovic, V., and Pytharouli, S. (2020). Automatic detection and classification of microseismic events from super-sauze landslide using convolutional neural networks. Abstract [S052_0009] presented at *2020 Fall Meeting, AGU*.

Johnson, J. B., and Palma, J. (2015). Lahar infrasound associated with Volcan Villarrica's 3 March 2015 eruption. *Geophysical Research Letters*, 42(15), 6324–6331. https://doi.org/10.1002/2015GL065024

Keith, S. E., Daigle, G. A., and Stinson, M. R. (2018). Wind turbine low frequency and infrasound propagation and sound pressure level calculations at dwellings. *Journal of the Acoustical Society of America*, 144(2), 981–996. https://doi.org/10.1121/1.5051331

Kiser, E., Palomeras, I., Levander, A., Zelt, C., Harder, S., Schmandt, B., Hansen, S., Creager, K., and Ulberg, C. (2016). Magma reservoirs from the upper crust to the Moho inferred from high-resolution Vp and Vs models beneath Mount St. Helens, Washington State, USA. *Geology*, 44(6), 411–414. https://doi.org/10.1130/G37591.1

Koper, K. D., Hutko, A. R., Lay, T., and Sufri, O. (2012). Imaging short-period seismic radiation from the 27 February 2010 Chile (MW 8.8) earthquake by back-projection of P, PP, and PKIKP waves. *Journal of Geophysical Research: Solid Earth*, 117, B02308. https://doi.org/10.1029/2011JB008576

Krischer, L., Smith, J., Lei, W., Lefebvre, M., Ruan, Y., Sales de Andrade, E., Podhorszki, N., Bozdağ, E., and Tromp, J. (2016). An adaptable seismic data format. *Geophysical Journal International*, 207(2), 1003–1011. https://doi.org/10.1093/gji/ggw319

Langet, N., Maggi, A., Michelini, A., and Brenguier, F. (2014). Continuous kurtosis-based migration for seismic event detection and location, with application to Piton de la Fournaise volcano, La Réunion. *Bulletin of the Seismological Society of America*, 104(1), 229–246. https://doi.org/10.1785/0120130107

Le Pichon, A., Pilger, C., Ceranna, L., Marchetti, E., Lacanna, G., Souty, V., et al. (2021). Using dense seismo-acoustic network to provide timely warning of the 2019 paroxysmal Stromboli eruptions. *Scientific Reports*, 11(14464). https://doi.org/10.1038/s41598-021-93942-x

Li, Z., Peng, Z., Hollis, D., Zhu, L., and McClellan, J. (2018). High-resolution seismic event detection using local similarity for Large-N arrays. *Scientific Reports*, 8, 1646. https://doi.org/10.1038/s41598-018-19728-w

Marchetti, E., Ripepe, M., Campus, P., Le Pichon, A., Vergoz, J., Lacanna, G., et al. (2019a). Long range infrasound monitoring of Etna volcano. *Scientific Reports*, 9, 18015. https://doi.org/10.1038/s41598-019-54468-5

Marchetti, E., Walter, F., Barfucci, G., Genco, R., Wenner, M., Ripepe, M., McArdell, B., and Price, C. (2019b). Infrasound array analysis of debris flow activity and implication for early warning. *Journal of Geophysical Research*, 124(2), 567–587. https://doi.org/10.1029/2018JF004785

Marty, J. (2019). The IMS infrasound network: Current status and technological developments. In: A. Le Pichon, E. Blanc, and A. Hauchecorne (Eds.), *Infrasound monitoring for atmospheric studies: Challenges in middle-atmosphere dynamics and societal benefits*, (pp. 91–124). Cham: Springer. https://doi.org/10.1007/978-3-319-75140-5_1

Meng, L., Ampuero, J. P., Luo, Y., Wu, W., and Ni, S. (2012). Mitigating artifacts in back-projection source imaging with implications for frequency-dependent properties of the Tohoku-Oki earthquake. *Earth, Planets and Space*, 64(12), 1101–1109. https://doi.org/10.5047/eps.2012.05.010

Morton, E. A., and Arrowsmith, S. J. (2014). The development of global probabilistic propagation look-up tables for infrasound celerity and back-azimuth deviation. Seismological Research Letters, 85(6), 1223–1233. https://doi.org/ 10.1785/0220140124

Nakata, N., Chang, J. P., Lawrence, J. F., and Boué, P. (2015). Body wave extraction and tomography at Long Beach, California, with ambient-noise interferometry. *Journal of Geophysical Research: Solid Earth*, 120, 1159–1173. https://doi.org/1002/2015JB011870

Olson, J. V, and Szuberla, C. A. L. (2008). Processing infrasonic array data, In D. Havelock., S. Kuwano, and M. Vorländer (Eds.), *Handbook of Signal Processing in Acoustics*, (pp. 1487–1496). New York: Springer. https://doi.org/10.1007/978-0-387-30441-0_81

Pilger, C., Ceranna, L., Ole Ross, J., Vergoz, J., Le Pichon, A., Brachet, N., et al. (2018). The European Infrasound Bulletin. *Pure and Applied. Geophysics*, 175, 3619–3638. https://doi.org/10.1007/s00024-018-1900-3

Ramirez-Lopez, L., Behrens, T., Schmidt, K., Viscarra-Rossel, R. A., Demattê, J. A. M., and Scholten, T. (2013). Distance and similarity-search metrics for use with soil vis–NIR spectra. Geoderma, 199, 43–53. https://doi.org/10.1016/j.geoderma.2012.08.035

Raspet, R., Abbott, J.-P., Webster, J., Yu, J., Talmadge, C., Alberts, K. II, et al. (2019). New systems for wind noise reduction for infrasonic measurements. In: A. Le Pichon, E. Blanc, and A. Hauchecorne (Eds.), *Infrasound monitoring for atmospheric studies: Challenges in middle-atmosphere dynamics and societal benefits*, (pp. 91–124). Cham: Springer. https://doi.org/10.1007/978-3-319-75140-5_3

Rübsamen, M., and Gershman, A. B. (2008). Direction-of-arrival estimation for nonuniform sensor arrays: From manifold separation to Fourier domain MUSIC Methods, *IEEE Transactions on Signal Processing*, 57(2), 588–599. https://doi.org/10.1109/TSP.2008.2008560

Ruigrok, E., Gibbons, S., and Wapenaar, K. (2017). Cross-correlation beamforming. *Journal of Seismology,* 21(3), 495–508. https://doi.org/10.1007/s10950-016-9612-6

Samson, J. C., and Olson, J. V. (1981). Data-adaptive polarization filters for multichannel geophysical data. *Geophysics*, 46, 10, 1423–1431. https://doi.org/10.1190/1.1441149

Schwaiger, H. F., Iezzi, A. M., and Fee, D. (2019). AVO-G2S: A modified, open-source Ground-to-Space atmospheric specification for infrasound modeling. *Computers & Geosciences*, 125, 90–97. https://doi.org/10.1016/j.cageo.2018.12.013

Sit, S., Brudzinski, M., and Kao, H. (2012). Detecting tectonic tremor through frequency scanning at a single station: Application to the Cascadia margin. *Earth and Planetary Science Letters*, 353–354, 134–144. https://doi.org/10.1016/j.epsl.2012.08.002

Stähli, M., Sättele, M., Huggel, C., McArdell, B. W., Lehmann, P., Van Herwijnen, A., Berne, A., Schleiss, M., Ferrari, A., Kos, A., et al. (2015). Monitoring and prediction in

early warning systems for rapid mass movements. *Natural Hazards and Earth System Sciences*, 15, 905–917. https://doi.org/10.5194/nhess-15-905-2015

Vallance, J. W. (1999). Postglacial lahars and potential hazards in the White Salmon River system on the southwest flank of Mount Adams, Washington. *U.S. Geological Survey Bulletin*, 2161. https://doi.org/10.3133/b2161

Wang, J., and Tanimoto, T. (2020). Estimating near-surface rigidity from low-frequency noise using collocated pressure and horizontal seismic data. *Bulletin of the Seismological Society of America,* 110(4), 1960–1970. https://doi.org/10.1785/0120200098

Watson, L. M., Dufek, J., Dunham, E. M., and Mohaddes, D. (2020). Computational aeroacoustic simulations of infrasound signals from volcanic eruptions. Abstract [S006-06] presented at *2020 Fall Meeting, AGU*.

Waxler, R., Assink, J., Hetzer, C., and Velea, D. (2017). NCPAprop—A software package for infrasound propagation modeling. *The Journal of the Acoustical Society of America*, 141, 3627. https://doi.org/10.1121/1.4987797

Woodward, R., Israelsson, H., Bondár, I., McLaughlin, K., Bowman, J. R., and Bass, H. (2005). Understanding wind-generated infrasound noise. *Proceedings of the 27th Seismic Research Review: Ground-based nuclear explosion monitoring technologies*, 866–875. Retrieved from https://www.osti.gov/servlets/purl/1027447

Xu, Y., Koper, K. D., Sufri, O., Zhu, L., and Hutko, A. R. (2009). Rupture imaging of the M_W 7.9 12 May 2008 Wenchuan earthquake from back projection of teleseismic P waves. *Geochemistry, Geophysics, Geosystems*, 10, Q04006. https://doi.org/10.1029/2008GC002335

Zhu, W., Mousavi, S. M., and Beroza, G. C. (2019). Seismic signal denoising and decomposition using deep neural networks. *IEEE Transactions on Geoscience and Remote Sensing*, 57, 11, 9476–9488. https://doi.org/10.1109/TGRS.2019.2926772

Zumberge, M. A., Berger, J., Hedlin, M. A. H., Husmann, E., Nooner, S., Hilt, R., and Widmer-Schnidrig, R. (2003). An optical fiber infrasound sensor: A new lower limit on atmospheric pressure noise between 1 and 10 Hz. *Journal of the Acoustical Society of America*, 113, 2474–2479. https://doi.org/10.1121/1.1566978

Appendix 1. Preliminary Chapter 2 Work

The material presented in this appendix was developed during work on chapter 2. These topics include preliminary strategies developed to improve reverse time migration (RTM) results, but were ultimately not pursued due to time or publication space limitations, as well as implementation challenges and method effectiveness. Selected results from nonvolcanic events are also included here. Authors, affiliations, acknowledgments, and resources are as per chapter 2. Some material was presented at conferences 2018–2019.

A1.1. Cross-Correlation Beamforming

One approach which shows promise in improving our RTM approach is analogous to cross-correlation beamforming (e.g., Ruigrok et al., 2017), where station traces are replaced with the cross-correlation function between themselves and a template trace. The template can be: 1) from a station known to record eruptions well; or 2) instead of choosing a template (given that the location of events are often unknown a priori), the algorithm can automatically search for which trace would make the nominally best template.

The process is as follows: (1) determine where the center of the event is in absolute time by convolving the template envelope/trace with itself; (2) find event times for each other trace by cross-correlating the template with those traces; (3) use (1) and (2) together to calculate where the events are in absolute time for each trace; (4) replace each trace with the appropriately shifted cross-correlation time-series. I.e., where there was an event waveform, there is now a cross-correlation function; (5) optionally mask traces with low cross-correlation values. This procedure comes after normalization in preprocessing, and the resulting data are not re-normalized.

Stacking the cross-correlation functions can improve detector function (DF) signal-to-noise ratios (SNR) dramatically compared to stacking waveform envelopes, i.e., the primary method in chapter 2. For example, comparing Figure 1 here vs. Figures S3 in chapter 2, and similarly Figure 2 vs. Figure S4, shows that volcanic events are more prominent here. As discussed in chapter 2, much of this effect is due to well correlated traces at arrays. Location accuracy is relatively low here, however. Notably, this approach doesn't generally reduce swimming artifacts/peak broadness, which was the original intent given the stacked functions should be sharper than otherwise. Such artifacts remain independent of stacking method. However, replacing the cross-correlation functions with delta functions may improve results. Parameters that are effective in with cross-correlation beamforming may differ from those use in the standard RTM procedure used in chapter 2. Figure 1 for instance, compared to the methodology presented in chapter 2, filters from 0.5–1.0 Hz, smooths with a 60 s window, subtrends with 1,800 s point spacing, does not use automatic gain control (AGC) or peak emphasis steps, and uses 20 m/s intervals for the celerity range.

We did not incorporate this approach in the principle analysis because, for year-round use, the algorithm cannot rely on a specific template trace due to seasonal changes in the dominant stratospheric wind direction. Consequently, the method is sensitive to optimizing automated template formation, an aspect still under investigation. In addition to RTM however, cross-correlation information via this method, or others (e.g., Bergen and Beroza, 2018, and references therein) may be used in alternate location strategies, such as inversions relying on time difference of arrivals (e.g. Cochran and Shearer, 2006; Fee et al., 2016, and references therein).
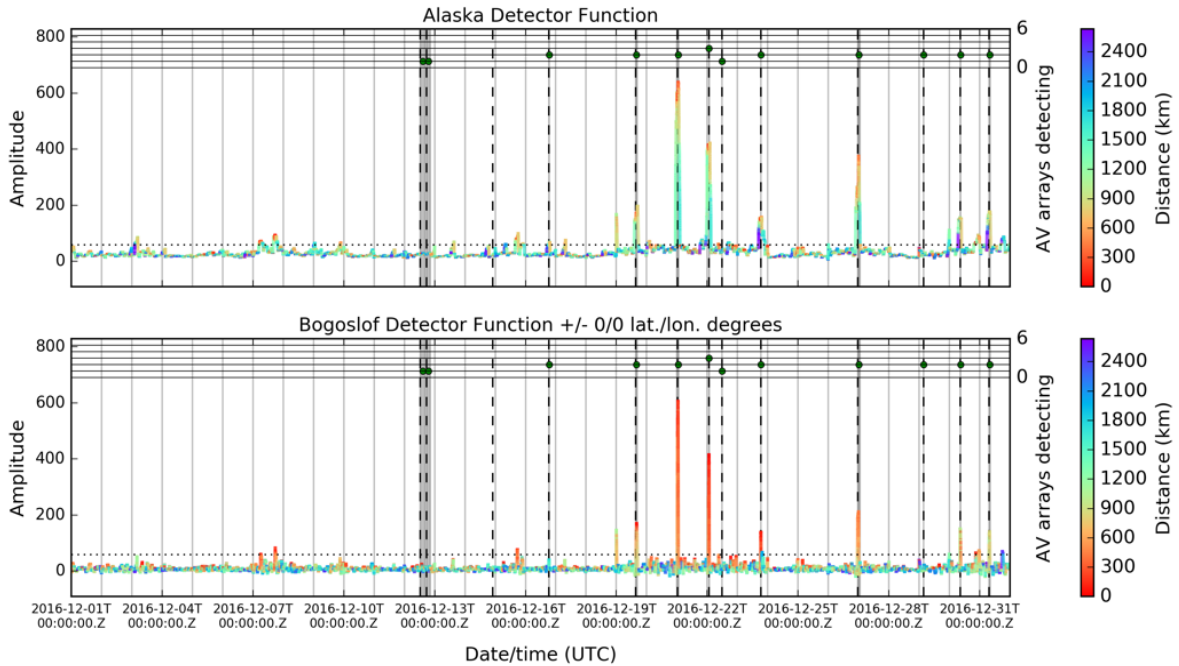
Figure 1. Cross-correlation beamforming RTM results. (a) Alaska-wide detector function (DF) whose variation principally reflects eruptions from Bogoslof during the indicated month. DFs use all available infrasound sensors within 2,000 km of Bogoslof. Colored dots on the second y-axis indicate the number of AVO infrasound arrays were cataloged as having detected infrasound (Coombs et al., 2019). Vertical dashed lines mark the onset of all cataloged events, regardless of infrasound activity, with durations marked by gray bars. The mislocation to Bogoslof for each DF sample is shaded. The horizontal dashed line is equivalent to 12.5 dB on the Alaska-wide DF. (b) As per (a), though the DF reflects variation specifically at the spatial grid node coincident with Bogoslof (i.e., is equivalent to the stack corresponding to this grid node).
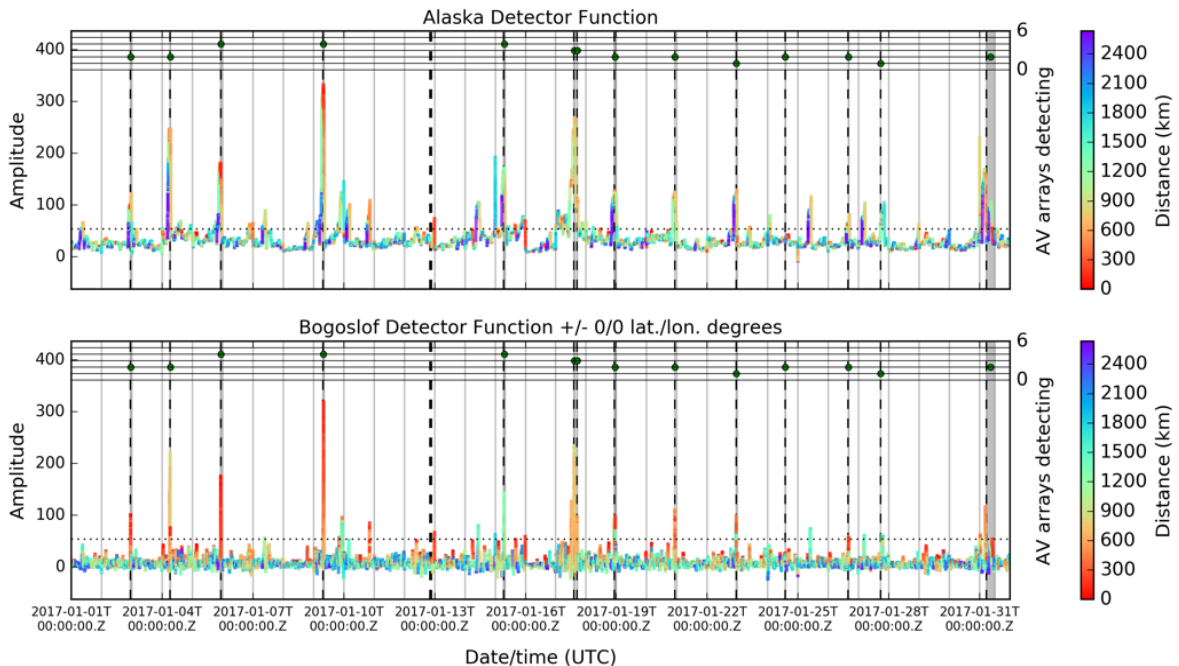
Figure 2. As per Figure 1 for January 2017.

A1.2. Coherence Weighting

Given co-location of seismic and infrasound sensors at the majority of stations, we have begun exploring use of ground-coupled air-waves (GCAs) to improve detection/location capabilities (Ichihara et al., 2012; Fee et al., 2017) using the regional networks in our study. For example, seismo-acoustic coherence analysis may be used to weight/enhance the SNR of volcanic infrasound signals (Matoza and Fee, 2014 and references therein; Fee et al., 2017; McKee et al., 2018) and thus RTM stacks. Alternatively, once GCAs are isolated, amplitude-based location methods could be applied. We assess several eruptions at Bogoslof, Cleveland, and Pavlof (Fee et al., 2017) to identify if using coherence weighted volcanic infrasound with RTM would be viable. We make the following initial observations:

(1) These events generate a sparse presence of volcanic GCAs at up to 1,700 km, with no clear distribution of coherence or infrasound amplitude with distance;

(2) Coherence from non-volcanic sources is common. These non-volcanic coherence patterns can be long or short duration, narrow or broadband, and of various intensities (Figure 3). Some of the waveforms coincident with this non-volcanic coherence appear on multiple proximal stations indicating a real source. Some of the coherence may be recording or processing artifacts;
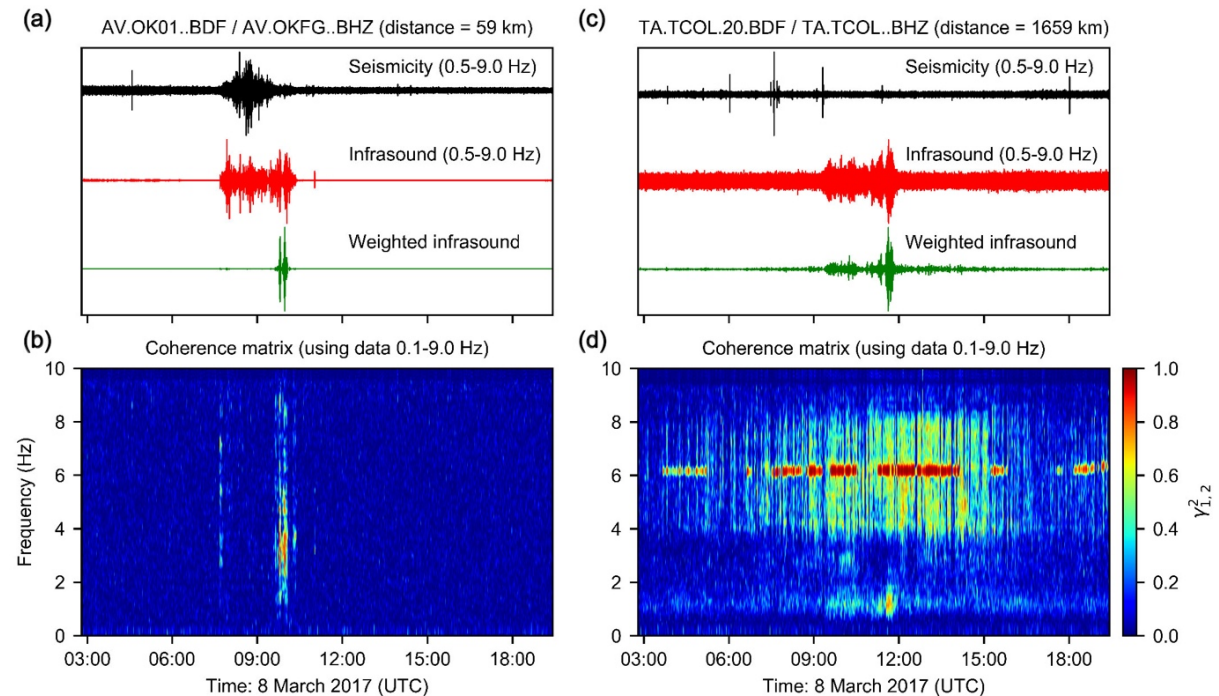

Figure 3. Coherence of Bogoslof data on 8 March 2017. (a) 16 hours of filtered seismic, filtered infrasound, and coherence weighted filtered infrasound data from a station 59 km from Bogoslof. (b) Coherence matrix of infrasound and seismic data. Coherence from the eruption is observed primarily from 2.0–4.0 Hz, with a temporal gap coincident with changes in the acoustic-seismic ratio. Here the unweighted infrasound would be preferred for RTM stacking. (c, d) As per (a, b) but from a station at 1,659 km from Bogoslof, in Fairbanks, Alaska (Figure 1a, chapter 2).. Acoustic arrivals are between ~09:30 and 12:00, either recorded directly by infrasound sensors or as ground-coupled airwaves on the seismic sensor. In Figure 3d, the coherence matrix shows a number of sources of strong coherence, however, indicating the complexity needed in an automated coherence weighting process.

(3) At close proximity to the volcano (e.g., < 100 km) coherence may be unusually low where direct seismic waves negate recording of clear GCAs. This is seen for example for Bogoslof on 8 March 2017 at stations on Okmok (Figure 3a) and Makushin. These coherence observations may also reflect changes in the acoustic-seismic ratio coincident with vent flooding (Lyons et al., 2020).

Considering the above, if all infrasound data based was weighted solely on coherence, useful infrasound from stations that were close to the origin, or infrasound that simply didn't lead to good coherence could be lost. Similarly, non-volcanic coherence may be incorporated by treating all coherence equally. A rigorous strategy will be required in order to incorporate GCAs of this nature into a stacking algorithm. For example, requiring a minimum degree and duration of coherence within frequency bands that are less susceptible to non-volcanic coherence. However, a full treatment of such strategies is beyond the scope of this study.

An example of an event which permits are more straightforward implementation is the 18/19 December 2018 UTC bolide/fireball located between Kamchatka and Alaska at 25.6 km altitude (CNEOS, 2019). This event is the second largest in the last 35 years, with a calculated total impact energy of 173 kilotons (CNEOS, 2019). Clear ground-coupled airwaves are widely identified across Alaska (Figures 4 and 5), enabling use of the weighted infrasound in our RTM scheme. Comparative record sections (Figure 5) show the weighted infrasound having significantly improved SNR. DFs are shown in Figure 6, with similar character to the synthetic examples determined for such a source location (Figure 11b, chapter 2). The DF amplitudes and SNR reflect those in the record sections.
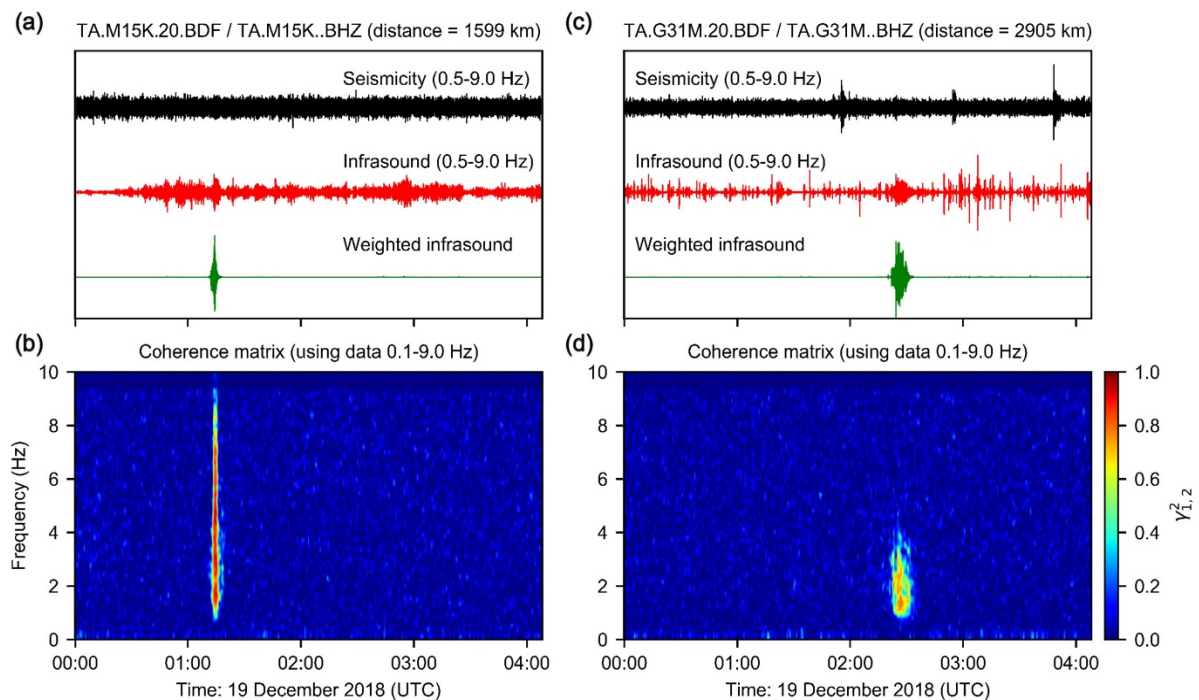

Figure 4. Coherence of data from large bolide on 18/19 December 2018. (a) ~4 hours of filtered seismic, filtered infrasound, and coherence weighted filtered infrasound data from a station at 1,599 km from the published origin (CNEOS, 2019). (b) Coherence matrix of infrasound and seismic data. Coherence from the event is observed clearly at 01:13. (c, d) As per (a, b) but from a station at 2,905 km from the origin. For both stations, the coherence weighted infrasound shows the event more clearly and is preferred for RTM stacking.
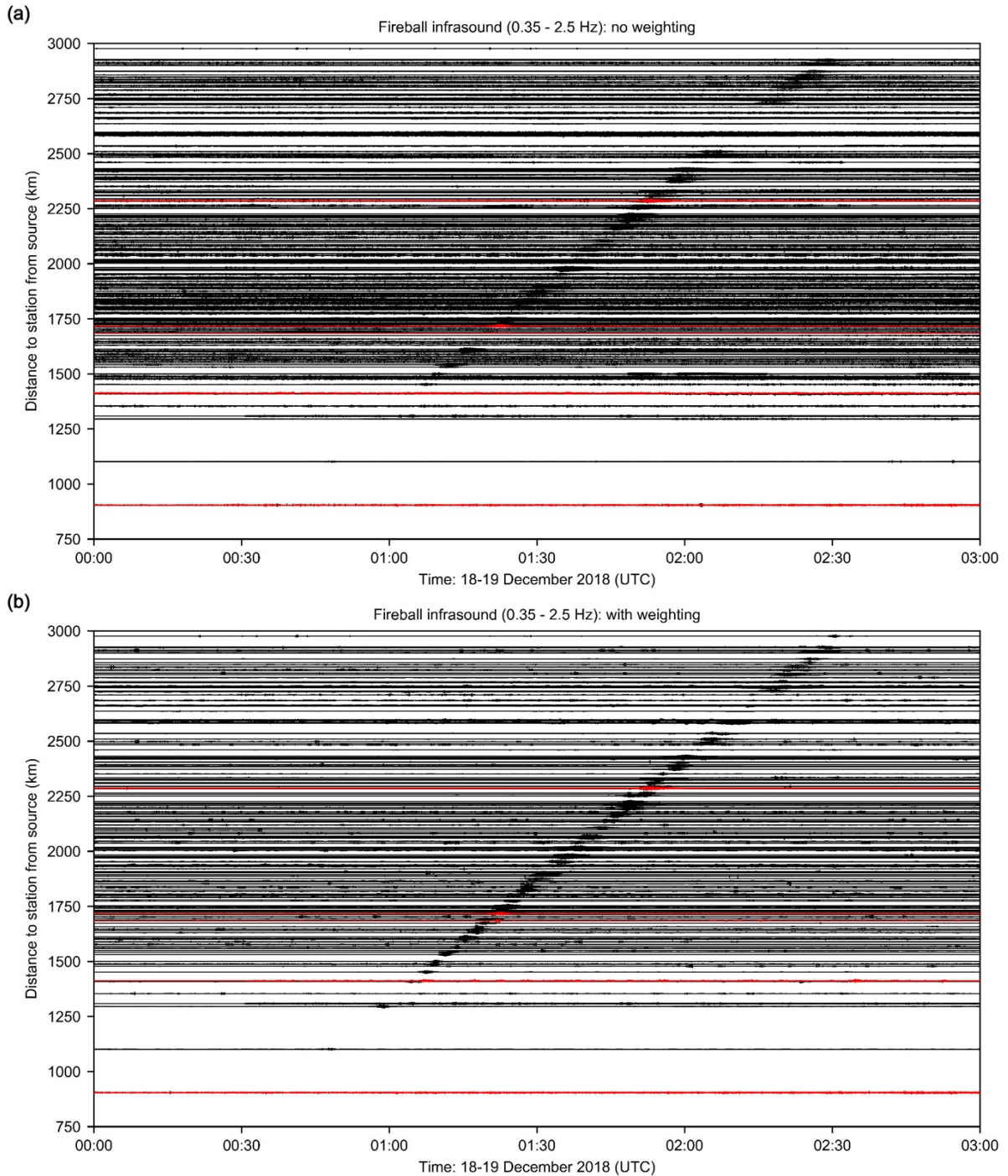
Figure 5. (a) Infrasound record section of a relatively large fireball/bolide on 18/19 December 2018 (filtered 0.35–2.5 Hz). Waveforms have been self-normalized. Array elements are colored red, and non-array sensors colored black. There are clear arrivals to 3,000 km though some of these are obscured by noise. (b) As per (a) but using coherence weighted infrasound (green traces from Figure 4). The noise from (a) is effectively removed by the weighting process, leaving relatively clear signals. The filter range was chosen according to the typical peak coherence band in plots such as Figure 4.
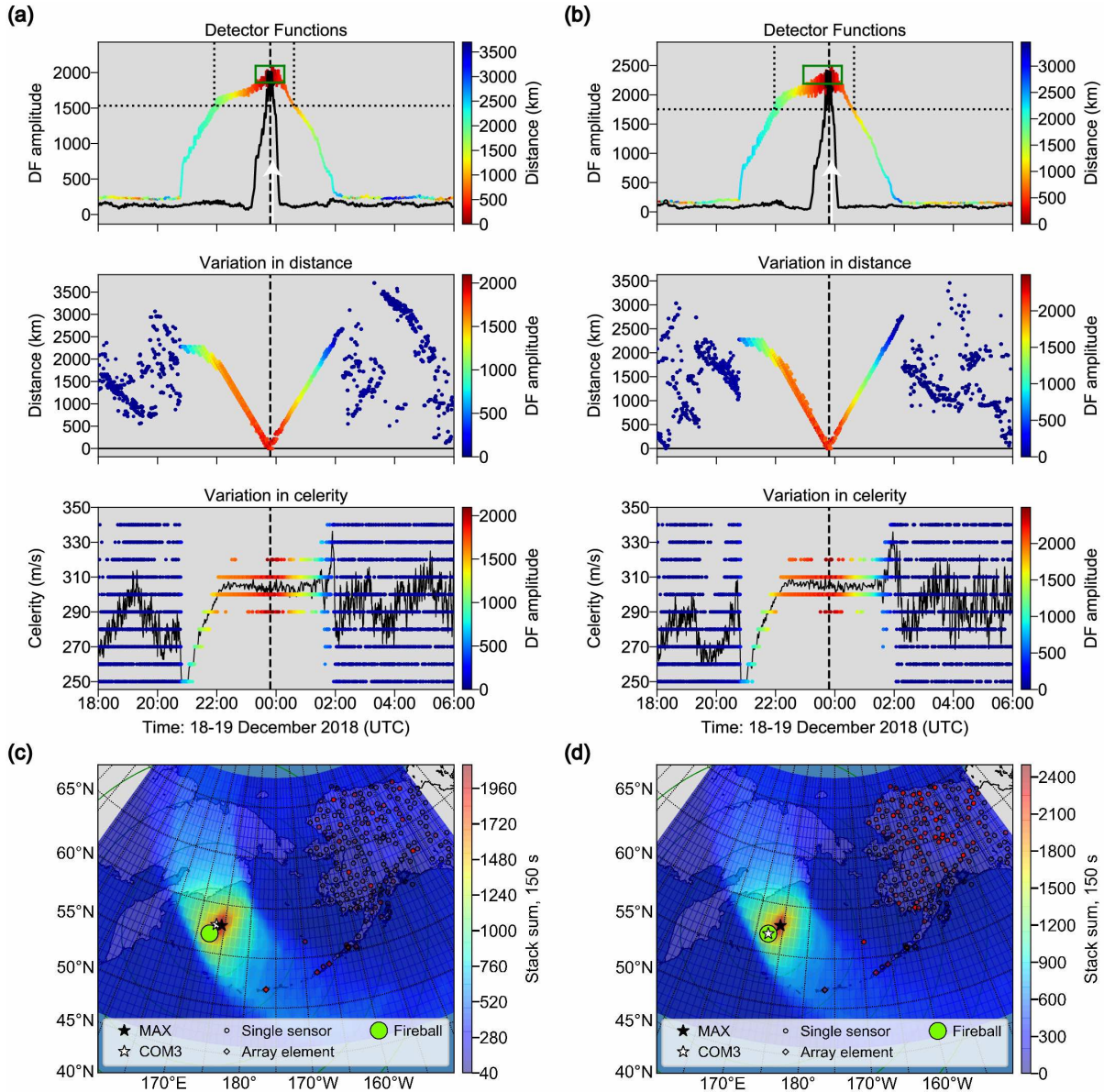
Figure 6. (a) Non-weighted infrasound for fireball event. Top panel: Grid-wide DF (colored by basic distance) and true-source specific DFs (colored black) for the fireball event on 18–19 December 2018 UTC. Matching amplitudes between the two DFs, marked in black, indicate basic locations coincident with the true source location. Final location estimates for the event are performed only on the high amplitude values boxed with solid green lines. Data is from all available infrasound sensors within 3,000 km of the fireball. Due to the summation process in forming the DF, the DF amplitude can be higher than the number of normalized waveform envelopes being stacked. The vertical dashed line is the cataloged event onset (CNEOS, 2019). A white arrow indicates the time of the maximum amplitude. Second panel: Variation in basic distance (section 2.5, chapter 2) over time. Third panel: Variation in celerity over time, reflecting primarily stratospheric arrivals for the event peak. As discussed in section 3.6, chapter 2, the majority of the DF profiles are due to source geometry artifacts. (b) Coherence weighted infrasound for fireball event. Details as per (a). (c) Time-slice of summed-stack amplitudes, taken at the time of the maximum grid-wide DF from (a). The locations determined by RTM are close to those provided by CNEOS (2019). (d) as per (c) but for the coherence weighted infrasound. The COM3 location estimate is at the provided/true source coordinates. Given the magnitude of the event, the results between the two datasets are relatively similar. However, the DF of the coherence-weighted data is higher, and has improved source accuracy vs. the non-weighted data.

A1.3. Earthquake-Induced Infrasound

This section provides some additional details regarding three earthquakes detected and located with RTM during the Bogoslof eruption sequence, and briefly mentioned in chapter 2. The earthquakes are as follows: (1) the M 7.9 earthquake southeast of Kodiak Island in the Gulf of Alaska on 23 January 2018; (2) the M 6.4 earthquake southwest of Kaktovik, Alaska on 12 August 2018; (3) the M 7.1 earthquake in Anchorage, Alaska on 30 November 2018 (Figure 7). RTM provides location estimates 0–100 km from the reported epicenters, with infrasound stations recording these events to distances of 1,800 km, 600 km and 1,250 km for events (1), (2), and (3) respectively. Shani-Kadmiel et al. (2018a) show that for the 2018 Anchorage earthquake, that infrasound was likely generated by steep topography around the Cook Inlet. Notably, that study uses backprojection methods with data from only the IMS IS53 array, following the methods of Shani-Kadmiel et al. (2018b).

Event 1: https://earthquake.usgs.gov/earthquakes/eventpage/us2000cmy3/
Event 2: https://earthquake.usgs.gov/earthquakes/eventpage/ak20076877/
Event 3: https://earthquake.usgs.gov/earthquakes/eventpage/ak20419010/
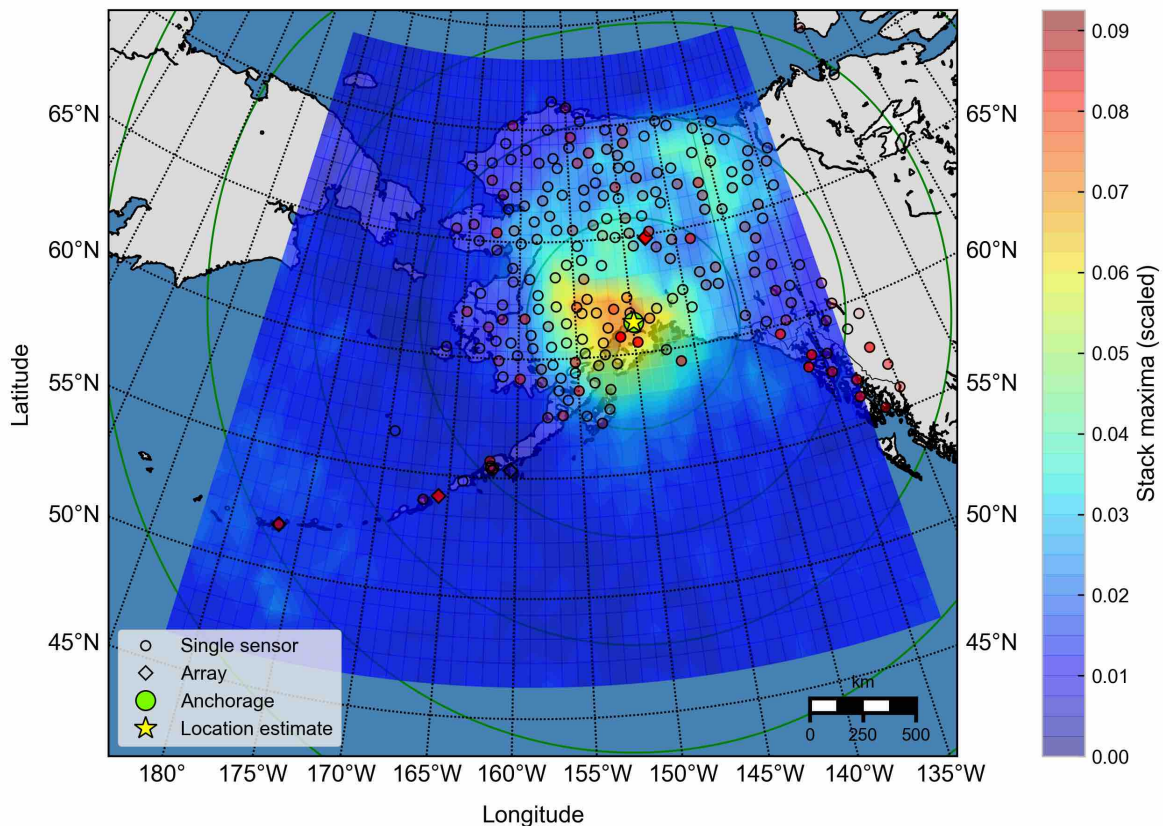

Figure 7. Locating the 30 November 2018 M7.1 Anchorage earthquake with RTM. The event was detected by many stations around Alaska, with the high azimuthal coverage providing a well constrained and accurate source location estimate. The color scale represents the amplitude of time-aligned data stacks at each grid location. Sensors are shaded red proportional to stack contribution for the corresponding source time. Circles are at 500 km spacing.

A1.4. Travel Times from Atmospheric Propagation Models

This section describes an initial foray into mitigating atmospheric path effects on waveforms, which affects trace alignment and the resulting stack amplitude. In the RTM scheme presented in chapter 2, at each time step, traces are stacked using a linear celerity, keeping those stacks that produce the highest amplitudes from the range of celerities tested. In reality, however, celerity varies with azimuth and distance, and is sensitive to atmospheric structures and wind effects that can produce multipathing. One potential result is "branching", where arrivals are unevenly staggered with distance due differing celerities. Compensating for these issues would improve trace alignment during stacking, and thus the resultant DF SNR. Section A1.1. on cross-correlation beamforming is also an effort to use trace alignment, but as signals are emergent and waves change with distance, such approaches can be challenging. In order to obtain realistic travel times between potential sources and stations, an atmospheric model, wind model, and wave propagation software are needed. The former can be relatively up-to-date 12 hour forecasts (e.g., AVO-G2S, Schwaiger et al., 2019), or a daily average of meteorological conditions from long-term observations (e.g., NRLMSISE-00, Picone et al., 2002; HWM-14, Drob et al., 2015), depending on the desired balance of computational efficiency and model accuracy.
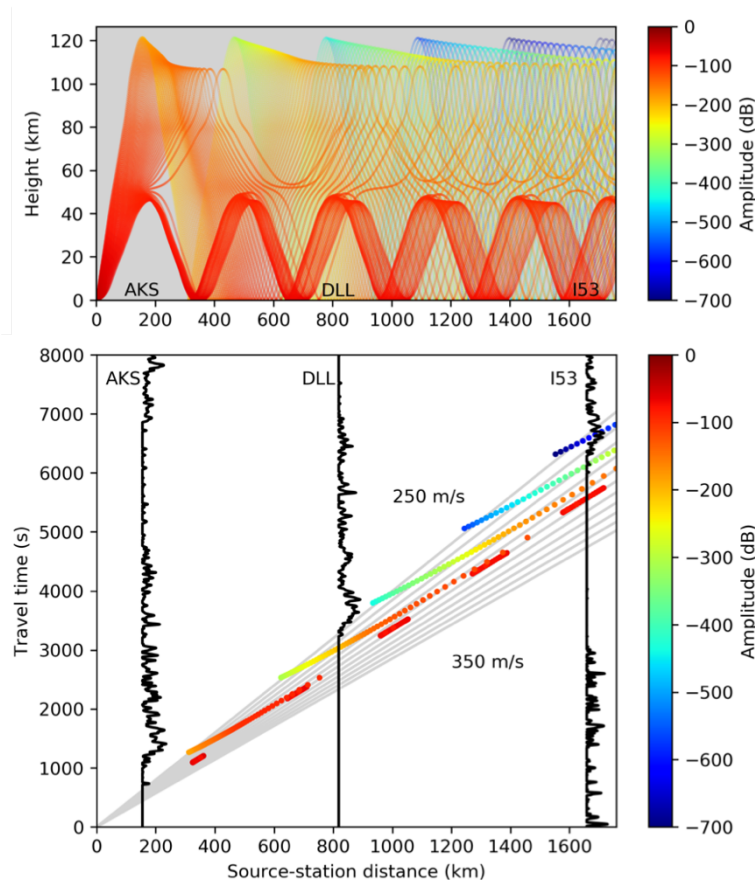

Figure 8. GeoAc ray-tracing (Blom and Waxler, 2012) through an averaged atmospheric model (based on NRLMSISE-00 and HWM-14) for 8 March 2017 Bogoslof eruption. This shows a poor match between predicted and observed arrivals at infrasound stations AKS, DLL, and IS53. The atmospheric profile was calculated with the soon to be publicly available Automated Rapid Climatological Azimuth Deviation Estimation (ARCADE) program (Rodrigo de Negri, University of California, Santa Barbara).

Figure 8 illustrates ray tracing through an average atmospheric model for the day of the 8 March 2017 Bogoslof eruption. A stratospheric duct and thermospheric returns lead to multiple predicted arrivals at three selected stations along a transect between Bogoslof and Fairbanks, Alaska. This example shows some of the expected complications from an average model and simple propagation scheme, such as arrivals predicted in observed shadow zones, and observed signals starting after predicted. In such schemes, traces could be weighted based on predicted attenuation coupled with wind noise assessments. The reader is referred to Schwaiger et al. (2020) for a thorough treatment of infrasound propagation and corresponding observations during the Bogoslof eruption.

References

Bergen, K. J., and Beroza, G.C. (2018). Detecting earthquakes over a seismic network using single-station similarity measures. *Geophysical Journal International*, 213(3), 1984–1998. https://doi.org/10.1093/gji/ggy100

Blom, P., and Waxler, R. (2012). Impulse propagation in the nocturnal boundary layer: Analysis of the geometric component. *The Journal of the Acoustical Society of* America, 131, 3680-3690. https://doi.org/10.1121/1.3699174

CNEOS. (2015). *Fireballs: Fireballs and Bolide Data*. Retrieved from: https://cneos.jpl.nasa.gov/fireballs/

Cochran, E., and Shearer, P. (2006). Infrasound events detected with the Southern California Seismic Network. *Geophysical Research Letters*, 33, L19803. https://doi.org/10.1029/2006GL026951

Coombs, M. L., Wallace, K., Cameron, C., Lyons, J. J., Wech, A., Angeli, K., and Cervelli, P. (2019). Overview, chronology, and impacts of the 2016–2017 eruption of Bogoslof volcano, Alaska. *Bulletin of Volcanology*, 81(11), 1–23. https://doi.org/10.1007/s00445-019-1322-9

Drob, D. P., Emmert, J. T., Meriwether, J. W., Makela, J. J., Doornbos, E., Conde, M. et al. (2015), An update to the Horizontal Wind Model (HWM): The quiet time thermosphere. *Earth and Space Science*, 2, 301–319. https://doi.org/10.1002/2014EA000089

Fee, D., Haney, M., Matoza, R., Szuberla, C., Lyons, J., and Waythomas, C. (2016). Seismic envelope-based detection and location of ground-coupled airwaves from volcanoes in Alaska. *Bulletin of the Seismological Society of America*, 106(3), 1–12. https://doi.org/10.1785/0120150244

Fee, D., Haney, M. M., Matoza, R. S., Van Eaton, A. R., Cervelli, P., Schneider, D. J., and Iezzi, A. M. (2017). Volcanic tremor and plume height hysteresis from Pavlof Volcano, Alaska. *Science*, 355(6320), 45–48. https://doi.org/10.1126/science.aah6108

Ichihara, M., Takeo, M., Yokoo, A., Oikawa, J., and Ohminato, T. (2012). Monitoring volcanic activity using correlation patterns between infrasound and ground motion. *Geophysical Research Letters*, 39, L04304. https://doi.org/10.1029/2011GL050542

Lyons, J. J., Iezzi, A. M., Fee, D., Schwaiger, H. F., Wech, A. G., and Haney, M. M. (2020). Infrasound generated by the 2016–17 shallow submarine eruption of Bogoslof volcano, Alaska. *Bulletin of Volcanology*, 82(19). https://doi.org/10.1007/s00445-019-1355-0

Matoza, R. S., and Fee, D. (2014). Infrasonic component of volcano-seismic eruption tremor. *Geophysical Research Letters*, 41, 1964–1970. https://doi.org/10.1002/2014GL059301

McKee, K., Fee, D., Haney, M., Matoza, R. S., and Lyons, J. (2018). Infrasound signal detection and back azimuth estimation using ground-coupled airwaves on a seismo-acoustic sensor pair. *Journal of Geophysical Research: Solid Earth*, 123, 6826–6844. https://doi.org/10.1029/2017JB015132

Picone, J. M., Hedin, A. E., Drob, D. P., and Aikin, A. C. (2002). NRLMSISE-00 empirical model of the atmosphere: Statistical comparisons and scientific issues. *Journal of Geophysical Research*, 107(A12), 1468. https://doi.org/10.1029/2002JA009430

Ruigrok, E., Gibbons, S., and Wapenaar, K. (2017). Cross-correlation beamforming. *Journal of Seismology,* 21(3), 495–508. https://doi.org/10.1007/s10950-016-9612-6

Schwaiger, H. F., Iezzi, A. M., and Fee, D. (2019). AVO-G2S: A modified, open-source Ground-to-Space atmospheric specification for infrasound modeling. *Computers & Geosciences*, 125, 90–97. https://doi.org/10.1016/j.cageo.2018.12.013

Schwaiger, H. F., Lyons, J. J., Iezzi, A. M., Fee, D., and Haney, M. M. (2020). Evolving infrasound detections from Bogoslof volcano, Alaska: Insights from atmospheric propagation modeling. *Bulletin of Volcanology*, 82(27). https://doi.org/10.1007/s00445-020-1360-3

Shani-Kadmiel, S., Assink, J., Fee, D., and Evers, L. (2018a). *Special Event: North of Anchorage, Alaska: International Monitoring System (IMS) array IM.I53US*. Retrieved from http://ds.iris.edu/ds/nodes/dmc/specialevents/2018/11/30/north-of-anchorage-alaska/

Shani-Kadmiel, S., Assink, J. D., Smets, P. S. M., and Evers, L. G. (2018b). Seismoacoustic coupled signals from earthquakes in central Italy: Epicentral and secondary sources of infrasound. *Geophysical Research Letters*, 45(1), 427–435. https://doi.org/10.1002/2017GL076125

Appendix 2. Preliminary Chapter 3 Work

This appendix presents preliminary research for chapter 3, which was presented as an online poster at the online Annual Geophysical Union conference in December 2020. This material focuses more on reverse time migration (RTM) techniques than chapter 3, and uses entirely unsupervised noise reduction methods. Authors, affiliations, acknowledgments, resources, and references are as per chapter 3.

Title

Infrasonic backprojection with the EarthScope Transportable Array in Alaska: Improving detection and localization of explosive volcanism via noise reduction

Abstract

The current deployment of the EarthScope Transportable Array (TA) in Alaska affords an unprecedented opportunity to study explosive volcanic eruptions using a relatively dense regional seismoacoustic network. Since 2016, seven volcanoes have erupted in Alaska with a range of magnitudes and styles. The 2016–2017 eruption of Bogoslof in particular produced seventy explosive eruptions. Such events provide a unique validation data set to examine the ability of different network configurations and processing strategies to detect, locate, and characterize remote volcanic eruptions in Alaska. When incorporating the TA and regional infrasound stations, a simple envelope-based backprojection technique, and automated event identification process, is able to capture up to 85% of the infrasound generating events from Bogoslof that were cataloged by the Alaska Volcano Observatory (Sanderson et al., 2020). Notable limitations to the scheme come from anisotropic atmospheric propagation, and low signal-to-noise (SNR) conditions, with wind being the dominant noise source. Here we focus on improving waveform data processing to reduce noise and so enhance signal detection and source location accuracy during backprojection. Additional evaluation metrics include degree of SNR improvement, any signal distortion, need for manual data labeling, and computational cost. The latter point is particularly relevant to real-time data processing applications. We compare a range of recently developed techniques that separate signals and noise in the spectral domain, including within the same frequency band. Examples include block thresholding, non-negative matrix factorization, and singular spectrum analysis. Such noise reduction on individual waveforms (i.e., pre-stack processing) can improve many basic analyses, given that SNR enhancements do not rely on combining traces (or stacking of other functions; i.e., co-stack strategies) in order to improve coherence and isolate events. We further compare results of the pre- and co-stack methods (e.g., phase-weighting, adaptive F-statistic time-series), as well as combinations of both techniques. More broadly, trace-based noise reduction can increase the value of isolated infrasound sensors in places where an array, or spatial averaging equipment, is impractical.

A2.1. Background and Motivation

The EarthScope Transportable Array (TA) in Alaska affords an unprecedented opportunity to study explosive volcanic eruptions using a relatively dense regional seismo-acoustic network (Figure 1). Since 2016, seven volcanoes have erupted in Alaska with a range of magnitudes and styles, including 70 explosive eruptions from Bogoslof during

2016–2017 (e.g., Coombs et al., 2019). Notable limitations to infrasound source location techniques come from anisotropic atmospheric propagation, and low signal-to-noise (SNR) conditions, with wind being the dominant noise source. Here we focus on improving waveform data processing to reduce noise and so enhance signal detection and source location accuracy.

Signals from Bogoslof often have similar character to wind in both the time and frequency domains (Fee et al., 2020; also Matoza et al., 2011 re. Eyjafjallajökull), providing a challenge for noise-signal separation. In part this is due to attenuation and remote detection, but also the often submarine nature of the eruptions (e.g., Lyons et al., 2019).

In this study we use data from all infrasound sensors within 2,000 km of Bogoslof, including the TA, several arrays operated by AVO, and an array which is part of the International Monitoring System array (IS53).
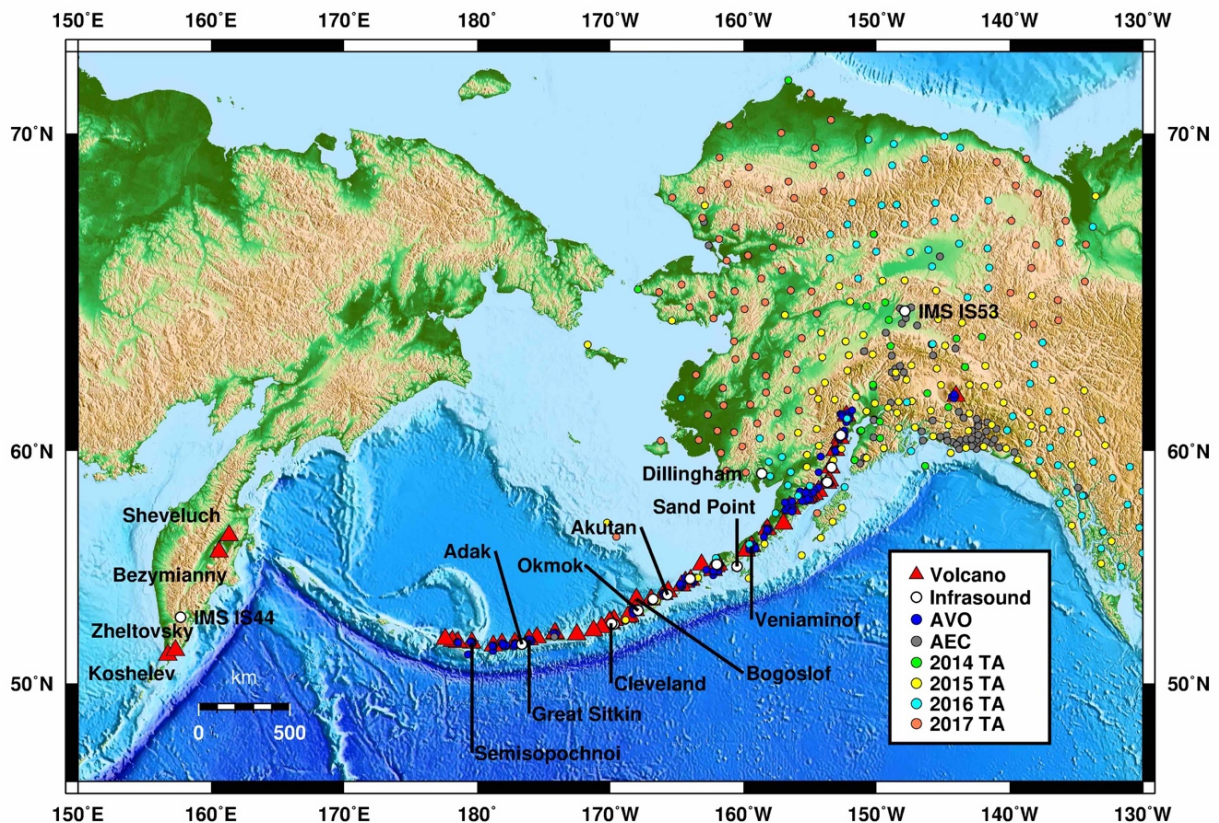

Figure 1. Locations of historically active volcanoes and available seismic (S) and infrasound (I) data in Alaska during the course of the Bogoslof eruption, 2016–2017. During 2020, several additional infrasound arrays have been installed by the Alaska Volcano Observatory in the Aleutian Islands. Some Transportable Array stations will be removed entirely starting from 2021, while others are being adopted by existing regional networks.

A2.2. Methodology

Backprojection is a "delay and stack" grid search approach for locating events. As per Figure 2, for each trial source location on a grid, sections of waveforms from each station are extracted, aligned, and stacked. The grid search is performed for a range of celerities (range/time, 250–350 m/s), and then we retain the highest amplitude from all stacks at each time step to form a detector function (DF). The grid node which gives the highest amplitude

in the DF is assumed to be the event source. Details of the data preprocessing, detection, and location methodologies can be found in Sanderson et al. (2020).

In this study, we compare how linear stacking compares to three advanced stacking techniques from seismology, namely: (1) phase-weighted stacking (PWS; Schimmel and Paulssen, 1997), (2) robust stacking (Pavlis and Vernon, 2010), and (3) selective stacking (Yang et al., 2020). Each of these "co-stack" methods, though differing in implementation, penalize traces that do not share common waveform elements, and thus noise is reduced.

We also examine the impacts of "pre-stack" noise reduction, which takes place on each individual trace prior to enveloping during preprocessing (Figure 2b). There is relatively limited literature on denoising individual seismic or infrasound traces (e.g., Cabras et al., 2012; Carniel et al., 2014; Zhu et al., 2019; Williams et al., 2020), as SNR enhancement is usually via stacking. Methods which don't require full supervision (training with signals and noise) enable the backprojection results to include non-volcanic events and facilitate application to a wider range of data sets.
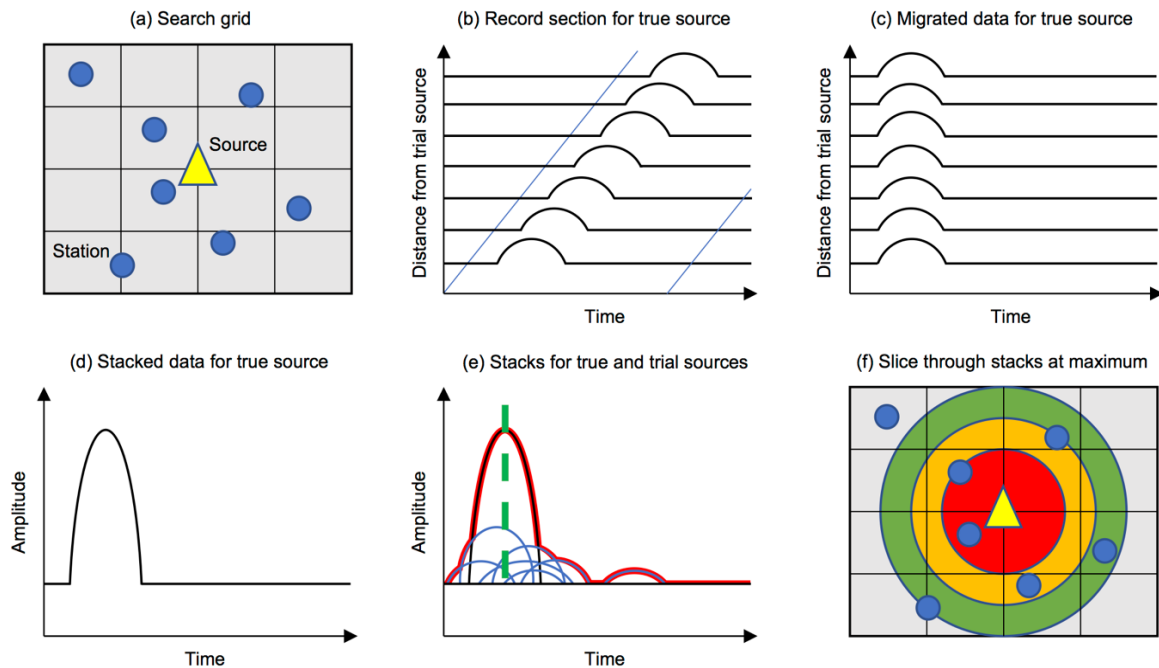

Figure 2. (a) Signal source and stations within a grid of trial source nodes. (b) Envelopes recorded by stations when using true source as the trial source. Data sections are extracted according to modeled celerity (diagonal blue lines). (c) Data sections from (b) are reverse migrated in time to the projected origin time. (d) The migrated data are stacked. (e) Stacks for all grid nodes. The stack for the true source (colored black) has the highest amplitude; stacks far from the true origin have small stacks (colored blue). A simple DF is the running maxima of all these stacks (colored red). The time of the DF maximum is marked with a green dashed line. (f) Contoured map of stack amplitudes at the time of the DF maximum in (e). Hotter colors toward the center are associated with stacks with higher amplitudes. Correct source locations are only provided by choosing times from (e) when the stack from the true source node is the highest.

For initial evaluation of pre-stack denoising methods we compared how well and how consistently different kinds of noise were reduced relative to volcanic signals for a range of distances, station designs, as well as computational times. We proceeded with a spectral noise gating method (after Sainburg and Amr, 2019). This method operates by masking trace

elements that have lower power frequency components than statistical thresholds derived from a designated noise-only section. For simplicity with this semi-supervised approach, the "noise" is set here to be the entire trace.

A characteristic example of the effectiveness of the method is shown in Figure 3, where the persistent background noise (primarily microbaroms) is effectively removed. The mean SNR in the band 0.1–5 Hz is 9.3 dB before denoising and 27.4 dB after denoising, representing a 295% increase in SNR by denoising. This calculation uses a window before the event as a noise estimate. Much of the wind noise at the end of the day remains however. Changes in the event amplitude and shape occur in both cases.
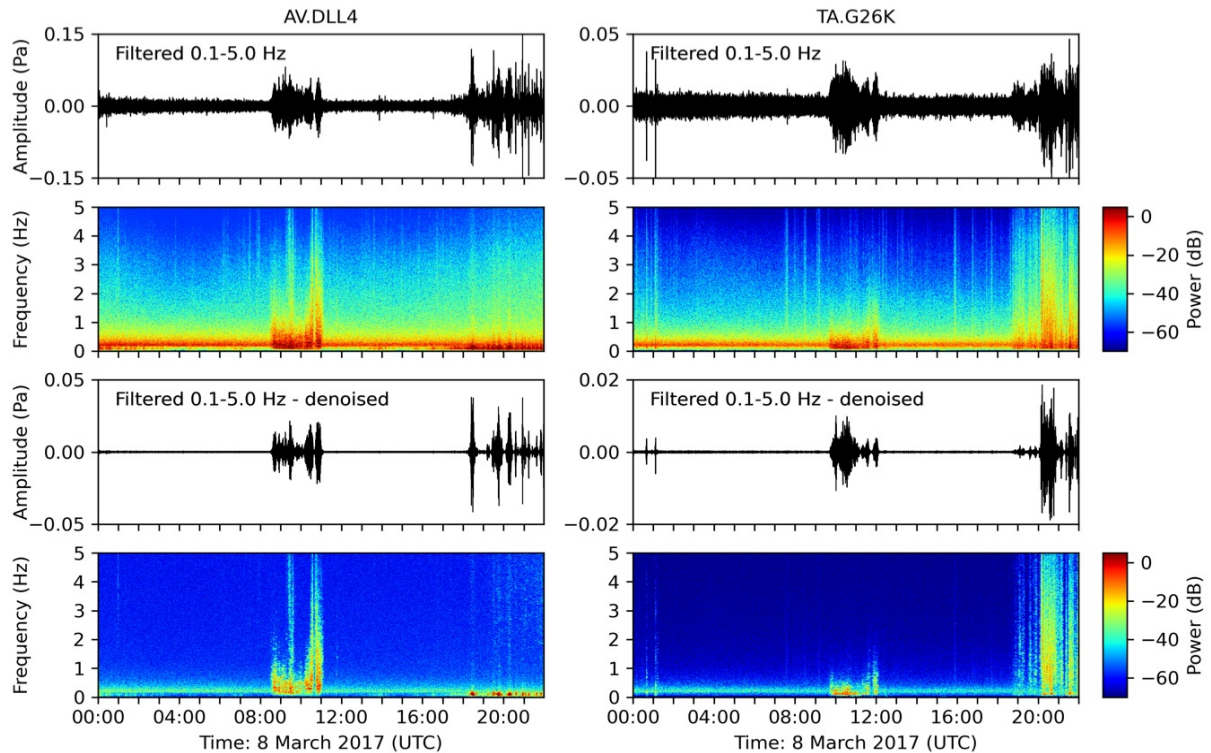

Figure 3. Waveforms and spectrogram examples showing before denoising (top) and after denoising (bottom) using a spectral gating method. Event from Bogoslof on 8 March 2017 (middle of day) recorded on station AV.DLL4 (left, 820 km away) and TA.G26K (right, 1,950 km away). The high amplitude oscillation at the end of day is assumed to be wind noise. The color scale has a reference of 1 Pa².

A2.3. Results

Figure 4 illustrates some effects that different processing options can have. Denoising does not affect the overall SNR of the DFs in this case, but does modulate the sharpness and amplitude of the DF peaks. This is important as location estimates are performed on the samples making up the tops of each peak. If the maximum values of DFs happen to represent grid nodes far from the source, then the mislocation value (source distance error) will be high. Although the denoised robust stack will give relatively poor location estimates, the SNR is high enough to show a third pulse of the eruption, which none of the other combinations illustrate clearly.
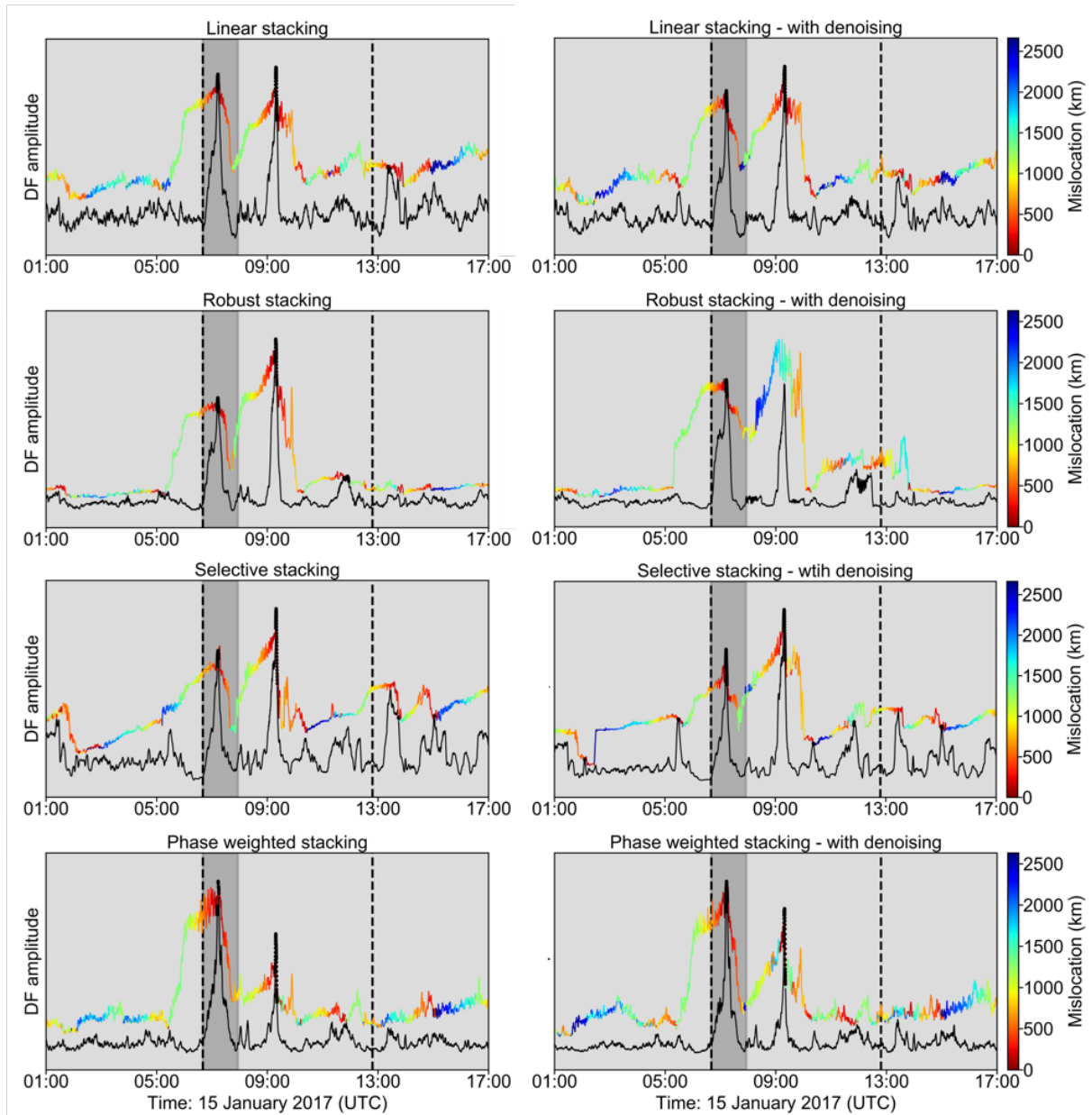
Figure 4. Examples of stacking methods used during this study using event from Bogoslof on 15 January 2017, with and without denoising during preprocessing. The black trace is the stack of traces assuming Bogoslof is the source location. The colored trace is the DF. Mislocation is the distance of the corresponding grid node from Bogoslof. The vertical black dashed lines mark the duration of seismic activity based on the AVO catalog (Coombs et al., 2019), and the dark grey shaded area is the cataloged infrasound activity. Black dots show intersections of the Bogoslof stack and DF, implying those parts represent the true source location.

Table 1 also contains a measure of the area under a receiver operating characteristic (ROC) curve, which is a metric showing how well a detection scheme correctly classifies detections against a catalog of events. An area of 1 would indicate there is a DF threshold above which all cataloged events (with recorded infrasound) are detected, and there are no false positives. A 0.5 area value indicates thresholds have no ability to discriminate.

These results are generally affected by the change in stratospheric wind direction over the course of the eruption (Sanderson et al., 2020; Schwaiger et al., 2020). A more detailed analysis of relative performance between the schemes for different kinds of events and different time periods is left to future work.

Table 1. Performance of processing schemes outlined in this paper. CPU times are calculated using a 3.1 GHz processor on a stack of 119 traces of length 17,280 samples (24 hours at 0.2 samples per second). The selective stack results use a correlation coefficient threshold of 0.3, and PWS uses a power of 2. The detection threshold is 12.5 dB.

	Linear stack		Robust stack		Selective stack		PWS	
	Noisy	Denoised	Noisy	Denoised	Noisy	Denoised	Noisy	Denoised
Mean area under monthly ROC curve (%)	75	70	73	70	74	72	76	70
Event detection vs. AVO infrasound catalog (/61)	70.5% + 2 others	68.9% + 1 other	70.5% + 2 others	67.2% + 3 others	60.7% + 1 other	70.5% + 2 others	73.8% + 4 others	68.9% + 3 others
Median mislocation for detected events (km)	350	365	373	483	360	524	505	518
Mean CPU time (s)	0.0007		0.04		0.03		0.16	

A2.4. Discussion

Denoised traces may lead to higher mislocation if waveform shapes are changed to the extent that waveform features no longer align. Another factor is that signals with very low SNR are reduced further as they fall below the statistical thresholds for the denoising mask. These factors also affect event detection rates.

A limitation to the performance of all the stacking methods comes from the way in which celerities were used to account for variable travel times in the atmosphere. Use of a realistic propagation model would likely improve the alignment of arrivals and thus SNR (e.g., Shani-Kadmiel et al., 2018).

The common/general processing parameters used here were primarily tuned for noisy linear stacking, whereas other common parameters may work better depending on the configuration. Similarly, the effects of tuning parameters for the denoising and stacking methods could be explored.

Future work could focus on the impulsive wind components specifically. Some approaches show promise in this regard, but perform inconsistently. Figure 5a shows how wind noise at the end of the day is reduced well by methods 2 and 3. This station has a mechanical noise filter such that the wind character is constrained to a narrow band below that of the event (Figure 3). This enables methods 2 and 3 to discard the stationary and relatively low frequency wind.

In contrast, Figure 5b shows how these same two methods preserve the wind but remove the signal as it is now the event that is relatively stationary and low frequency vs. the wind (Figure 3). Methods 4 and 5 however, which are essentially methods 2 and 3 operated in reverse, preserve the event rather than the wind (unlike in Figure 5a). Method 1, which is used for the results in Table 1, is relatively consistent in retaining more of the event at each station, but the SNR changes little vs. the wind.
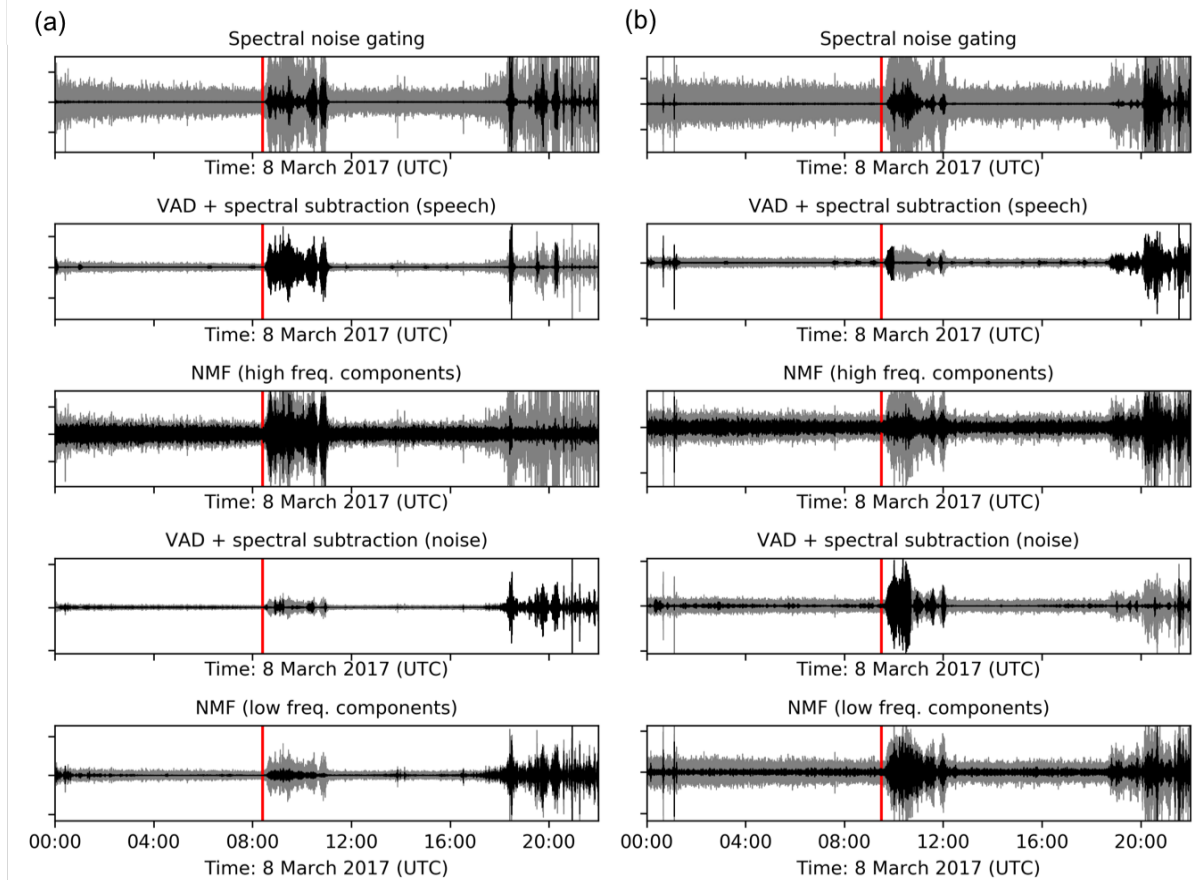
Figure 5. Bogoslof eruption on 8 March 2017. (a) Comparison of trace-denoising strategies at station AV.DLL4 (infrasound array element, 820 km from source). Gray traces are filtered 0.1-5 Hz, black traces are denoised gray traces. Y-limits are scaled to the extremes of the denoised data. Red lines indicate the predicted onset based on AVO catalogs and a celerity of 280 m/s. VAD = Voice Activity Detection, after Boll (1979) (https://doi.org /10.1109/ICASSP.1979.1170696). NMF = Non-negative Matrix Factorization, a process of dividing a time-frequency representation into components which can then be clustered and masked to retain only the components of interest. (b) As per (a), but for station TA.G26K (1,950 km from source).

A2.5. Conclusions

A "one scheme fits all data sets" signal enhancement strategy is a challenging task due to potentially high variability in signal and noise character at the same infrasound station over the space of a few hours. In the preliminary results presented here, we find that linear and PWS stacking strategies perform best. Computationally, it is more efficient to enhance the SNR of backprojected data during pre-stack processing than during stacking itself. Trace-based denoising using a spectral gating approach typically did not benefit results with the Bogoslof data set. Future success will likely require a semi-supervised approach with a cascade of signal-noise separation algorithms involving adaptive processing. For data sets where signals and noise share fewer properties, denoising algorithms may be simpler, and the benefits to backprojection more pronounced.

Noise reduction on individual waveforms can likely improve results from many analysis types aside from location strategies and is an important area of future study. More broadly, trace-based noise reduction can increase the value of isolated infrasound sensors in places where an array, or spatial averaging equipment, is impractical.

Appendix 3. Popocatépetl Deployments

Following the November 2019 CONVERSE (Community Network for Volcanic Eruption Response) meeting in Fairbanks, Alaska, a website began development in order to share practical information about volcano infrasound, and make infrasound science more accessible to a wider community (https://sites.google.com/view/volcano-infrasound/home). Part of this website includes "best practices" for installing infrasound sensors under a range of scenarios. I was asked to contribute to the section on long-term installs, and chose to describe work at Popocatépetl volcano, Mexico, that I participated in during my PhD program. The following focuses on a deployment from 2017 to 2018, as well as introduces the station design deployed in 2021, which continues to operate at the time of writing. I was primarily responsible for designing and building the seismoacoustic stations in the first project, as well as the infrasound stations in the current deployment. This material is standalone, and not referred to elsewhere in the dissertation.

A temporary seismoacoustic station (ATLI) was deployed from September 2017 to June 2018 at Atlimeyaya (Puebla, Mexico) by representatives of Universidad Nacional Autónoma de México (UNAM), and the University of California, Santa Barbara (UCSB) (Figure 1a). This site was chosen in order to determine the value of regional infrasound stations for observing eruptive activity from Popocatépetl volcano, 15.8 km to the west-northwest. Some of the site considerations included: (1) ability to house the footprint of the infrasound array, equipment vault, and solar panels; (2) permission of the local community, (3) security; (4) ease of access/visiting; (5) shape and directivity of the crater; (6) local noise sources; and (7) the presence of nonvolcanic sources with similar back azimuths to Popocatépetl.

The infrasound component of the station used four Hyperion IFS-3111 sensors (Figure 1b) to form a triangular array (aperture ~50 m), with a central element. Each sensor had a high-frequency shroud to reduce wind noise, and capability to record pressures ±500 Pa on scale (1,000 Pa full-scale range). The vertical and radial components from a broadband seismometer (Nanometrics 120-s Trillium Compact Posthole), co-located with the central infrasound sensor, were also recorded. Sensor cables were buried in conduit within trenches, and infrasound sensors hidden within vegetation. A six-channel REF TEK 130S digitizer recorded the data at 200 Hz. The system was powered by ~200 W of solar, with panels attached to the roof of a building, and angled based on the latitude and winter sun elevation (Figure 1c). The panels were grounded to a buried copper post. The battery, solar charge controller, digitizer, and fuse system were housed inside the building in a small metal cabinet (Figure 1d). The primary installation challenge was creating and sealing a port in the building wall for cables to pass through.

The kind of system described can be used where site security is good as large solar panels are easily visible from distance, and the array footprint makes it potentially conspicuous, with the multiple sensors often being unattended. Cable conduits should be buried to a depth such that they cannot be unearthed by e.g., animals, vehicles, and changes in land use, etc. Consideration should be given to nonvolcanic hazards, such as earthquakes, flooding, and lightning, which may affect the site. These factors are particularly important in cases where a station is not telemetered, as such issues will not immediately be discovered.

For the current deployment at Popocatépetl (2021+), we are using modified station designs, employing single infrasound sensors rather than arrays, in order to minimize station

footprints and maximize the number of potential sites that can be occupied. The sensors are housed inside the enclosure, with a hose connecting the sensor to the atmosphere. A flexible design allows the enclosure to be placed inside or outside a building, with lengths for the sensor hose, and cables for GPS and solar panels easily customizable (Figure 1e). Several of the stations use a Chaparral Model 64 (M64) ultra-high pressure (UHP) sensor (±1,000 Pa), which uses less power than the aforementioned Hyperions, enabling smaller solar panels. The relatively high dynamic range M64s were selected for the closest sites to the volcano in order to avoid waveform clipping. Infrasound sensors, including the Hyperion, can often be set up (at purchase) with any peak to peak amplitude range, however. For this experiment, each infrasound sensor is also co-located with a broadband seismometer.

In terms of logistical challenges, one of the foremost is identifying appropriate locations that address the aforementioned site requirements. This reconnaissance work requires several trips to evaluate a range of potential sites and establish any specific installation considerations. A second challenge is transporting equipment between the USA and Mexico. Long-term but still temporary imports such as these require administrative preparation and documentation to make sure there are no critical holdups in customs or airport security. Equipment has been taken on aircraft with field personnel, as well as shipped. This latter option enables travel arrangements to be made only once equipment clears customs.

Results from the 2017–2018 deployment focus on air to ground signal coupling of five well-recorded Vulcanian explosions. Please see Matoza et al. (2019) and Mendo-Pérez et al. (2021) for further details of the research, and http://ds.iris.edu/mda/5K/ATLI/ for additional instrumentation specifications and data access.
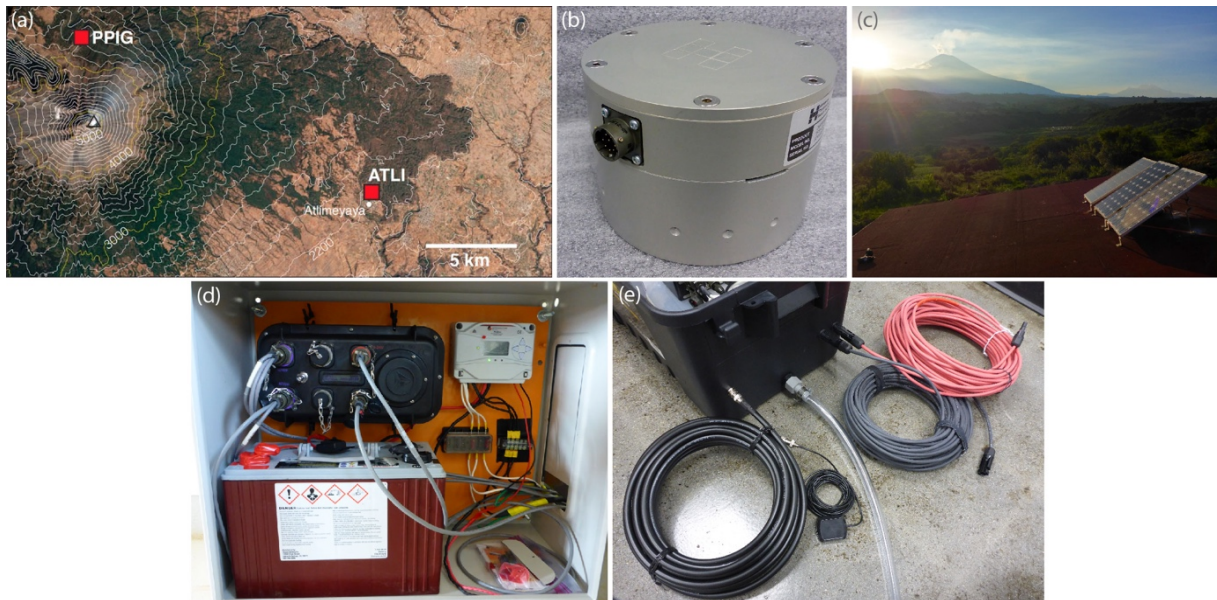

Figure 1. (a) Geometry of Popocatépetl and the ATLI array, after Matoza et al. (2019). PPIG is a seismic station operated by the Servicio Sismológico Nacional (SSN), of the Instituto de Geofísica, Universidad Nacional Autónoma de México (UNAM). (b) Hyperion sensor deployed at the ATLI array, from 2017–2018. (c) Solar panels at ATLI, with Popocatépetl in the background. (d) ATLI electronics enclosure, featuring a digitizer, battery, solar controller, and fuse system. (e) Station design for 2021+ Popocatépetl deployments. Lengths for the GPS cable, sensor hose, and solar panel cables can be easily customized and attached to external ports on the vault.

References

Matoza, R. S., Arciniega-Ceballos, A., Sanderson, R. W., Mendo-Pérez, G., Rosado-Fuentes, A., and Chouet, B. A. (2019). High-broadband seismoacoustic signature of Vulcanian explosions at Popocatépetl volcano, Mexico. *Geophysical Research Letters*, 46, 148–157. https://doi.org/10.1029/2018GL080802

Mendo-Pérez, G., Arciniega-Ceballos, A., Matoza, R. S., Rosado-Fuentes, A., Sanderson, R. W., and Chouet, B. A. (2021). Ground-coupled airwaves template match detection using broadband seismic records of explosive eruptions at Popocatépetl volcano, Mexico. *Journal of Volcanology and Geothermal Research*, 419, 107378. https://doi.org/10.1016/j.jvolgeores.2021.107378

Fin